CRANFIELD INSTITUTE OF TECHNOLOGY

SCHOOL OF MECHANICAL ENGINEERING

DEPARTMENT OF FLUID ENGINEERING AND INSTRUMENTATION

Ph.D THESIS

Academic Year 1991-1992

Y. F. XU

THEORETICAL AND EXPERIMENTAL STUDY OF TURBINE FLOWMETERS

Supervisor: Dr. J. HEMP

February 1992

This thesis is submitted for the degree of
DOCTOR OF PHILOSOPHY

IMAGING SERVICES NORTH
Boston Spa, Wetherby
West Yorkshire, LS23 7BQ
www.bl.uk

VOLUME CONTAINS CLEAR OVERLAYS

OVERLAYS HAVE BEEN SCANNED SEPERATELY AND THEN AGAIN OVER THE RELEVANT PAGE

To YIYUN

SUMMARY

A vortex shedding model is developed to predict the flow fields around turbine flowmeter blades. This model is used to simulate the flow separation and reattachment in the leading edge areas and the wake flows of the blades. Lewis's inverse blade design method is developed and quite successfully applied to simulate the displacement effect of the separation bubbles in the leading edge areas.

A new method is introduced to apply the Kutta condition in unsteady flows around the blades with separation points on a blade surface or the flow with blade interaction. This method does not require a large amount of iterative calculation.

A model is built up to predict the turbine flowmeter performance when the inlet flow conditions are known. The panel method is applied to predict the inlet flow conditions for the cases without inlet swirl.

An experimental study of the flow inside a turbine flowmeter is carried out using Laser Doppler Anemometry(LDA) to measure the throughout velocity fields around a flowmeter at different flowrates and with different inlet swirls. A clear picture of the flow field is thus obtained. The measured results are also used to validate the developed turbine flowmeter performance prediction model.

The numerical prediction are tested with experimental results. The theoretical and experimental data agree with each other very well in the cases without inlet swirl and reasonably well in other tested cases with inlet swirl.

ACKNOWLEDGEMENTS

I am sincerely grateful to whose who gave me any pleasure and help during the time of this work. Many friends of mine and members of the department, both staff and students, have offered their invaluable help and continuous encouragement from the very beginning of my time in Cranfield. Particularly, I would like to thank

H.K. Versteeg for his invaluable guidance in my first year, the great effort who has made to help me in the progress of this work and the continuous help after his leaving.
Dr John Hemp for the enormeous help he gave to me until the finish of this work.
Professor R.C. Baker for his encouragement and technical guidance at the beginning of my experimental work.
D. MacLeod who can always give me the wanted signals through his great electronic talent and his wonderful personality.
Professor M.L. Sanderson for the generous department financial support of my last year and his hospitality.
Dr M.V. Morris for her readiness to sort out my grant and administration probelms.

From all of them, I have learned a great deal and those will be beneficial to me through my life.

In addintion, I would like to thank the **Chinese Government** for the grant of my living expenditure in the past several years and **British Council** for the sponsorship of my study.

Finally and never the least, I would to pay my tribute to my wife, **Yiyun Chen**, who helped me to pass the most diffcult time of my life and suffered so much during the time of this work. It is her who make the possibility of the completion of this work. I shall never be able to adequately express my gratitude for the love and support she has shown me.

CONTENTS

English Symbols

A	area
$A_{i,j,k}$	velocity coefficient at the ith point by the vorticity associated with γ_j in the kth panel
b	flat plate half thickness
$b_i(s,t)$	stream function boundary value at point s and time t
B	blade thickness
C	blade chord
C_d	drag coefficient, $D/(\rho U_\infty^2 C/2)$
c_f	blade surface friction coefficient
C_ℓ	lift coefficient, $L/(\rho U_\infty^2 C/2)$
C_p	pressure coefficient, $p/(\rho U_\infty^2/2)$
$d(P,Q)$	distance between point P and point Q
D	diameter
D_h	hydraulic diameter
e	internal energy per unit mass
$e(x)$	relative uncertainty of variable x
f	friction coefficient
f_d	laser doppler frequency
f_s	frequency difference between the two laser beams after their bragg cells
$\vec{F}$	fluid body forces
F	forces
F_m	mechanical friction inside flowmeter bearing

F_μ	viscous friction inside flowmeter bearing
h	gap inside flowmeter bearing
Δh	total energy jump between flow regions
H	shape parameter of boundary layer, δ^*/θ
$H1$	boundary layer parameter, $(\delta-\delta^*)/\theta$
i	unit vector of the imaginary part of a complex variable
$Im[f(x_j)]$	imaginary part of a complex function $f(x_j)$
k	reduced frequency of oscillating blade
k_1, k_2, k_3	combination constants
K	laser constant
$K_{i,j}$	velocity coefficient of the jth point to the ith point;
$K'_{i,j}$	velocity coefficient of the jth shed vortex to the ith point
L	lift force
L_j	semilength of the jth panel
ℓ	length
LHS	left hand side of an equation
N	number of node point on blade surface
N_b	number of blades
N_v	vortex number inside wake
$\vec{n}$	unit vector in the normal direction
n_a	air refractive index
n_f	fluid refractive index
P	pressure
P_s	average pressure in a time period
$\vec{q}$	heat flux
q	source strength
Q	flowrate (m^3/h)
r	radius
R	given radius
R_{core}	vortex core size
Re	Reynolds number
Re^*	displacement thickness Reynolds number $u\delta^*/\nu$
Re_θ	momentum thickness Reynolds number $u\theta/\nu$
$Rea[f(x_j)]$	Real part of a complex function $f(x_j)$
Re_b	half blade thickness Reynolds number ub/ν

RHS	right hand side of a equation
s	coordinate along blade surface
s	position of point S (x_s, y_s)
S	space of cascade
Δt	time step
TI	turbulent intensity as a percentage
t	time
u,v	velocity components in x and y direction or axial and circumferential components
U_∞	magnitude of the free stream flow
U,V	velocities parallel and normal to the blade surface
V_b	normal velocity on the blade surface
U_c	pipe central velocity
U_e	velocity at boundary layer edge
U_r	rotating speed of rotor, ωr
V	velocity
V_c	vortex convective velocity
V_E	entrainment rate
$\vec{V}$	general velocity, u i + v j
v_a, v_r, v_Φ	axial, radial and circumferential velocity components
W	weight
w	relative velocity
x,y,z	coordinates
x',y'	relative coordinates
z	position of point Z (x_z, y_z)
$\bar{Z}$	inverse position of point Z

Greek symbols

α	flow angle or incidence angle
β	blade stagger angle
$E_{i,j}$	stream function coefficient at the ith point due to the jth panel
γ	vortex strength
δ'	distance of the nascent vortex for the body surface

δ	thickness of boundary layer
δ^*	displacement thickness of boundary, $\int_0^{\delta} \frac{(U_e-u)}{U_e} dy$
$\delta f(x_i)$	uncertainty of function $f(x_i)$
η	vortex diffusion velocity
ι	average gap inside a bearing
θ	momentum thickness of boundary layer, $\int_0^{\delta} \frac{u(U_e-u)}{U_e^2;} dy$
θ	half intersection angle(HIA) of the laser system or angle
$\Delta\theta$	radian of a panel
κ	curve curvature
λ	laminar boundary parameter, $\theta^2(du_e/ds)/\nu$
λ	wavelength of the laser beams
μ	fluid absolute viscosity
ν	kinematic viscosity, μ/ρ
ρ	fluid density
Γ	circulation
Γ_e	equivalent vorticity
Γ_o	vortex initial circulation
σ	vortex core
τ	shear stress
τ_w	shear stress on the wall surface
T	torque
T_b	bearing friction
T_d	driving torque
T_{disc}	disc friction torque
x	solid surface roughness
Φ	velocity potential
r,Φ,z	polar coordinates
Ψ	stream function
ω	angular velocity

Subscripts

a	air
b	body or boundary
crit	critical
e	edge of boundary layer
f	fluid
fw	far wake region
g	swirl generator
h	rotor hub
i	inviscid flow
i,j,k	node number
is	inlet section
l	lower surface
lw	leading edge wake
m	mean value
max, min	maximum and minimum
new, old	present and previous time step
r	radial direction or reattachment point
re	relative
ref	reflecting
s	separation point
sh	shear layer
sou	source
t	rotor tip
tw	trailing edge wake
u	upper surface
vor	vortex
w	wall surface
w	wake
x,y	in x and y direction
o	initial
∞	free stream flow
$+\infty,-\infty$	infinite far upstream and far downstream
Φ	angular corrdinate

LIST OF FIGURES

LIST OF TABLES

CHAPTER ONE

INTRODUCTION

The idea of the turbine flowmeter was first suggested by Robert Hooke that a small windmill might be used for measuring air velocity and a four vaned rotor was demonstrated for this purpose. About one hundred years later, German engineer Woltmannn developed a propeller current-meter for water velocity measurement(Hutton, 1986). The modern turbine flowmeter was first introduced in U.S.A. for measuring liquid fuel flow for rockets in 1930's and later for aircraft applications. Following the development of design methods and bearing materials, the modern turbine flowmeter has achieved good reliability, good repeatability, high accuracy, fast response, long life and tolerance to dirt, all at reasonable cost. Its digital output which is almost proportional to the flowrate makes flowrate measurements and flow totalization fairly straight forward. Nowadays, turbine flowmeters are widely used in process and control.

1.1 Meter Characteristics

Turbine flowmeters have been accepted as a proven technology for flow measurement with high accuracy and repeatability. However, because a turbine flowmeter usually consists of one rotor supported by hydrodynamic journal or thrust bearings, the moving parts are

inherent in the design and any physical alteration of certain parameters causes the flowmeter performance to change. The main factors influencing the performance include the meter design parameters, inlet velocity profile, fluid properties, installation and the working environments.

—— Flowmeter Parameters

The performance of a turbine flowmeter varies with its design parameters. These parameters include rotor blade shape and the stagger angle, surface finish, tip clearance, shape of the hub head and flowmeter bearing. Through a correct combination of these parameters, special requirements of a flowmeter can be achieved. However, any changes in these parameters cause the flowmeter performance to change.

The tip clearance (its shape and its size) contributes to the tip friction. By increasing the tip clearance, the inner part of the pipe wall boundary layer can be made to lie inside the tip clearance, so the rotor is subject to a more uniform velocity profile. Consequently the dependence of the flowmeter coefficient on the inlet velocity profile is decreased and the performance linearity can be improved. On the other hand, because the rotor only responds to the flow through it, some accuracy of the meter would be lost.

The condition of the flowmeter bearing is another major factor contributing to the linearity and repeatability of the turbine flowmeter. As the flow impinges on the rotor blade, a thrust load is developed which has to be borne by the bearing. In addition, the weight of the rotor is also supported by the bearing. When the meter is running at small flowrates, the bearing friction produces non-linear performance. For the gas turbine flowmeter, bearing friction produces its influence over a larger flowrate range.

The flowmeter inlet velocity profile is very much dependent on the flowmeter hub head shape. Generally speaking, the hub nose influence is reduced as the length of the straight hub section before the rotor increases.

—— Inlet Velocity

In most of the existing literature about turbine flowmeters, the

inlet velocity profile is assumed uniform. In order to maintain this requirement, a long straight upstream pipe section with flow straighteners, a long straight hub section before the rotor and a high hub-to-tip ratio are needed. Even so, the boundary layer on pipe wall and flowmeter hub would still distort the inlet velocity profile. In practical uses of a turbine flowmeter, it is always difficult to maintain the uniform inlet velocity condition. Additionally, the inlet velocity profile changes with the Reynolds number of the pipe flow. As the driving torque on the turbine flowmeter blades depends on the inlet velocity profile, the behaviour of a turbine flowmeter also changes with the pipe flow Reynolds number.

—— Fluid Viscosity

One of the disadvantages of the turbine flowmeter is its sensitivity to the metering fluid viscosity. Generally, the flowmeter's non-linear range increases progressively as the viscosity increases. However, the repeatability of the performance of the flowmeter is not affected as the viscosity changes. The influence of the viscosity is twofold. Firstly, the inlet velocity profile to the flowmeter changes with the viscosity. As the viscosity increases, the boundary layer displacement effect to the main flow becomes larger, the velocity distribution becomes more non-uniform from the hub to the tip. Secondly, viscosity produces shear flows on the blade surfaces, hence a friction force or a retarding torque is produced on the rotor. At the same time, the friction inside the bearing and the tip clearance also increase with the viscosity. These effects combine to lower the rotor speed as viscosity increases. As pointed out by Salami, the actual effect of viscosity on flowmeter performance very much depends on the design of the turbine meter. Salami's experimental results show a 40% drop of meter coefficient in the viscosity range 1 - 400 centistoke for a tested flowmeter(Salami, 1981). It is also important to note that the viscosity is a temperature dependent parameter. While a turbine flowmeter is applied in temperature changing environments, the flowmeter performance becomes temperature dependent.

—— Swirl Flow

All turbine flowmeters are designed and calibrated under the condition of swirl free flow. If swirl does occur in the flow, it causes a large change in the meter coefficient. Even if a flow straightener is installed before the flowmeter, the swirl cannot be diminished completely in most cases. As to the the influence of swirl, a most comprehensive study is conducted by Millington et al in NEL(1986). In their experiment, single bend and different combinations of double bends are adopted to generated swirl flows with different strengths. Several groups of commercial turbine flowmeters are examined at different distances from the swirl generator. The percentage of the meter factor change is small and never exceeds 0.5% for a single bend. Whereas the error for the double bend swirl is much bigger. The sign of the meter factor change depends on the sense of the swirl. A positive change corresponds to the swirl with the same direction as the rotor rotation, a negative change for the swirl against the rotor rotation.

1.2 Aim of This Study

Even though the turbine flowmeter has been widely used in industry, because of the manufacturing variations, every flowmeter has to be calibrated in a laboratory before it can be used and it has to be recalibrated regularly during its life. These calibrations increase turbine flowmeter application cost. On the other hand, laboratory calibrations cannot cover all the flow conditions which would be encountered by flowmeters in their applications. When the applying conditions are different from the laboratory ideal conditions, the measurement accuracy is doubtful. Aim to obtain an accurate turbine flowmeter performance curve under its real working conditions, numerical modelling is here adopted to achieve this objective.

Apart from numerical modelling, a deep and wide understanding of the flow patterns inside the turbine flowmeter under various inlet flow conditions is obtained through an experimental study. The experimental results are also used to validate the numerical model.

CHAPTER TWO

LITERATURE REVIEW

2.1 Flow Inside a Turbine Flowmeter Rotor

The physical laws, which govern the flow inside turbine flowmeters, are the conservation of mass, momentum and energy. These equations are

Continuity

$$\frac{\partial \rho}{\partial t} + \nabla \cdot (\rho \vec{V}) = 0 \qquad (2.1.1)$$

Momentum

$$\frac{\partial \vec{V}}{\partial t} + \vec{V} \cdot \nabla \vec{V} = \frac{-\nabla p}{\rho} + \vec{F} + \nu \nabla^2 \vec{V} \qquad (2.1.2)$$

Energy

$$\rho \frac{De}{Dt} = \frac{\partial E}{\partial t} - \nabla \vec{q} + \Phi^* \qquad (2.1.3)$$

here, $\partial E/\partial t$ is the rate of heat produced per unit volume by external agencies, ∇q is the rate of heat loss through conduction and Φ^* is the

energy dissipation function.

To solve these equations, one more equation relating pressure to density and temperature should be introduced.

As to the flow inside turbine flowmeters, the flow is assumed to be adiabatic, steady and incompressible; temperature keeps constant throughout a flowmeter. Viscous effects of the flow are restricted inside the boundary layers. The flow outside the boundary layers over blades, pipe wall and hub surfaces can be treated as an inviscid flow. The equations governing the flow outside these boundary layers are

$$\nabla \cdot \vec{V} = 0 \qquad (2.1.4)$$

$$\vec{V} \cdot \nabla \vec{V} = \frac{-\nabla p}{\rho} + \vec{F} \qquad (2.1.5)$$

$$\nabla e = 0 \qquad (2.1.6)$$

So the flow is governed by the Euler equations.

From the energy equation,the Bernoulli equation can be derived. It is

$$\frac{p}{\rho} + \frac{V^2}{2} + \frac{\partial \Phi}{\partial t} = \text{constant} \qquad (2.1.7)$$

While a turbine flowmeter is running under ideal design conditions, the flow is inviscid, the inlet flow to its rotor is uniform and swirl free, the friction inside the flowmeter bearing is also reduced to zero. Under these assumptions, the upstream and downstream velocities of the flowmeter rotor is in the axial direction and the flow inside the rotor is in an equilibrium state in radial direction. The equation is

$$\frac{dp}{\rho\, dr} = \frac{V_\Phi^2}{r}$$

However, the ideal design conditions can never be totally satisfied in actual applications of turbine flowmeters. The inlet velocity profile to the rotor is not uniform due to fluid viscosity, frictions inside the bearing and the tip clearance always exist. All these effects cause the velocity field throughout the rotor to be

different from that under ideal conditions, the flow inside the rotor is three dimensional. Fortunately, the radial velocity component is always quite small apart from in the areas very close to the hub and the tip, so the actual flow inside a turbine flowmeter rotor can be simplified to two dimensional flows on cylindrical surfaces with reasonable accuracy. All those two dimensional flows are governed by two dimensional Euler equations. The solutions to these two dimensional cylindrical flows are the solutions to their corresponding two dimensional potential cascade flows.

Two dimensional potential flow can be solved by a number of methods. Among them, conformal transformation, singularity method and finite element method have been successfully applied to the flow round airfoils. In recent years, great progress has been made in the application of finite difference and finite element techniques, but conformal transformation and singularity methods are still being used to solve some potential flow problems, especially for the flows around bodies with non-aerodynamic shapes. As to the flow around turbine flowmeter blades, the blades usually have the same rectangular shape, so flow separations occur at the sharp points on blade surfaces and wake flows would establish behind them. As pointed out by Strickland(1986), the most successful analytical treatments to date of the bluff body flows have involved the use of a vortex panel or vortex sheet representation of the body surface along with a discrete vortex representation of the wake. To simulate the flows around turbine flowmeter blades, the singularity method is adopted in this study. In this chapter, singularity methods and discrete vortex models for separated flow simulations are reviewed. Additionally, the methods for turbine flowmeter performance prediction are also included in this chapter.

2.2 Singularity Method

This method uses the linear property of the velocity potential function of singularities in a flow field. While there are a number of singularities inside a flow field, the total velocity potential at a point is the sum of the velocity potential of those singularities at

this point(Karamcheti, 1966). It can written as

$$\Phi = \Phi_1 + \Phi_2 + \Phi_3 + \ldots = \sum_{i=1}^{n} \Phi_i \qquad (2.2.1)$$

here Φ_i means the velocity potential of the ith singularity.

And the velocity components in the flow field are

$$u = \frac{\partial \Phi}{\partial x} = \sum_{i=1}^{n} \frac{\partial \Phi_i}{\partial x} \qquad (2.2.2)$$

$$v = \frac{\partial \Phi}{\partial y} = \sum_{i=1}^{n} \frac{\partial \Phi_i}{\partial y} \qquad (2.2.3)$$

For an individual singularity, Laplace's equation is satisfied, i.e.

$$\nabla^2 \Phi_i = 0 \qquad (2.2.4)$$

The linearity of the Laplace equation ensures the sum velocity potential of all these singularities also satisfies the Laplace equation, i.e.

$$\nabla^2 \Phi = \nabla^2 \sum_{i=1}^{N} \Phi_i = 0 \qquad (2.2.5)$$

Because Laplace's equation is automatically satisfied in the flow field with singularities, the flow problem becomes a boundary value problem.

In the general case, several bodies are moving with respect to each other. The boundary condition on these bodies should be a known function of time and positions for a solution using singularity method. The boundary condition can be written as

$$V = V_b(t,s) \qquad (2.2.6)$$

Three boundary conditions are usually used(Versteeg, 1987). One is the Dirichlet boundary condition,i.e. zero slip velocity condition as

used by Lewis(1981), it can be written as

$$\Phi(s,t) = b_1(s,t) \qquad (2.2.7)$$

The second is the Neumann boundary condition. It requires the normal velocity on the body surfaces to be zero as used by Kim and Mook(1985), i.e.

$$\frac{\partial\Phi(s,t)}{\partial n} = V_b(s,t) \qquad (2.2.8)$$

here $V_b(s,t)$ is the surface velocities of the bodies.

The last is a mixed boundary condition, i.e.

$$\Phi(s,t) = b_1(s,t) \qquad s \subset B_1 \qquad (2.2.9)$$

and

$$\frac{\partial\Phi(s,t)}{\partial n} = V_b(s,t) \qquad s \subset B_2 \qquad (2.2.10)$$

with $B = B_1+B_2$

In two dimensional flows, the stream function also satisfies Laplace's equation, i.e.

$$\nabla^2 \Psi = 0 \qquad (2.2.11)$$

So the stream function can be used just as effectively as the velocity potential function in two dimensional flow simulations.

Flow analysis through singularity method requires exact satisfaction of the boundary condition on body surfaces. Usually, the body surfaces are divided into a number of elements and singularities are distributed on the elements. As a result of this discretization, a set of algebraic equations are obtained by enforcing the boundary condition on the elements. Solving these algebraic equations, the intensities of those discrete singularities can be obtained and consequently the flow field can be calculated.

A model given by Kelloy was reviewed by Hess et al(1966). This method is based on the integral equation of source distribution on a body surface. It can be used for flows around two or three dimensional bodies of arbitrary shape. To have an insight of the model, a unit source at point s is considered. The velocity potential at point z induced by this unit source is written as

$$\Phi = \frac{1}{d(z,s)} \qquad (2.2.13)$$

where d(z,s) is the distance between these two points.

While an arbitrary body is represented with distributed sources, the total velocity potential at point z due to all the sources on the body surface is

$$\Phi = \iint \frac{q(s)}{d(z,s)} ds \qquad (2.2.14)$$

Satisfying the boundary condition on the body surface, an equation is obtained by allowing the point z to approach a point on the body surface. The obtained equation is

$$2\pi q(z) - \iint \frac{\partial}{\partial n} \left(\frac{1}{d(z,s)} \right) q(s)ds + \vec{V}_\infty \cdot \vec{n}(z) = V_b(z) \qquad (2.2.15)$$

By applying boundary condition at a number of points on the body surface, a set of linear algebraic equations are obtained about unknown source densities on the body surface.

Vortices can also be employed to simulate potential flows around arbitrary body or bodies. In an inviscid flow, the velocity discontinuity from the stream velocity outside the body to zero on the body surface implies the existance of a vortex sheet between them. To simulate the flow around a body, the body surface is represented by a number of continuous vortex elements which separates the outer stream flow to the inner motionless flow. Consider a vortex element with vorticity γds at position s, the velocity induced by this vortex element at position z in a two dimensional flow field is

$$V = u - iv = \frac{\gamma(s)ds}{2\pi i(s-z)} \qquad (2.2.16)$$

While the body is represented by distributed vortex elements, the total induced velocity at position z due to all the vortex elements on the body surface is

$$V = u - iv = \frac{1}{2\pi i} \iint \frac{\gamma(s)}{s-z} ds \qquad (2.2.17)$$

In cascade flow, there are a infinite number of bodies spaced apart with pitch S. If the cascade extends in the y direction, the velocity induced at position z by this cascade is

$$V = \frac{1}{2Si} \iint \gamma(s) \coth[\frac{\pi}{S}(s-z)] ds \qquad (2.2.18)$$

The total velocity at position z including the free stream flow is

$$V = u_\infty - iv_\infty + \frac{1}{2Si} \iint \gamma(s) \coth[\frac{\pi}{S}(s-z)] ds \qquad (2.2.19)$$

A successful model using surface vorticity to simulate single cascade flow was introduced by Martensen, this model was reviewed by Gostelow(1984). In the flow simulation, the vorticity distribution on a cascade surface is chosen so that the cascade surface is a streamline in the flow and the vorticity distribution is identical to the surface velocity. These conditions are satisfied by applying the boundary condition on the blade surface: zero normal velocity on the blade surface or zero tangential velocity just inside the surface vortices.

In the model, the positions of the vortices on the body surface are expressed as

$$s = f(\lambda') \qquad (2.2.20)$$

As the point z approaches the blade surface, its position can also be expressed using the same function as for the surface vortices, i.e.

$$z = f(\lambda) \qquad (2.2.21)$$

With the normal velocity boundary condition, the obtained equation is

$$2\mathrm{Im}[V_\infty f'(\lambda)] = \int \mathrm{Im}[K(\lambda,\lambda')]\gamma(\lambda')d\lambda' \qquad (2.2.22)$$

With the tangential velocity boundary condition, the obtained equation is

$$\gamma(\lambda) = 2\mathrm{Re}a[V_\infty f'(\lambda)] + \int \mathrm{Re}a[K(\lambda,\lambda')]\gamma(\lambda')d\lambda' \qquad (2.2.23)$$

here the function $K(\lambda,\lambda')$ is given as

$$K(\lambda,\lambda') = \frac{1}{iS} f'(\lambda) \coth\{\frac{\pi}{S}[f(\lambda')-f(\lambda)]\} \qquad (2.2.24)$$

Further analysing the flow, the position function $f(\lambda)$ is written as

$$f(\lambda)=m(\lambda)+in(\lambda) \qquad (2.2.25)$$

Substituting (2.2.25) into equation(2.2.23), the obtained equation is

$$\gamma(\lambda)= 2u_\infty m'(\lambda)+2v_\infty n'(\lambda) + \int k(\lambda,\lambda')\gamma(\lambda')d\lambda' \qquad (2.2.26)$$

where

$$k(\lambda,\lambda') = \frac{1}{S} \frac{n'(\lambda)\sinh\{\frac{2\pi}{S}[m(\lambda)-m(\lambda')]\}-m'(\lambda)\sin\{\frac{2\pi}{S}[n(\lambda)-n(\lambda')]\}}{\cosh\{\frac{2\pi}{S}[m(\lambda)-m(\lambda')]-\cos\{\frac{2\pi}{S}[n(\lambda)-n(\lambda')]\}} \qquad (2.2.27)$$

Applying these equations to the divided body surface as shown in fig.2.1, the resulted algebraic equations are

$$V_\infty(s_m) + \sum_{n=1}^{N} K(s_m,s_n)\gamma_n\Delta s_n = 0 \qquad m=1,2,3,... \qquad (2.2.28)$$

When the body contour is smooth, the influence coefficients satisfy

$$\int k(\lambda,\lambda')ds = 1 \qquad (2.2.29)$$

Martensen synthesized the flow from a combination of three basic

flows as shown in fig.2.2. These three flows are: a flow with zero inlet angle and zero circulation, a flow with 90 degree inlet angle and zero circulation, and a flow with unit circulation.

The equations governing these three basic flows are:

$$\begin{cases} a(\lambda) - \int k(\lambda,\lambda')a(\lambda')\,d\lambda' = 2m'(\lambda) \\ \int a(\lambda')\,d\lambda' = 0 \end{cases} \tag{2.2.30}$$

$$\begin{cases} b(\lambda) - \int k(\lambda,\lambda')b(\lambda')d\lambda' = 2n'(\lambda) \\ \int b(\lambda')\,d\lambda' = 0 \end{cases} \tag{2.2.31}$$

$$\begin{cases} \gamma(\lambda) - \int k(\lambda,\lambda')\gamma(\lambda')d\lambda' = 0 \\ \int \gamma(\lambda')d\lambda' = 1 \end{cases} \tag{2.2.32}$$

$a(\lambda)$ is the solution to the flow with zero inlet angle and zero circulation;

$b(\lambda)$ is the solution to the flow with 90 degree inlet angle and zero circulation;

$\gamma(\lambda)$ is the solution to the flow with unit circulation.

The combination is controlled by the kinematic condition of the cascade flow. The synthesized result is

$$v(\lambda) = \frac{\left[u_\infty a(\lambda) + 0.5\,(v_{+\infty}+v_{-\infty})\,b(\lambda) + \Gamma\,\gamma(\lambda)\right]}{\sqrt{m'(\lambda)^2 + n'(\lambda)^2}} \tag{2.2.33}$$

u_∞ is the x component of the velocity infinitely far upstream of the cascade;

$v_{+\infty}, v_{-\infty}$ are the y components of the velocities infinitely upstream and downstream of the cascade.

Γ is the circulation around the individual cascade blade.

2.3 Separation and Wake Simulations

2.3.1 Vortex Shedding

In the singularity method, the boundary value should be a continuous function of positions along body surfaces for a unique

solution, so the body surfaces should have continuous smooth contours In the flow around a body with a sharp edge, the infinite curvature produces a discontinuity of the blade surface. In this kind of flow, Kutta-Joukowsky condition should be satisfied at the sharp point for a unique solution, this condition is named as the Kutta condition. Under the Kutta condition, continuous static pressure distribution is required at a sharp edge, i.e.

$$P_l = P_u \qquad (2.3.1)$$

As the result of the velocity discontinuity at this sharp point, vortices may be shed into the flow.

As pointed out by Giesing(1969), the intensity of the shed vortex is directly related to the velocity at the sharp edge point. The vortices in the wake must have been physically located on the body surface before being swept into flow as free vortices. While they are locating on the body surface, their vorticity intensities are equal to the velocity difference cross the boundary layers at the shedding points and their convective velocities are half the local velocities. In inviscid flow, the thickness of the boundary layer on the blade surface is infinitesimal, the shed vortices start from their separation points on the surface and their vorticities keep constant in their movement.

In the potential flow around an airfoil with sharp trailing edge as shown in fig.2.3, the Bernoulli equation can be applied on the blade surface. The equation derived from the Bernoulli equation relates the blade circulation to the velocities at the trailing edge points as

$$\frac{\partial(\Phi_l-\Phi_u)}{\partial t} = \frac{\partial \Gamma}{\partial t} = \frac{1}{2}\left(U_u^2 - U_l^2 \right) \qquad (2.3.2)$$

Equation(2.2.2) is given by Basu and Hancock(1978) and as well as Poling(1986).

In unsteady flow, velocity discontinuity indicates a change of blade circulation. As a result of this circulation change, vortices are shed from the trailing edge.

Two vortex shedding models have been used in the past: fixed nascent vortex position and variable nascent vortex position. In the

fixed position model, the shed vortices go into the wake from a selected point(called velocity point) near the separation point. The velocity at this point is used to calculate the vortex shedding rate. The shedding rate is

$$\frac{\partial \Gamma}{\partial t} = 0.5U_s^2 \qquad (2.3.3)$$

The selected shedding position of nascent vortices is interpreted as boundary layer edge at the separation point by Kiya and Arie(1977, 1980). However, in accordance with the fluctuation of the separated shear flow, the thickness of the boundary layer at a separation point would oscillate in a certain range. The edge position of the shear layer at a separation point can not be predicted accurately due to the singularity. In the application of this model, the position of the selected point is decided on the basis of previous experience and trial calculations.

In the calculation of the separated flow behind a flat plate at a very large incidence angle by Kiya et al, the fixed point is called the velocity point, as shown in fig.2.4. The distance from the velocity point to the plate surface was examined in the range $\delta'/2\ell$ =0.01—0.015. ℓ is the plate semilength. In the computational trials, the simulation was found to be rather irregular for $\delta'/2\ell$ =0.01. A general satisfactory simulation was obtained for $\delta'/2\ell$ =0.015.

The second model was used by Sarpkaya(1975) to simulate the flow around a circular cylinder. In this model, the vortex shedding rate is

$$\frac{\partial \Gamma}{\partial t} = 0.5U_{sh}^2 \qquad (2.3.4)$$

U_{sh} is the average transportation velocity of the first four vortices from each shear layer at the separation point.

The nascent vortex position is chosen to satisfy the Kutta condition and the no-slip boundary condition at the separation point.

When this model is used to simulate the separated flow around a cylinder, the nascent vortex is placed at a point with distance δ' over the cylinder surface(with its image at the inverse point) at the separation point with a suitable time step. The position of the nascent vortex is

$$z_j = (1+\frac{\delta'}{R})\exp[i(\pi-\theta_{s,j})] \qquad (2.3.5)$$

and

$$1+\frac{\delta'}{R} = \frac{1+|\Gamma_j|/(2\pi U_{s,j})}{1-|\Gamma_j|/(2\pi U_{s,j})} \qquad (2.3.6)$$

In the calculations, it is found that the position and circulation of the nascent vortices have a strong influence on the predicted forces and pressures. Practically, the circulations of the shed vortices decays in time and space. In equation(2.3.3), the vorticity of a nascent vortex depends on the selected velocity position. So it is important to chose a right starting position so as to obtain the correct amount of circulation reduction to simulate fluid viscosity.

2.3.2 Vortex Shedding for Separation Simulations

Vortex shedding method can be used with either conformal transformation or the singularity method to simulate the separated flow around bodies. Conformal transformation is mainly used for the flows around bodies of rectangular or circular shape. In the simulation of the flow around a circular cylinder by Sarpkaya and Schoaff(1979), the flow is represented by a doublet located at the centre of the cylinder and vortices are shed into the flow from mobile separation points. To maintain the cylinder surface to be a streamline in the flow field, every vortex in the wake flow has its image vortex with the same strength at its inverse point inside the cylinder in this model. The complex potential of the flow field is

$$w(z) = -V_\infty\left(z+\frac{R^2}{\bar{z}}\right)+\frac{i}{2\pi}\sum_{m=1}^{N_v}\Gamma_m\left[\ln(z-z_m)-\ln\left(z-\frac{R^2}{\bar{z}_m}\right)\right] \qquad (2.3.8)$$

The vortex shedding rate is

$$\frac{\Delta\Gamma}{\Delta t} = 0.5U_s^2 \qquad (2.3.9)$$

The positions of the nascent vortices are chosen so to satisfy the Kutta condition at the edge of the body.

Convection of the vortices in the wake flow is governed by

$$z_i(t+\Delta t) = z_i(t) + \Delta t\, \vec{V}_i \qquad (2.3.10)$$

Nagano et al(1982) analyzed a two dimensional flow past a rectangular prism with height h and depth d using a combination of conformal mapping and the vortex shedding method. The rectangle is transformed to a circle and separated vortices are shed into the flow at fixed points near the image of the rectangle corner points. The positions of these points are based on a boundary layer estimation. The predicted lift and drag show the same trend as measured data, but it fails to predict the large increase of drag in the vicinity of d/h=0.62.

Using the combination of conformal transformation with the vortex shedding model, the flow around airfoils can also be simulated. Poling et al(1987) used Joukowski's transformation to map the flow around an airfoil into a flow around a cylinder. Although the conformal mapping method can take the exact boundary condition into account, it is not always easy to transfer an arbitrary two dimensional body to a circle as pointed out by Kuwahara and Takami(1984). On the other hand, the use of conformal transformation for two dimensional flow requires a complicated rule to calculate the velocities in the physical plane(Sarpkaya, 1989).

Compared with conformal transformations, the singularity method can be used more directly and generally for flow simulations, even can be extended for separated flows. A surface vorticity model is given by Lewis(1981, 1983) to simulate flows around arbitrary two dimensional bodies. In this model, body surface is represented by panels of constant vorticity. Using the Dirichlet boundary condition, the governing equations of the flow are

$$\sum_{n=1}^{N} k(s_m,s_n)\gamma(s_n)\Delta s_n = -V_\infty[\cos(\alpha_\infty)\frac{dx_m}{ds} + \sin(\alpha_\infty)\frac{dy_m}{ds}]$$

$$- \frac{1}{2\pi} \sum_{k=1}^{N_v} \Gamma_k K'(s_m,s_k) \qquad (2.3.11)$$

where $k(s_m,s_n)$ are

$$k(s_m,s_n) = K(s_m,s_n) \qquad \text{for } m \neq n$$

$$= K(s_m,s_n) - 0.5 \qquad \text{for } m = n \qquad (2.3.12)$$

$K(s_m,s_n)$ and $K'(s_m,s_k)$ are the velocity influence coefficients of the vortices on a blade surface and inside the wake respectively.

$$K(s_m,s_n) = \frac{1}{2\pi} \frac{-(x_m-x_n)(dy/ds)_m+(y_m-y_n)(dx/ds)_m}{(x_m-x_n)^2+(y_m-y_n)^2} \qquad (2.3.13)$$

For a body surface with curvature, the self induced influence velocity coefficient of an element is modified to

$$k(s_m,s_m) = -\frac{1}{2} + \frac{\Delta\theta_m}{4\pi} \qquad (2.3.14)$$

Using this method, the separated flow around a cylinder was predicted. The predicted surface pressure distribution upstream of the separation points is in good agreement with experimental data.

In the singularity model, the boundary condition is only satisfied at a limited number of points on the body surface. Surface leakage due to the boundary condition approximation could cause some errors in the solution. One method to compensate for this disadvantage is to use velocity potential function or stream function on the body surface to calculate the velocity on every element instead of directly calculating the velocity at the control point. In this approximation, the average velocity on every element of the body surface satisfies the boundary condition.

Sarpkaya and Ihrig(1986) used the stream function in their simulation of impulsively started steady flows about rectangular

prisms. The predicted and measured normalized forces show reasonable agreement with respect to the frequency of oscillations, i.e., the Strouhal number is correctly predicted. However, the amplitudes of the predicted forces are somewhat larger.

Using the discrete vortex method to simulate separated flows around airfoils, several models have been proposed. Vezza et al(1985a) used the method to predict interaction between an airfoil and its wake. In the simulation of a impulsively-started flow and the flows around an oscillating blade, vortices are shed from the blade trailing edge. The vortex shedding rate is controlled by the Kutta condition at the trailing edge as equation (2.3.2) and one vortex is shed in to the wake flow in every time step. The vorticity of the nascent vortex is obtained using Kelvin's theorem, i.e.

$$\Delta\Gamma = \Gamma_b(t) - \Gamma_b(t+\Delta t) \qquad (2.3.15)$$

The position of the nascent vortex is decided from the trailing edge flow. The nascent vortex leaves the blade trailing edge in the same direction as the local streamline and the distance of it from the trailing edge is equal to the convective distance in one time step. Because the nascent vortex intensity is related to the trailing edge velocity, and this velocity is an unknown in the calculation, the solution is obtained iteratively.

In the model proposed by Krammre(1982), wake flow is a combination of a steady and an unsteady part. The steady part is simulated by two parallel rows of contrarotating point vortices lying behind the blade. These vortex rows start from a fixed point near the airfoil trailing edge and the strengths of the vortices are determined so as to produce the Reichardt velocity distribution along the wake central line between the two vortex rows. The velocity distribution in the wake centre is

$$V_m = 0.98 \sqrt{c_d/x} \qquad (2.3.16)$$

here x is the distance from the blade trailing edge.

The unsteady wake is taken into consideration by allowing vortices to shed from the trailing edges. Their vorticities are obtained using Thomsons'theorem of constant circulation rate with respect to time of the flow field.

Vezza et al(1985b) also develop a model for the flow around aerofoils with separation on blade surface. In this flow, the flow around an airfoil is divided into several regions by the separation lines from the separation points on the blade surface. A difference in the total energy exists on crossing the bound from one region into another.

The obtained Kutta condition from the separated flow is

$$\frac{\gamma_s^2}{2} - \frac{\gamma_n^2}{2} = \frac{\partial \Gamma}{\partial t} \qquad (2.3.17)$$

In the calculation, the separation point on the blade surface is given apriori. One vortex is shed from the separation point in every time step in the local separation line direction, this direction is found through iterative calculation.

Psarudakis used both vortices and sources to simulate wake flow. In the calculation, the meanline of an airfoil wake is assumed from the trailing edge and it is represented by consecutive line segments. The viscous wake displacement thickness effect is simulated by sources with an intensity of

$$q(s)=d(U_e\delta^*)/ds \qquad (2.3.18)$$

The viscous curvature effect is represented by vortex distributions with intensity of

$$\gamma(s)=-\kappa U_e(\delta^*+\theta) \qquad (2.3.19)$$

where κ is the curvature of the mean wake streamline.

Oliver(1982) proposed a double vortex sheet method for the viscous flow around an airfoil. This double vortex sheet method is a development of single vortex sheet which defines a potential function which can describe a flow with the same mass and momentum flux as the viscous flow. In this model, the two vortex sheets have equal strength and the transport velocity of the inner layer is one third of the outer layer transport velocity, their positions are decided by boundary layer consideration. This model allows the modelling of the integral properties of the viscous region and retains the advantages of potential flow.

2.4 Boundary Layer Calculation

The discrete vortex method can also be used for boundary layer simulations(Chorin, 1978). The intensity of the created vortex sheets over body surface for boundary layer simulation per unit length is

$$\gamma = \int_{\delta}^{\delta} \frac{\partial u}{\partial y} dy = u_e \qquad (2.4.1)$$

The motion of these vortices inside the boundary layer is described by boundary layer equations and approximated by following formulae

$$\begin{aligned} x_i(t+\Delta t) &= x_i(t) + u_i \Delta t \\ y_i(t+\Delta t) &= y_i(t) + v_i \Delta t + n_i \end{aligned} \qquad (2.4.2)$$

where n_i is the diffusion velocity,

The more widely used model to calculate the effect of the boundary layer is to simulate the displacement of the boundary layer to the main flow by adding a displacement thickness onto the blade surface. However, because of the huge computer time involved in the iterative calculation and the sensitivity of the Kutta condition to the growth of the boundary layer near the trailing edge, direct adding of displacement thickness has convergence difficulty. To overcome this difficulty, sources are placed on the line elements which are used in the surface vorticity method for displacement simulation(1975). The strength of these sources given by Lighthill(1958) are

$$q = \frac{d(U_e \delta^*)}{ds} \qquad (2.4.3)$$

In the simulation, the blade surface remains a streamline in the flow field.

The displacement thickness of boundary layer can be calculated only when the boundary layer integral equation is combined with the equations of laminar and turbulent boundary layers. In the integral equation, the velocity at the boundary layer edge is required. In the first order approximation of boundary layer, the velocity on the blade

surface is used to approximate the velocity at boundary edge.

The integral equation of the boundary layer with second order accuracy was introduced by East(1981). In this model, the inviscid velocity on the blade surface is required instead of the velocity at the boundary layer edge. The resulted integral boundary equation is

$$\frac{d\bar{\theta}}{ds} - (\bar{H} + 2 + M_{iw}^2)\frac{\bar{\theta}}{U_{iw}}\frac{d(U_{iw})}{ds} - \frac{\tau_w}{\rho_{iw}U_{iw}^2} = 0 \qquad (2.4.4)$$

where $\bar{\theta}$ and $\bar{H}$ are the boundary layer momentum thickness and shape parameter based on the velocity on the blade surface.

To simulate the displacement effect of the boundary layer in this model, a transpiration velocity (normal velocity) is enforced on the body surface. This velocity is given by

$$\rho_{iw}V_{iw} = \frac{d(\rho_{iw}U_{iw}\delta^*)}{ds} \qquad (2.4.5)$$

Combining the integral equation with the entrainment equation and the lag-entrainment equation, Hastings(1987) et al used this model to predict the maximum lift on airfoil NACA 4412 with separated boundary layer. The predicted results are in good agreement with the experimental data.

Using the normal velocity concept, the aerodynamics of the parachute can be simulated by the discrete vortex method. The normal velocity given by Strickland(1986) is a function of the pressure difference cross the parachute surface as

$$\frac{V_n}{V_\infty} = \frac{(\Delta c_p)^{0.5}}{K} \qquad (2.4.6)$$

where K is a flow coefficient based on the parachute porosity.

2.5 Vortex Models for Flow Simulation

Since the vortex method was first introduced by Rosenhead, many techniques have been proposed to improve the stability and reality of

the simulated results as reviewed by Leonard(1980). Owing to the increase in calculating speed and storage of modern computers, the discrete method has been applied to simulate complicated flows. During its applications, several vortex models have been commonly used.

——— *Point vortex*

The point vortex method was first introduced by Rosenhead in 1931. In this model, the movement of a free vortex sheet is approximated by a system of vortex elements. The vorticity on each vortex element is concentrated into a finite number of point vortices for simulation proposes. The velocity components induced by those point vortices are

$$u_{i,j} = -\frac{1}{2\pi} \sum_{\substack{j=1 \\ i\neq j}}^{N} \frac{(x_i - x_j)\,\Gamma_j}{|d_{i,j}|^2}$$

$$v_{i,j} = \frac{1}{2\pi} \sum_{\substack{j=1 \\ i\neq j}}^{N} \frac{(y_i - y_j)\,\Gamma_j}{|d_{i,j}|^2} \qquad (2.5.1)$$

But in many cases, the motion of the involved vortices achieves a chaotic state. As given by Saffman and Baker(1979), some investigators tried to get rid of this irregular motion by increasing the number of the used vortices with decreased vorticities, but too many vortices can create even more serious singular effects. Point vortex simulations cannot produce a reasonable simulation of some flows.

——— *Vortex core*

It has been shown that the vortex chaotic motion in point vortex model is due to the velocity singularities at the locations of the point vortices and their vicinity. To avoid this problem, vortex bubble method is widely accepted. In this model, every vortex has a finite core over which its vorticity is distributed. Various distributions have been assumed, such as a Gaussian distribution, constant velocity distribution and constant vorticity distribution and so on.

Kuwahara and Takami(1973) proposed a vorticity distribution using the Navier–Stokes equation for a single point vortex. Γ used in equation (2.5.1) is

$$\Gamma=\Gamma_0*\{1-\exp(\frac{\sigma^2}{4\nu t})\} \qquad (2.5.2)$$

where Γ_0 and σ are starting vorticity and core size of a vortex respectively. Due to diffusion, the core size increases with time is $\sqrt{4\nu t}$.

Chorin(1973) introduced a linear vorticity distribution. Here Γ in equation (2.5.1) is:

$$\Gamma=\begin{cases}\Gamma_0 & d>\sigma\\ \Gamma_0 d/\sigma & d<\sigma\end{cases} \qquad (2.5.3)$$

Chorin(1973) also suggested a core with stream function as

$$\Psi=\begin{cases}\Gamma\ell og(d)/2\pi & d>\sigma\\ \Gamma(d/\sigma)/2\pi & d<\sigma\end{cases} \qquad (2.5.4)$$

Spalart et. al(1981) used a simple distribution which can get rid of the singular effect completely. Γ in the equation (2.5.1) is

$$\Gamma=\frac{\Gamma_0 d^2}{d^2+\sigma^2} \qquad (2.5.5)$$

Hence, the simulation accuracy is very much dependent on the used core size. Clement and Maull(1975) believe that the model of discrete vortex with core is justifiable and useful results can be obtained provided a fine balance is drawn between using a large number of vortices to represent the fine scale and a crude integration scheme to suppress the chaotic motion. There are several different opinions about the core size. Chorin(1973) takes $2\pi\sigma$ equal to the average distance ℓ between the vortices along the boundary on which the vortices are created. On the other hand, Milinazzo and Saffman(1977) believe that σ should be as small as possible and take σ as $\ell/50$. But Hald and Prete(1978) suggest that σ should be in order of $\ell^{2/3}$. Due to the variations of these parameters, i.e. vortex core size and

vorticity distribution over the core, the solution of this method depends on them to some extent.

Panaras(1987) examined the vortex/airfoil interaction using both discrete point vortices and vortex with core when vortices pass by an airfoil. In the discrete method, a large vortex is approximated by four layers of vortices with small vorticity. In every layer, the vorticity is uniformly distributed over a number of finite cores. The pressure distribution along the blade surface is calculated using both models. When the vortex is far from blade surface, both methods give the same results. But when the vortex is close to the blade surface, the pressure pulse on the blade surface produced by the finite core method is significiently smaller and smoother than that by discrete point vortices.

——— *Vortex panel*

In the vortex panel model, a vortex sheet is divided into a number of straight or curved segments with polynomial vorticity distribution. The singularity effect is proportional to $1/d^2$ in the point vortex model, but drops to $\ln(1/d)$ in the panel model near the panel ends. In first order panel simulation, straight segments are used and the distribution of vorticity is linear on every segment. In second order panel simulation, the curvature of a panel is considered and the second derivative of the singularity distribution along the panel is constant. The panels used for vortex sheet representation are chosen in such a way that the spatial discretization error is uniform along the sheet. The size of these panels depends on the curvature of the vortex sheet. A criterion given by Hoeijmakers(1983) for chosing the panel size is

$$\Delta s = \min(\Delta_{max},\ r\Delta\theta_{max}) \qquad (2.5.6)$$

here Δ is the basic panel size, $\Delta\theta_{max}$ and r are the radian and the average radius of a panel.

In a flow simulation, panels are orientated in the local velocity direction and there is no static pressure difference across them.

——— *Vortex-in-cell*

The vortex-in-cell is a powerful method to decrease the computing time and remove vortex singularities. In two dimensional flow, the

flow field is divided into meshes. The vorticity inside a mesh is allocated to its four corner points according to an area weight scheme as shown in fig.2.5 (Leonard, 1980). The allocated vorticities are

$$\Gamma_i = \Gamma_n A_i / A^2 \qquad i=1,2,3,4 \tag{2.5.7}$$

where A is the area of the cell in which the nth vortex is resided and Γ_i are the allocated vorticities at the mesh corner points.

In two dimensional, incompressible and inviscid flow, the Poisson equation is

$$\nabla^2 \Psi = -\Gamma \tag{2.5.8}$$

In the calculation, Poisson equation is expressed as

$$\left(\frac{\partial^2}{\partial^2 x} + \frac{\partial^2}{\partial^2 y}\right)\Psi_{i,j} = -\Gamma_{i,j} \tag{2.5.9}$$

When the vorticities at all the corner points are known, the stream function $\Psi_{i,j}$ can be obtained by solving the above equation using finite difference techniques. And the velocity field can calculated using the following formulae

$$u_{i,j} = \frac{\Psi_{i,j+1} - \Psi_{i,j-1}}{2\Delta\ell}$$

$$v_{i,j} = \frac{\Psi_{i+1,j} - \Psi_{i-1,j}}{2\Delta\ell} \tag{2.5.10}$$

where $\Delta\ell$ is the dimension of the meshes.

An example of using Cloud-in-cell vortex mothod is given by Graham and Basuki(1984) simulating the unsteady flows through a cascade. The lift distortion caused by the wake flow from the upstram of the blades was computed.

2.6 Turbine Flowmeter Performance Prediction Review

The main effects which influence a turbine flowmeter performance given by Furness(1982a, 1982b) are

(1) Flowmeter design parameters,

(2) Bearing,

(3) Fluid properties, such as viscosity and density,

(4) Flowmeter working enviroments, such as temperature and pressure across the flowmeter;

(5) Its installation.

An accurate performance prediction of a turbine flowmeter can be obtained only when all of those influences are carefully approximated. The most basic performance prediction can be obtained directly using the angular momentum approach. Although this prediction can give reasonable results, it cannot satisfy the accuracy requirement in modern industries, especially when a turbine flowmeter is running in conditions which are different from its design and calibration conditions. Many attempts have been made to obtain an accurate predictions of flowmeter performance under various applying conditions.

Lee and Karlby(1960) presented a model of turbine flowmeter performance in viscous flow. The model is restricted to steady, incompressible and viscous flows. Using two dimensional flow assumption, the flow from the hub to the tip is represented by the flow on an average section. The radius of this average section is

$$\bar{r} = \left(\frac{r_t^2 + r_h^2}{2} \right)^{1/2} \qquad (2.6.1)$$

By applying the angular momentum conservation law, the driving torque on the average section can be obtained. When the turbine flowmeter achieves its equilibrium state at certain flowrate, the derived meter coefficient is

$$\frac{\omega}{Q} = \left(\frac{\tan\beta}{\bar{r}A} \right) - \left(\frac{T_b}{\bar{r}\rho Q^2} \right) - \left(\frac{T_f}{\bar{r}\rho Q^2} \right) \qquad (2.6.2)$$

If the mechanical friction inside flowmeter bearing is ignored and the rotor blade is assumed to be thin, smooth and aerodynamic, the viscous resistance to the rotor is then mainly due to the blade form drag and the secondary flow drag. The form drag is a function of

Reynolds number and the secondary drag is a function of flow velocity. The derived equation for the flowmeter coefficient thus becomes

$$\frac{\omega}{Q} = \frac{\tan\beta}{\bar{r}A} - K_1 C_s - K_2 C_f \qquad (2.6.3)$$

where C_f and C_s are the blade surface skin friction coefficient and secondary flow friction coefficient.

When the flowmeter is working at different flowrates, the flow inside the flowmeter is in a different state, different skin friction coefficients are needed to calculate the corresponding skin friction and secondary flow friction. Using this model, the hump section of a flowmeter calibration curve is predicted as the flow state on the blade surfaces changes from laminar to turbulent.

An experimental investigation was done by Jepson(1969) to examine the inlet velocity influence on the flowmeter performance. In this theory, the inlet flow profile is assumed to be axi- symmetric and the flowmeter bearing friction is ignored. The derived meter coefficient is

$$\frac{n}{AU_m} = \frac{r_o^2}{2KA} \frac{\int_{r_h}^{r_t} \left(\frac{U}{U_{max}}\right)^2 r^2 dr}{\int_o^{r_o} \left(\frac{U}{U_{max}}\right) r dr \int_{r_h}^{r_t} \left(\frac{U}{U_{max}}\right) r^2 dr} \qquad (2.6.5)$$

This formula shows that the meter coefficient is a constant for constant inlet velocity profile.

In their experimental study, symmetric and asymmetric flows were induced in the flowmeter inlet by mounting axisymmetric and asymmetric orifices at the front of the flowmeter. The difference in the flowmeter coefficient is very significant among those tested cases. In actual applications of turbine flowmeters, bends and valves in the pipe line could create distortions to the inlet velocity profile. Consequently, changes can be caused in the flowmeter performance.

An extensive investigation of the tip clearance influence on a turbine flowmeter performance was made by Hutton and Tan(Hutton, 1982). In the model, the total flowrate through a flowmeter includes

the flowrate through the rotor Q_r and the flowrate through the tip clearance Q_c. Only the flowrate Q_r contributes to the flowmeter performance and Q_c is a leakage flowrate. The flowmeter coefficient is

$$\frac{n}{Q} = \frac{n}{Q_r}\left(1 - \frac{Q_c}{Q}\right) \qquad (2.6.5)$$

Because the leakage flow varies with the metering flowrate, the flowmeter coefficient changes accordingly. However an empirical relation between the leakage flowrate and the total flowrate is found as

$$\frac{Q_c}{Q} = g - \frac{k}{Q} \qquad (2.6.6)$$

where g and k are constants.

Combining equation(2.6.5) and equation(2.6.6), the flowmeter coefficient is written as

$$\frac{n}{Q} = \left(P - \frac{R}{Q^2}\right)\left(1 - g - \frac{k}{Q}\right) \qquad (2.6.7)$$

where P and R are functions of flowmeter blade lift, drag coefficients, retarding torques and blade geometries.

In equation(2.6.7), the performance of a flowmeter depends on the balance between Pk/Q and $R(1-g)/Q^2$. The hump section of a flowmeter calibration curve can be explained. The rising section of the calibration curve will only occur if the value of k is sufficiently big compared with the retarding torque. This happens when the tip clearance is large. Also there is no rise section in the calibration curve in a flowmeter with a small tip clearance.

Salami(1984) built a model in which both blade wake flow and tip leakage flow were considered. The lift and drag coefficients of the turbine blades are here correlated from the data of a single flat plate. The lift coefficient is

$$C_\ell = 2\pi\alpha \qquad (2.6.8)$$

The drag coefficient is

$$C_d/C_{do} = 0.045\alpha^2 + 0.104\alpha + 1 \qquad (2.6.9)$$

The influence of the wake flow is approximated by adopting finite

span wing theory. The wake flow causes a modification in the inlet attack angle to the blade. The modification is

$$\Delta\alpha = \frac{C_\ell}{F(AR,\tau)} \qquad (2.6.10)$$

The leakage flow inside the rotor tip clearance causes a retaining lift at the blade tip. This leakage flow V_t is a function of tip clearance size, attack angle at the tip section and the resistance inside the tip clearance. The torque caused by the leakage flow is

$$T_t = BV_t^2 \qquad (2.6.11)$$

Under these assumptions, the equation for the flowmeter performance can be derived. In the prediction, the tip leakage flow constant B is assumed to be constant for all flowrates, so the leakage flow only causes an overall rise and fall of the flowmeter calibration curve and no horizontal distortion is produced by the tip clearance. This model can be used for the flowmeter with inlet swirl providing the inlet velocity profile is known.

Blows(1981) built a model based on aerodynamic considerations of the flowmeter blades. In this model, the assumptions of symmetric inlet flow, free swirl and no deviation of the flow leaving the blade trailing edge are made. Then order magnitude analysis is used to examine all the lift and drag forces on the rotor. The derived flowmeter coefficient only depends on the driving torque and the retarding torques of the blade form drag and the bearing. The equation is

$$T_d - T_f - T_b = 0 \qquad (2.6.12)$$

In this model, it is found that the tip clearance and the viscosity have a particular effect on the meter performance. From the predicted results, an overall rise and horizontal distortion of the performance curve are found as the tip clearance changes. Viscosity causes the rise section to be delayed and smoothed in flowmeter calibaration curve. These results general agree with the experimental data. The predicted results show that the performance of a meter hinges on the behaviour of blade lift force from the hub to the tip.

Aim to present an analysis model for the meter coefficient under given flow conditions and meter geometry, Tsukamoto and Hutton(1985)

apply the angular momentum law to the blades in different radial positions. In this model, the flow deviation after the rotor is obtained from the boundary theory given by Schlichting. Considering the frictions of journal bearing, surface disk , the tip clearance and hub surface, the equilibrium equation for the meter is

$$T_d = T_b + T_h + T_t + T_{disc} \qquad (2.6.13)$$

After numerical approximations of the driving and those retarding torques, a dimensionless meter coefficient equation is derived. The meter coefficient is a function of Reynolds number, inlet flow condition and meter geometry. The predicted results are in agreement with experimental data, but this model is limited to helical flowmeters.

CHAPTER THREE

THE SINGULARITY METHOD

3.1 Introduction

Many investigators are currently doing research on the flow around blades or blade cascades. Although much progress has been made in this area, there are still many problems needed to be solved in the prediction of these flows. The singularity method is one of the methods for flow prediction and is especially popular in aerodynamic calculation. This method is powerful for modelling potential flow around arbitrary bodies and can also be used to simulate boundary layers and wake flows. Hess and Smith(1966) have concluded that a variety of two- and three- dimensional flows can be simulated by this method, but most of their attention is given to the method of source simulation. Martensen(Gostelow,1984) gives an extensive consideration of the vortex singularity method. Using the vortex method, good results are obtained by Wilkinson(1964).

A numerical model is described in this chapter for finding the solutions to incompressible two dimensional potential flows around blades or cascades, the boundary layer and the wake flow are not involved in this chapter. Vortex panels are used in this model and the Kutta condition is applied to obtain a unique solution to each of those flow problems.

To get a solution to a problem, the following information is required:

(1) blade geometry

(2) inlet flow condition

(the magnitude and the direction of the free stream flow)

(3) exit flow condition

(3.1) the angle of the flow leaving the blade trailing edge

or (3.2) the blade circulation

or (3.3) the Kutta condition.

Then the following results can be obtained:

(1) velocity distribution around the blade.

(2) pressure distribution around the blade.

(3) lift and drag coefficient of the blade.

(4) the blade circulation if it is not specified initially.

3.2 Algorithm

3.2.1 General Mathematical Description

The problem is to calculate the potential flow exterior to an arbitrary body R as given by following figure

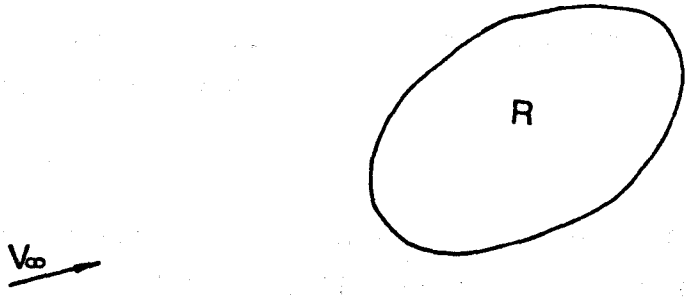

The fluid velocity at a point in the flow field is

$$\vec{V} = \vec{V}_\infty + \vec{V_1} \qquad (3.2.1.1)$$

where

$\vec{V}_\infty$ is the uniform free stream flow.

$\vec{V}_1$ is the velocity disturbance due to the body R.

In potential flow, the Laplace equation holds. So

$$\vec{V} = \text{grad}\ (\Phi) \qquad (3.2.1.2)$$

and

$$\nabla^2 \Phi = 0 \qquad (3.2.1.3)$$

The Neumann boundary condition is used in this model, i.e.

$$\frac{\partial \Phi}{\partial n} = V_b \qquad (3.2.1.4$$

or

$$\frac{\partial \Psi}{\partial s} = - V_b \qquad (3.2.1.5)$$

When the body is stationary, the normal velocity on the blade surface is zero, i.e.

$$V_b = 0 \qquad (3.2.1.6)$$

This is the solid boundary condition which states that there is no flow flux across the blade surface.

As well as the boundary condition, the Kutta condition has to be applied to obtain a unique solution to the problem. In the followings, the flows around blades or cascades are concerned, the Kutta condition is expressed as

$$C_{pl} = C_{pu} \qquad (3.2.1.7)$$

This equation comes from the requirement of the static pressure continuity around the trailing edge. Thus, the pressure coefficients at the points on both the upper and the lower surface at the blade trailing edge are equal. Equations from (3.2.1.5) and (3.2.1.7) together constitute a well posed problem for the solution to the potential flows around blades or cascades.

3.2.2 Flow Governing Equations

In order to get a solution to a potential flow around blades or blade cascades using the singularity method, the blade surface is divided into small straight elements and every element is represented by a vortex panel as shown in fig.3.1. The control point of every panel is chosen at its centre. When the endpoints of every panel are located on the blade contour and the panels are straight, the control point is not exactly on the blade contour unless the local curvature of the blade surface is zero as shown in fig.3.2. In the present model, the trailing edge is a discontinuous point and this point is not chosen as a panel endpoint, the two endpoints of the panels on the upper and lower surfaces near the trailing edge are located very close to the trailing edge, so the discrete contour is slightly open at the trailing point instead of a completely closed polygon. Under this discretization, there are N nodes on the blade contour and only N-1 control points are defined on the N-1 panels. If the panel size is properly chosen, the control point on every panel should approach close enough to the blade surface. The discretization is restricted by the total number of the panels used to represent the blade contour and the minimum size of a panel. Too many panels means too many unknowns in the calculation, a huge amount of computing time is then necessary and strong singular effects then exist between panels due to the small distances between them. However, the maximum size of a panel is also constrained by the suitability of the quasi-linear approximation to the continuous velocity distribution on the blade surface. Obviously, the accuracy of the method is sensitive to the size of the panel, so the resulted polygon must be an appropriate representation of the original blade contour. This can be achieved by using reasonably small panels in the region where the blade surface has large curvature so that the panels have a good representation to the original blade and the linear distribution is an accurate approximation of the large gradient of the velocity. Large panels can be used in the regions with low curvature.

The equations governing the flow around blades or cascades are obtained under the following conditions: (A) the boundary condition, equation (3.2.1.5) is satisfied at all the control points on the divided blade surfaces; (B) the Kutta condition, equation(3.2.1.7) is applied at every blade trailing edge.

In the flow field, the velocity at every point consists of the contributions from both the free stream flow and the vortices on the blade surfaces. The free stream flow is expressed as

$$\vec{V}_\infty = U_\infty (\cos \alpha_\infty \vec{i} + \sin \alpha_\infty \vec{j}) \qquad (3.2.2.1)$$

The normal component of the free stream flow at the ith control point on the blade surface is

$$V_{\infty,i} = U_\infty \left[\cos \alpha_\infty \left(\frac{dy}{ds}\right) - \sin \alpha_\infty \left(\frac{dx}{ds}\right) \right]_i \qquad (3.2.2.2)$$

here s is the coordinate along the blade surface from the trailing edge point on the upper side to the trailing edge point on the lower side.

In a two dimensional potential flow, the velocity components at a point are

$$U = \frac{\partial \Psi}{\partial n}$$

$$V = \frac{\partial \Psi}{\partial s} \qquad (3.2.2.3)$$

Where Ψ is the total stream function at a point in the flow field, including the influence of both the free stream flow and the blade surfaces. Because the free stream influence has already been expressed in equation (3.2.2.2), the stream function used in the following discussion only consists of the contribution from the vortices on the blade surfaces.

From equation (3.2.2.3), the normal velocity at a point on the ith panel induced by a vortex element on the jth panel is

$$\Delta V_{i,\Delta j} = \frac{\partial \Psi_{i,\Delta j}}{\partial s} \qquad (3.2.2.4)$$

where Δj denotes a vortex element on the jth panel.

The average normal velocity on the ith panel induced by the vortex element is

$$V_{i,\Delta j} = \frac{\int_{s_i}^{s_{i+1}} \Delta V_{i,\Delta j} ds_i}{\Delta s_i} \qquad (3.2.2.5)$$

where $\Delta s_i = s_{i+1} - s_i$

Substituting equation(3.2.2.4) into equation (3.2.2.5), the average normal velocity becomes

$$V_{j,\Delta j} = \frac{\int_{s_i}^{s_{i+1}} \frac{\partial \Psi_{i,\Delta j}}{\partial s_i} ds_i}{\Delta s_i}$$

$$= \frac{\Psi_{i+1,\Delta j} - \Psi_{i,\Delta j}}{\Delta s_i} \qquad (3.2.2.6)$$

The total average normal velocity on the ith panel induced by the whole jth panel is

$$V_{i,j} = \int_{s_j}^{s_{j+1}} V_{i,\Delta j} \, ds_j \qquad (3.2.2.7)$$

where j and j+1 are the node numbers of the jth vortex panel.

Substituting equation (3.2.2.6) into equation (3.2.2.7) , the obtained total normal velocity formula is

$$V_{i,j} = \frac{1}{\Delta s_i} \left[\int_{s_j}^{s_{j+1}} \Psi_{i+1,\Delta j} \, ds_j - \int_{s_j}^{s_{j+1}} \Psi_{i,\Delta j} \, ds_j \right]$$

$$= \frac{E_{i+1,j} - E_{i,j}}{\Delta s_i} \qquad (3.2.2.8)$$

here $E_{i,j}$ and $E_{i+1,j}$ are the stream function values at the ith and the (i+1)th nodes by the whole jth panel. Thus

$$E_{i+1,j} = \int_{s_j}^{s_{j+1}} \Psi_{i+1,\Delta j} \, ds$$

$$= \int_{s_j}^{s_{j+1}} \frac{\gamma}{2\pi} \ln|d_1| \, ds \qquad (3.2.2.9)$$

where

$$|d_i| = \sqrt{(x_{i+1}-x)^2 + (y_{i+1}-y)^2}$$

The vorticity distribution is assumed linear on each panel, so the vorticity distribution on the jth panel can be expressed as

$$\gamma = \gamma_j \frac{L_j - s}{2L_j} + \gamma_{j+1} \frac{L_j + s}{2L_j} \qquad (3.2.2.10)$$

where L_j is the semilength of the jth panel, s is the coordinate from the central point of the panel in the direction from the jth node to the (j+1)th node, γ_j and γ_{j+1} are the vortex strengths at the two nodes.

Substituting equation(3.2.2.10) into (3.2.2.9), the steam function $E_{i+1,j}$ is

$$E_{i+1,j} = \frac{1}{2\pi}\left[\gamma_j \int_{-L_j}^{L_j} \frac{L_j - s}{2L_j} \ln|d_i| ds + \gamma_{j+1} \int_{-L_j}^{L_j} \frac{L_j + s}{2L_j} \ln|d_i| \right] ds$$

$$= A_{i+1,j,j}{}^*\gamma_j + A_{i+1,j+1,j}{}^*\gamma_{j+1} \qquad (3.2.2.11)$$

where $A_{i,j+1,j}$ indicates stream function coefficient at the ith node due to the vorticity associated with the vortex strength γ_{j+1} on the jth vortex panel. The formula of $A_{i,j+1,j}$ is given in Appendix A.

The stream function $E_{i,j}$ is deduced in the same manner as $E_{i+1,j}$ and the obtained formula is

$$E_{i,j} = A_{i,j+1,j}{}^*\gamma_{j+1} + A_{i,j,j}{}^*\gamma_j \qquad (3.2.2.12)$$

Substituting $E_{i,j}$ and $E_{i+1,j}$ into equation (2.2.2.8), the average normal velocity in the ith panel induced by the j-th panel is

$$V_{i,j} = \frac{(A_{i+1,j+1,j} - A_{i,j+1,j})}{\Delta s_i} \gamma_{j+1} + \frac{(A_{i+1,j,j} - A_{i,j,j})}{\Delta s_i} \gamma_j \qquad (3.2.2.13)$$

Instead of using the local normal velocity at the control point as the boundary condition on each panel, the average normal velocity on

each panel is used in the present model. The total normal velocity on each panel on the blade surface induced by all the vortices on the blade surfaces can be written as

$$V_i = \sum_{j=1}^{N} K_{i,j}\,\gamma_j \qquad (3.2.2.13)$$

where $K_{i,j}$ is the total normal velocity influence coefficient on the ith panel due to the vorticity connected with the vortex strength γ_j. This vorticity is linearly distributed on the (j-1)th and the jth panels. The coefficients are

$$K_{i,j} = \frac{A_{i+1,j,j} - A_{i,j,j} + A_{i+1,j,j-1} - A_{j,j,j-1}}{\Delta s_j} \qquad 1 < j < N$$

$$= \frac{A_{i+1,1,1} - A_{i,1,1}}{\Delta s_i} \qquad j=1$$

$$= \frac{A_{i+1,N,N-1} - A_{i,N,N-1}}{\Delta s_i} \qquad j=N$$

(3.2.2.14)

Applying equation(3.2.1.5) at the ith panel, the following equation is obtained

$$\sum_{j=1}^{N} K_{i,j}\ \gamma_i + U_\infty\{\cos\alpha_\infty\ (\frac{dy}{ds})_i - \sin\alpha_\infty\ (\frac{dx}{ds})_i\} = V_{bi} \qquad (3.2.2.15)$$

Rearranging the above equation, it becomes:

$$\sum_{j=1}^{N} K_{i,j} * \gamma_j = V_{bi} - U_\infty\ [\cos\alpha_\infty\ (\frac{dy}{ds})_i - \sin\alpha_\infty\ (\frac{dx}{ds})_i]$$

$$= RHS_i \qquad (3.2.2.16)$$

When the blade is moving, the RHS is

$$RHS_i = -\vec{V}_\infty \cdot \vec{n} + \vec{U}_r \cdot \vec{n} \qquad (3.2.2.17)$$

where U_r is the blade velocity at the ith control point.

In the two dimensional flows with rotor/stator interaction, the rotating speed of a blade is U_r as shown in fig.3.3 , the RHS is

$$RHS_i = -U_\infty\left[\cos\alpha_\infty\left(\frac{dy}{ds}\right)_i - \sin\alpha_\infty\left(\frac{dx}{ds}\right)_i\right] - U_r\left(\frac{dx}{ds}\right)_i \qquad (3.2.2.18)$$

If the blade is oscillating about an axis as shown in fig.3.4 , the velocity of the ith control point is

$$\vec{U}_r = \vec{\omega} \times \vec{r}_{i,o} \qquad (3.2.2.19)$$

where $\vec{r}_{i,o}$ is the position vector from the axis of the rotation to the ith control point.

By applying equation(3.2.1.5) on each panel, N-1 equations with N unknowns are obtained, so the solution to these equations is not unique. To define a unique solution, the Kutta condition is applied at the blade trailing edges in the calculation.

3.3. The Kutta Condition

The Kutta condition requires that no infinite value appears at the blade trailing edge in the solutions of either flow velocity or pressure. In other words, the Kutta condition asks the blade to produce such a circulation that the flow leaves the trailing edge smoothly. In fact, there are several equivalent expressions for the Kutta condition. One expression for the blade with sharp trailing edge states that fluid cannot move around the sharp trailing edge, so the trailing point must be a stagnation point or the velocity at the upper surface trailing point is equal to that at the lower surface trailing edge. Another expression states a requirement for the static pressure continuity at the trailing edge. In steady flow, the trailing edge is taken to be a stagnation point for a blade with non-zero trailing edge angle and the streamline from the trailing edge

bisects the tangents from the upper and lower surfaces at the trailing edge. For a cusp trailing edge blade, in order to avoid pressure discontinuity at the trailing edge, the velocities on the upper and lower surfaces at blade trailing edge should be equal.

In potential flow, the Bernoulli equation is valid. So for the points on the upper and lower surfaces at the trailing edge, the Bernoulli equation is

$$\frac{U_u^2}{2} + \frac{P_u}{\rho} + \frac{\partial \Phi_u}{\partial t} = \frac{U_l^2}{2} + \frac{P_l}{\rho} + \frac{\partial \Phi_l}{\partial t} \tag{3.3.1}$$

Since the Kutta condition requires static pressure continuity at the trailing edge

$$P_u = P_l \tag{3.3.2}$$

Substituting equation(3.3.2) into (3.3.1), the obtained equation is arranged as

$$\frac{(U_u^2 - U_l^2)}{2} = \frac{\partial(\Phi_l - \Phi_u)}{\partial t} = \frac{\partial \Gamma}{\partial t} \tag{3.3.3}$$

where $\Gamma = \Phi_l - \Phi_u$

In steady flow,there is no circulation change around the blades, i.e.

$$\frac{\partial \Gamma}{\partial t} = 0 \tag{3.3.4}$$

Therefore, the equation expressing the Kutta condition for steady flow is

$$U_u = U_l \tag{3.3.5}$$

In steady flow, there is no circulation change around a blade, so no wake flow is formed behind it. In unsteady flow, even for a cusped trailing edge blade, the velocity on upper and lower surfaces at the trailing edge are no longer equal. The equation (3.3.3) indicates a change in the blade circulation, so vortices are shed into the wake. The wake flow simulation is presented in the coming chapters.

3.3.1 A New Applying Method of the Kutta Condition

In steady flow, the equations defined by the boundary condition and the Kutta condition are linear and their solution can be obtained directly. But for the unsteady flow, the Kutta condition is a nonlinear equation. Here, in order to present a general calculating method which can be used for both steady and unsteady flows, the nonlinear Kutta condition is involved in the discussion.

In an unsteady flow, the disadvantages is that the Kutta condition introduces a non-linear equation and it is difficult to combine this non-linear equation with the linear equations from the boundary condition to get the potential solution.

The direct method that can be used to solve this problem is iterative. Since a blade surface is represented by many vortices and several blades may be involved in the calculation, this method can be time consuming.

In the method given by Maskell(Basu and Hancock, 1978), the flow is supposed to leave the blade parallel to either the upper or lower trailing edge surface depending on the sign of the shed vortex. When the shed vorticity is anti-clockwise, the flow leaves the trailing edge parallel to the lower trailing edge surface; whereas, the flow leaves the trailing edge parallel to the upper trailing edge surface when the shed vortex is clockwise. After the direction of the vortex leaving the trailing edge is known to be parallel to one blade surface at the trailing edge, the velocity on the other side is zero at the trailing edge for the blade with non-zero trailing edge angle, this is the extra equation needed to obtain a unique solution to equations(3.2.2.16). But it may be difficult to determine the exit flow direction in some cases.

Another method is Martensen's method(Gostelow, 1984). In this method, the flow is split into three basic flows as reviewed in chapter 2. Those basic flows are the flow with zero inlet angle and zero circulation, the flow with 90 degree inlet angle and zero circulation, and the flow with 90 degree inlet angle and unit circulation. After the solutions to these basic flows are obtained, these solutions are superimposed to obtain the solution to the original problem. Unfortunately, the Martensen method is mainly

designed for single cascade flow.

Here, a new method is introduced to obtain the solution to unsteady flows. In this method, it is unnecessary to guess the exit flow condition in advance. The method can be easily applied for the flows with a single blade or a single cascade and the flows with interaction among blades or cascades. For the convenience of presentation, the flow around two blades or two cascades is discussed.

In potential flow, Laplace's equation governs the flow, so the flow can be split into several basic potential flows. The solution to the original problem is a linear combination of the solutions to these basic flows. In a flow around blades or cascades, the flow is split into four basic flows as presented in fig.3.5. These four flows are defined with four different trailing edge conditions. In each set of these basic flows, an extra equation is supplied for each cascade or blade to obtain a unique solution.

As for the basic flows, their solutions can be obtained very easily through the linear equations defined by the boundary condition and the trailing edge flow conditions. The correct combination of these basic flow solutions is controlled by the Kutta condition.

For every basic flow, the boundary condition is

$$\sum_{j=1}^{2N} K_{i,j}\ \gamma_j = RHS_i \qquad i=1,2,\ldots,2N-2 \qquad (3.3.1.1)$$

A linear combination of the equations governing the four basic flows gives

$$\sum_{j-1}^{2N} K_{i,j}\ [\ k_1\ \gamma^{(a)}_j + k_2\ \gamma^{(b)}_j + k_3\ \gamma^{(c)}_j + k_4\ \gamma^{(d)}_j\ ] = (k_1+k_2+k_3+k_4)\ RHS_i \qquad i=1,2,\ldots,2N-2 \qquad (3.3.1.2)$$

where $\gamma^{(a)}$, $\gamma^{(b)}$, $\gamma^{(c)}$ and $\gamma^{(d)}$ are the solutions to the four basic flows and k_i are combination factors.

To find the solution to the original flow problem, four equations are needed to decide the four combination factors. The first equation

comes from the influence of the free stream flow. The total influence of the free stream flow expressed by the combination of these four basic flows should equal to its actual influence. This requires

$$(k_1 + k_2 + k_3 + k_4) = 1 \qquad (3.3.1.3)$$

On the other hand, the Kutta condition is satisfied by the original flow. So more equations can obtained by applying the Kutta condition to the trailing edge for each blade or cascade.

On examining the four basic flows, only three of them are found to be independent(Appendix B). So only three of the four basic flows are necessary to obtain the solution to the problem and

$$k_1 + k_2 + k_3 = 1 \qquad (3.3.1.4)$$

Therefore the combination factors can be decided uniquely by equation(3.3.1.4) and two equations from the Kutta condition, consequently a unique solution is obtained to the original problem.

3.3.2 *Solutions by the New Method*

Since only three basic flows are necessary to decide the solution to the original flow problem, basic flow a, b and c are chosen in the discussion. The vortex intensities at the nodes on the blade surface are

$$\gamma_j = k_1 \gamma_j^{(a)} + k_2 \gamma_j^{(b)} + k_3 \gamma_j^{(c)} \qquad j = 1,2,\ldots\ldots,2N \qquad (3.3.2.1)$$

where N pivotal points are located on each blade surface.

The circulation around each blade is

$$\Gamma = k_1\Gamma^{(a)} + k_2\Gamma^{(b)} + k_3\Gamma^{(c)} \qquad (3.3.2.2)$$

The vortex intensities at the four trailing edge points of two blades are

$$\begin{aligned}
\gamma_1 &= k_1\gamma_1^{(a)} + k_2\gamma_1^{(b)} + k_3\gamma_1^{(c)} \\
\gamma_N &= k_1\gamma_N^{(a)} + k_2\gamma_N^{(b)} + k_3\gamma_N^{(c)} \\
\gamma_{N+1} &= k_1\gamma_{N+1}^{(a)} + k_2\gamma_{N+1}^{(b)} + k_3\gamma_{N+1}^{(c)} \\
\gamma_{2N} &= k_1\gamma_{2N}^{(a)} + k_2\gamma_{2N}^{(b)} + k_3\gamma_{2N}^{(c)}
\end{aligned} \qquad (3.3.2.3)$$

where 1,N,N+1,2N are four pivotal points at the two cascade or blade trailing edges.

In the basic flow (a)

$$\gamma_1^{(a)} = 0$$
$$\gamma_{N+1}^{(a)} = 0 \qquad (3.3.2.4)$$

In basic flow (b)

$$\gamma_N^{(b)} = 0$$
$$\gamma_{N+1}^{(b)} = 0 \qquad (3.3.2.5)$$

In basic flow (c)

$$\gamma_1^{(c)} = 0$$
$$\gamma_{2N}^{(c)} = 0 \qquad (3.3.2.6)$$

Substituting these vortex strengths into equation (3.3.2.3), the total vortex strengths at the trailing edge points are

$$\gamma_1 = k_2 \gamma_1^{(b)}$$
$$\gamma_N = k_1 \gamma_N^{(a)} + k_3 \gamma_N^{(c)}$$
$$\gamma_{N+1} = k_3 \gamma_{N+1}^{(c)}$$
$$\gamma_{2N} = k_1 \gamma_{2N}^{(a)} + k_2 \gamma_{2N}^{(b)} \qquad (3.3.2.7)$$

The Kutta condition is applied to each blade or cascade. The obtained equations are

$$U_1^2 - U_N^2 = 2 \frac{\partial \Gamma_1}{\partial t} \qquad (3.3.2.8)$$

$$U_{N+1}^2 - U_{2N}^2 = 2 \frac{\partial \Gamma_2}{\partial t} \qquad (3.3.2.9)$$

The circulations around blades or cascades can be calculated using equation (3.3.2.2) and they are substituted into equations (3.3.2.8) and (3.3.2.9), the resulted equations are

$$\gamma_1^2 - \gamma_N^2 = 2\frac{\partial \Gamma_1}{\partial t}$$

$$= 2\frac{\partial}{\partial t}\left[k_1\Gamma_1(a) + k_2\Gamma_1(b) + k_3\Gamma_1(c)\right] \qquad (3.3.2.10)$$

$$\gamma_{N+1}^2 - \gamma_{2N}^2 = 2\frac{\partial \Gamma_2}{\partial t}$$

$$= 2\frac{\partial}{\partial t}\left[k_1\Gamma_2(a) + k_2\Gamma_2(b) + k_3\Gamma_2(c)\right] \qquad (3.3.2.11)$$

Substituting $\gamma_1, \gamma_N, \gamma_{N+1}$ and γ_{2N} in (3.3.2.7) into the equations (3.3.2.10) and (3.3.2.11), two equations about unknowns k_1, k_2 and k_3 can be obtained.

In the equations (3.3.1.4), (3.3.2.10) and (3.3.2.11), there are three unknowns, so k_1, k_2 and k_3 can be determined. But two solutions can be obtained and only one of them is correct, the right choice is made by confirming there is no reverse flow on the blade surface at the trailing edge.

In the steady flow around a single blade or cascade, the second blade or cascade is ignored, only basic flow(a) and flow (b) are then needed. The equation from the Kutta condition(3.3.5) is

$$U_U = U_l \qquad (3.3.2.12)$$

Which implies

$$\gamma_1 = -\gamma_N \qquad (3.3.2.13)$$

From equation (3.3.2.7), the vortex strengths at the blade trailing edge are

$$\gamma_1 = k_2 * \gamma_1(b)$$
$$\gamma_N = k_1 * \gamma_N(a) \qquad (3.3.2.14)$$

Subsituting equation(3.3.2.14) into (3.3.2.13), the combination factor k_1 is

$$k_1 = \frac{\gamma_1(b)}{\gamma_1(b) - \gamma_N(a)} \qquad (3.3.2.15)$$

In the unsteady flow around a single blade or cascade, the equation for one combination factor comes from the Kutta condition(3.3.3) and it is

$$p*k_1^2 + q*k_1 + r = 0 \qquad (3.3.2.16)$$

where

$$p = [\gamma_1(b)]^2 - [\gamma_N(a)]^2$$

$$q = -2[\gamma_1(b)]^2 - 2[\Gamma_1(a) - \Gamma_1(b)]/\Delta t$$

$$r = [\gamma_1(b)]^2 - 2[\Gamma_1(b) - \Gamma(t-\Delta t)]/\Delta t$$

The other combination factor is given by

$$k_2 = 1 - k_1$$

Using this method, no iterative calculation or guessing about the flow situation at the blade trailing edges is made, the Kutta condition is strictly satisfied in each blade or cascade.

3.4 Calculation Details

3.4.1 Velocity on Blade Surfaces

By solving the above linear equations, the vortex strength at the N nodes can be obtained. Because of the boundary condition on the blade surface, the velocity on the blade surface is equal to the intensity of the local vortex panel, i.e.

$$U(s_i) = \gamma_i \qquad (3.4.1.1)$$

3.4.2 Pressure Coefficient at Control Points

The pressure coefficient is defined as

$$C_p = \frac{P}{0.5\rho U_\infty^2}$$

By applying the Bernoulli equation, the pressure coefficient on the blade surface can be obtained. In steady flow, it is

$$C_p = 1 - \left(\frac{U}{U_\infty}\right)^2 \qquad (3.4.2.1)$$

For stationary blades in unsteady flow, the coefficient is

$$C_p = 1 - \left(\frac{U}{U_\infty}\right)^2 - \frac{2}{U_\infty^2}\,\frac{\partial \Phi}{\partial t} \qquad (3.4.2.2)$$

In unsteady flow around a moving blade, the pressure coefficient is

$$C_p = 1 - \left(\frac{U}{U_\infty}\right)^2 + \left(\frac{U_r}{U_\infty}\right)^2 - \frac{2}{U_\infty^2}\,\frac{\partial \Phi}{\partial t} \qquad (3.4.2.3)$$

3.4.3 Lift Coefficient

The lift force acting on a blade is an integration of the pressure around the blade contour. It is

$$L = \oint P\, ds = -\oint \rho \left(\frac{U^2}{2} + \frac{\partial \Phi}{\partial t}\right) ds \qquad (3.4.3.1)$$

The lift coefficient using the chord as a characteristic length is defined as

$$C_\ell = \frac{L}{\rho U_\infty^2 C/2} \qquad (3.4.3.2)$$

3.4.4 Velocity at a Point in the Flow Field

The velocity components at a point(x,y) outside the blade contours are calculated using the following formulae

$$u = u_\infty - \frac{1}{2\pi} \sum_{i=1}^{N} \frac{(y-y_i)\gamma_i \Delta s_i}{(x-x_i)^2+(y-y_i)^2} \qquad (3.4.4.1)$$

$$v = v_\infty + \frac{1}{2\pi} \sum_{i=1}^{N} \frac{(x-x_i)\gamma_i \Delta s_i}{(x-x_i)^2+(y-y_i)^2} \qquad (3.4.4.2)$$

3.5 Calculation of Cascade Flows

When a cascade flow is considered, where there are an infinite number of blades, the velocity influence coefficient must be modified to incorporate the mutual influence between the blades.

In a cascade, the velocity components at a surface point(x_i,y_i) induced by a vortex, located at (x_j,y_j) and with vorticity Γ and space S, are

$$\vec{V}_{i,j} = \frac{\Gamma}{2S} (\vec{i}\, u_{i,j} + \vec{j}\, v_{i,j}) \tag{3.5.1}$$

where

$$u_{i,j} = \frac{-\sin[\frac{2\pi}{S}(y_i-y_j)]}{\cosh[\frac{2\pi}{S}(x_i-x_j)] - \cos[\frac{2\pi}{S}(y_i-y_j)]} \tag{3.5.2}$$

$$v_{i,j} = \frac{\sinh[\frac{2\pi}{S}(x_i-x_j)]}{\cosh[\frac{2\pi}{S}(x_i-x_j)] - \cos[\frac{2\pi}{S}(y_i-y_j)]} \tag{3.5.3}$$

The normal velocity component at the i-th control point due to the j-th point vortex on the cascade surface is

$$V_{i,j} = u_{i,j} (\frac{dy}{ds})_i - v_{i,j} (\frac{dx}{ds})_i \tag{3.5.4}$$

where $u_{i,j}$ and $v_{i,j}$ are the velocity components in x and y directions at the ith control point due to the jth point vortex according to equations(3.5.2) and (3.5.3).

The normal velocity influence coefficient is

$$K_{i,j} = -\frac{1}{2S}\,\frac{\sinh\left[\frac{2\pi(x_i-x_j)}{S}\right]\left(\frac{dx}{ds}\right)_i + \sin\left[\frac{2\pi(y_i-y_j)}{S}\right]\left(\frac{dy}{ds}\right)_i}{\cosh\left[\frac{2\pi(x_i-x_j)}{S}\right] - \cos\left[\frac{2\pi(y_i-y_j)}{S}\right]}\Delta s_j \qquad i\neq j \qquad (3.5.5)$$

The velocity at the control point induced by the vortex panel itself is the same as for the vortex on a single blade surface, the normal velocity coefficient is also the same as that for the vortex on a single blade.

Because the flow field is periodic in cascade flows, only one blade in a single cascade is needed to be concerned in the calculation with the cascade influence coefficients. The calculating procedure is the same as that for a single blade.

In the present method, the concerned blades are represented by vortex panels. Due to the difficulty in obtaining the mutual influence coefficient of vortex panels in a cascade, the influence coefficient of the jth cascade vortex panel at the ith panel is calculated using the following rule

$$K_{i,j} = K_{i,j}^{p} + K_{i,j}^{c.p} - K_{i,j}^{point} \qquad (3.5.7)$$

$K_{i,j}^{p}$ is the influence coefficient on the ith panel due to the jth panel on the concerned single blade surface of the cascade. Its vorticity is linearly distributed along the panel. The coefficient can be calculated from equation(3.2.2.14);

$K_{i,j}^{cp}$ is the influence coefficient on the ith panel due to the similarly positioned point vortices on the jth panel in each cascade blade. The point vortex is located at the midpoint of the jth panel and has the same vorticity as the vortex panel on each blade. The coefficient is calculated through equation(3.5.5).

$K_{i,j}^{point}$ is the influence coefficient on the ith panel due to the point vortex located at the midpoint of the jth panel on the concerned single blade surface in the calculation. The normal velocity coefficient is calculated using the following equations.

$$K_{i,j}^{point} = -\frac{1}{2\pi}\frac{(x_i-x_j)\left(\frac{dx}{ds}\right)_j + (y_i-y_j)\left(\frac{dy}{ds}\right)_i}{(x_i-x_j)^2+(y_i-y_j)^2} \qquad (3.5.8)$$

In the flow involving cascades with different spaces, the flow repeats over several cascade spaces. In order to make every blade surface to be a streamline, several blades have to be included in the calculation. The equations governing the flow become:

$$\sum_{i=1}^{N*N_b} K_{j,i} * \gamma_i = RHS_j \qquad (2.5.6)$$

$$j=1,2,\ldots,(N-1)N_b$$

where N_b is the total number of blades in one period in which flow features repeat pitchwise. The Kutta condition also has to be applied to the trailing edge of every involved blade.

3.6 Results and Conclusion

In this chapter, a numerical model has been built for two dimensional potential flows around blades or cascades in both steady and unsteady states. A new method is introduced to apply the Kutta condition and some results are presented. In fig 3.6, the calculated pressure distribution on airfoil NACA A006 with zero incidence is compared with the exact solution given by Abbot et al(1959), the agreement between them is very good. In fig 3.7, the pressure distribution on the same blade with 4 degree incidence is presented.

CHAPTER

FOUR

WAKE SIMULATIONS

4.1 Wake Flow Simulation

In the real flow around blades, vortices are shed into the flow from the separation points on the blade surfaces, hence wake flows exist. After reviewed the unsteady flows inside turbomachines, Platzer(1977) concludes that the wake from single stage can generate significant flow non-uniformity and unsteadiness. So an accurate potential model of the flow around blades should include the influence of the free stream flow, the potential interaction between blades and the wake flows as shown fig.4.1. The equations governing this flow are obtained by maintaining blade surfaces being streamlines under all these influences. The equations are

$$\sum_{j=1}^{N_b*N} K_{i,j}\ \gamma_j + \sum_{k=1}^{N_v} K'_{i,k}\ \gamma_k = RHS_i \qquad i=1,2,3,\ldots,(N-1)N_b \qquad (4.1.1)$$

Which can be rearranged as

$$\sum_{j=1}^{N_b*N} K_{i,j}\ \gamma_j = RHS_i - \sum_{k=1}^{N_v} K'_{i,k}\ \gamma_k \qquad i=1,2,3,\ldots,(N-1)N_b \qquad (4.1.2)$$

here N_v is the total number of the vortices in the wake flow, N_b is the total number of the blades involved in the calculation and RHS_i mean the same as in equation(3.2.2.16)

In this model, the interaction between blades and their wake flows is simulated by the interaction between the employed vortices. The simulation starts when the first vortex is shed and continues until a wake flow is fully established. During the process, the flow is unsteady due to the developing wake flows. The result of the simulation is stable wake flows in a steady flow or a periodic wake flow in an unsteady flow.

4.2 The Kutta Condition

In the wake flow simulation, the Kutta condition is still needed to obtain a unique solution to the problem. In the case when flow separation happens either before the flow reaches the blade trailing edge or at the blade trailing edge, the Kutta condition is applied at the separation points. In the scheme shown in fig.4.2, a and b, c and d are two pairs of points just beside two separation points on one blade surface and the separated flows divide the flow field around the blade into two regions. In both flow regions, the flows are still inviscid potential flows and the blade surface remains a streamline.

In region R1, points b and c are on the same streamline, applying the Bernoulli equation between b and c gives

$$\frac{U_b^2}{2} + \frac{\partial \Phi_b}{\partial t} + \frac{P_b}{\rho} = \frac{U_c^2}{2} + \frac{\partial \Phi_c}{\partial t} + \frac{P_c}{\rho} \qquad (4.2.1)$$

or

$$\frac{P_b - P_c}{\rho} = \left(\frac{U_c^2}{2} + \frac{\partial \Phi_c}{\partial t} \right) - \left(\frac{U_b^2}{2} + \frac{\partial \Phi_b}{\partial t} \right) \qquad (4.2.2)$$

The Bernoulli equation can be applied to points a and d in region R2 in the same way, the obtained equation is

$$\frac{U_a^2}{2} + \frac{\partial \Phi_a}{\partial t} + \frac{P_a}{\rho} = \frac{U_d^2}{2} + \frac{\partial \Phi_d}{\partial t} + \frac{P_d}{\rho} \qquad (4.2.3)$$

or

$$\frac{P_a-P_d}{\rho} = \left(\frac{U_d^2}{2} + \frac{\partial\Phi_d}{\partial t}\right) - \left(\frac{U_a^2}{2} + \frac{\partial\Phi_a}{\partial t}\right) \qquad (4.2.4)$$

As summarized by Smith(1982,1986), the position of the line vortex in the flow is located in such way that the total transverse force on each lengthwise element is zero. On the blade surface, because points a and b are both very close to the same separation point but on different side of the separated vortex sheet and there should be no static pressure difference across a vortex sheet, so

$$P_a = P_b \qquad (4.2.5)$$

Points c and d are in the same situation as points a and b, then

$$P_c = P_d. \qquad (4.2.6)$$

From equations(4.2.5) and (4.2.6), the following equation can be obtained

$$\frac{P_a - P_d}{\rho} = \frac{P_b - P_c}{\rho} \qquad (4.2.7)$$

Substituting equations(4.2.2) and (4.2.4) into equation (4.2.7), the result is

$$\left(\frac{U_c^2}{2} + \frac{\partial\Phi_c}{\partial t}\right) - \left(\frac{U_b^2}{2} + \frac{\partial\Phi_b}{\partial t}\right) = \left(\frac{U_d^2}{2} + \frac{\partial\Phi_d}{\partial t}\right) - \left(\frac{U_a^2}{2} + \frac{\partial\Phi_a}{\partial t}\right) \qquad (4.2.8)$$

Rearranging this equation, it becomes

$$\frac{1}{2}\left(U_b^2 - U_a^2 + U_d^2 - U_c^2\right) = \frac{\partial(\Phi_a-\Phi_b+\Phi_c-\Phi_d)}{\partial t} \qquad (4.2.9)$$

Just behind a separation point, the velocity is zero on the blade surface. So

$$U_a = 0 \text{ and } U_d = 0$$

The circulation around the blade is

$$\Gamma = \Phi_a-\Phi_d+\Phi_c-\Phi_b \qquad (4.2.10)$$

So equation(4.2.9) can be written as

$$\frac{1}{2}(U_b^2 - U_c^2) = \frac{\partial \Gamma}{\partial t} \qquad (4.2.11)$$

This is the Kutta condition for the flow around a blade with two separation points.

4.3 Vortex Shedding

The wake simulation begins when the free stream flow is zero and the blades are stationary, so no circulation exists around the blades. Then the uniform free stream flow begins to be set up. When fluid moves around a blade surface with a sharp trailing edge, a flow with very high acceleration is produced at the trailing edge point at the first instant. Owing to the viscosity of the fluid, this flow cannot last for a long time. Instead vortices are shed from the sharp point, a velocity discontinuity across the separated vortex sheet appears and a circulation is produced around the blades at the same time. In some cases, due to fluid viscosity and adverse pressure gradient on the blade surface, the flow separates from the blade surface before reaching the trailing edge and vortices are shed from the separation point on the blade surface.

In the flow around a blade with a cusp trailing edge and there is no separation before the flow reaches the blade trailing edge, the vortices are convected into the flow from both the upper and lower surfaces at blade trailing edge. In steady inviscid flow, equal and opposite vortices are shed into the wake at the trailing edge from the upper and the lower surface at the same time, they cancel each other immediately after they are shed and no wake can be established. For unsteady flow, the vortices shed over the upper and the lower surface do not always cancel each other and a wake can be formed as fig.4.3.

As to the inviscid potential flow around a blade with a blunt trailing edge is concerned, the potential flow should follow the blade surface to a stagnation point in the blade trailing area and the Kutta condition should be valid at this stagnation point. Even this is an accurate representation of the potential flow around the blade, large acceleration would cause the simulated flow to be far from the real

flow in the trailing edge area due to the large curvature of the local blade surface. In this potential approach, flow is assumed to separate from the blade surface at the sharp points and a wake flow is formed behind the blade as fig.4.4.

According to Kelvin's theorem, the vorticity should be conserved in the inviscid flow subject to irrotational body forces. Therefore the change in the circulation around the blade satisfies the following equation

$$\frac{\partial \Gamma}{\partial t} = -\frac{\partial \Gamma_w}{\partial t} \qquad (4.3.1)$$

here Γ is the circulation around the blade and Γ_w is the total circulation in the wake flow.

To simulate the separated flows, vortex sheets are shed from the separation points. The vortex sheets are represented by vortex panels in the region near the separation points and point vortices in the region far from the separation points. In this calculation, one vortex panel is shed from each separation point in each time step.

Because the vortex sheet is shed into the flow continously from every separation point, the vorticity on the vortex panels should be also continuously distributed. The intensity of the nascent vortex panel at the separation point must have the same intensity as the local surface vorticity, i.e.

$$\gamma = \gamma_s \qquad (4.3.2)$$

and the convective velocity of the nascent panel leaving the separation point is

$$V_c = U_s/2 \qquad (4.3.3)$$

where U_s is the local velocity at the separation point on the blade surface.

The circulation of the nascent vortex panel during a time step Δt is

$$\Delta\Gamma = \int_0^{\Delta t} 0.5\, U_s^2 \, dt \qquad (4.3.3)$$

When there are several separation points on a blade surface, the vorticities of the nascent vortices from these separation points in

one time step are

$$\Delta\Gamma_i = \int_0^{\Delta t} 0.5\, \gamma_{s,i}^2\, dt \qquad (4.3.4)$$

The positions of the nascent vortices in the wake flow are determined by the flows at the separation points. The nascent vortices should leave the separation points in the same direction as the local streamlines. The lengths of these nascent vortex panels are the convective fluid displacement in the time step while they are shed. The lengths are given by

$$\ell_i = \int_0^{\Delta t} V_{c,i}^* dt \qquad (4.3.5)$$

The endpoint locations of the nascent panels in the wake flow are

$$\left.\begin{aligned} x_i &= x_{si} + \ell_i \cos\theta_i \\ y_i &= y_{si} + \ell_i \sin\theta_i \end{aligned}\right\} \qquad (4.3.6)$$

where θ_i are the flow directions at the separation points.

When a separation is at the trailing edge of an airfoil, the leaving angle of the flow is as discussed in Appendix C. But for the flow around a blade with blunt trailing edge, the separated flow is in the local flow direction at the separation point.

In this chapter, viscosity effect is not considered, so the shed vortices leave the blade at the separation points. As the matter of fact, a boundary layer always exists on the blade surface in the real flows, so these vortices are shed into the wake not exactly from the separation points on the blade surface, but from the boundary layer at these points. In the calculation after this chapter, the vortex sheet is shed into the wake at the gravity centre of the approximated boundary layer vorticity profile at each separation point instead of at the separation points on the blade surface.

4.4 Vortex Motion

The motion of the vortices inside the wake is governed by

following equations

$$\left.\begin{aligned} x_i(t+\Delta t) &= x_i(t) + u\Delta t \\ y_i(t+\Delta t) &= y_i(t) + v\Delta t \end{aligned}\right\} \qquad (4.4.1)$$

In the above formulae, u and v contain contributions from the free stream flow, the blades and the wake flow. Among those contributions, the convective velocity components produced by point vortices in the wake can be calculated using the following formulae,

$$u = \frac{dx}{dt} = -\sum_{i=1}^{n} \Gamma_i \frac{y - y(i)}{2\pi d^2}$$

$$v = \frac{dy}{dt} = \sum_{i=1}^{n} \Gamma_i \frac{x - x(i)}{2\pi d^2}$$

where $d=\{[x-x(i)]^2+[y-y(i)]^2\}^{1/2}$

(4.4.2)

These formulae are singular near the location of every point vortex. This can make the motion of some vortices erratic. In order to produce a smooth and regular velocity distribution in the flow field, each vortex is supposed to possess a core over which its vorticity is spread. The core size and the vorticity distribution in the core can be chosen according to the physical properties of the simulated fluid and mathematical characteristics of the involved equations. From the mathematical point of view, the core size is decided so that the vortices cannot produce a strong singular effect in the velocity field. According to fluid properties, the wake flow is always in turbulent state. The separated vortex structure usually has an expanding core due to diffusion and a velocity defect is caused after the separation point. The core size also depends on the separated flow structure. From numerical experience, the recommended core size is about 0.5 percent of the blade dimension as used by Spalart et al. While the core size is chosen in the right range, a smooth flow field is produced and the solution to the problem is not sensitive to the core size and its vorticity distribution. So the right core size can

be found by computational trials. The used core size in the calculation is 0.5 percent of the blade chord.

After vortices leave the separation points, their shape is continuously changing in a real flow due to the turbulent mixing and diffusion. Hence the core size would become bigger and both its shape and vorticity distribution become irregular. In the present calculations, only the inviscid flow is considered, the vorticity of the vortices in the wake is kept constant and their core sizes are also assumed not to change during their motion. Within the core, it is assumed that the velocity induced by vortex itself is linearly distributed across the core like a forced vortex, the induced velocity reaches zero at the centre of the core and the maximum at its edge. The influence of a vortex in the region outside its core is assumed to be the same as for a point vortex at the core centre.

4.5 Pressure Coefficient

When the velocity field is known, Bernoulli's equation is used to calculate the pressure distribution on the blade surface. The pressure coefficient is defined as

$$C_p = \frac{P}{\rho U_\infty^2/2} \qquad (4.5.1)$$

By applying Bernoulli's equation, the pressure coefficient can be expressed as

$$C_p = 1 - \left(\frac{U}{U_\infty}\right)^2 + \left(\frac{U_r}{U_\infty}\right)^2 - \frac{2}{U_\infty^2}\frac{d\Phi}{dt} \qquad (4.5.2)$$

When the blade is stationary, $U_r=0$.

In region R1 as shown in fig.4.2, the pressure coefficient can be got using the above equation directly.

In region R2, the Bernoulli equation can still be used between the points on the blade surface. Thus

$$\frac{P}{\rho} + \frac{U^2}{2} + \frac{\partial\Phi}{\partial t} = \frac{P_a}{\rho} + \frac{U_a^2}{2} + \frac{\partial\Phi_a}{\partial t} \qquad (4.5.3)$$

Because $U_a=0$, then

$$\frac{P}{\rho} = \frac{P_a}{\rho} - \frac{U^2}{2} - \frac{\partial(\Phi_a-\Phi)}{\partial t} \qquad (4.5.5)$$

Therefore, the pressure coefficient inside the separated region R2 is

$$C_p = C_{p,a} - \left(\frac{U}{U_\infty}\right)^2 - \frac{2}{U_\infty^2}\frac{\partial(\Phi_a-\Phi)}{\partial t} \qquad (4.5.6)$$

Because points a and b are on the different side of the same separated vortex sheet, the pressures at these two points are equal, i.e.

$$C_{p,a} = C_{p,b} \qquad (4.5.7)$$

Substituting equation(4.5.7) into (4.5.6), the pressure coefficient at a point on the blade surface in the region R2 is

$$C_p = C_{p,b} - \left(\frac{U}{U_\infty}\right)^2 - \frac{2}{U_\infty^2}\frac{\partial(\Phi-\Phi_a)}{\partial t} \qquad (4.5.8)$$

$C_{p,b}$ can be obtained by applying the Bernoulli equation in the region R1.

In the calculation of the pressure coefficient, the change rate of velocity potential is necessary. In the calculation of the velocity potential, the contributions from the free stream flow, the blade and the wake flows are considered separately. As to the velocity potential at point p induced by vortices in the wake flow is concerned, because the vorticity of those vortices is assumed to be constant during their motion, the velocity potential induced by them is only a function of the relative positions between point P and these vortices. After the velocities of these vortices are known, the relative positions between them and point P become known functions of time. The time derivative of the velocity potential at point P due to a vortex in the wake can be evaluated by the following formula given by Greitzer(1979)

$$\frac{\partial\Phi_i}{\partial t} = \frac{\partial\Phi_i}{\partial x'}\frac{\partial x'}{\partial t} + \frac{\partial\Phi_i}{\partial y'}\frac{\partial y'}{\partial t} \qquad (4.5.9)$$

where x' and y' are relative positions of point P with respect to the vortex in the wake. They are given by

$$x' = x_p - x_i$$
$$y' = y_p - y_i \qquad (4.5.10)$$

$\partial\Phi/\partial x'$ and $\partial\Phi/\partial y'$ are the velocity components in the x and y directions induced at point P by the vortex. For cascade flow, these velocity components are

$$u^o = \frac{\partial\Phi_i}{\partial x'} = -\frac{\Gamma}{2S}\,\frac{\sin(2\pi y'/S)}{\cosh(2\pi x'/S) - \cos(2\pi y'/S)}$$

$$v^o = \frac{\partial\Phi_i}{\partial y'} = \frac{\Gamma}{2S}\,\frac{\sinh(2\pi x'/S)}{\cosh(2\pi x'/S) - \cos(2\pi y'/S)} \qquad (4.5.11)$$

$\partial x'/\partial t$ and $\partial y'/\partial t$ are the relative velocity components in the x and y directions of point P relative to the vortex. They are given by

$$\frac{\partial x'}{\partial t} = \frac{\partial x_p}{\partial t} - \frac{\partial x_i}{\partial t}$$
$$= u_p - u_{vor,i} \qquad (4.5.12)$$

$$\frac{\partial y'}{\partial t} = \frac{\partial y_p}{\partial t} - \frac{\partial y_i}{\partial t}$$
$$= v_p - v_{vor,i} \qquad (4.5.13)$$

When point P is stationary in the fixed coordinate system, then

$$\frac{dx'}{dt} = -u_{vor,i}$$
$$\frac{dy'}{dt} = -v_{vor,i} \qquad (4.5.14)$$

so the change rate of the velocity potential at point P due to a vortex in the wake flow is:

$$\frac{\partial \Phi_i}{\partial t} = u^o (u_p - u_{vor,i}) + v^o (v_p - v_{vor,i}) \qquad (4.5.15)$$

In the wake flow, there may be a lot of vortices. The total velocity potential induced by the wake flow is

$$\Phi = \sum_{i=1}^{N_v} \Phi_i \qquad (4.5.16)$$

And the change rate of the velocity potential is

$$\frac{\partial \Phi}{\partial t} = \sum_{i=1}^{N_v} \frac{\partial \Phi_i}{\partial t} \qquad (4.5.17)$$

The velocity potential of the free stream flow is

$$\Phi = u_\infty x + v_\infty y$$

$$= U_\infty [\cos\alpha_\infty x + \sin\alpha_\infty y] \qquad (4.5.18)$$

The change rate of the velocity potential at point P caused by the free stream flow is

$$\frac{\partial \Phi}{\partial t} = U_\infty (\cos\alpha_\infty \frac{\partial x}{\partial t} + \sin\alpha_\infty \frac{\partial y}{\partial t})$$

$$= U_\infty (u_p \cos\alpha_\infty + v_p \sin\alpha_\infty) \qquad (4.5.19)$$

When calculating the velocity potential at point P induced by the vortices on the blade surfaces, it should be noted that not only the relative positions between them and point P are changing with time while the blades are moving, the strength of the vortices themselves are also changing due to the unsteady disturbances from the wake flows and the interaction between the involved blades. In that case, the velocity potential due to the vortices on the blade surfaces has to be differentiated with respect to time. The change rate of the velocity potential is:

$$\frac{\partial \Phi}{\partial t} = \frac{\Phi(t+\Delta t) - \Phi(t)}{\Delta t} \qquad (4.5.20)$$

here $\Phi_{(t+\Delta t)}$ and $\Phi(t)$ are the velocity potentials at point P due to the vortices on the blade surfaces at time $t+\Delta t$ and t respectively.

The velocity potential induced at point P(x,y) by a cascade vortex with vorticity Γ at location[x(i),y(i)] in the y direction given by Lamb(1945) is

$$\Phi(j,i)=\frac{\Gamma}{2S}\,\mathrm{atan}\left\{\tanh\left(-\frac{\pi[x-x(i)]}{S}\right)\cot\left(\frac{\pi[y-y(i)]}{S}\right)\right\} \tag{4.5.21}$$

In order to reduce computing time, the calculation of velocity potential on the blade surface is further simplified. The velocity potential difference between any two points in the flow field is the integration of the velocity along any path between them, it can be written as

$$\Phi_a-\Phi_b=\int_a^b \vec{v}\,d\vec{s}=\int_a^b (u\,dx+v\,dy)$$

$$=\sum_{i=1}^{N}(u_i\,\Delta x_i+v_i\,\Delta y_i) \tag{4.5.22}$$

here the path between points a and b is divided into N elements for numerical integration, Δx and Δy are the lengths of the i-th element in x and y directions, u_i and v_i are the velocity components in the x and y directions at the element.

In this calculation, because only the pressure on the blade surface is required, so only the velocity potential on blade surface needs to be determined. Through equation (4.5.22), the velocity potential on the blade surface can be obtained by integrating the velocity along the blade surface from a point where the velocity potential is known. This starting point is taken as a reference point. The velocity potential at this reference point has to be calculated using equations(4.5.15), (4.5.19) and (4.5.20). When the velocity potential at the reference point is known, the velocity potential at any point on blade surface is obtained by integrating the velocity along blade surface from the reference point. Hence

$$\Phi_i=\Phi_{re}+\int_0^{s_i} U(s,t)ds$$

$$=\Phi_{re}+\sum_{j=1}^{N_i} U_j(t)\Delta s_j$$

$$=\Phi_{re}+\Phi^*_i \qquad (4.5.23)$$

The velocity potential time derivative on the blade surface are

$$\frac{\partial\Phi_i}{\partial t}=\frac{\partial\Phi_{re}}{\partial t}-\frac{\partial\Phi^*_i}{\partial t} \qquad (4.5.24)$$

4.6 The Far Wake Region

After the first vortex is shed from the separation points, more and more vortices are continuously shed into the wake as the simulation develops. There would be a lot of vortices involved in the calculation before a stable result is achieved. Too many vortices in the wake could need huge computing time. To reduce the computing time, some approximations have to be made. Fortunately, as the vortices move away from the blade surface, the interaction between them and the blades decreases and tends to a constant. For the flow around a single blade or several blades, the influence of the vortices on the distant blade surfaces tends to zero. As to the vortices in the wake of a cascade are concerned, because the wake flow forms a cascade wake as well, the influence of those vortices on the blade cascade reaches a constant as they move away from the blades. The velocity induced in the calculating domain by these vortices in the far wake region can be approximated by the following formulae from equations(3.5.2) and (3.5.3) as

$$u=0 \qquad (4.6.1)$$

$$v=-\frac{\Gamma}{2S} \qquad (4.6.2)$$

When the axial distance between a separated vortex and the blade trailing edge is more than one cascade space, the maximum error caused by the above approximation is about 0.01% for an unit vortex. Since only the flow near the blade surface is of interest. So it is unnecessary to follow the exact movement of these vortices in the wake region far from the blade surface unless a very high accuracy is required. On the other hand, the flow field in the far wake region becomes uniform in the real flow as the unsteady wake flow decays away. The experimental results of Lakshminarayana and et al(1982) show that the effects of a turbomachine blade wake nearly disappear beyond about a half-chord downstream of the trailing edge. The average velocity in the far wake region can be easily obtained through mass conservation law.

In the calculations, the wake flow after the last downstream cascade is divided into three regions as shown in fig.4.5. One is the near region. The movement of the vortices in this region is governed exactly by equation(4.4.1). The flow is assumed to be uniform in the second region which is just downstream of the near wake region. The velocity is fixed by the continuity equation.

In cascade flow, the velocity components in the second region are

$$u_{fw} = u_\infty$$
$$v_{fw} = u_{fw} \tan\beta \qquad (4.6.3)$$

In the flow around a single blade or several blades, flow velocity components are

$$u_{fw} = u_\infty$$
$$v_{fw} = v_\infty \qquad (4.6.4)$$

The movement of the vortices in the second region is not exactly governed by equation (4.4.1) and the interference between the vortices inside this region is ignored.

The third region is the downstream of the second region. It is called the far wake region. All the vortices moving into this region are merged together. The moving velocity of the merged vortex is the same as the vortices in the second region. The vorticity of the merged vortex Γ_{fw} is the sum of the vorticities of all those vortices that

move into the far wake region and the influence of it on the flow field around the cascade is independent of its location in the far wake .

The size of these wake regions depends on required accuracy and availiable computing time.

In cascade flow, the velocity components due to the vortices in far wake region can be calculated using the following formulae:

$$u=0 \qquad (4.6.5)$$

$$v=-\frac{\Gamma_{fw}}{2S}$$

The velocity potential due to the vortices in the far wake region is from formula (4.5.15) as

$$\frac{\partial \Phi}{\partial t} = u^{o}\ (u_p - u_{fw}) + v^{o}\ (v_p - v_{fw}) \qquad (4.6.6)$$

Substituting the equation (4.6.5) into (4.6.6), the velocity potential time derivative becomes

$$\frac{\partial \Phi}{\partial t} = -\frac{\Gamma_{fw}}{2S}\ (v_p - v_{fw}) \qquad (4.6.7)$$

Γ_{fw} is the vorticity of the merged vortex in the far wake region.

4.7 Computing Procedure

The calculation starts when the blades are stationary and the flow is zero. This is registered as t=0. Afterward, the free stream flow and the motion of the blades are set up, vortices begin to shed from the separation points at the same time. As the calculation goes on, vortices are continuously shed from the separation points into the wake flow. The calculation continues until a stable solution is achieved. The procedure for wake simulation is:

(1) An unsteady potential calculation is done with the starting vortex is shed at each separation point.

(2) The nascent shed vortices in last step move to their new

position in one time step and the movement is governed by equation (4.4.1)

(3) The moving blades go to a new position;

(4) The RHS_j of equation(4.1.2) under the influence of all the vortices in the wake flow and the blades in their new positions are calculated;

(5) A new potential solution is obtained using the recalculated RHS. At the same time, new vortices are shed at these separation points.

(6) The vortices which have already inside the wake flow move to their new positions in one time step;

(7) the calculations are repeated from step (3) until a stable result is obtained.

Usually, the result begins to become stable when the first shed vortex in the wake goes into the far wake region.

4.8 Calculation Details

4.8.1 Approximation of The Nascent Vortex Panel

At t=0, the free stream flow is zero and the blade is stationary, blade circulation is also zero. After a time step Δt, the free stream velocity increases to U_∞ and a circulation is developed around the blade. At the same time, the starting vortices are shed into the wake. Due to a lack of flow information at the separation points at the beginning, the positions and directions of the starting vortices can only be given approximately, so the solution of the first time step has to be found by iteration. To start the iteration, no separation is assumed on the blade surface, a potential solution is obtained. Then the starting vortices at the separation points are enforced according to the obtained flow conditions at these separation points from the first iteration. The starting vortices are represented by vortex panels, their lengths are their convecting distances in the first time step, i.e.

$$\ell_i = \int_0^{\Delta t} 0.5U_{s,i}\, dt \qquad (4.8.1)$$

where i denotes the ith separation point on blade surface.

Because the time step is quite small, equation (4.7.1) can be approximated by

$$\ell_i = 0.5U_{s,i}\Delta t \qquad (4.8.2)$$

The orientation of these panels are in the same direction as local streamlines. If the flow is separated at a sharp point, the starting panel is put in the direction parallel to the local blade surface just before the separation point. One end of the each shed panel is at the separation point and the coordinate of the other end is inside the wake flow at

$$x_i = x_s + \ell_i \cos(\theta_i)$$

$$y_i = y_s + \ell_i \sin(\theta_i) \qquad (4.8.3)$$

where θ_i are the local streamline directions.

The flow with the influence of the modified starting vortices is recalculated. Hence another flow solution can be obtained. Modifying the starting vortex at every separation point after every iteration, the calculation is repeated until a convergent result is achieved. Then the calculation goes to the next time step.

To start a new time step, the length of the nascent vortex panels obtained from equation(4.8.1) are approximated by

$$\ell_i = \frac{1}{4}\left[U_{s,i}(t) + U_{s,i}(t+\Delta t)\right] \Delta t \qquad (4.8.4)$$

The vorticity distribution on every panel is assumed linear, vortex intensity of the nascent panel at each separation point is equal to the surface vorticity at the separation point and the vortex strength at the other end of the panel inside wake is put equal to the vortex strength at the separation point in the previous time step.

The distribution is

$$\gamma_i = \left(\frac{\ell_i - s}{\ell_i}\right) \gamma_{s,i}(t+\Delta t) + \left(\frac{s}{\ell_i}\right) \gamma_{s,i}(t) \qquad 0 < s < \ell_i \qquad (4.8.5)$$

The length ℓ_i of the nascent vortex panel at every separation point is a function of the vortex strength at the separation point as

equation(4.8.4) and its direction is also a function of the velocity at the separation point when the separation doesn't occur at a sharp point on the blade surface. This means the influence coefficients of the nascent vortex panels contain unknowns and are not linear functions, so the equation system obtained from equation(4.1.2) is not linear. In the simulation, because the time step is small, the flow at a separation point should not change very much in one time step, so the flow situation at the separation point in the previous time step can be used to approximate the length and direction of the nascent vortex panel quite accurately as

$$\gamma_{s,i}(t+\Delta t) \approx \gamma_{s,i}(t) \tag{4.8.6}$$

and the panel length from equation (4.8.2) is

$$\ell_i = \frac{1}{2} U_{s,i}(t)^* \Delta t \tag{4.8.7}$$

Now, the influence coefficient of $\gamma_{s,i}(t+\Delta t)$ is known and equations (4,1,2) become linear. After a solution is obtained, the accuracy of the approximation(4.8.6) has to be checked after every iteration. If the error is out of tolerance, the calculation has to be repeated with $\gamma_{s,i}(t+\Delta t)$ in equation(4.8.4) equalling to its value in previous iteration.

4.8.2 Vortex Panel Simulation

In the near region behind a separation point, the separated vortex sheet is represented by vortex panels in this model. By using panels, the singular effect is reduced compared with the point vortices. In the panel model, the vorticity of each panel is constantly distributed along its length and the total vorticity keeps contant during its convection. The length of a panel in the wake keeps changing while it is carried away by the flow. The endpoint positions of each vortex panel in the wake flow are recorded from the moment when it is shed from a separation point. The positions of these ends are renewed in every time step during its movement using equation (4.4.1). The vortex panel always lies on the straight line between these two ends.

4.8.3 Vortex Spliting

Because the calculating time step cannot be very small in the simulation, so the curved separated vortex sheet in the wake flow cannot be simulated exactly by straight vortex panels and point vortices, especially when the the wake flow is being stretched by flow or encounters a blade. As pointed out by Bromilow and Clement(1982), the sheet may have to be rediscretised in some case to obtain an accurate representation to the continuous vortex sheet during the simulation. On the other hand, the tendency of the distance between two vortices in the wake to increase in the numerical simulation suggests that the region contains the vortices which tend to become elongated in the actual flow. To simulate this effect, vortices are split into several smaller vortices when ever the distance between two successive shed point vortices or the length of a vortex panel is bigger than a certain value. In this calculation, the critical distance for vortices or panels to be split is two core size. The created vortex through a split is put at the middle of the two vortices giving birth to it. The vorticity of the new vortex is set at one third of the total vorticity of the original two vortices. The vorticities of the original vortices are reduced to two third of their original vorticity to keep the circulation constant as shown in fig.4.6.

4.8.4 Group Interaction

In the calculation, the result becomes stable only when the interaction between the wake flow and the blades tends to be stable. Usually, it takes long time to get a stable simulation, many vortices may be involved in the wake simulation. In the calculation, the computing time is decreased by introducing group interaction. Having the same effact as the vortices in the far wake region, it is obvious that the influence of a vortex at a point tends to a constant when the axial distance between them is large in cascade flow. So, in the calculation of the induced velocities and velocity potential at one

point, all the vortices beyond a certain distance from this point are supposed to generate the same influence in terms of unit vorticity. The velocity components are

$$u = 0$$

$$v = -\frac{1}{2S} \qquad (4.8.8)$$

The influence of these vortices in this approximation is represented by an equivalent vortex. The vorticity of the equivalent vortex Γ_e is just the total vorticity of all the vortices in this approximation. It is

$$\Gamma e = \sum_{i=1}^{N} \Gamma_i \qquad (4.8.9)$$

The induced velocity components are

$$U=0$$

$$V = -\frac{\Gamma_e}{2S} \qquad (4.8.10)$$

It is important to remember that the vortices upstream of this point have opposite influence at the point as to the vortices in its downstream in this appoximation. In the calculations, the equivalent vortex is assumed downstream of the point, so the vorticity sign of the upstream vortices in this appoximation should be changed before it is added in equation (4.8.9). The group interaction is only a measure for reducing computing time, there is no new vortex formed in the simulated flow field.

4.8.5 Vortex Merging

To reduce the total number of the vortices inside the simulation, merging of the vortices in the wake flow is also allowed at the same time as vortex shedding. Vortex merging is assumed to happen only when the vortices are far from the blade surface and one vortex is

very close to another. During merging, the vorticity of the new vortex through the merging is the sum of the vorticities of the merged vortices and it is located at the vorticity centre between them. Merging is controlled by the required resolution. The magnitude of the leading term in the produced error because of the merging given by Spalart and Leonard(1981) is

$$\frac{\Gamma_i \Gamma_j \mid Z_i - Z_j \mid}{\mid \Gamma_i + \Gamma_j \mid \; d^2} \qquad (4.8.11)$$

where Z_i, Z_j are the positions of the two merged vortices and d is the average distance from the merged vortices to the blade surfaces. In the calculations, merging occurs only when two vortices go closer than half vortex core diameter and both of them are downstream of the last blade trailing edge more than 0.6 chord. The error in term of the induced velocity on the blade surface by the merging is about 10^{-4} U_∞/C. When vortices having opposite signs are merged under the above rule, the local error is larger because of the small difference in their vorticities.

Using merging, computing time can be reduced and the behaviour of the flow field becomes much smoother as the strong singular effect between these merged vortices is reduced.

4.8.6 Vortex Motion Near a Blade Surface

When flow separates before the blade trailing edge or when one blade is upstream of another, there may be vortices moving along the blade surface. These vortices must be prevented from penetrating the blade surface during the simulation. In the calculation of flow around a moving blade, some vortices which are already very close to the blade surfaces can fall inside the blade contours after the blade moves to its new position or when these vortices are moving with the local velocity in one time step. To prevent this penetration, three measures are taken. The first is to decrease the time step in the simulation. Small time step introduces too many vortices in the calculation and makes the simulation time consuming.

The second is to reduce the moving time steps only for the

vortices near the blade surfaces. This measure can force these vortices to move more accurately along the local streamlines, and hence the chance of them going into the blade contours is decreased.

While vortices are approaching the blade surface, the moving time steps of them are decided according to their moving speed. The extent to which a smaller moving time step is used is controlled by the available computing time. The smaller are the moving time steps of the vortices, the less is the chance that the vortices go into the blade contour, but the greater is the calculating time. In the calculations, the thickness of the region in which the smaller moving time step is used near the blade surface is ten percent of the blade chord(see fig.4.8). The total number of moving steps of the vortices near blade surface in one simulation step is

$$N_t = \mathrm{INT}(\Delta t V/\sigma + 1) \qquad (4.8.12)$$

where V is the vortex velocity. The moving time step of the vortices near the blade surface is

$$\delta t = \Delta t/N_t \qquad (4.8.13)$$

This ensures that no vortex near the blade surface can move more than one core distance in its one moving time step.

Even though the second method can prevent the vortices from going too close to the blade surfaces in their movement, some vortices could still fall into the blade contours after the blades move to their new positions. The third measure to prevent vortices from going inside the blade contours is reflection of the vortices away from the blade surfaces if they still go very close to the blade surface under the above two measures as fig.4.7(as used by Vezza and Galbraith,1985b). In the calculations, the minimum allowed distance of a vortex from the blade surfaces is one core size, so reflection occurs only when the normal distance of a vortex from the blade surfaces is less than one core size. The thickness of the reflecting region at which reflection happens is given by following formula

$$d_{ref} = \Delta t U_r + \sigma \qquad (4.8.14)$$

here U_r is the speed of the blade and d_{ref} is the thickness of the reflecting region.

The thickness d_{ref} keeps vortices from going inside the region

where the distance of a vortex from the blade surfaces could be less than one core size after blade moves to a new position in one time step. However, this formula is suitable only for the front side of the moving blade. On the back side, the thickness of the reflecting region is

$$d_{ref} = \sigma \qquad (4.7.15)$$

4.9 Results and Discussion

In this chapter, a potential flow model is built up for calculating airfoil flows with separations. Using this model, the wake flows around oscillating airfoils have been predicted and the results are compared with some reference data. In fig.4.9 and 4.10, the simulated wake configurations of oscillating airfoil NACA 23012 are presented, very clear vortex streets are obtained in those cases. For airfoil NACA0012, the lift force is obtained for sinusoidal oscillations about an axis 1/4 chord from its leading edge with zero mean oscillating angle and reduced frequency of $\omega c/(2U_\infty)=0.4$. From the results presented in fig.4.11, it can be seen that the wake flow does influence the airfoil characteractics very much. Due to the wake flow, the lift force is reduced and lift coefficient loop of one complete oscillation becomes narrower than the results without wake. As shown in fig.4.12, the predicted results with wake flow and no boundary layer are quite similar in shape to the measured results, but an overall lift rise is predicted. Using the integral boundary model(presented in paragraph 6.2.2), the predicted results with boundary layer and wake are closer to the experimental data. The difference between them may be due to fluid viscosity in the tested low Reynolds number flow given by Vezza et al and possible boundary layer separation on the blade surface during the oscillation.

CHAPTER FIVE

THE FLOW AROUND TURBINE FLOWMETER BLADES

5.1 Introduction

In the last few chapters, a numerical model has been built up to simulate the potential flows around airfoils and the predicted results have been compared with some experimental and analytical data. In applying the model to predict the flow around turbine flowmeter blades, some special problems arise and have to be solved before the flowmeter performance can be accurately predicted. In the flows around turbine flowmeter blades, because the blade profiles are designed with a square shape for production reasons, flow separation inevitably occurs at both leading and trailing corner points of the blades. These separated flows can cause a decrease of lift and an increase of drag on the blades. The leading edge separation occurs at the two corner points in the leading edge area and vortices are shed from the separation points. Usually when vortices pass by a blade, pressure distortion would be caused on the blade surface as measured by Favier et al(1985), Booth(1986) and Sugeng(1986). Fortunately, these separated leading edge flows around the turbine flowmeter blade usually reattach to the blade surface downstream of the separation points and form equilibrium separated bubbles. In the blade trailing edge area, vortices are shed into the flow from the blade trailing

edge sharp points and a wake flow is established behind the blade as fig.5.1. In this chapter, the built vortex shedding model is applied to the flows around the tested flowmeter blades to obtain their aerodynamic characterictics.

Some research work has already been carried out to investigate the separated leading edge flows of flat plates. A flow visulization study conducted by Ota et al (1981) observed the leading edge separation and the reattachment flows around flat plates with different leading edge shapes in Reynolds number Re_b between 40— 2000. The reattachment point is decided by observing aluminium powder motion near the reattachment zone. From the experimental results, the leading edge flow separation and reattachment phenomena are placed in three classes. These are:

(i) Laminar separation and laminar reattachment. This occurs in the flows with low Reynolds numbers. Here, the separated laminar shear flow reattaches to the plate surface in a laminar state and the reattachment length increases quickly as Reynolds number increases.

(ii) Laminar separation and turbulent reattachment. Here, the separated laminar shear flow becomes turbulent before it reattaches to the plate surface. Before the flow reattaches to the flat surface, an undulated flow is produced inside the separated flow. An increase in the Reynolds number accelerates the undulation and consequently causes a decrease in reattachment length.

(iii) Turbulent separation and turbulent reattachment. In this kind of flow, the separated shear flow becomes turbulent immediately downstream of the separation point and reattaches to the plate surface in a turbulent state. The separated flow is now almost independent of Reynolds number, so the reattachment length shows little variation with Reynolds number.

From experimental data, the reattachment length is found to be in a parabolic relation with Reynolds number Re_b. The relation is expressed as

$$\frac{\ell}{b} = K\, Re_b^{\,n}$$

here K and n are determined from experimental data. They are different for plates with different nose apex angles and Reynolds numbers.

In the experiment, the transition Reynolds number of the flow from laminar separation and laminar reattachment to laminar separation and turbulent reattachment is also determined. At the transition point, a distinct undulation of the separated shear layer is observed firstly near the reattachment point. An approximated relation between the transition Reynolds number and the plate nose shape is found as

$$Re_{tr} = 120(b/\ell_p)^{-5/4}$$

where ℓ_p is the half length of the flat plate nose.

In Ota's experiment, all the data is obtained in viscous flow around a single flat plate and the flow incidence angle is zero. The separations on the upper and lower surfaces are symmetric.

In the two dimensional cascade flows simplified from the flowmeter rotor at different radial positions, because of the change of cascade stagger angle, nose shape, chord and space, the reattachment length must vary from the hub to the tip even under the same flowrate. Also when the flowmeter is running at different flowrates, its inlet velocity profile is changing and is not uniform, the leading edge separation and reattachment flows must change accordingly.

The flows around these two dimensional cascades can be simulated using the built model. However the time step has to be very small to simulate the instantaneous development of the separated vortex flow. To simulate the leading edge separated flows, because the separated vortices are so close to the blade surface and are rapidly developing with time, the simulation time step must be very small. A vortex shedding time step recommended by Nagano et al (1982) for leading edge flow simulation is

$$\Delta t_{lw} = 0.02b/U_\infty \qquad (5.1.1)$$

In the trailing edge wake simulation, because the shed vortices are moving away from the blade surface and their influences on the flow around the blade are decreasing with time, so the time step can be longer compared with that in the leading edge flow simulation. The commonly used time step[Kiya and Arie(1977), Basu and Hancock(1978), Katz(1981)] is

$$\Delta t_{tw} = (0.02\text{—}0.05)C/U_\infty \qquad (5.1.2)$$

Hence the leading edge simulation needs a much smaller time step than that in trailing edge wake simulation. When these two flows are included in a simulation at the same time, the leading edge simulating time step has to be used. There would be a lot of vortices involved in the calculation before stability is achieved.

To reduce the computing time, the influence of the flow separations at the leading edge and the trailing edge are considered separately. Firstly, the leading edge separation and reattachment flows are simulated with the wake flow at the same time only for several selected flow cases to determine the relation between the reattachment length and inlet flow conditions and blade geometries using the built model. When these relations are known, the reattachment length on any other flow case between those selected cases are obtained directly through linear interpolation. The displacement influence of the leading edge flow separation and reattachment is simulated by including the leading separated bubble as an extra part of blade surface. To determine the separation bubble shape, the adopted boundary condition is that the streamwise pressure is constant in the separated region as assumed by Kadhim and Railly (1982) for the calculation of the separated cascade flows. With this boundary condition and the reattachment length, the separation bubble shape is found through an inverse method given by R.I. Lewis. Then the flow around the modified body with wake flow can be simulated using the trailing edge simulation time step as given by formula (5.1.2). Consequently, the pressure and lift on the turbine blades can be obtained. Using this separate consideration of the separated leading edge and the trailing edge flows, only a few leading edge flows are simulated with the leading edge simulation time step, so the computing time can be reduced and more reasonable results can be obtained.

As far as the Reynolds number influence is concerned, only when the flow Reynolds number is quite small, a rapid change of the reattachment length with Reynolds number is found by Ota et al. According to the measured results by Ota et al and Kottke et al, there is only a small change in the leading edge reattachment length for the plates with a square leading edge while the Reynolds number is over 200. In present calculations, the variations in the reattachment length with Reynolds number is ignored when the Reynolds number Re_b is

over 200. The aerodynamic characteristics of the blade when Reynolds number R_{eb} is below 200 are obtained from the simulated results by interpolations.

5.2 Simulation of the Separated Leading Edge Flows

5.2.1 Mathematical Model

Using the established potential flow model to simulate the flow around a turbine flowmeter blade, the separation lines from the separation points on the blade surface divide the whole flow field around the blade into several regions as shown in fig.5.2. In any of these regions, the blade surface remains a streamline.

Inside the regions, flows are still assumed to be potential and the Bernoulli equation can be used for the points on the blade surface. Applying the Bernoulli equation to region R4 between point 1 and point 8 gives

$$\frac{\gamma_1^2}{2} + \frac{p_1}{\rho} + \frac{\partial \Phi_1}{\partial t} = \frac{\gamma_8^2}{2} + \frac{p_8}{\rho} + \frac{\partial \Phi_8}{\partial t} \qquad (5.2.1)$$

Rearranging the above equation, the resulted equation is

$$\frac{P_1 - P_8}{\rho} = \left(\frac{\gamma_8^2}{2} + \frac{\partial \Phi_8}{\partial t}\right) - \left(\frac{\gamma_1^2}{2} + \frac{\partial \Phi_1}{\partial t}\right) \qquad (5.2.2)$$

The Bernoulli equation can be applied to the other three regions in the same manner as to the region R4, the obtained equations are

in region R2

$$\frac{P_3 - P_2}{\rho} = \left(\frac{\gamma_2^2}{2} + \frac{\partial \Phi_2}{\partial t}\right) - \left(\frac{\gamma_3^2}{2} + \frac{\partial \Phi_3}{\partial t}\right) \qquad (5.2.3)$$

in region R1

$$\frac{P_5 - P_4}{\rho} = \left(\frac{\gamma_4^2}{2} + \frac{\partial \Phi_4}{\partial t}\right) - \left(\frac{\gamma_5^2}{2} + \frac{\partial \Phi_5}{\partial t}\right) \qquad (5.2.4)$$

in region R3

$$\frac{P_7 - P_6}{\rho} = \left(\frac{\gamma_6^2}{2} + \frac{\partial \Phi_6}{\partial t}\right) - \left(\frac{\gamma_7^2}{2} + \frac{\partial \Phi_7}{\partial t}\right) \qquad (5.2.5)$$

Adding equations (5.2.2), (5.2.3), (5.2.4) and (5.2.5) together, the left and right hands of the resulting equation are

$$LHS = \frac{(P_1-P_2) + (P_3-P_4) + (P_5-P_6) + (P_7-P_8)}{\rho} \qquad (5.2.6)$$

and

$$\begin{aligned} RHS = & \left(\frac{\gamma_8^2}{2} + \frac{\partial \Phi_8}{\partial t}\right) - \left(\frac{\gamma_1^2}{2} + \frac{\partial \Phi_1}{\partial t}\right) \\ & + \left(\frac{\gamma_2^2}{2} + \frac{\partial \Phi_2}{\partial t}\right) - \left(\frac{\gamma_3^2}{2} + \frac{\partial \Phi_3}{\partial t}\right) \\ & + \left(\frac{\gamma_4^2}{2} + \frac{\partial \Phi_4}{\partial t}\right) - \left(\frac{\gamma_5^2}{2} + \frac{\partial \Phi_5}{\partial t}\right) \\ & + \left(\frac{\gamma_6^2}{2} + \frac{\partial \Phi_6}{\partial t}\right) - \left(\frac{\gamma_7^2}{2} + \frac{\partial \Phi_7}{\partial t}\right) \end{aligned} \qquad (5.2.7)$$

At every separation point, the static pressure on the two sides of the separated vortex sheet should be equal. Therefore, the following relationships apply

point a	$P_1 = P_2$
Point b	$P_3 = P_4$
point c	$P_5 = P_6$
point d	$P_7 = P_8$

Subtituting these pressure relations into formula (5.2.6) gives

$$LHS = 0 \qquad (5.2.8)$$

After a flow separation on a blade surface, the velocity behind the separation point is zero, then

point a $\quad \gamma_1 = 0$

point b $\quad \gamma_3 = 0$

point c $\quad \gamma_6 = 0$

point d $\quad \gamma_8 = 0$

Substituting these velocities into equation (5.2.7) and rearranging the equation gives

$$\frac{1}{2}(\gamma_2^2+\gamma_4^2-\gamma_5^2-\gamma_7^2) = \frac{\partial}{\partial t}(\Phi_1-\Phi_2+\Phi_3-\Phi_4+\Phi_5-\Phi_6+\Phi_7-\Phi_8) \qquad (5.2.9)$$

The circulation around the blade is

$$\Gamma = \Phi_1-\Phi_8+\Phi_3-\Phi_2+\Phi_5-\Phi_4+\Phi_7-\Phi_6$$

$$= \Phi_1-\Phi_2+\Phi_3-\Phi_4+\Phi_5-\Phi_6+\Phi_7-\Phi_8 \qquad (5.2.10)$$

Finally, the equation can be written as

$$\frac{1}{2}(\gamma_2^2+\gamma_4^2-\gamma_5^2-\gamma_7^2) = \frac{\partial \Gamma}{\partial t} \qquad (5.2.11)$$

This equation is a form of the Kutta condition for the flow around a turbine flowmeter blade. Combining this equation with the equations obtained from the boundary condition on the blade surface, a unique solution is defined.

5.2.2 An Analysis of the Simulated Results

Using the built potential simulation model, the following results are obtained. The simulated leading edge flows for flat plates with different leading edge shapes at zero incidence angle are shown in

fig.5.3. The simulated reattachment length for the flat plates with half apex angles of 30^{o}, 60^{o} and 90^{o} are compared with Kottke's experimental data at the highest Reynolds number of 10000[Ota et al(1981)]. The comparison presented in fig.5.4 shows a good agreement between the simulated results and measured data.

In the tested turbine flowmeter of this research, the blade stagger angle varies from 30 degrees to about 50 degrees from the hub to the tip and the space/chord ratio of the cascades varies between 0.52 to 0.8. Apart from these cascade geometrical variations, the inlet velocity profile to the rotor changes with flowrate and is non-uniform from the hub to the tip. Consequently, the leading edge flows should be different at different radial positions and change with flowrate. In the results presented here, several representative leading edge separated flows are simulated and some conclusions are drawn from the results.

The simulated results for the cascades at the rotor's hub, midspan and tip sections with zero incidence angle are presented in fig.5.5. In the three simulations, the cascade stagger angle, space and chord corresponding to the hub, midspan and tip areas are given in following table.

Table 5.1 Turbine Flowmeter Blade Geometries

Radial sections	Blade stagger angle β(deg)	Space S(inch)	Chord C(inch)
Tip	49.16	1.2315	1.5445
Midspan	40.85	0.9205	1.3352
Hub	29.79	0.6095	1.1638

The leading edge separation and reattachment regions are quite similar in these three cases on both upper and lower surfaces at zero incidence. Only a very small difference is found in the bubble length on the upper surface due to the geometrical variations. It can be concluded from these results that the reattachment length difference caused by cascade geometrical changes from the hub to the tip in the tested flowmeter is so small that it can be ignored. Therefore, the

leading edge flow characteristics of the midspan section can be used as an approximated representative of the flows at different radial sections. When a large reattachment length differences between the tip and hub cascades exist in some flowmeters in the application of this model, the midspan cascade cannot be used as a representative of all the cascades between the hub and the tip, several cascades from different radial positions have to be considered.

To find the influence of the inlet flow condition on the leading edge flow separation and reattachment of the tested flowmeter, an examination is conducted on the midspan cascade with several different incidence angles. For the results shown in fig.5.6, the incidence angle to the blade changes from -8 degrees to 8 degrees. On the upper surface, when the incidence angle continuously increases from -8 to -4 degrees, the ratio of the reattachment length to the half blade thickness increases from 4.6 to 6.15. However, if the incidence is further increased to 4 degrees, the ratio drops from 6.15 to 4.8 and remains constant when the incidence is further increased to over 4 degrees. According to the characteristics of flow separation and reattachment given by Ota et al, the flow state at both separation point and reattachment point could be laminar while the incidence is below -4 degrees. The flow state at the reattachment point becomes turbulent for the flows with incidence angle between -4 degrees and 4 degrees, and the separated flow becomes turbulent very quickly after the separation point when the incidence exceeds 4 degrees. On the lower surface, as the incidence angle increases from negative to zero degree, the ratio stays at 4.6, so the flow state at both separation and reattachment points should be turbulent. The reattachment length begins to decrease and drops to zero when the incidence angle goes up to 8 degrees. Hence the flow state at both separation and reattachment points is laminar for the flows within this incidence range and no separation occurs as incidence angle is further increased.

To summarise the simulation results, the relation between the reattachment length and incidence angles for the midspan cascade of the tested turbine flowmeter rotor is presented in the following table.

TABLE 5.2 Simulated Relation Between the Leading Edge Reattachment Length ℓ_r and the Incidence Angle for the Midspan Cascade

Angle \ ℓ_r	upper surface $\ell_r/(B/2)$	lower surface $\ell_r/(B/2)$
*12	4	0
8	4	0
4	4	4.3
0	4.8	4.6
-4	6.15	4.6
-8	4.6	4.6
*-12	3.05	4.6

* indicates the derived results.

5.3 Modification of the Blades Leading Edge Contour

In the model given by Roberts(1980) for the leading edge reattachment flow, the flow in the leading edge area is divided into two main regions by a streamline as shown in fig.5.7: (1) the recirculation bubble contained between the dividing streamline and the blade surface, (2) the free shear layer outside the recirculating bubble. These two regions can be further divided into parts upstream and downstream of a transit point. Upstream of the transit point, the free shear layer is in a laminar state and is incapable of creating any significant diffusion. The static pressure is constant in this region. Downstream of the transit point, interaction between the recirculating flow and the outer shear flow is present and is able to cause enough energy diffused from the freestream fluid by entrainment to cause the flow reattachment. The interaction causes strong energy dissipation and consequently a rapid pressure drop from the transit point to the reattachment point. In Roberts's model, a constant energy dissipation and a linear velocity distribution is assumed between the transit point and the reattachment point. At the reattachment point, a turbulent boundary layer exists.

In the model presented here, the influence of the leading edge separated flow on the pressure distribution over the blade surface is calculated by modifying the blade contour in the SR region (separation and reattachment region) to simulate its displacement effect. To simulate this displacement effect, the streamline between the free shear layer and the recirculating region is taken as the modified blade surface. The modification is done under the assumption of a constant streamwise static pressure around the leading edge separation bubble(Kadhim and Railly, 1982). To find the modified blade contour in the SR region, the inverse design method given by R.I. Lewis is adopted here. After the modification, the new blade contour forms a streamline in the flow field and the pressure is kept constant inside the SR region on the modified blade surface.

In every calculated flow case around the flowmeter blades, the reattachment length is decided according to table 5.2. Because the influence of the wake flow on the reattachment length has already been included in the results presented in table 5.2, the wake effect is also included in the interpolated reattachment lengths. With the constant pressure assumption and the interpolated reattachment length, the accurate leading edge modification can be found.

5.3.1 Mathematical Model for Blade Modification

With inviscid potential flow assumption, the modified blade contour still forms a streamline in the flow field and the Bernoulli equation is valid for points on the modified blade contour. Given points a and b are two points on a streamline, the Bernoulli equation is

$$\frac{u_{i,a}^2}{2} + \frac{p_{i,a}}{\rho} + \frac{\partial \Phi_{i,a}}{\partial t} = \frac{u_{i,b}^2}{2} + \frac{p_{i,b}}{\rho} + \frac{\partial \Phi_{i,b}}{\partial t} \qquad (5.3.1)$$

or

$$\frac{p_{i,a} - p_{i,b}}{\rho} = \frac{u_{i,b}^2 - u_{i,a}^2}{2} + \frac{\partial \Phi_{ab}}{\partial t} \qquad (5.3.2)$$

When points a and b are both inside the SR region, then

$$p_{i,a} = p_{i,b} \tag{5.3.3}$$

In steady flow, substituting equation (5.3.3) into equation(5.3.1) gives the velocity relation as

$$u_{i,a} = u_{i,b} \tag{5.3.4}$$

In viscous flow, the pressure on a blade surface is influenced by the boundary layer. The relation between the real pressure on a blade surface and the inviscid results given by Lock and Firman(1982) is

$$\frac{p_i - p}{\rho u_i^2} = \kappa^*(\theta+\delta^*) \tag{5.3.5}$$

So the real pressure on the blade surface is

$$p = p_i - \kappa^*(\theta+\delta^*)\rho u_i^2 \tag{5.3.6}$$

Using the assumption of constant real pressure inside the SR region on the blade surface, the following equation is obtained

$$\frac{p_{i,a} - p_{i,b}}{\rho} = \kappa_a^*(\theta_a+\delta_a^*)u_{i,a}^2 - \kappa_b^*(\theta_b+\delta_b^*)u_{i,b}^2 \tag{5.3.7}$$

In steady viscous flow, the obtained velocity relation using equations (5.3.2) and (5.3.7) is

$$\frac{u_{i,a}}{u_{i,b}} = \left[\frac{1+2\kappa_b^*(\theta_b+\delta_b^*)}{1+2\kappa_a^*(\theta_a+\delta_a^*)}\right]^{1/2} \tag{5.3.8}$$

When the fluid becomes ideal, θ and δ^* are zero, then a constant velocity condition is obtained as equation(5.3.4)

Inside the SR region, the free shear layer outside the recirculation bubble remains the same state as the separation point until the transit point as concluded by Roberts. Due to lack of imformation on the transit point, θ and δ^* are assumed to be constant over the SR region.

κ^* is the boundary layer displacement thickness curvature. It is

$$\kappa^* = \kappa_w + \frac{d^2\delta^*}{ds^2} \tag{5.3.9}$$

As the displacement thickness is constant, $\kappa^* = \kappa_w$, κ_w is the

curvature of the separation bubble inside the SR region.

To determine the boundary layer state at the leading edge separation points, the flow is approximated to a stagnation flow as used by Nagano, Naito and Takata(1982). The boundary layer thickness given by Schlichting for a stagnation flow is

$$\delta = 2.4 \sqrt{\frac{\nu}{a}} \tag{5.3.10}$$

here a is taken as the velocity gradient in the vicinity of the stagnation point, θ and δ^* are obtained through velocity profile integration as

$$\theta = 0.117\delta \tag{5.3.11}$$

and

$$\delta^* = 0.282\delta \tag{5.3.12}$$

In this boundary layer approximation, equation(5.3.8) can be used to determine the modified leading edge blade shapes in steady flows.

However, no linear velocity relation between the points inside the SR region can be obtained from the Bernoulli equation in unsteady flows, this causes some difficulties in calculation. In this simulation, because of the adopted iterative procedures in the leading edge modification(in paragraph 5.3.2), equation(5.3.8) can be used.

When the reattachment length is known, the boundary conditions controlling the blade modification are

(a) inside SR region

$$\frac{u_{i,m}}{u_{i,n}} = \left[\frac{1+2\kappa_n^*(\theta_n+\delta_n^*)}{1+2\kappa_m^*(\theta_m+\delta_m^*)}\right]^{1/2} \tag{5.3.13}$$

where m and n are any two points inside the SR region.

(b) outside the SR region on the blade surface

$$\Psi_m = \Psi_n \tag{5.3.14}$$

where m and n are any two points on the blade surface ontside the SR region.

Because the separation bubble shape is unknown, an iterative calculation has to be employed to determine the shape. Applying Lewis's method(1982), the precedure to obtain the modified blade contour is:

(i) To start the calculation, an initial blade contour is chosen. Here, the original blade contour is chosen. Using the velocity relation (5.3.4) or (5.3.13) in the SR region, the potential flow around this initial blade is obtained by solving the equations from the boundary condition on the blade surface and the Kutta condition.

When the solution is obtained, the velocity components in the flow field can be calculated using the following formulae

$$u_i = u_\infty + \sum_{j=1}^{N} A_{i,j}\,\gamma_j \qquad (5.3.15)$$

$$v_i = v_\infty + \sum_{j=1}^{N} B_{i,j}\,\gamma_j \qquad (5.3.16)$$

$A_{i,j}$ and $B_{i,j}$ are the induced velocity influence coefficients in x and y direction respectively here.

(ii) The streamline from the separation point is calculated.

In the flow field, the elements on a streamline are located in the local velocity direction. The positions of those points on a streamline can be calculated using the following formulae

$$x_{i+1} = x_i + \Delta s \cos(\alpha_i)$$

$$= x_i + \Delta s \frac{u_i}{\sqrt{u_i^2+v_i^2}} \qquad (5.3.17)$$

$$y_{i+1} = y_i + \Delta s \sin(\alpha_i)$$

$$= y_i + \Delta s \frac{v_i}{\sqrt{u_i^2+v_i^2}} \qquad (5.3.18)$$

here α_i is the local velocity vector and Δs is a selected length for finding the streamline.

In inviscid flows, the streamline stemmed from a separation point on the blade surface must have the same stream function value as the separation point. And because the separation point and the reattachment point are both on the same blade surface, so they must be on the same streamline, hence the separated streamline from the separation point must intersect the blade surface at the reattachment point. The calculated streamline and the blade surface outside the SR region form a new blade contour.

In viscous flow, the streamline starts from the displacement boundary layer edge at the separation point. With this starting point, the displacement of the free shear layer is included in this simulation.

(iii) The modified new contour is used as a new initial blade surface, and the calculation is repeated from step (i) until the modified blade surface satisfies the required accuracy under the boundary conditions. Then the calculation is terminated and the required blade contour is obtained.

During the modification, instead of using the new contour as the initial blade surface for the next iteration directly, relaxation is introduced. Thus the new y positions of the nodes on the blade contour are taken as

$$y_i^{new} = k^* y_i^{old} + (1-k) y_i^{new} \qquad (5.3.19)$$

where k is a relaxation factor. The used k is 0.5.

The x positions of the nodes on the blade contour are not changed during the iteration.

5.3.2 Influence of the Wake flow on the Leading Edge Blade Modification

The separated leading edge and the trailing edge flows certainly influence each other during their development. However, neither of them is known in advance. The only known conditions are the reattachment length and that the pressure around the separation bubble

is constant. To obtain the accurate leading edge blade contour modifications, an iterative calculation is employed to take account of the influence of the trailing edge flows on the leading edge flows because they are considered separately. The calculating procedure is

(1) Without the trailing edge wake flow, the first modification to the leading edge blade contour is obtained following the precedure given paragraph 5.3.1. The resulting blade contour is the first approximation to the separated leading edge flow.

(2) With the modified blade contour, the trailing edge wake flow is simulated by the model described in chapter four.

(3) Under the influence of the simulated trailing wake flow from step (2), the leading edge modification is conducted again as step (1).

(4) The calculation is repeated from step (2) until an accurate and stable blade leading edge modified contour is obtained.

In the above procedure, the leading edge modification at step (3) is conducted under the influence of the simulated stable wake flow from step (2), this is the reason why equation(5.3.8) can be used in the process.

In cascade flow, the axial distance between the leading edge and trailing edge flows is quite large, and the influence between them is small. As shown in fig.5.9 and fig.5.10, after only the second modification, an quite accurate leading edge blade contour has already obtained.

The modified leading edges of the flowmeter rotor blade with various blade geometries and incidence angles are presented in fig.5.11 and fig.5.12. On comparing the modified blade contours and the separated vortex sheet trajectories in the leading edge flow simulations, the agreement is found to be very good between them. Because the separated vortex sheet should be on a streamline in the flow field, this means the displacement of the separated vortex bubbles to the external flow is are approximated correctly.

5.3.3 Results of Blade Surface Modification

In equation(5.3.13) which governs the leading edge modification, the velocity relation at the points inside the SR region is a function of the local boundary thickness. Obviously, boundary layer thickness is very much dependent on the Reynolds number Re_b. From Ota's experimental results, the reattachment length shows only a small change with Reynolds numbers while R_{eb} is over 200 for the plate with a square leading edge. This result suggests that the separated flow is in turbulent state in this flow range. In the various simulations of the flow around flowmeter blades, even the simulated results show the variation of the flow state at the reattachment point with the incidence angle, because the viscosity effect is not included in the present model, the reattachment length change with the Reynolds number cannot be predicted, so the reattachment length is assumed to be the same as the simulated inviscid results for all the cases with Reynolds number over 200. As shown in fig.5.12 to fig.5.14, the simulated separation bubbles change with the Reynolds numbers are presented. While Reynolds number is small, viscous effects are very strong, so the separated flow is restricted to a region near the blade surface. The separation bubble becomes bigger as Reynolds number increases. Corresponding to the separation bubble variations, the pressure distributions are also changed in the leading edge area. However the pressure distributions after flow reattachment are almost the same for the flows with different Reynolds numbers, these pressure characteristics are also found in Gaster's experimental results for turbomachine blades. So the separation bubble has little influence on its downstream pressure distribution. Theoretically, the pressure should be constant inside the SR zone in the results presented here. Due to the very large bubble surface curvature in this region and the restricted minimum panel size, there is a pressure change near the separation points and the reattachment points in the simulated results.

5.4 Results and Discussion

So far, the modifications of the blade leading edges are obtained

to simulate the influence of the leading edge separation and reattachment on the aerodynamic characteristics of the flowmeter blades. To predict the performance of a flowmeter under various inlet conditions, it is necessary to obtain a complete aerodynamic characteristics of the flowmeter blades in different radial positions. In the tested flowmeter, due to the blade geometrical changes from the hub to the tip, their aerodynamic behavior is different. Using the developed model, The predicted results of the blades in different radial sections for various Reynolds numbers and flow incidence angles are presented here.

In fig.5.15, the simulated trailing edge wake flows for the midspan section with incidence angle 8 degrees and -4 degrees are given. Clear wake configurations were formed behind the blade trailing edge in both cases. The time step used was 0.015. The fluctuation of F_y and F_x during the wake flow development is presented in fig.5.16 and fig.5.17 for the case with -4 degrees incidence angle. At the beginning of the simulation, very large fluctuations exist in both lift and drag, and the forces tend to a constant as time goes by. However, due to the periodic vortex street, small fluctuations in both F_x and F_y remains.

As concluded in paragraph 5.2.2, the reattachment length changes with the blade shape and the flow Reynolds number while Re_b is over 200 are ignored. The relation between the the reattachment length and the incidence angle is obtained from table 5.2. The Reynolds number Re_b effect is included by applying equation (5.3.13) to determine the separation bubble shape. In fig.5.18 and fig.5.19, the simulated lift and drag characteristics of the flowmeter blades from the hub to the tip are presented for a Reynolds number of 29500. Due to the blade variations from the hub to the tip, both the lift and the drag depend very significantly on the radial positions. In the hub section, the blade space is small, so both lift and drag forces are very much lower than that at the tip section. On every radial section, the lift and the drag on a blade are also changing with Reynolds numbers. From fig.5.20 to fig.5.24, the lift and drag force variation with Reynolds number for the hub and the tip sections is presented. Generally speaking, viscous effect decreases lift and increases drag.

CHAPTER SIX

THE PREDICTION OF TURBINE FLOWMETER PERFORMANCE

6.1 Performance Prediction Equation

The equation for turbine flowmeter performance prediction is derived from the angular momentum theorem. It is

$$T_d - T_b - T_{disc} - T_h - T_t = I\frac{d\omega}{dt} \qquad (6.1.1)$$

When a flowmeter is applied in the conditions of stable inlet flow and without any unsteady disturbances, all the torques acting on the rotor must balance each other all the time, so the rotor speed remains constant. The performance equation becomes

$$T_d = T_b + T_t + T_h + T_{disc} \qquad (6.1.2)$$

However, when a flowmeter is working in unsteady flow conditions, such as in the wakes flow from the rotor's upstream or in pulsating flows, T_d becomes time-dependent, the rotational speed of the rotor then fluctuates accordingly. Equation(6.1.1) should be used for performance prediction in those flows.

To predict the performance of a turbine flowmeter, all the torques on the rotor should be accurately modelled. In this chapter, models for all these torques are discussed and the performance of the tested turbine flowmeter is predicted.

6.2 Driving Torque

When flow passes through a turbine flowmeter, lift forces are produced on the rotor blades and these forces drive the rotor rotation.

In a helical blade turbine flowmeter, under the assumption of a uniform inlet velocity profile, the rotor blade is designed to have the same incidence angle from the hub to the tip. Even so, the pressure distributions on the rotor blades still vary with radius due to the blade geometrical variations. On the other hand, the boundary layers on both the pipe wall and the flowmeter hub cause the flowmeter inlet velocity profile to be non-uniform. The flow near the pipe wall and the hub surface is slowed down, consequently the flow attack angles to the blade become negative in these regions and positive in the midspan region of the rotor. The blade blockage to the flow is also different at various radial positions, and the centrifugal effect is present when the circumferential velocity component is not zero. The centrifugal effect becomes especially important when there is swirl inside the inlet flow. To predict the flow around a turbine flowmeter rotor, its inlet velocity profile must be known. A numerical model is developed in this chapter to predict the flowmeter inlet velocity profiles for the flowmeter without inlet swirl.

6.2.1 Inlet Velocity Profile

The flow inside a turbine flowmeter is actually a three dimensional flow, but the radial component is very small except in the hub and tip areas and its effect is ignored here. The flow field inside the rotor is thus simplified into the flows on an infinite number of cylindrical surfaces from the hub to the tip. The flow on every cylindrical surface is in an equilibrium state in the radial direction and is treated as a two dimensional cascade flow.

Ideally, the inlet velocity profile for the flowmeter rotor is on the section where is free of the rotor's disturbance. Because there is

only limited space in the tested flowmeter between the hub head and the rotor in which the inlet flow is allowed to develop, the inlet sections of those simplified two dimensional flows has to be chosen inside this limited space, so the inlet section chosen in the calculation is the section with minimum combined disturbance from the hub head and the rotor.

To calculate the inlet velocity profile, the flowmeter rotor is replaced with a hemi-oval ended cylinder having the same diameter as the hub. The result of this replacement is that the flow between the pipe and the hub becomes an axisymmetric annulus flow as shown in fig.6.1 and can be simulated by the singularity method. To calculate this annulus flow, both the pipe wall and the hub surface are represented by ring sources with constant intensity and the x axis is taken as the axis of the pipe. Fig.6.2 illustrates a unit source ring with radius r in the plane x=b. As given by Hess and Smith(1966), the velocity potential at point(x,y,0) due to the source ring is

$$\Phi = -\frac{1}{2\pi}\int_0^{\pi}\frac{r\,d\phi}{d}$$

$$= -\frac{1}{2\pi}\int_0^{\pi}\frac{r\,d\phi}{[(x-b)^2+r^2+y^2-2yr\cos\phi]^{1/2}} \qquad (6.2.1)$$

The corresponding axial and radial velocity components are

$$u = \frac{\partial\Phi}{\partial x} = \frac{r}{2\pi}\int_0^{\pi}\frac{(x-b)\,d\phi}{[(x-b)^2+r^2+y^2-2yr\cos\phi]^{3/2}} \qquad (6.2.2)$$

$$v = \frac{\partial\Phi}{\partial y} = \frac{r}{2\pi}\int_0^{\pi}\frac{(y-r\cos\phi)\,d\phi}{[(x-b)^2+r^2+y^2-2yr\cos\phi]^{3/2}} \qquad (6.2.3)$$

To obtain a potential flow solution to the problem, solid boundary condition is assumed on the pipe wall and the hub surface, these can be written as

$$\sum_{j=1}^{N} K_{i,j}\,q_j + \vec{V}_\infty\cdot\vec{n}_i = 0$$

$$i=1,2,3,\ldots N \qquad (6.2.4)$$

and the influence coefficients $K_{i,j}$ are

$$K_{i,j} = \vec{u}_{i,j}\cdot\vec{n}_i + \vec{v}_{i,j}\cdot\vec{n}_i \qquad (6.2.5)$$

From equations(6.2.2) and (6.2.3), $u_{i,j}$ and $v_{i,j}$ are

$$u_{i,j} = \frac{r_j\Delta s_j}{2\pi}\int_0^{\pi}\frac{(x_i-x_j)d\phi}{[(x_i-x_j)^2+r_i^2+r_j^2-2r_ir_j\cos\phi]^{3/2}} \qquad (6.2.6)$$

$$v_{i,j} = \frac{r_j\Delta s_j}{2\pi}\int_0^{\pi}\frac{(r_i-r_j\cos\phi)d\phi}{[(x_i-x_j)^2+r_i^2+r_j^2-2r_ir_j\cos\phi]^{3/2}} \qquad (6.2.7)$$

To determine the mutual influence coefficients between ring sources, a line segment, as shown in fig.6.3, is considered. The positions of points on this segment can be expressed as

$$\begin{aligned} a &= r_0 + \ell\sin\beta \\ b &= \ell\cos\beta \end{aligned} \qquad (6.2.8)$$

The velocity potential at point P(x,y,0) induced by this line segment is obtained by substituting x_j and y_j with a and b in equations (6.2.6) and (6.2.7) and integrating the resulting equations with respect to ℓ from $-\Delta s_j/2$ to $\Delta s_j/2$. The integration is conducted using Simpson's integration rule. During the integration, every segment is subdivided into sub-elements. The recommended number of the subelements by Hess and Smith is $16\Delta s_j/d_{min}$, where d_{min} is the distance of point P to the closer endpoint of the segment.

However, the above integration cannot be used for calculating the velocity induced by a segment at its own control point. To calculate the self induced velocity, a line segment is divided into three parts as shown in fig.6.4, The velocity induced at the midpoint by parts A and B can still be calculated using equations(6.2.6) and (6.2.7). To calculate the contribution from the central part, equations(6.2.6) and (6.2.7) are expanded in powers of d/r_0 and integrated from $\ell=-d$ to $\ell=d$. The formulae obtained for the self-induced velocity components are

$$u' = -\frac{\sin\beta}{4\pi}\left(\frac{d}{r_o}\right)\left\{1+\frac{1}{144}\left(\frac{d}{r_o}\right)\left[13+6\sin^2\beta+6\ell n\left(\frac{d}{8r_o}\right)\right]\right\} \tag{6.2.9}$$

$$v' = \frac{-1}{2\pi}\left(\frac{d}{r_o}\right)\left\{\left[\sin^2\beta+\ell n\left(\frac{d}{8r_o}\right)\right]-\frac{1}{48}\left(\frac{d}{r_o}\right)^2\left[3\cos^2\beta-2\sin^4\beta+3\ell n\left(\frac{d}{8r_o}\right)\right]\right\} \tag{6.2.10}$$

d is chosen by trial and error processes. The d suggested by Hess and Smith is

$$d = 0.08r_o \quad \text{if} \quad 0.08r_o < \Delta s_j/2$$

or

$$d = \Delta s_j/2 \quad \text{if} \quad 0.08r_o > \Delta s_j/2 \tag{6.2.11}$$

In the above calculation, the control point is assumed from the outset to lie on the element. The part of velocity arising from the limiting process of $d \to 0$ is not included, the components are

$$u'' = -\sin\beta/2$$
$$v'' = \cos\beta/2 \tag{6.2.12}$$

So the total self-induced velocity coefficients for a ring source at its own control point are

$$u = u^{(A)} + u^{(B)} + u' + u''$$
$$v = v^{(A)} + v^{(B)} + v' + v''$$

Because only a limited length of the pipe and the hub can be involved in the calculation and the solid boundary condition is satisfied in those area, the inlet condition is controlled by the flowrate through the pipe and U_∞ is taken as an unknown. The equation for flowrate control is

$$\sum_{j=1}^{N} K_{n+1,j}\, q_j + \pi r_p^2 U_\infty = Q \tag{6.2.14}$$

where

$$K_{n+1,j} = \int_0^{r_p} 2\pi r u(r)_j dr$$

$$= \sum_{k=1}^{M} 2\pi r_k u_{k,j} \Delta r_k \qquad (6.2.15)$$

Using the equations from (6.2.4) and (6.2.14), the potential solution of the flow inside the flowmeter annulus can be calculated.

In the actual flow, owing to the boundary layers on both the pipe and the hub surfaces, the velocity profile inside the annulus is very different from the potential flow profiles. The boundary layer on the pipe wall is fully developed at the front of the flowmeter rotor and the boundary layer on the hub surface develops from the nose of flowmeter hub head, these two boundary layers are considered separately in the calculation.

The boundary layer on the flowmeter hub surface starts from the nose point of the hub and is assumed to be a thin layer up to the flowmeter rotor, it is calculated using the integral boundary layer theory. During the simulation of this boundary layer, the displacement of the pipe wall boundary layer is considered by adding the displacement flowrate to the flowrate Q in equation (6.2.14).

6.2.2 Calculation of the Hub Surface Boundary Layer

6.2.2.1 Laminar boundary layer

The laminar boundary layer calculation is conducted using Thwaites(1949) method and Prandtl's boundary layer equation.

The momentum thickness,θ, is calculated using

$$\theta^2 - \theta_o^2 = \frac{0.45\nu}{U_e^6} \int_0^s U_e^5 \, ds \qquad (6.2.2.1)$$

where s is the blade surface length starting from the hub nose point.

An empirical relation given by Cebeci and Bradshaw(1977) is used to calculate the shape factor H. It is

$$H = 2.61 - 3.75\lambda + 5.24\lambda^2 \qquad \text{for } 0 < \lambda < 0.1$$

$$= 2.088 + \frac{0.0731}{\lambda + 0.14} \qquad \text{for } -0.1 < \lambda < 0 \qquad (6.2.2.2)$$

where

$$\lambda = \frac{\theta^2}{\nu} \frac{dU_e}{ds} \qquad (6.2.2.3)$$

The boundary layer displacement thickness, δ^* , is

$$\delta^* = H\theta \qquad (6.2.2.4)$$

6.2.2.2 Boundary layer transition

The transition of the boundary layer from a laminar state to a turbulent state is based on a modified Seby' correlation(Goulas and Heritage, 1985).

Instantaneous transition with no laminar separation bubble is assumed when $\lambda = 0.09$ or $R_{e\theta} > R_{ecrit}$, and

$$R_{ecrit} = \frac{10^3}{1.2+0.7TI} + 10 \left[\frac{\lambda + 0.09}{0.0106+0.036TI} \right]^{2.62} \qquad (6.2.2.5)$$

and $R_{e\theta}$ is the Reynolds number based on the boundary layer momentum thickness and TI is the turbulence level of the free stream flow.

Immediately after transition, θ is assumed to be unchanged and H is calculated from one of the following formulae

(1) $\lambda > 0.0$ or

$\lambda < 0$ and $R_{e\theta} > 2500$

$$H = 1.754 - 0.0647 \ln (R_{e\theta}) + 0.001916 [\ln(R_{e\theta})]^2 \qquad (6.2.2.6)$$

(2) $\lambda < 0$ and $R_{e\theta} < 2500$

$$H = 1.754 - 0.0647\ln(R_{e\theta}) + 0.001916 [\ln(R_{e\theta})]^2 + [1.32-126\lambda(R_{e\theta})^{-0.732}]-4 \qquad (6.2.2.7))$$

6.2.2.3 Turbulent boundary layer

A successful integral method for turbulent boundary layer calculations was introduced by Head(1958, Head and Patel,1969). This method is based on entrainment rate. If $\delta(s)$ is the boundary layer thickness and Q(s) is the volume flow inside the boundary layer,then

$$Q(s)= \int_0^{\delta(s)} u(s)dy \qquad (6.2.2.8)$$

The entrainment rate V_E is the increasing rate of Q along the surface, i.e.

$$V_E = \frac{dQ}{ds} = \frac{d}{ds} \int_0^{\delta(s)} u(s)dy \qquad (6.2.2.9)$$

Using the definition of displacement thickness of the boundary layer, V_E can be written as

$$V_E = \frac{d[U_e(\delta-\delta^*)]}{ds} \qquad (6.2.2.10)$$

or

$$\frac{V_E}{U_e} = \frac{1}{U_e}\frac{d}{ds}[U_e(\delta-\delta^*)] = \frac{1}{U_e}\frac{d(U_e\theta H1)}{ds} = G(H1)$$

so

$$\frac{d(U_e\theta H1)}{ds} = U_e\, G(H1) \qquad (6.2.2.11)$$

where

$$H1= \frac{\delta-\delta^*}{\theta} \qquad (6.2.2.12)$$

Functions H and G are determined from experimental data. The correlation between H and H1 used here is given by Kline et al(1981).

Introducing new parameters h and Λ, they are defined as

$$h = \frac{H-1}{H} \qquad (6.2.2.13)$$

and

$$\Lambda = \frac{\delta^*}{\delta} \qquad (6.2.2.14)$$

A relation between h and Λ is established from experimental data as

$$\frac{h}{\Lambda} = 1.5 + 0.179\left(\frac{V_t}{\Lambda}\right) + 0.32\left(\frac{V_t}{\Lambda}\right)^2 \qquad (6.2.2.15)$$

here V_t/Λ is an implicit function of Re^* and Λ, It is

$$\frac{V_t}{\Lambda} = \frac{1/\Lambda - 2}{0.05 + \ln(kRe^*) - \ln(V_t/\Lambda)} \qquad (6.2.2.16)$$

where k is the Von Karmen constant and Re^* is Reynolds number of the boundary layer displacement thickness.

The dependence of h on displacement thickness Reynolds number is very weak, especially in the separated region. The relation between H and H1 used by Goulas and Heritage(1985) is

$$h = 1.5\Lambda \qquad (6.2.2.17)$$

Using equation(6.2.2.17), an expression of H in terms of H1 can be obtained in form of

$$H = H1 - 1 \pm \sqrt{(H1-1)^2 - 2H1} \qquad (6.2.2.18)$$

The function G used here is developed by Bardina et al(1981) and Ferziger et al(1982). This has been used successfully for diffuser flows and applied to the boundary layer on the blade surfaces by Goulas(1985). It is

$$G = 0.0083(1-\Lambda)^{-2.5} \qquad (6.2.2.19)$$

Ludwieg-Tillman(1949) gave a relation between local skin friction, boundary layer displacement thickness Reynolds number and shape

parameter H. This correlation is adopted in the present calculation. It is

$$c_f = 0.246\ 10^{-0.678H}\ R_{e\theta}^{-0.268} \qquad (6.2.2.20)$$

$$R_{e\theta} = \frac{U_e\ \theta}{\nu} \qquad (6.2.2.21)$$

6.2.2.4 Representation of the boundary layer

The are two simple approaches to represent the boundary displacement effect: the body modification method and the surface transpiration method. In the body modification method, The displacement thickness of the boundary layer is added to the solid surface directly and the inviscid flow around the modified body is used for approximating the boundary layer displacement around the original body. The disadvantage of this method is the large amount of computing time because the final displacement of the boundary layer is found through iteration. The solid surface has to be renewed and divided after every iteration and the influence matrix has to be updated at the same time. In the transpiration method, a transpiration velocity is enforced on the original body surface to produce the same displacement effect as the boundary layer. The transpiration velocity is updated after every iteration, but no solid surface modification is necessary, so the influence coefficient matrix remains the same during the calculation. In the present calculation, the second method is adopted.

The transpiration velocity V used for simulating the boundary layer displacement is given by Lighthill(1958), it is related to the change of displacement thickness along the body surface as

$$V = \frac{d(U_e\ \delta^*)}{ds} \qquad (6.2.2.22)$$

This transpiration velocity is generated by the sources distributed on the same panels used for blade surface representation, the strength of the sources is given by

$$q = V \qquad (6.2.2.23)$$

When these sources are introduced, a normal velocity is induced at every control point. The surface vortices then have to be modified to maintain the solid boundary condition under the joint influence of both vortices and sources.

6.2.2.5 Boundary layer velocity profile

When the boundary layer thickness on the flowmeter hub surface is known, the velocity profile is determined using the boundary layer theory.

In the development of most boundary layer, the laminar boundary layer always becomes turbulent very quickly, so only the turbulent velocity profile is considered here. According to boundary layer theory[Moran(1976), Schlichting(1960)], the turbulent boundary layer consists of laminar sublayer, buffer layer, inner layer and outer layer. Different velocity profiles exist in those layers.

To describe the velocity profiles inside the turbulent boundary layer, the friction velocity u_τ and y^+ are introduced. They are defined by

$$u_\tau = \sqrt{\frac{\tau_w}{\rho}} \qquad (6.2.2.24)$$

and

$$y^+ = \frac{u_\tau\, y}{\nu} \qquad (6.2.2.25)$$

In the laminar sublayer, because it is very thin, the velocity is assumed linear and satisfies following equation

$$\frac{u}{u_\tau} = y^+ \qquad (6.2.2.26)$$

Buffer layer is a transition layer between the sublayer and the inner layer. In the inner layer, the velocity distribution is supposed to satisfy

$$\frac{\partial u}{\partial y} = \frac{u_\tau}{l} \qquad (6.2.2.27)$$

here the mixing length l is a function of the distance from the wall surface, it is

$$l = \kappa y \qquad (6.2.2.28)$$

Substituting the mixing length into equation(6.2.2.27), the obtained velocity profile is

$$\frac{u}{u_\tau} = \frac{1}{\kappa} \ln y^+ + C \qquad (6.2.2.29)$$

where κ and C are determined by experiment as $\kappa=0.4$ and $C=5.2$.

In the outer layer, Coles(Moran, 1976) gave a law as the wake based on experimental data as

$$\frac{u}{u_\tau} = \frac{1}{\kappa} \ln y^+ + C + \frac{2}{\kappa} \Pi(x) \sin^2\left[\frac{\pi y}{2\delta(x)}\right] \qquad (6.2.2.30)$$

Equation (6.2.2.30) can be used for both the inner layer and the outer layers. When the boundary layer thickness on the hub surface is known, the velocity profile transits from linear distribution to log distribution directly without the buffer layer in present calculation and the profiles in the inner and the outer layers are determined from equation(6.2.2.30).

6.2.2.6 Boundary layer on the pipe wall

The boundary layer on the pipe wall is in a fully developed turbulent state and totally determined from boundary layer theory. In the fully developed flow in smooth walled pipe, the wall friction coefficient in turbulent flow given by Nikuradse(Fox, 1977) is

$$f = 0.0032 + 0.221/R_e^{0.237} \qquad (6.2.2.31)$$

and the corresponding wall stress is

$$\tau_W = \rho u^2 f/8 \qquad (6.2.2.32)$$

Because the flow is inside an annulus, the Reynolds number and the velocity in equations (6.2.2.31) and (6.2.2.32) should be based on the pipe flow with the equivalent hydraulic diameter and the same flowrate as the annulus flow.

Thus, the friction velocity can be determined by substituting equations (6.2.2.31) and (6.2.2.32) into (6.2.2.24), and the velocity profile can be determined as well.

Between the pipe wall boundary layer and the boundary layer on flowmeter hub surface,there is a region which is influenced by both boundary layers and there is no direct velocity profile formula for this region. The velocity distribution here is obtained by a mathematical fitting between the edge of the hub surface boundary layer and a point inside the pipe wall boundary layer which is determined by maintaining the annulus flowrate.

6.2.3 Driving Torque

The lift on a two dimensional cascade blade can be expressed as

$$L = \frac{1}{2} \rho U_\infty^2 C_\ell C \qquad (6.2.3.1)$$

The flow field inside the rotor is simplified to two dimensional flows on an infinite number of cylindrical surfaces and the flow on each cylindrical surface is treated as a two dimensional cascade flow. The driving torque produced by the blades on individual section is

$$dT_d = Lr\, dr$$

$$= 0.5\rho V_{is}^2 C_\ell C r dr \qquad (6.2.3.2)$$

here V_{is} is the velocities on the flowmeter inlet section.

The total driving torque on the rotor is an integration of all the cascade torques from the hub to the tip. It is given by

$$T_d = 0.5\rho N_b \int_{r_h}^{r_t} C_\ell C V_{is}^2 r\, dr \qquad (6.2.3.3)$$

Among the cylindrical flows from the hub to the tip, only a finite

number of them are chosen as representatives and their solutions are found using the built numerical model. The solutions to the flows between those representative flows are interpolated from the simulated results. Using this approach, the total driving torque on the rotor can be calculated using the following formula

$$T_d = 0.5\rho N_b \sum_{i=2}^{N} 0.5(C_i C_{\ell_i} V_{is_i}{}^2 r_i + C_{i-1} C_{\ell_{i-1}} V_{is_{i-1}}{}^2 r_{i-1}) \Delta r_i \qquad (6.2.3.4)$$

6.2.4 Friction on the Blade Surfaces

In the model for the flows around the flowmeter blades, the separated leading edge flows and the wake flows of a blade is counted, but the boundary layer after the flow reattachment is not included. However, the simulated results show the dependence of the flow state at the reattachment point on the incidence angle according the reattachment length behaviors. The boundary layers on the blade surfaces certainly have produced retarding torques on the rotor. Here, the friction produced by the boundary layers is determined by the Reynolds number and the incidence angle.

According to the experimental data given by Ota et al and Kottke et al, the transition Re_b from a laminar reattachment to a turbulent reattachment for the plates with a square leading edge is between about 120 and 200. In this calculation, The transition Reynolds number Re_b is given 200. When Re_b is below 200, the starting state of the boundary layer at the reattachment point is laminar, the friction coefficient is

$$f = 1.328\ (Re_\ell)^{-0.5} \qquad (6.2.4.1)$$

When Re_b is over 200, the state of the boundary layer at the reattachment point on the blade surfaces is mainly influenced by the incidence angle. The results in chapter 5 show:

When $\alpha > -4^\circ$ on the upper surface and $\alpha > 4^\circ$ on the lower surface, the starting state is laminar, f is calculated by equation(6.2.4.1)

When $\alpha > -4^{\circ}$ on the upper surface and $\alpha < 4^{\circ}$ on the lower surface, the boundary layer state at the reattachment point becomes turbulent and the used friction coefficient is given by Schlichting as

$$f = 0.455/[\log(Re_{\ell})]^{2.58} \qquad (6.2.4.2)$$

6.3 Tip Clearance Friction

An expression for the retarding torque produced by the fluid inside the tip clearance is given by Thompson and Grey(1973). It is

$$T_t = [\rho(r_t\omega)^2/2]C_t r_t B_t f_t \qquad (6.3.1)$$

where

$$f_t = 2/R_{et} \qquad Re_t < 1000$$

$$= 0.016/Ret^{0.25} \qquad R_{et} > 1000$$

and

$$R_{et} = \omega r_t(r_p - r_t)/\nu$$

6.4 Bearing Friction

Bearing friction is one of the major frictions influencing a flowmeter performance. In the tested flowmeter, the rotor is rotating on the shaft as fig.6.5. While the rotor is rotating, the fluid between the rotor shell and shaft surface forms a pressurized fluid film. The friction inside the bearing is dependent on the thickness of this fluid film because this film determines the bearing lubrication state. However the thickness of the fluid film is a function of the rotor speed.

In terms of physical bearing operation, three states of lubrication exist as described by Ryffel and Geronimo(1984). At small flowrates, the fluid film is very thin and it is not thick enough to prevent the solid surfaces from rubbing each while the rotor is running, this is the boundary lubrication state and mechanical friction exists inside the bearing in this state. The mechanical friction has its biggest

magnitude when the metering flowrate is very small and decreases to zero when the metering flowrate increases to such a value that a fully hydraulic lubrication is achieved inside the bearing. In the fully hydraulic lubrication state, the solid surfaces are totally separated by the fluid film. A mixed lubrication state exists between the boundary and the fully hydraulic lubrication states. The mechanical friction coefficient variation in the mixed lubrication state is supposed to be linear from its maximum to zero in the fully hydraulic lubrication state. The fluid viscous friction inside the bearing thus changes with fluid film thickness.

Inside the bearing of the tested flowmeter, the lubrication in section b is always in a hydraulic state due to the design(see fig.6.5a), only the lubrication state in sections a and c is changing with the metered flowrate. In the model presented here, friction equations for the three lubrication states are developed.

6.4.1 Lubrication Frictions

When the rotor speed is low and the fluid film is thinner than the total roughness of the two facing surfaces of the bearing, these two surfaces touch each directly during the rotor's rotation. The total roughness of the two facing bearing surfaces is

$$x_t = x_r + x_s \qquad (6.4.1)$$

According to Barwell(1979), the roughness of a milled steel surface is 110μin.

The maximum friction exists when the rotor is almost stationary. The mechanical friction coefficient given by Ryffel and Geromino in boundary lubrication is between 0.08 and 0.12. In this calculation, f_o is given the value of 0.1.

While the rotor is rotating, a force is produced on the suspended rotor through the fluid film as shown in fig.6.6 [Barwell(1979), Massey(1989)]. The force components in those bearing sections are

$$F_{\tau i} = \frac{\pi \mu \omega r_2 l_i^3}{4 \iota_i^2} \frac{\epsilon_i}{\sqrt{(1-\epsilon_i^2)^3}} \qquad (6.4.2)$$

$$F_{ni} = \frac{\mu\omega r_2 \ell_i^3}{\iota_i^2} \frac{\epsilon_i^2}{(1-\epsilon_i^2)^2} \qquad (6.4.3)$$

$$i=a,b,c$$

where ϵ_i is the ecentricity ratio of the bearing gap(see fig.6.6), i.e.

$$\epsilon_i = e/\iota_i \,. \qquad (6.4.4)$$

In the tested flowmeter, the total F_τ and F_n of the tested flowmeter are

$$F_\tau = F_{\tau a} + F_{\tau b} + F_{\tau c}$$

$$= \omega\,(P_a + P_b + P_c) \qquad (6.4.5)$$

where

$$P_i = \frac{\pi\mu r_2 \ell_i^3}{4\,\iota_i^2} \frac{\epsilon_i}{\sqrt{(1-\epsilon_i^2)^3}} \qquad i=a,b,c$$

and

$$F_n = F_{na} + F_{nb} + F_{nc}$$

$$= \omega\,(Q_a + Q_b + Q_c) \qquad (6.4.6)$$

where

$$Q_i = \frac{\mu r_2 \ell_i^3}{\iota_i^2} \frac{\epsilon_i^2}{(1-\epsilon_i^2)^2} \qquad i=a,b,c$$

In the design of the flowmeter bearing, sections a and c are symmetric about section b, so

$$\epsilon_a = \epsilon_c$$

and

$$\epsilon_b = \epsilon_a \iota_a / \iota_b$$

The total force on the rotor through the fluid film is

$$F = \sqrt{F_n^2 + F_\tau^2}$$

$$= \omega \sqrt{(P_a + P_b + P_c)^2 + (Q_a + Q_b + Q_c)^2} \qquad (6.4.7)$$

Radial aerodynamic forces acting on the rotor is balanced themselves in ideal design, the force produced by the fluid film on the rotor should balance its weight, i.e.

$$F = W \qquad (6.4.8)$$

For the bearing lubrication to be fully hydraulic, the minimum fluid film thickness in sections a and c of the bearing must be at least equal to the surfaces roughness as given by equation(6.4.1). The corresponding ecentricities are

$$\epsilon_o = \epsilon_{ao} = \epsilon_{bo} = 1 - x_t/\iota_a$$

and

$$\epsilon_{bo} = \epsilon_o \iota_a/\iota_b \qquad (6.4.9)$$

This is the critical ecentricity with regarding to the lubrication state inside the bearing. when the eccentricity is smaller than ϵ_o, the bearing lubrication is in a fully hydraulic state.

From equations (6.4.7) and (6.4.8), the rotating speed corresponding to the critical ecentricity is

$$\omega_o = \frac{W}{\sqrt{(P_a + P_b + P_c)_o^2 + (Q_a + Q_b + Q_c)_o^2}} \qquad (6.4.10)$$

where subscript o indicates the value at the critical ecentricity.

When the rotor speed is higher than ω_o, fully hydraulic lubrication is achieved inside the bearing and mechanical friction drops to zero.

Before a fully hydraulic lubrication is achieved, mechanical friction is a function of ecentricity and is assumed to drop linearly from its maximum value to zero. At a given rotation speed, the corresponding ecentricity can be calculated using equations (6.4.7) and (6.4.8). Then the mechanical friction coefficient is

$$f = f_o[1 - \iota_a(1-\epsilon)/x_t] \quad . \qquad (6.4.11)$$

The mechanical friction inside the bearing is

$$F_m = fW \tag{6.4.12}$$

6.4.2 Fluid Viscous Friction

The viscous frictions caused by the fluid inside the bearing sections are

$$F_{\mu i} = \int_0^{2\pi} \int_0^{\ell_i} \tau r d\phi d\ell \qquad i=a,b,c \tag{6.4.13}$$

Because the gap in the bearing is very small, the flow in it is laminar and the shear stress in the lubrication fluid is

$$\tau = \mu \frac{\omega r}{h_i} \tag{6.4.14}$$

Ignoring the end effects on the shear stress and substituting equation(6.4.14) to (6.4.13), the frictions inside the bearing become

$$F_{\mu_i} = \mu\omega r_2^2 \ell_i \int_0^{2\pi} \frac{d\phi}{h_i} \tag{6.4.15}$$

here h_i is the clearance between the bearing and its house. It can be expressed as

$$h_i = \iota_i[1+\epsilon_i\cos(\phi)] \tag{6.4.16}$$

Substituting equation(6.4.16) into equation (6.4.15), the viscous frictions in the bearing are

$$F_{\mu_i} = \frac{\mu\omega r_2^2 \ell_i}{\iota_i} \frac{2\pi}{\sqrt{1-\epsilon_i^2}} \tag{6.4.17}$$

The total fluid viscous friction in the bearing of the tested flowmeter is

$$F_\mu = F_{\mu a} + F_{\mu b} + F_{\mu c}$$

Because ϵ_i vary with the rotor speed, the viscous friction in the

bearing is a function of the rotor speed.

The total friction torque in the bearing is

$$T_b = (F_m + F_\mu)r_2 \qquad (6.4.18)$$

6.5 Viscous Friction on the Hub Surfaces

The boundary layers on the hub surfaces also produce frictions. When a flow passes through a turbine flowmeter, a shear layer is estabished on every hub surface, and the direction of the shear stress is opposite to the relative velocity of the flow. The shear stress on the hub surface is

$$\tau = \mu \frac{\partial w}{\partial r} \qquad (6.5.1)$$

This stress can be divided into axial and circumferential components and only the circumferential component produces a retarding torque. As given by Tsukamoto and Hutton(1985), the friction torque on surface AB is

$$T_h = (\rho/2)w_h^2 A_h r_6 \sin(\beta_h) f_h \qquad (6.5.2)$$

where

$$f_h = 1.328 R_{eh}^{-0.5} \quad R_{eh} < 2.5 \times 10^5$$

$$= 0.074 R_{eh}^{-0.2} \quad R_{eh} > 2.5 \times 10^5$$

$$R_{eh} = w_h C_h / \nu$$

$$A_h = 2\pi r_6 \ell_h - N_b B_h C_h$$

The frictions on the other surfaces are appoximated to the friction on a rotating disk with a radius r_h and are calulated using the formula given by Schlichting. The formula is

$$T_{disk} = (\rho/2)\omega^2 r_h^5 f_{disc} \qquad (6.5.3)$$

where

$$f_{disc} = 3.87\ Re_{disk}^{-0.5} \quad Re_{disc} < 3\times10^5$$

$$= 0.145\ Re_{disk}^{-0.2} \quad Re_{disc} > 3\times10^5$$

$$Re_{disc} = r_h^2 \omega / \nu$$

6.6 Results and Discussions

Using the panel method developed for annulus velocity prediction, the predicted potential inlet velocity profiles of the flowmeter is presented in fig.6.7. It can be seen that the potential flow velocity profiles become flat very quick after the hub nose section. However, due to the boundary layers on the annulus surfaces, the actual velocity profile is very much changed and depends on the flowrate. The predicted velocity profiles with and without the boundary layers at section B (see fig.6.1) for flowrates with annulus mean velocities of 0.764m/s and 1.75m/s are presented in fig.6.8.

When the inlet velocity is known, the performance curve of a flowmeter with free swirl inlet condition can be predicted. To obtain the curve, the lift and drag characteristics of the flowmeter rotor blades in chapter 5 have to be used.

The flowmeter coefficients for any other flowrates are obtained by iteration. The procedure is:

(1) An initial rotor speed is given,

(2) All the torques acting on the rotor under the initial speed are calculated using the models developed in this chapter,

(3) Because there is no unsteady disturbance to the rotor, equation (6.1.2) is applied in the prediction. Comparing the calculated driving torque and the total retarding torque, the initial rotor speed is lowered when the driving torque is smaller and increased when the retarding torque is smaller.

(4) The readjusted speed is used as a new initial speed and the calculation is repeated from step (2). Iteration is terminated when equation(6.1.2) is satisfied to the desired accuracy.

In fig.6.9, the predicted flowmeter performance curve is presented. In the predicted results, there is only a small non-linear section is found and the flowmeter coefficient is very stable for large flowrates.

In fig.6.10, the effect of the tip clearance is given. The result

of the tip clearance change is a large flowmeter coefficient variation. As the clearance increases, the retarding torque produced by the flow inside the pipe boundary layer becomes smaller, so the flowmeter coefficient increases.

CHAPTER SEVEN

EXPERIMENTAL STUDY

7.1 Introduction

Knowledge of the flow characteristcs inside turbine flowmeters is a pre-condition to improve their design and performance. In this chapter, an experiment was designed to measure the flow fields inside a turbine flowmeter under different inlet flow conditions and flowrates by the use of Laser Doppler Anemometry(LDA). The objectives of this study are to produce a clear understanding of the flow fields inside the turbine flowmeter. The measurement results are used to validate the developed numerical models as well.

LDA is a non-intrusive and fast response velocity measuring technique which measures the speed of the small suspended particles inside the fluid. The principle of LDA can be found in Durst(1981) and SME(1989). Because of its advantages, LDA is used widely for the measurements of turbulent flows and the flows inside machinery. There are two types of LDA, the forward scatter system and the backward scatter system. In the forward scatter system, the laser beams have to penetrate the test section and the doppler signals are picked up by a photomultiplier located on the side of the test section opposite to that of the laser system. The backward scatter system is used on those occasions when the laser beams cannot penetrate the test section and the doppler signals have then to be received on the same side as the laser system. In its applications in turbomachinery, the backward

system is usually used to measure the flow inside blade passages as Dring et al(1982). A Backward scatter system was used in the present experiment.

The flow inside the turbine flowmeter has axial, circumferential and radial components. Using the LDA system, the axial and circumferential components can be easily measured, but it is difficult to measure the radial component directly(Ferreira,1988). However, the radial component is expected to be very small, so only the axial component u and circumferential component v were measured in this experiment.

7.2 Test Rig and Equipment

7.2.1 Test Rig

The experimental measurements were carried out in a specially designed rig to test the performance of a 4" turbine flowmeter. The layout of the rig is shown in fig.7.1. It consisted of a pump, two sump tanks, a reference vortex flowmeter and a test section. Other assessories, such as a flow straightener, a bypass and valves, were built into the rig to condition and control the flow through the tested turbine flowmeter.

The test section is shown in fig.7.2. It consisted of a swirl generator, turbine flowmeter and a perspex box. The swirl generator was fixed onto the 4" pipe by four screws through the pipe wall. Four swirl generators were tested in the experiments. Their blade twist angles were 8, 4, -4 and -8 degrees respectively. Different swirls could be produced in the inlet flow of the flowmeter by use of these swirl generators. The turbine flowmeter section was specially designed as shown in fig.7.3. It consisted of three parts, two aluminium flanges and a central perspex section. These three parts could be easily dismantled and assembled. The turbine flowmeter was located in the perspex pipe by sliding its three stator vanes along three channels in the perspex pipe and its circumferential position was also fixed by these channels. These three parts were assembled by four bolts between the flanges. Before these bolts were tightened, the

perspex pipe with the flowmeter could be rotated about the pipe in relation to the two flanges. A perspex matching box was designed to improve the doppler signals quality. This box was tightly held on the aluminium pipe wall, but could be slighly rotated around the pipe axis for its circumferential position adjustment. Because the refractive index of water is quite close to that of perspex, the reflected light from the curved pipe surface was reduced by means of the surrounding water filled in the box.

Throughout the measurement programme, the pipe wall and the matching box were polished every week with ICI perspex polish liquid and the water inside the test circuit was changed every week. When the water was being drained away, the rig pump was left running at the beginning to allow the nascent mud deposit on the inner pipe wall to be washed away. To reduce external influence on the measurement, the water temperature was controlled at 25± 2.4 ^{o}C using two heaters when the temperature was low and cold tap water when the temperature was high.

7.2.2 LDA System

The Laser Doppler Anemometry system used in the experiments is a back scatter system developed by Goulas(Goulas and Versteeg, 1985) which is capable of measuring one velocity component in either a rotating or a stationary system at one time. A schematic diagram of the measurement system and a photograph of the optical system are shown in fig.7.4 and fig.7.5. The used laser source was a LEXEL MODEL 95 Argon ion laser operated at green wavelength (514nm). When a beam is emitted from the source, it passes through a group of transmiting optics, a polarisation plate and a beam splitter. The polarisation plate matches the laser and the beam splitter and the beam splitter splits the incoming laser beam into two parallel beams of 50mm distance and the same intensity. These two parallel laser beams pass through a frequency shift system based on acoustic optic modulators(bragg cells). In each bragg cell, an acoustic wave is generated by a piezolectric transducer bonded at its end. This acoustic wave perturbs the refraction index of the material inside the bragg cell and acts as a phase grating. The setting angle of the bragg cell can be adjusted

continuously by means of a screw against a spring. By adjusting the angle of the bragg cell, +1st, -1st or 0th order diffracted beams can be optimised. The two parallel beams pass through different bragg cells and come out with different frequencies. The resonant frequencies of the two used pizoelectric transducers are 37.6MHz and 40 MHz respectively. Due to the low velocity in the test section, the used frequency difference between the two laser beams was chosen at 2.4 MHz. Thereafter, the two beams pass through a beam steering module with the aid of which the distance between them can be slightly adjusted to ensure that they cross each other at their waists beyond the front convex-plane lens in order to form an optimised control volume.

Inside the control volume, interference fringes are produced. When there are particles crossing these fringes, the light signals scattered from these particles give information of the local velocity in the control volume. If the particle size is comparable to the fringe size and its density is suitable, the local velocity can be accurately measured. The particles used in the measurement are the natural particles suspended in tap water.

The scattered signal from the focal point is received by a small high quality mirror behind the front lens and focused on the pinhole of a photomultiplier(PM) by a set of plane-convex lenes. The PM is mounted on a platform which can be moved in three directions and rotated in a horizontal plane as shown in fig.7.5. Through adjustment of the PM position, the scattered doppler signal should be exactly focused at the cathode of the PM and thus amplified. The used PM has a 4ns response time and operates at 1200V voltage. The output of the PM is fed into a signal processing system.

During the measurement, the control volume is moved to the required positions by the adjusting platform mechanism shown in fig.7.6.

7.2.3 Signal Processing System

The used signal processing system consisted of a spectrum analyser(SA), a spectrum analyser controller(SAC), a sample and hold system, a circumferential positioning system and a microcomputer, as

shown in fig.7.7. The SA was supplied by Hewlett Packard. It has three inter-connected sections i.e. 141T display, 8553B RF section and 8552A IF section, and works in the frequency domain. The working frequency range is defined at the front panel by setting the central frequency and scan width on the RF section. When the PM output is fed to the spectrum analyser, the analyser's output is an inverse of the spike which occurs when there is coincidence in time between the laser doppler signal and the RF filter of the spectrum analyser. The scan frequency of the SA comes from the SAC. While the SAC is working, a 0-8V ramp is produced in every scan period and the detected laser burst is represented by the corresponding voltage in the 0—8V ramp.

Since the flow inside the turbine rotor is time dependent, an analogue output of the spectrum analyser related to time is required and this is achieved using a circumferential positioning system. In this positioning system, an optic fibre is located in a hole on the pipe wall opposite the laser system in the flowmeter rotor section. When the rotor is rotating, the pulse output from this fibre indicates alignment of the turbine rotor tip with the optic fibre light beam. These pulses are fed into a ramp generator and trigger a 0—5V ramp. The output voltage value between 0 to 5V corresponds to one space between two blades. The analogue outputs of the position measurement system and the spectrum analyser are fed into a six- channel sample and hold system and recorded by the microcomputer at the same time.

During experiments, while one laser beam was cut by a blade, very strong light was reflected back. Such a strong light could temporarily blind or even permanently damage the PM. In order to protect the PM from being blinded, a circuit was designed to switch off the PM before any of the laser beams was cut by a rotor blade. The theoretical switch-off time is the period which starts when one laser beam begins to be blocked by a rotor blade(position A) and finishes when the other beam is no longer blocked by the same blade(position B) as shown in fig.7.8. Hence no signal could be received while the blade was travelling from position A to B. However, the switch-off time had to be slightly longer than the theoretical period in case of flow pulsations. To trigger the switch-off circuit, the signal from the optic fibre was used and the switch off time was adjusted through a time-delay box. The actual switch-off time was adjusted by comparing

the optic fibre signals and the signals from the photomultipler(with the switch-off circuit dismounted). During this adjustment, an attenuation lens had to be located at the front of the photomultiplier to protect it.

7.2.4 Tested Turbine Flowmeter

The turbine flowmeter tested in the experiments is a TV/4/1000 helical turbine flowmeter provided by Hydril UK Ltd. The main geometrical dimensions are as in table 7.1.

Table 7.1 Turbine Flowmeter Dimensions

Blade number N_b	10
Blade thickness B(mm)	1.25
Tip radius r_t(mm)	49.78
Tip blade stagger angle β_t(deg)	49.16
Tip clearance(mm)	1.02
Hub radius r_h(mm)	24.64
Hub blade stagger angle β_h(deg)	29.79
Rotor blade axial length ℓ(mm)	25.65
Pipe diameter r_p(mm)	50.80

7.2.5 Swirl Generators

Four swirl generators were designed for the use in the experiments. Each produced a different swirl in the turbine flowmeter inlet flow. The blades of these swirl generators were twisted from a flat disc as shown in fig.7.9. The installation of a swirl generator is illustrated in fig.7.2. In the hub area of a swirl generator, there is a very small transition area in which the twist angle changes from 90 degrees to the required angle near the core. The twist angle is defined as positive when it is in the same direction as the rotor rotation and negative when it is in the opposite direction. The geometries of these swirl generators are given in table 7.2.

Table 7.2 : Swirl Generators Dimensions

	case B	case C	case D	case E
Blade number	10	10	10	10
Tip radius (mm)	48.7	48.7	48.7	48.7

Tip blade angle β_g(degree)	4	8	-4	-8
Tip blade Length (mm)	22.82	22.82	22.82	22.82
Trans Radius: (mm)	21.53	21.53	21.53	21.53
Core radius: (mm)	12.7	12.7	12.7	12.7

7.2.6 Measured Stations

The flow velocities in and near the flowmeter rotor was measured on 11 axial sections from the upstream of the rotor to its downstream as shown in fig.7.10 and at 8 radial positions on every axial section. the axial and radial positions of the measurement stations are shown in following tables. The axial positions given in the following tables are related to a upstream step cross section of the perspex pipe as shown in fig.7.3 and 7.10. The position of the reference section is determined using laser signals as described in Appendix D.4.1.1.

Table 7.3 Axial Positions of the Measured Cross Sections

Station No	Axial Position(mm)	
1	22	
2	26	
3	30	
4	34	
5	37	
	39	------ blade leading edge
6	41	
7	46	
8	51	
9	57	
10	61	
	64.6	------ blade trailing edge
11	68	

Table 7.4 Radial Measurement Positions on Each Cross Section

Station No	Radius r(mm)	r/R_p
A	47.48	0.934
B	45.48	0.895
C	42.82	0.843
D	40.16	0.791
E	37.50	0.738

F	34.18	0.672
G	30.85	0.607
H	28.82	0.567

To validate the flowmeter performance prediction model, the inlet flow conditions are required. The axial position of the inlet section has to be decided from the measured results(as discussed in next chapter). On this inlet section, the disturbance from the hub nose and the flowmeter rotor should be both small. The radial measurement stations on the inlet section are as given in table 7.5.

Table 7.5 Radial Positions of the Measurement Stations (inlet velocity profile measurement)

Station No	Radius(mm)	r/R_p
a	47.49	0.935
b	46.16	0.908
c	44.82	0.882
d	42.82	0.843
e	40.82	0.804
f	38.82	0.764
g	36.82	0.725
h	34.82	0.685
i	32.82	0.646
j	31.48	0.620
k	30.15	0.594
l	28.82	0.567

7.3 Data Processing

Experimental data are stored in the microcomputer in a set of three arrays. The first array stores the total number of the samples at each position, the second stores the sum of the velocity samples at each position and the third stores the square sum of the velocity samples at each point. From those stored data, the velocity distribution in the blade passage can be obtained.

On the inlet cross section, the flow is supposed to be axisymmetric. The mean velocity is given by following expression

$$\bar{V}_i = \frac{1}{N_i} \sum_{j=1}^{N} V_{i,j} \qquad (7.1)$$

where subscript i indicates an individual velocity component and N_i is

the total sample number.

The turbulent intensity is

$$TI_i = \frac{v_i'}{\bar{V}_i} \qquad (7.2)$$

where

$$v_i' = \sqrt{\frac{\sum_{j=1}^{N} (V_{i,j} - \bar{V}_i)^2}{N}} \qquad (7.3)$$

The flow field inside the turbine flowmeter rotor is considered to be a non-uniform flow. With the LDA system, the detected instantaneous doppler signals were put in correspondence with the signals from the position measurement system. The measured velocity is thus registered at 64 equally spaced points in each blade space. The data for every point were stored in three arrays, i.e. the total number of samples $N(\Phi_j)_i$, the sum of velocity samples $V(\Phi_j)_i$ and the square of the velocity samples. The velocity and the turbulent intensity are calculated using the same equation as (7.1) and (7.2) with N_i replaced by $N(\Phi_j)_i$ and V_i replaced by $v(\Phi_j)_i$.

Examples of the measured axial velocity distributions between blades at radial section C from the upstream of the rotor (axial station No.4) to its downstream are presented in table 7.6 and 7.7. Looking over these tables, the regions in the flowmeter rotor where the velocity can be measured using the LDA system are clearly visualised. The zero velocity region corresponds to the region where strong reflected signals were produced as the beam were cut by a rotor blade. The photomultiplier was switched off during that time, so no doppler signal was detected.

From the results, it can also be seen that there is not much variation in the velocity distributions between blades throughout the flowmeter rotor. The same kind of results were found at various flowrates and under different inlet flow conditions. Because of this, only the mean velocity inside the flowmeter rotor is of significance. The measurements are therefore processed according to the following

Table 7.6 Measured Flow Field Between Blades

(case A, radial section C, flowrate: 32.56m³/h)

Φ_j	$N_{\Phi j}$	$u_{\Phi j}$	$TI_{\Phi j}$	Φ_j	$N_{\Phi j}$	$u_{\Phi j}$	$TI_{\Phi j}$	Φ_j	$N_{\Phi j}$	$u_{\Phi j}$	$TI_{\Phi j}$	Φ_j	$N_{\Phi j}$	$u_{\Phi j}$	$TI_{\Phi j}$
1	52	1.389	0.074	1	0	0.000	0.000	1	0	0.000	0.000	1	81	1.529	0.067
2	37	1.366	0.070	2	0	0.000	0.000	2	0	0.000	0.000	2	73	1.528	0.063
3	43	1.395	0.085	3	0	0.000	0.000	3	0	0.000	0.000	3	68	1.526	0.076
4	68	1.377	0.085	4	3	1.471	0.068	4	0	0.000	0.000	4	74	1.513	0.081
5	46	1.365	0.084	5	4	1.473	0.047	5	0	0.000	0.000	5	80	1.498	0.065
6	76	1.364	0.087	6	20	1.497	0.059	6	0	0.000	0.000	6	49	1.532	0.074
7	62	1.385	0.077	7	72	1.505	0.069	7	0	0.000	0.000	7	83	1.521	0.088
8	46	1.375	0.088	8	67	1.492	0.085	8	0	0.000	0.000	8	71	1.502	0.071
9	53	1.373	0.077	9	58	1.486	0.073	9	0	0.000	0.000	9	66	1.507	0.098
10	42	1.384	0.078	10	60	1.476	0.088	10	0	0.000	0.000	10	56	1.510	0.061
11	57	1.364	0.098	11	84	1.489	0.069	11	0	0.000	0.000	11	73	1.513	0.074
12	60	1.386	0.078	12	74	1.497	0.067	12	0	0.000	0.000	12	5	1.541	0.074
13	37	1.396	0.066	13	52	1.506	0.077	13	0	0.000	0.000	13	0	0.000	0.000
14	55	1.351	0.095	14	68	1.493	0.086	14	0	0.000	0.000	14	0	0.000	0.000
15	65	1.382	0.107	15	81	1.498	0.096	15	0	0.000	0.000	15	0	0.000	0.000
16	59	1.386	0.083	16	89	1.470	0.074	16	0	0.000	0.000	16	0	0.000	0.000
17	57	1.371	0.081	17	83	1.498	0.097	17	0	0.000	0.000	17	0	0.000	0.000
18	38	1.389	0.089	18	54	1.483	0.079	18	0	0.000	0.000	18	0	0.000	0.000
19	62	1.379	0.109	19	76	1.496	0.065	19	44	1.511	0.071	19	0	0.000	0.000
20	71	1.363	0.086	20	73	1.488	0.088	20	83	1.520	0.078	20	0	0.000	0.000
21	70	1.358	0.078	21	85	1.486	0.082	21	58	1.491	0.081	21	0	0.000	0.000
22	37	1.396	0.121	22	69	1.471	0.094	22	55	1.490	0.075	22	0	0.000	0.000
23	63	1.376	0.083	23	74	1.503	0.068	23	69	1.516	0.070	23	0	0.000	0.000
24	62	1.368	0.101	24	70	1.476	0.082	24	70	1.506	0.070	24	0	0.000	0.000
25	51	1.391	0.090	25	88	1.503	0.071	25	77	1.505	0.090	25	0	0.000	0.000
26	43	1.370	0.083	26	61	1.490	0.067	26	52	1.504	0.073	26	0	0.000	0.000
27	49	1.393	0.079	27	76	1.484	0.077	27	88	1.485	0.075	27	0	0.000	0.000
28	50	1.361	0.090	28	74	1.482	0.081	28	79	1.519	0.072	28	0	0.000	0.000
29	53	1.373	0.074	29	62	1.469	0.082	29	71	1.497	0.086	29	0	0.000	0.000
30	48	1.365	0.077	30	71	1.504	0.076	30	59	1.484	0.069	30	42	1.533	0.052
31	61	1.394	0.088	31	77	1.505	0.081	31	72	1.504	0.076	31	62	1.536	0.066
32	55	1.395	0.096	32	82	1.477	0.075	32	63	1.514	0.060	32	78	1.493	0.092
33	57	1.395	0.117	33	71	1.470	0.076	33	42	1.500	0.058	33	43	1.531	0.072
34	54	1.370	0.091	34	68	1.489	0.067	34	85	1.518	0.064	34	108	1.500	0.076
35	50	1.386	0.093	35	66	1.497	0.078	35	55	1.501	0.073	35	78	1.505	0.081
36	49	1.371	0.084	36	81	1.479	0.074	36	74	1.505	0.083	36	53	1.515	0.064
37	60	1.376	0.085	37	95	1.468	0.097	37	78	1.499	0.075	37	81	1.511	0.080
38	42	1.425	0.086	38	49	1.478	0.079	38	66	1.486	0.066	38	73	1.499	0.078
39	65	1.391	0.072	39	74	1.479	0.090	39	76	1.505	0.085	39	61	1.514	0.079
40	45	1.394	0.075	40	82	1.491	0.081	40	71	1.500	0.090	40	58	1.509	0.055
41	63	1.397	0.086	41	58	1.504	0.063	41	69	1.492	0.078	41	78	1.517	0.064
42	59	1.384	0.083	42	74	1.511	0.069	42	53	1.492	0.079	42	83	1.517	0.086
43	60	1.404	0.079	43	70	1.484	0.085	43	71	1.528	0.062	43	53	1.506	0.093
44	57	1.386	0.075	44	76	1.467	0.069	44	70	1.518	0.072	44	76	1.514	0.068
45	52	1.412	0.076	45	53	1.478	0.085	45	89	1.495	0.077	45	89	1.507	0.068
46	48	1.409	0.066	46	67	1.473	0.076	46	60	1.504	0.065	46	70	1.511	0.077
47	54	1.350	0.076	47	71	1.453	0.082	47	68	1.516	0.055	47	64	1.515	0.051
48	57	1.379	0.085	48	63	1.510	0.089	48	78	1.507	0.090	48	68	1.519	0.062
49	43	1.359	0.091	49	64	1.471	0.075	49	67	1.506	0.069	49	72	1.511	0.072
50	59	1.388	0.105	50	62	1.488	0.080	50	59	1.519	0.075	50	63	1.510	0.078
51	63	1.362	0.096	51	80	1.489	0.076	51	89	1.514	0.080	51	60	1.506	0.052
52	57	1.386	0.101	52	75	1.454	0.081	52	73	1.513	0.060	52	65	1.505	0.088
53	51	1.357	0.110	53	62	1.483	0.078	53	82	1.480	0.076	53	67	1.530	0.087
54	53	1.398	0.100	54	93	1.490	0.061	54	52	1.511	0.068	54	65	1.548	0.063
55	54	1.362	0.090	55	81	1.502	0.073	55	82	1.508	0.070	55	63	1.511	0.075
56	49	1.418	0.069	56	58	1.494	0.086	56	62	1.507	0.064	56	72	1.536	0.082
57	58	1.372	0.081	57	65	1.486	0.078	57	76	1.470	0.075	57	67	1.525	0.061
58	29	1.412	0.064	58	34	1.476	0.076	58	51	1.489	0.094	58	62	1.498	0.067
59	55	1.384	0.085	59	0	0.000	0.000	59	68	1.507	0.063	59	71	1.494	0.067
60	49	1.395	0.081	60	0	0.000	0.000	60	63	1.487	0.086	60	80	1.513	0.059
61	54	1.373	0.069	61	0	0.000	0.000	61	73	1.508	0.073	61	85	1.516	0.057
62	46	1.361	0.083	62	0	0.000	0.000	62	65	1.485	0.073	62	56	1.519	0.082
63	57	1.394	0.066	63	0	0.000	0.000	63	74	1.504	0.067	63	67	1.524	0.066
64	55	1.377	0.080	64	0	0.000	0.000	64	86	1.499	0.071	64	71	1.539	0.052

Table 7.7 Measured Flow Field Between Blades

(case A, radial section C, flowrate: 32.56m³/h)

Φ_j	N_{Φ_j}	u_{Φ_j}	TI_{Φ_j}	Φ_j	N_{Φ_j}	u_{Φ_j}	TI_{Φ_j}	Φ_j	N_{Φ_j}	u_{Φ_j}	TI_{Φ_j}	Φ_j	N_{Φ_j}	u_{Φ_j}	TI_{Φ_j}
1	79	1.534	0.070	1	75	1.513	0.076	1	61	1.505	0.089	1	55	1.447	0.108
2	55	1.506	0.074	2	58	1.491	0.062	2	75	1.499	0.068	2	47	1.471	0.073
3	49	1.497	0.091	3	53	1.488	0.102	3	64	1.476	0.096	3	58	1.469	0.104
4	67	1.507	0.084	4	58	1.484	0.084	4	70	1.508	0.078	4	59	1.415	0.092
5	80	1.529	0.084	5	85	1.498	0.088	5	49	1.536	0.069	5	58	1.427	0.117
6	53	1.499	0.089	6	49	1.491	0.092	6	55	1.526	0.068	6	38	1.475	0.109
7	67	1.524	0.078	7	53	1.494	0.071	7	60	1.503	0.074	7	55	1.425	0.106
8	71	1.520	0.082	8	72	1.517	0.069	8	67	1.528	0.071	8	55	1.386	0.102
9	64	1.475	0.093	9	68	1.505	0.064	9	70	1.529	0.067	9	48	1.453	0.086
10	48	1.494	0.092	10	55	1.511	0.080	10	66	1.523	0.087	10	37	1.418	0.108
11	66	1.512	0.076	11	65	1.514	0.072	11	59	1.530	0.066	11	53	1.423	0.124
12	50	1.531	0.067	12	69	1.492	0.084	12	60	1.518	0.067	12	59	1.457	0.100
13	77	1.516	0.088	13	74	1.491	0.092	13	67	1.489	0.093	13	71	1.457	0.104
14	49	1.536	0.053	14	61	1.516	0.068	14	50	1.517	0.072	14	37	1.445	0.075
15	67	1.540	0.070	15	57	1.505	0.073	15	63	1.518	0.062	15	64	1.456	0.109
16	69	1.500	0.070	16	70	1.508	0.060	16	76	1.497	0.071	16	48	1.428	0.098
17	73	1.514	0.051	17	69	1.510	0.058	17	51	1.491	0.084	17	58	1.455	0.102
18	66	1.518	0.080	18	68	1.517	0.063	18	81	1.521	0.089	18	45	1.468	0.074
19	59	1.518	0.067	19	52	1.530	0.070	19	55	1.515	0.058	19	56	1.431	0.099
20	61	1.496	0.071	20	60	1.508	0.068	20	79	1.504	0.082	20	62	1.452	0.093
21	56	1.511	0.061	21	67	1.482	0.083	21	65	1.502	0.072	21	55	1.442	0.091
22	54	1.497	0.085	22	59	1.504	0.063	22	62	1.522	0.073	22	45	1.421	0.107
23	84	1.511	0.074	23	55	1.528	0.077	23	49	1.514	0.074	23	54	1.449	0.109
24	66	1.527	0.054	24	83	1.496	0.072	24	70	1.484	0.087	24	61	1.440	0.119
25	77	1.479	0.100	25	66	1.471	0.094	25	67	1.523	0.078	25	58	1.463	0.092
26	58	1.534	0.080	26	60	1.516	0.070	26	60	1.520	0.076	26	60	1.432	0.095
27	74	1.522	0.057	27	76	1.497	0.064	27	49	1.518	0.059	27	51	1.439	0.113
28	64	1.508	0.068	28	80	1.528	0.076	28	71	1.525	0.072	28	52	1.419	0.099
29	33	1.520	0.068	29	71	1.485	0.079	29	89	1.537	0.084	29	68	1.444	0.085
30	0	0.000	0.000	30	63	1.500	0.084	30	48	1.507	0.095	30	40	1.378	0.136
31	0	0.000	0.000	31	71	1.487	0.085	31	70	1.512	0.092	31	45	1.442	0.104
32	0	0.000	0.000	32	68	1.513	0.074	32	50	1.497	0.082	32	50	1.460	0.106
33	0	0.000	0.000	33	62	1.509	0.085	33	80	1.486	0.098	33	52	1.442	0.101
34	0	0.000	0.000	34	62	1.506	0.072	34	76	1.532	0.068	34	70	1.422	0.111
35	0	0.000	0.000	35	78	1.496	0.090	35	81	1.498	0.079	35	65	1.428	0.116
36	0	0.000	0.000	36	38	1.543	0.061	36	54	1.509	0.065	36	47	1.446	0.111
37	0	0.000	0.000	37	72	1.497	0.103	37	84	1.518	0.097	37	57	1.436	0.112
38	0	0.000	0.000	38	78	1.498	0.090	38	77	1.515	0.080	38	57	1.429	0.099
39	0	0.000	0.000	39	43	1.486	0.084	39	77	1.501	0.080	39	67	1.419	0.118
40	0	0.000	0.000	40	0	0.000	0.000	40	62	1.502	0.086	40	35	1.489	0.068
41	0	0.000	0.000	41	0	0.000	0.000	41	64	1.532	0.056	41	59	1.434	0.101
42	0	0.000	0.000	42	0	0.000	0.000	42	87	1.520	0.085	42	66	1.415	0.109
43	5	1.491	0.049	43	0	0.000	0.000	43	70	1.535	0.080	43	68	1.429	0.099
44	61	1.506	0.075	44	0	0.000	0.000	44	63	1.507	0.070	44	38	1.447	0.100
45	78	1.514	0.073	45	0	0.000	0.000	45	23	1.546	0.051	45	51	1.437	0.102
46	74	1.532	0.072	46	0	0.000	0.000	46	0	0.000	0.000	46	69	1.435	0.095
47	48	1.503	0.089	47	0	0.000	0.000	47	0	0.000	0.000	47	46	1.455	0.121
48	77	1.521	0.073	48	0	0.000	0.000	48	0	0.000	0.000	48	57	1.410	0.122
49	72	1.500	0.084	49	0	0.000	0.000	49	0	0.000	0.000	49	67	1.453	0.088
50	65	1.520	0.083	50	0	0.000	0.000	50	0	0.000	0.000	50	57	1.465	0.095
51	65	1.489	0.115	51	0	0.000	0.000	51	0	0.000	0.000	51	56	1.405	0.127
52	60	1.542	0.071	52	0	0.000	0.000	52	0	0.000	0.000	52	69	1.431	0.104
53	69	1.523	0.095	53	0	0.000	0.000	53	0	0.000	0.000	53	45	1.410	0.123
54	63	1.504	0.071	54	53	1.491	0.083	54	0	0.000	0.000	54	52	1.433	0.115
55	57	1.508	0.092	55	58	1.483	0.097	55	0	0.000	0.000	55	53	1.430	0.123
56	73	1.511	0.065	56	49	1.493	0.101	56	0	0.000	0.000	56	44	1.428	0.122
57	81	1.512	0.088	57	71	1.525	0.073	57	0	0.000	0.000	57	60	1.429	0.110
58	82	1.508	0.088	58	69	1.541	0.079	58	0	0.000	0.000	58	49	1.441	0.127
59	65	1.525	0.089	59	61	1.493	0.080	59	17	1.511	0.072	59	62	1.407	0.117
60	56	1.523	0.091	60	63	1.521	0.086	60	55	1.529	0.076	60	48	1.427	0.096
61	64	1.510	0.060	61	62	1.498	0.067	61	65	1.507	0.070	61	36	1.468	0.076
62	63	1.500	0.112	62	85	1.492	0.087	62	57	1.508	0.065	62	35	1.491	0.098
63	45	1.525	0.061	63	75	1.517	0.073	63	74	1.511	0.072	63	26	1.415	0.151
64	65	1.500	0.073	64	59	1.506	0.076	64	48	1.488	0.111	64	16	1.453	0.141

equations.

$$V(\phi_j)_i = \frac{\sum_{j=1}^{64} N(\phi_j)_i V(\phi_j)_i}{\sum_{j=1}^{64} N(\phi_j)_i} \qquad (7.4)$$

and

$$TI(\phi_j)_i = \frac{\sum_{j=1}^{64} N(\phi_j)_i TI(\phi_j)_i}{\sum_{j=1}^{64} N(\phi_j)_i} \qquad (7.5)$$

7.4 Measurement Uncertainties

7.4.1 Uncertainties in CVP and HIA

In any experimental system, uncertainties always exist in the measured variables. In this experiment, uncertainties not only exist in the LDA system and the data processing system, but also the test section and its integration with the LDA system, so the measured velocity has certain level of uncertainty. All the causes of uncertainties are discussed in appendix D . The uncertainties in the Control Volume Position(CVP) and the Half Intersection Angle(HIA) are presented here.

The uncertainties in the CVP and the HIA can be calculated by applying error propagation theory into the calculation of the CVP and the HIA. The results are presented in the following tables.

Table 7.8 Uncertainties in Axial Velocity Measurement

Point	R_i (mm)	δR_i (mm)	δX_i (mm)	δZ_i (mm)	θ_i (°)	$\delta\theta_i$ (°)
A	47.48	0.766	0.604	0.231	4.867	0.08

B	45.48	0.766	0.606	0.233	4.867	0.08
C	42.82	0.767	0.608	0.236	4.867	0.08
D	40.16	0.768	0.610	0.239	4.867	0.08
E	37.50	0.770	0.612	0.242	4.867	0.08
F	34.18	0.772	0.615	0.245	4.867	0.08
G	30.85	0.775	0.617	0.249	4.867	0.08
H	28.82	0.777	0.618	0.251	4.867	0.08

Table 7.9 Uncertainties in Circumferential Velocity Measurement

Point	R_i (mm)	δR_i (mm)	δX_i (mm)	δZ_i (mm)	θ_i (°)	$\delta\theta_i$ (°)
A	47.48	1.138	0.659	0.222	4.953	0.211
B	45.48	1.135	0.659	0.223	4.950	0.212
C	42.82	1.130	0.660	0.225	4.945	0.213
D	40.16	1.126	0.660	0.228	4.940	0.213
E	37.50	1.121	0.660	0.231	4.935	0.214
F	34.18	1.116	0.660	0.234	4.928	0.215
G	30.85	1.110	0.661	0.239	4.922	0.217
H	28.82	1.107	0.661	0.241	4.919	0.217

7.4.2 Uncertainties in Laser Constant

The uncertainties in the measured velocity stem from the uncertainties of the HIA and the data processing system.

The velocity measured by the LDA is

$$V=K(f_d-f_s) \tag{7.6}$$

The laser constant of the system in air is

$$K=\frac{\lambda}{2\sin(\theta)} \tag{7.7}$$

where λ is the wavelength of the laser used in the laser system and θ is the half intersection angle (HIA) of the two laser beams in the fluid.

When the measurement is conducted in a liquid with refractive index n_f, the wavelength of the laser beam in this liquid is

$$\lambda_f = n_a\lambda_a/n_f \tag{7.8}$$

so the laser constant becomes

$$K = \frac{n_a\lambda_a}{2n_f\sin\theta_f} \tag{7.9}$$

θ_a and θ_f being the HIA in air and in the liquid respectively.

Ignoring uncertainties in the laser wavelength and the refractive indices, the uncertainty of the laser constant is

$$\delta K = \frac{n_a \lambda_a}{2\sin\theta_f \tan\theta_f} \delta\theta_f \qquad (7.10)$$

—— Axial velocity measurement

In the axial velocity measurements, the relation between θ_f and θ_a is

$$\sin\theta_f = n_a \sin\theta_a / n_f \qquad (7.11)$$

Substituting equation(7.11) into equation (7.9), the laser constant becomes the same as the constant in air, i.e.

$$K = \frac{\lambda_a}{2\sin\theta_a} \qquad (7.12)$$

and its uncertainty is

$$\delta K = \frac{K\delta\theta_a}{\tan\theta_a} \qquad (7.13)$$

Substituting the measured data in air (given in Appendix D) into the above equation, the laser constant is

$\delta K = 0.0285$

The laser constant for axial velocity measurement is

$K = 2.279927 \pm 0.0285$

——Circumferential velocity measurements

However, there is no direct relation between θ_f and θ_a as in equation(7.11) in circumferential velocity measurement due to the curvature of the pipe wall. The laser constant and its uncertainty should be calculated using equations (7.9) and (7.10).

The uncertainty in the HIA inside the pipe changes with control volume positions, so the uncertainty in the laser constant for circumferential velocity measurement changes accordingly. The predicted laser constants and their uncertainties are presented in the following table.

Table 7.10 Laser Constant Uncertainties
(circumferential measurement inside rotor)

No.	Radius (mm)	K	δK	δK/K (%)
A	47.48	2.2352	0.0950	4.249
B	45.48	2.2366	0.0956	4.272
C	42.48	2.2388	0.0962	4.297
D	40.16	2.2411	0.0964	4.301
E	37.50	2.2434	0.0970	4.326
F	34.18	2.2465	0.0973	4.331
G	30.85	2.2493	0.0980	4.357
H	28.82	2.2506	0.0986	4.380

7.4.3 Uncertainty in the Measured Velocity

The velocity measured by the LDA system is

$$V = K(f_d - f_s) \qquad (7.14)$$

and its uncertainty is

$$\delta V = \sqrt{(fd-fs)^2\delta K^2 + K^2(\delta f_d^2 + \delta f_s^2)} \qquad (7.15)$$

To estimate the uncertainties in the measured velocity, (f_d-f_s) is based on the mean velocity component for every measurement, i.e.

$$f_d - f_s = V_m/K \qquad (7.16)$$

As given in Appendix D

$\delta f_s = 2.734 \times 10^{-4}$MHz

The uncertainties in the measured velocity are:

— Axial velocities

K =2.279927

δK = 0.0285

δf_{d1}= 0.0128 MHz

—— flowrate 1

Q = 16.84 m^3/h

U_m = 0.7569 m/s

δu = 0.031m/s

—— flowrate 2

$Q = 30.87\ m^3/h$

$U_m = 1.3876\ m/s$

$\delta u = 0.034\ m/s$

— Circumferential velocity

The uncertainties in the circumferential velocity measurements are different for different radial positions. Using the maximum δK and K, and

$\delta f_{d_2} = 0.0116\ MHz$

The possible errors in the measured circumferential velocities are

—— flowrate 1

$Q = 16.84\ m^3/h$

$\delta v = 0.026 m/s$

—— flowrate 2

$Q_2 = 30.87\ m^3/h$

$\delta v = 0.027\ m/s$

7.5 Tested Cases

The conducted experiments cover the following cases:

—— Case A without inlet swirl generator
—— Case B with swirl generator of +4 degree blade angle
—— Case C with swirl generator of +8 degree blade angle
—— Case D with swirl generator of -4 degree blade angle
—— Case B with swirl generator of -8 degree blade angle

The flow fields throughout the flowmeter rotor were measured in these five cases. In case A, the measurements were done at flowrates of $16.84m^3/h$ and $30.87m^3/h$. In the another four cases, measurement was only done at a flowrate of $30.87m^3/h$. In each case, the performance curves of the tested flowmeter were also measured. The measured velocity data were registered under three or four digital names. For example, BL04 indicates the results on axial station 4 in

test case B at the larger flowrate and A04 indicates the profile in test case A on station 4 at the smaller flowrate.

In all five cases, inlet velocity profiles(both axial and circumferental components)were measured at six flowrates. Those flowrates were 11.23, 16.84, 22.46, 28.07, 33.68 and 39.30m^3/h.

CHAPTER EIGHT

EXPERIMENTAL DATA ANALYSIS AND COMPARISON WITH NUMERICAL RESULTS

8.1 Introduction

Using the experimental rig described in chapter 7, the flow fields throughout the flowmeter rotor were measured at 11 axial stations as defined in fig.7.10 and table 7.3 in all five test cases. From the measured velocity profiles, a clear understanding of the flow inside the turbine flowmeter was obtained. Based on this experimental study, the major objective is to develop a numerical model which can predict turbine flowmeter performance in various working conditions. The experimental results are also used to validate the developed numerical models.

In applying the numerical performance prediction model, the inlet flow conditions are needed. The inlet section position of the tested flowmeter, on which the combined disturbance from the flowmeter hub and the rotor was small, was determined from the measured velocity profiles and the velocity profiles on this inlet section were measured at a number of flowrates in each test case. In this chapter, the inlet velocity profiles predicted by the panel method is compared with the measured inlet profiles in case A. Using both predicted and measured inlet velocity profiles as the input data to the performance

prediction model, the flowmeter coefficients are calculated and compared with the corresponding measured coefficients.

8.2 Analysis of the Experimental Data

8.2.1 Developed Pipe Velocity Profile

Before measuring the flow profiles inside the turbine flowmeter, the fully developed velocity profile in the pipe cross section(without the turbine flowmeter) was measured to test the accuracy of the LDA system and check whether inlet swirl was produced by the experimental rig arrangement.

In fully developed pipe flow, the velocity profile satisfies power law, i.e.

$$\frac{u}{U_c} = (1-\frac{r}{R})^n \qquad (8.1)$$

At the tested flowrate 34.24m^3/h, the Reynolds number is

$$Re = \frac{U_m D}{\nu} = \frac{0.1016 \times 1.1}{10^{-6}} = 1.12 \times 10^5$$

The relation given by Schlichting between the flow Reynolds number and the power law exponent n is

Re	4×10^3	2.3×10^4	1.1×10^5	1.1×10^6	2×10^6	3.7×10^6
n	6	6.6	7	8.8	10	10

At the measured flowrate, n is 7.

A comparison between the measured and power law profiles is presented in fig.8.1. In this comparison, the measured axial velocity profile agrees with the power law profile very well, only small differences occur in the pipe wall area. In this area, the boundary layer influence becomes strong and LDA measurements are difficult due to the noise signals reflected from the pipe wall surface.

The measured circumferential velocity components are presented in fig.8.2. These are almost the same magnitude level as the system uncertainty given in paragraph 7.4.3. Hence the results show that no

obvious inlet swirl was generated by the arrangement of the experimental rig.

8.2.2 Flow Field Throughout the Flowmeter Rotor

The flow fields throughout the flowmeter rotor were measured in all five test cases. The measurement was conducted at flowrates of 16.84m^3/h and 30.87m^3/h in case A and the measurement was done only at flowrate 30.87m^3/h in cases B, C, D and E. Both axial and circumferential velocity profiles were measured at 11 stations from the upstream of the rotor to the downstream of the rotor. The results are presented in fig.8.3 to fig.8.38. In the presented results, the circumferential velocity component in the same direction as the rotor rotation is taken as positive and it is negative when it is in the direction opposite to the rotation. From these experimental results, the following conclusions can be drawn:

—The circumferential variations in the axial velocity components at the measurement stations are found to be quite small apart from in the boundary layer regions near blade surfaces. However the measurements in those boundary layer regions are blocked by the blade itself and there is no obvious velocity variation in the measurable area as presented in tables 7.6 and 7.7. The results presented in this chapter therefore only give the circumferential mean velocities throughout the rotor.

— Due to the existence of the flowmeter hub nose, the velocity profiles near the hub head are strongly disturbed and change very quickly in its vicinity. The results in fig.8.3 and fig.8.5 at the smaller flowrate and fig.8.9 and fig.8.11 for the larger flowrate in case A show that the flow is very much accelerated near hub surface. However, this influence decays very quick from station 1 to station 3 and the velocity profiles become reasonably constant between station 3 and station 4. Similar results are also found in other test cases. After station 4, the influence of the flowmeter rotor increases, the axial velocity profile begins to change accordingly. It can also be seen from fig.8.3 and fig.8.9 that the velocity ratio profiles at the same axial stations are different at different flowrates. In the hub

area, the velocity ratio at small flowrates is higher than that at larger flowrates. This is due to fluid viscosity as discussed in detail later.

— With a swirl generator upstream of the flowmeter, the measured velocity profiles are quite different from the profiles in case A without an upstream swirl generator. With inlet swirl, the axial velocity profiles are more curved from the hub to the tip and the flow in the hub area is very much slowed down compared with the results in case A. The reason for this is briefly discussed in the inlet velocity analysis section later. In the test cases B and C, the velocity profiles at station 4 are still far from uniform, so the inlet flow conditions are quite different from the ideal flowmeter inlet conditions.

—As the flow goes into the rotor, the most significant effect is blade blockage. The flow is accelerated at almost the same rate from the hub to the tip as soon as it enters the rotor. Theoretically, the blockage should be different at different radial positions, so the acceleration must also be different. The detected phenomenon may indicate a small radial velocity component in the leading edge area. However, there is no obvious change in the circumferential velocity components, only a slight change is detected at station 7. This change may be due to the effect of the separated leading edge flow.

—Inside the rotor, the flow continues to develop under the interaction with the blades and tends to become more uniform. The change in the leading edge area is greater than the change in other areas.

— After the trailing edge, blade blockage disappears and the flow slows down. Due to the variations of the blockage from the hub to the tip, the decceleration in the tip area is smaller than that in the hub area. The variations from the hub to the tip are smaller in case A than they are in other test cases. For the flow with inlet swirl, the flow in the hub area is decceleratedmuch more quickly than that in the tip area.

— After the blade trailing edge, a rapid circumferential velocity changes were detected due to the square shape of the trailing edge. To

examine the circumferential velocity after the trailing edge, the velocity at the trailing edge sharp points on both the upper and the lower surfaces are assumed equal and the continuity and momentum equations can be applied to a flow element fixed at the blade trailing edge as shown in fig.8.39.

The continuity equation gives

$$2h_0 u_1 \cos\alpha_1 = (2h_0+h_1) u_0 \cos\alpha_2 \qquad (8.2)$$

where α_1 and α_2 are the flow angles before and after the trailing edge.

Due to the infinitely small thickness of the element, the momentum equation in the y direction gives

$$2h_0 u_1^2 \sin\alpha_1 \cos\alpha_1 = (2h_0+h_1) u_0^2 \sin\alpha_2 \cos\alpha_2 \qquad (8.3)$$

From equations (8.2) and (8.3), the flow angle after the blade trailing edge is found to be

$$\tan\alpha_2 = \frac{2h_0+h_1}{2h_0} \tan\alpha_1$$

$$= \frac{S}{S-h_1} \tan\alpha_1 \qquad (8.4)$$

The circumferential flow angle change is directly linked to the blade blockage. From the hub to the tip, the rotor space is different, so the circumferential flow angle change is different. In the stationary coordinate, angle α_2 becomes more negative than angle α_1 from equation(8.4). This analysis is in agreement with the measured circumferential velocity profiles after the blade trailing edge.

8.2.3 Flowmeter Inlet Velocity Profiles

To validate the numerical flowmeter prediction model, the inlet velocity has to be measured. In the tested flowmeter, there is only limited space to allow the inlet flow to develop between the flowmeter hub head and the rotor. There is therefore no fully developed inlet section to those simplified two dimensional flows of the tested flowmeter.

The inlet section position is chosen as the one on which the combined effect of the hub head and the rotor is at its minimum and it is determined according to the measured velocity profiles before the flowmeter rotor. However, there are some differences in the velocity development among the tested cases. In case A, because there is no induced inlet swirl, the detected circumferential velocity is mainly due to the disturbance from the rotor and the flowmeter hub, and the measurement uncertainty. The results in case A are used to determine the position of the inlet section. It can be seen from figures 8.3 to 8.6 and figures 8.9 to 8.12 that a strong hub head distortion exists before section 3 and the axial velocity has become reasonably constant between section 3 and station 4. The circumferential components at the stations are small and quite constant. The measured results show that the influence from the flowmeter rotor is weak at station 3. So the inlet section in all cases is chosen at section 3. On this section, the inlet axial and circumferential velocity components were measured in all five test cases at six flowrates.

——Inlet axial velocity component

To validate the flowmeter performance prediction model, a complete inlet velocity profile is necessary. However, the velocity components at the points near both the pipe wall and the flowmeter hub can not be measured by LDA due to strong noise signals from either the pipe wall or the flowmeter hub surface, the velocity profile in these areas has to be obtained using the boundary theory given in chapter 6. Here, the total flowrate from the inlet velocity profile(the measured profile combined with the predicted profiles inside boundary layers) is checked against the reference vortex flowmeter reading. By this comparison, not only is the measured data checked, but the profiles in the boundary layers are also comfirmed. The flowrate obtained from the axial velocity on the inlet section is the integration of the axial velocity over the inlet section, i.e.

$$Q=\sum_{i=1}^{N-1} 0.5(u_i+u_{i+1})\pi(r_{i+1}^2-r_i^2) \qquad (8.5)$$

In the experimental rig, the flowrate through the tested flowmeter

is measured by a calibrated vortex flowmeter with an accuracy within one percent. The flowrate given by the reference vortex flowmeter is

$$Q = 3600f/K \quad (m^3/h) \qquad (8.6)$$

where f is the frequency output of the vortex flowmeter and K is the vortex flowmeter coefficient given by flowmeter calibration. The used vortex flowmeter coefficient is 6412.78.

The inlet axial velocity components, the integrated flowrates from the inlet velocity profiles and the comparisons with the reference flowrates from the vortex flowmeter are presented in the following tables.

Table 8.1 Inlet velocity and flowrate comparison(case A)

Radius	Q1	Q2	Q3	Q4	Q5	Q6
1.960*	0.382	0.571	0.747	0.919	1.097	1.281
1.915*	0.407	0.627	0.852	1.056	1.307	1.529
1.870	0.433	0.669	0.909	1.131	1.435	1.622
1.817	0.458	0.691	0.938	1.176	1.519	1.643
1.765	0.471	0.714	0.957	1.212	1.572	1.693
1.686	0.485	0.737	0.991	1.242	1.619	1.740
1.607	0.514	0.756	1.029	1.276	1.656	1.780
1.528	0.529	0.787	1.061	1.312	1.689	1.834
1.450	0.543	0.802	1.082	1.335	1.720	1.861
1.371	0.566	0.828	1.118	1.375	1.768	1.926
1.292	0.584	0.849	1.152	1.445	1.807	1.970
1.240	0.609	0.870	1.174	1.475	1.814	1.999
1.187	0.622	0.909	1.211	1.505	1.825	2.021
1.135	0.640	0.938	1.232	1.520	1.859	2.057
1.062*	0.598	0.865	1.121	1.376	1.704	1.887
0.989*	0.385	0.589	0.784	0.969	1.108	1.353
M.FR.	10.895	16.332	21.989	27.397	34.554	38.212
R.FR.	11.228	16.841	22.445	28.069	33.683	39.297
ERROR (%)	2.96	3.02	2.03	2.46	2.59	2.76

* indicates the predicted data inside the boundary layers

Table 8.2 Inlet velocity and flowrate comparison(case B)

Radius	Q1	Q2	Q3	Q4	Q5	Q6
1.960*	0.382	0.566	0.752	0.924	1.109	1.285
1.915*	0.460	0.657	0.918	1.118	1.393	1.595
1.870	0.490	0.709	0.990	1.199	1.490	1.745

1.817	0.500	0.740	1.016	1.225	1.500	1.799
1.765	0.525	0.759	1.048	1.260	1.550	1.816
1.686	0.540	0.780	1.066	1.320	1.590	1.860
1.607	0.545	0.803	1.103	1.360	1.620	1.880
1.528	0.556	0.812	1.120	1.395	1.650	1.950
1.450	0.580	0.822	1.130	1.411	1.700	1.970
1.371	0.562	0.820	1.120	1.400	1.670	1.960
1.292	0.555	0.815	1.100	1.389	1.660	1.960
1.240	0.559	0.800	1.080	1.360	1.640	1.920
1.187	0.550	0.790	1.050	1.330	1.590	1.880
1.135	0.540	0.780	1.041	1.300	1.550	1.800
1.062*	0.497	0.720	0.967	1.178	1.402	1.574
0.989*	0.385	0.549	0.707	0.859	1.008	1.153
M.FR.	11.126	16.217	22.179	27.433	33.092	38.675
R.FR.	11.228	16.841	22.455	28.069	33.683	39.297
ERROR (%)	0.91	3.71	1.21	2.26	1.76	1.58

Table 8.3 Inlet velocity and flowrate comparison(case C)

Radius	Q1	Q2	Q3	Q4	Q5	Q6
1.960*	0.382	0.574	0.760	0.929	1.100	1.286
1.915*	0.459	0.724	0.938	1.121	1.312	1.614
1.870	0.490	0.785	1.040	1.228	1.450	1.750
1.817	0.500	0.798	1.090	1.287	1.535	1.790
1.765	0.518	0.807	1.095	1.324	1.560	1.840
1.686	0.525	0.826	1.110	1.346	1.580	1.850
1.607	0.531	0.836	1.140	1.360	1.630	1.900
1.528	0.535	0.851	1.150	1.370	1.660	1.920
1.450	0.540	0.847	1.150	1.400	1.670	1.940
1.371	0.540	0.855	1.160	1.380	1.680	1.917
1.292	0.535	0.840	1.130	1.370	1.650	1.880
1.240	0.520	0.834	1.120	1.365	1.606	1.830
1.187	0.510	0.809	1.060	1.320	1.560	1.808
1.135	0.490	0.785	1.000	1.301	1.530	1.740
1.062*	0.450	0.718	0.890	1.197	1.397	1.534
0.989*	0.385	0.549	0.707	0.859	1.008	1.153
M.FR.	10.732	16.983	22.272	27.629	32.876	38.223
R.FR.	11.228	16.841	22.455	28.069	33.683	39.297
ERROR (%)	4.41	0.84	1.21	1.57	2.40	2.73

Table 8.4 Inlet velocity and flowrate comparison(case D)

Radius	Q1	Q2	Q3	Q4	Q5	Q6
1.960*	0.382	0.569	0.746	0.926	1.104	1.281

1.915*	0.438	0.689	0.895	1.119	1.366	1.586
1.870	0.470	0.740	0.954	1.210	1.469	1.724
1.817	0.490	0.755	0.975	1.250	1.500	1.771
1.765	0.504	0.770	1.018	1.290	1.560	1.800
1.686	0.520	0.800	1.064	1.340	1.601	1.880
1.607	0.540	0.830	1.075	1.368	1.650	1.930
1.528	0.545	0.855	1.083	1.395	1.660	1.940
1.450	0.555	0.865	1.099	1.387	1.670	1.927
1.371	0.560	0.873	1.102	1.372	1.660	1.920
1.292	0.546	0.860	1.088	1.360	1.650	1.900
1.240	0.540	0.850	1.080	1.320	1.635	1.870
1.187	0.520	0.830	1.050	1.300	1.620	1.830
1.135	0.500	0.810	1.030	1.260	1.600	1.800
1.062*	0.461	0.736	0.946	1.136	1.449	1.637
0.989*	0.385	0.549	0.707	0.859	1.008	1.154
M.FR.	10.783	16.848	21.738	27.313	33.181	38.443
R.FR.	11.228	16.841	22.455	28.069	33.683	39.297
ERROR (%)	3.96	0.0	3.19	2.69	1.49	2.17

Table 8.5 Inlet velocity and flowrate comparison(case E)

Radius	Q1	Q2	Q3	Q4	Q5	Q6
1.960*	0.382	0.570	0.753	0.931	1.102	1.280
1.915*	0.432	0.687	0.927	1.131	1.352	1.581
1.870	0.460	0.746	1.001	1.240	1.460	1.722
1.817	0.475	0.770	1.030	1.300	1.502	1.780
1.765	0.482	0.780	1.080	1.340	1.560	1.830
1.686	0.500	0.798	1.110	1.380	1.600	1.880
1.607	0.520	0.810	1.120	1.420	0.625	1.900
1.528	0.532	0.824	1.140	1.430	1.660	1.940
1.450	0.550	0.850	1.160	1.544	1.700	1.960
1.371	0.554	0.860	1.180	1.450	1.720	1.970
1.292	0.550	0.860	1.185	1.440	1.700	1.950
1.240	0.545	0.840	1.160	1.430	1.680	1.920
1.187	0.541	0.830	1.140	1.410	1.650	1.900
1.135	0.521	0.810	1.100	1.370	1.610	1.870
1.062*	0.472	0.732	0.973	1.216	1.440	1.681
0.989*	0.385	0.549	0.707	0.859	1.008	1.153
M.FR.	10.647	16.722	22.094	28.483	33.382	38.872
R.FR.	11.228	16.841	22.455	28.069	33.683	39.297
ERROR (%)	5.17	0.708	2.00	1.47	0.89	1.08

The differences between the integrated and the reference flowrates are very small in most cases. The absolute differences are of the same magnitude level in all cases and the relative errors are always larger

at the small flowrates.

The mean velocity in the tested turbine flowmeter is defined as

$$U_m = \frac{Q}{\pi(r_p^2 - r_h^2)} \qquad (8.7)$$

The differences in the mean velocity as calculated from the integrated flowrate and as given by the vortex flowmeter are listed in the following table.

Table 8.6 Inlet section mean velocity differences

	case A	case B	case C	case D	case E
Q1	0.015	0.005	0.022	0.020	0.026
Q2	0.023	0.028	0.001	0.002	0.005
Q3	0.020	0.013	0.008	0.032	0.016
Q4	0.031	0.028	0.020	0.034	0.019
Q5	0.039	0.026	0.036	0.022	0.013
Q6	0.048	0.028	0.048	0.038	0.019

The above table shows that the differences in the mean velocity from the integrated and reference flowrates are almost of the same level as predicted uncertainties in paragraph 7.4.3 and are therefore due to the uncertainties of the measurements.

The measured axial inlet velocity profiles for case A are presented in fig.8.40. The velocity ratio near the hub surface is quite high at small flowrates and drops with the increase of flowrate. The velocity variation near the pipe wall has just the opposite tendency. These profiles are thought mainly due to the nature of the fully developed pipe velocity profile before the flowmeter.

The fully developed velocity profile for the pipe flow in a laminar state is

$$\frac{u}{u_c} = 1 - \left(\frac{r}{R}\right)^2 \qquad (8.8)$$

and the ratio of the central to the average velocity is

$$\frac{u_c}{U_m} = 2. \qquad (8.9)$$

As Reynolds number increases(i.e. flowrate increase), the profile tends to the power law as equation (8.1) and the ratio of central to the section average velocity becomes

$$\frac{u_c}{U_m} = \frac{(2n+1)(n+1)}{2n^2} \qquad (8.10)$$

Comparing equation(8.9) and (8.10), the ratio between the central and section average velocities at small flowrates is higher than that at large flowrates and the ratio continuously drops as flowrate increases. Because the central velocity has a strong direct influence on the velocity near the hub surface, so the velocity ratio on the hub surface at small flowrates is higher than that at large flowrates. The velocity profile becomes more flat as flowrate increases.

It can be seen from figures 8.40 to 8.44 that the velocity near the hub in case A is higher than that in other test cases at the same flowrate. In the cases with swirl, the equations (8.1) and (8.7) are no longer valid. It is obvious that the flow velocity on the swirl generator core surface is reduced to zero due to the non-slip boundary condition, so the existence of the generator core slows the pipe central flow before the flowmeter. Therefore the flowmeter inlet velocity near the hub surface is also decreased in all the cases with a swirl generator compared with case A.

In all the test cases with swirl, the axial velocity ratio is higher at small flowrates and decreases as flowrate increases in the hub area. This variation with Reynolds number is similar to the results detected in case A. This is also due to the pipe velocity profile before the flowmeter. Generally speaking, the inlet velocity becomes more uniform as flowrate increases.

Among the cases with swirl, the velocity ratio profiles in cases B and D are more constant compared with cases C and E at all those examined flowrates.

—— Circumferential component

The circumferential velocity profiles measured on the inlet section in the tested cases are shown from fig.8.45 to fig.8.49. It can be seen from the results that only a small circumferential component is detected on the inlet section in case A. This component

may come from the flowmeter rotor influence because the inlet section is not far from the rotor leading edge. However, it is very small and has almost the same magnitude level as the predicted measurement uncertainties. Hence the disturbance from both the rotor and the flowmeter hub head is small on the inlet section.

When the swirl generator is installed, a quite large inlet circumferential component is detected. The measured results are now compared with the predicted inviscid flow results.

In inviscid flow, the circulation around any closed curve remains constant. The flow between the swirl generator and the flowmeter inlet section is axisymmetric, so the circulation around any circular streamtube centred on the pipe axis should be constant when the viscosity is ignored. Also a circular streamtube from the swirl generator should still be circular on reaching the flowmeter inlet section. The flowrate around such a streamtube is constant for flow continuity.

Supposing a circular streamtube after the swirl generator has radius r_g and circumferential velocity component u_g, the circulation of the streamtube is

$$\Gamma_g = 2\pi u_g r_g \tag{8.11}$$

The corresponding circumferential velocity on the inlet section is

$$u = \frac{\Gamma_g}{2\pi r} \tag{8.12}$$

On the flowmeter inlet section, the radius of the corresponding streamtube radius r is determined by flow continuity. Just downstream of the swirl generator, the circumferential velocity component is determined by the angle of the swirl generator blades. It is

$$u_g = v_g \tan\beta_g \tag{8.13}$$

where α_g is the twist angle of the swirl generator blades and v_g is the axial velocity component before the swirl generator blades which is obtained from the developed model for annulus flows in chapter 6.

Thus the circumferential velocity component on the inlet section is

$$u = \frac{v_g \tan\beta_g r_g}{r} \qquad (8.14)$$

The predicted results by equation (8.14) are compared with the measured results in figures 8.50 to 8.53.

The comparison is conducted for cases B, C D and E at flowrates of 22.46m^3/h and 39.30m^3/h. The agreement at the larger flowrate is better than that at the smaller flowrate. The reason is that equation(8.14) is only applicable in inviscid flows. At the larger flowrate, the Reynolds number is higher and the viscous effect is weaker, so the flow should be closer to ideal flow. The agreement in cases B and D are much better than that in cases C and E in which the swirl is strong.

As to the measured circumferential velocity in the other tested cases, The velocity ratio is quite constant in cases B and D at the tested flowrates, but in cases C and E, relatively large velocity ratio variations with flowrate were detected in the hub area. This phenomenon could correspond to the similar axial velocity profile variations as presented in figures 8.41 to 8.44. The nature of these velocity profiles suggests that the flow on the inlet section is still developing.

8.3 Comparison of Experimental and Numerical Data

8.3.1 Inlet Velocity Profile

The panel model presented in chapter 6 was used to predict turbine flowmeter inlet velocity profiles in case A. In this model, the boundary layers on both the pipe and the flowmeter hub surfaces are considered. Comparison between the measured and the predicted velocity profiles at mean velocities of 0.757m/s and 1.766m/s are presented in figures 8.54 and 8.55. The agreement at the larger flowrate is better than that at the smaller flowrate, especially near the hub surface. The reason is that the boundary layers on the annulus surfaces are thinner at the larger flowrate. Generally speaking, the prediction gives reasonable accuracy. However, the boundary layer on the pipe

wall are not exactly calculated with the displacement influence from the flowmeter hub and the boundary layer on the surface in the present model. Also the boundary layer on the hub surface is assumed thin, so the model wouldn't give very accurate answers at small flowrates.

8.3.2 Velocity Patterns Inside the Flowmeter Rotor

The developed numerical model for the flow around the flowmeter blades is a two dimensional model, the predicted axial mean velocity is only changed by blade displacement in the two dimensional cascade flow on account of flow continuity. As mentioned before, the presented experimental results is the mean velocities between blades. Hence only the circumferential velocity profiles are compared here.

The velocity triangle after the flowmeter rotor is as shown in fig.8.39, the absolute circumferential velocity is

$$\Delta v = \omega r - u \tan\beta \qquad (8.15)$$

Under ideal design conditions,i.e. uniform inlet velocity profile with frictionless flowmeter bearing and no inlet swirl, Δv is zero. Then

$$\frac{\omega}{u} = \frac{\tan\beta}{r} \qquad (8.16)$$

With the uniform inlet flow assumption, the designed blade angle β at radius r is

$$\frac{\tan\beta}{r} = \frac{\tan\beta_0}{r_0} \qquad (8.17)$$

where β_0 is the blade angle in the reference section at radius r_0.

Substituting equation(8.17) into (8.15), the circumferential velocity after the flowmeter rotor is

$$\Delta v = \omega r - ur \tan\beta_0/r_0$$

$$= r(\omega - u \tan\beta_0/r_0) \qquad (8.18)$$

The circumferential velocity component is thus a function of the radius and the axial velocity component inside the rotor.

In ideal flows, when swirl exists in the inlet flow, because the inlet axial velocity profile is uniform, the circumferential velocity profile is linearly distributed in the radial direction.

In actual flows, the ideal design conditions are never completely satisfied, so circumferential velocity components always exist inside and after the flowmeter rotor. The flow near the pipe wall and the hub surface is slowed down, so the axial velocity profile is not uniform and the radial distribution of the circumferential component is be curved consequently.

In the tested cases of the present experiment, the inlet axial velocity profile is not uniform and inlet swirl is present in several test cases. Also friction always exists inside the flowmeter bearing and there is interaction between the rotor and the liquid, such as the leading edge separations and the boundary layers. Therefore the circumferential component profiles of them are expected to be different from equation(8.18).

8.3.2.1 Calculation of the Circumferential Velocity Component

To predict the circumferential velocity , the inlet conditions are taken from the measured velocity profiles on the inlet section, so the non-uniform profile influence is included in the prediction. The measured rotor speed is also used in the determination of the inlet condition. The rotor speed was affected by the bearing friction, so the bearing friction influence is indirectly considered as well.

The flow inside the rotor is reduced to an infinite number of flows on cylindrical surfaces from the hub to the tip. On each radial section, the flow is two dimensional and the developed model can be applied to obtain the flow field. To get a complete flow field inside the rotor, the flow fields in a number of radial sections are predicted separately.

From the measured inlet velocity and the flowmeter coefficient, the inlet velocities and the angles relative to the coordinates fixed to the rotor can be obtained. In this chapter, comparisons of circumferential velocities in cases B, D and E are made. The relative inlet conditions at the radial sections, on which the velocity components are measured, are given in tables 8.7, 8.8 and 8.9.

Table 8.7 Inlet Conditions of Case B

Radial Station No:	1	2	3	4	5	6	7	8
Measured Data								
Radius (mm)	28.82	30.85	34.18	37.50	40.16	42.82	45.48	47.28
Blade Angle (deg.)	34.28	36.12	38.95	41.57	43.53	45.36	47.09	48.20
Rotor Speed (rad/s)	6.06	6.06	6.06	6.06	6.06	6.06	6.06	6.06
Axial Component (m/s)	1.39	1.45	1.50	1.51	1.47	1.42	1.35	1.31
Cir. component (m/s)	0.15	0.14	0.13	0.12	0.11	0.11	0.11	0.11
Input Data for Numerical Prediction								
Flow Angle (deg)	34.33	35.52	38.11	40.93	44.11	47.01	50.29	52.25
Inlet velocity (m/s)	1.69	1.78	1.90	2.00	2.04	2.08	2.11	2.14

Table 8.8 Inlet Conditions of Case D

Radial Station No:	1	2	3	4	5	6	7	8
Measured Data								
Radius (mm)	28.82	30.85	34.18	37.50	40.16	42.82	45.48	47.28
Blade Angle (deg.)	34.28	36.12	38.95	41.57	43.53	45.36	47.09	48.20
Rotor Speed (rad/s)	5.12	5.12	5.12	5.12	5.12	5.12	5.12	5.12
Axial Component (m/s)	1.39	1.43	1.48	1.49	1.48	1.44	1.37	1.31
Cir. component (m/s)	-0.12	-0.13	-0.12	-0.11	-0.10	-0.08	-0.08	-0.07
Input Data for Numerical Prediction								
Flow Angle (deg)	37.00	38.16	39.62	41.46	43.36	45.52	48.46	50.59
Inlet velocity (m/s)	1.74	1.82	1.92	1.99	2.03	2.05	2.06	2.07

Table 8.9 Inlet Conditions of Case E

Radial Station No:	1	2	3	4	5	6	7	8
Measured Data								
Radius (mm)	28.82	30.85	34.18	37.50	40.16	42.82	45.48	47.28
Blade Angle (deg.)	34.28	36.12	38.95	41.57	43.53	45.36	47.09	48.20
Rotor Speed (rad/s)	4.74	4.74	4.74	4.74	4.74	4.74	4.74	4.74
Axial Component (m/s)	1.46	1.51	1.57	1.55	1.51	1.46	1.40	1.33
Cir. component (m/s)	-0.19	-0.21	-0.22	-0.20	-0.18	-0.15	-0.15	-0.13
Input Data for Numerical Prediction								
Flow Angle (deg)	35.77	36.75	38.17	40.26	42.36	44.29	47.02	49.23
Inlet velocity (m/s)	1.80	1.89	2.00	2.04	2.04	2.04	2.05	2.04

The procedure for the flow field prediction in each radial section is the same as that for the prediction of the lift and drag given in chapter 5, i.e.

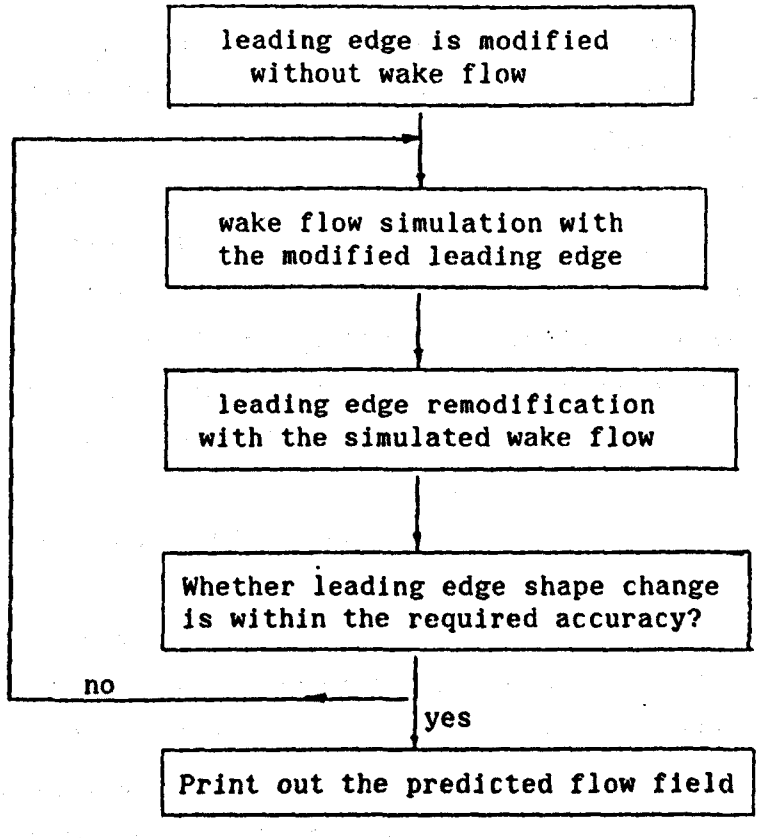

8.3.2.2 Comparison

The comparison of the circumferential velocity components in cases B, D and E are shown in figures 8.56 to 8.70. Generally speaking, The measured profiles are much flatter than the predicted profiles. As predicted by equation(8.18), the circumferential velocity is large in the tip section, reduces to a minimum in the midspan area where the axial velocity is higher and increases again in the hub area where the axial velocity is slowed down by the boundary layer. The model also predicts the rapid circumferential velocity change after the blade trailing edge.

In case D, the agreement between the predicted and measured profiles is quite good in most of the area and the trailing edge jump is also predicted as shown in figures 8.61 to 8.65. However, the agreement in case B is much worse than cases D and E. Several factors

could have contributed to this result. It can be seen from the inlet conditions given in tables 8.6 to 8.8 that the incidence angle in the tip area in case B is about 5 degrees but it is only 3 degrees in case D and 2 degrees in case E. Large incidence angle produces a large leading edge separation bubble. This could have contributed to the difference in case B. As concluded in 8.2.2, a small three dimensional flow may have developed in the leading edge area of the flowmeter rotor. This small three dimensional flow might have caused circumferential velocity redistribution in the rotor. On the other hand, the developed numerical model is only a potential model. Fluid viscosity effect is not considered in the simulation, but the viscosity could be strong in the boundary layer areas. Additionally, the measurement uncertainties of the inlet conditions could have an influence on the compared results.

8.3.3 Prediction of Flowmeter Performance

Using the model presented in chapter 6, the performance of a turbine flowmeter can be predicted providing the inlet flow conditions are given. The choice of the inlet section position for the tested flowmeter is based on the measured velocity profiles throughout the flowmeter rotor as described in paragraph 8.2.3.

The panel model developed for inlet velocity profile prediction is only suitable for flows without inlet swirl, so the pure theoretical performance curve is obtained only for case A. Using the predicted velocity profiles, the predicted flowmeter performance curved is compared with the measured curve in fig.8.71.

The flowmeter coefficients at the measured flowrates are also predicted using the measured inlet conditions. The predicted results are compared with the measured data in fig.8.72. The flowmeter coefficients at those flowrates are given in the following table.

Table 8.10 Flowmeter coefficient comparison(Case A)

	Q1	Q2	Q3	Q4	Q5	Q6
Measured Data	1.741	1.833	1.857	1.866	1.886	1.881

Predicted Data	1.802	1.852	1.862	1.866	1.872	1.871
Absolute Difference	0.061	0.019	0.005	0.00	-0.014	-0.010
Relative Difference (%)	3.50	1.04	0.27	0.0	-0.75	-0.53

In the other four cases, the flowmeter coefficients can only be predicted at those flowrates at which the inlet velocity profiles were measured as presented from table 8.2 to 8.5. The predicted performance curves are also compared with the measured data as shown in figures 8.73 to 8.76. The differences in the predicted and measured flowmeter coefficients at the tested flowrates are given in following tables.

Table 8.11 Flowmeter coefficient comparison(case B)

	Q1	Q2	Q3	Q4	Q5	Q6
Measured Data	1.983	2.021	2.020	2.022	2.031	2.022
Predicted Data	2.018	2.067	2.041	2.051	2.058	2.036
Absolute Difference	0.035	0.046	0.021	0.029	0.027	0.014
Relative Difference (%)	1.77	2.28	1.04	1.44	1.33	0.69

Table 8.12 Flowmeter coefficient comparison(case C)

	Q1	Q2	Q3	Q4	Q5	Q6
Measured Data	2.031	2.139	2.157	2.157	2.164	2.160
Predicted Data	2.187	2.215	2.208	2.179	2.165	2.143
Absolute Difference	0.156	0.076	0.051	0.022	0.001	-0.017
Relative Didderence (%)	7.68	3.55	2.36	1.02	0.05	-0.79

Table 8.13 Flowmeter coefficient comparison(case D)

	Q1	Q2	Q3	Q4	Q5	Q6
Measured Data	1.588	1.681	1.694	1.713	1.714	1.713
Predicted Data	1.684	1.725	1.742	1.749	1.756	1.753
Absolute Difference	0.096	0.044	0.048	0.036	0.042	0.040
Relative Difference (%)	6.04	2.62	2.83	2.10	2.45	2.34

Table 8.14 Flowmeter coefficient comparison(ease E)

	Q1	Q2	Q3	Q4	Q5	Q6
Measured Data	1.532	1.580	1.583	1.583	1.583	1.582
Predicted Data	1.549	1.634	1.640	1.649	1.650	1.652
Absolute Difference	0.017	0.054	0.057	0.062	0.067	0.070
Relative Difference (%)	1.11	3.42	3.60	3.92	4.23	4.42

It can be seen from the results that the predicted coefficients are quite accurate for the case without inlet swirl using the predicted inlet flow conditions. The difference here is below 1 percent when the flowrate is bigger than $10m^3/h$, and large difference exists at small flowrates. At small flowrates, the flowmeter inlet axial velocity becomes more non-uniform and a larger incidence angle occurs in the hub and tip areas. Consequently a large leading edge separation occurs. Furthermore, the lubrication state inside the bearing changes to boundary state from the fully hydraulic state at small flowrates. The linear mechanical friction change assumed in this transition may have contributed to the difference. Also the predicted velocity profiles in the boundary layers, especially in the pipe wall

boundary layer, have limited accuracy at small flowrates.

As to the predicted performance curves using the measured velocity profiles, case A shows the best agreement with the measured data among all the test cases. In case A, the predicted accuracy is within 1 percent from Q2 to Q6, this is in the linear operating range of the flowmeter. As explained in the inlet flow analysis, the swirl generator redistributes the flow at the front of the flowmeter, and the inlet velocity profiles are not as uniform as they are in case A. Consequently, the differences between the predicted and the measured data become bigger. In cases B, C and D, the absolute differences are almost of the same level, and the relative differences are small in case B and C and within 3 percent from Q2 to Q6. The absolute differences in case E are slightly increased in the linear range and the relative differences are below 4.23 percent. The non-uniform inlet velocity profile and the bearing friction are thought to be the main reasons for the differences between the compared results in cases B, C, D and E.

In all cases, the agreement at small flowrates is poorer. Apart from the reasons of non-uniform inlet flow and bearing friction, it can be seen from the results presented from table 8.1 to table 8.5 that the relative errors of integrated flowrates in all five test cases at small flowrates are higher than that at large flowrates. These inlet velocity profile errors have surely contributed to the predicted performance.

CHAPTER NINE

FINAL CONCLUSIONS

9.1 Introduction

In this thesis, a vortex model is developed to simulate the flow fields around turbine flowmeter blades. In the model, a new method of applying the Kutta condition is introduced. To deal with the flow separations at the leading edge of the square shaped flowmeter blades, Lewis's blade design method is quite successfully applied to simulate the displacement effect of the leading edge separation bubbles. A numerical model is also developed to predict the performance of turbine flowmeters under various inlet conditions. An experimental study is conducted to investigate the flow fields throughout the flowmeter rotor under different inlet conditions. The experimental results are also used to validate the developed numerical model.

Some conclusions have already been drawn after the results obtained in each chapter. In this chapter, general conclusions are given, including an assessment of the vortex model, the model for flowmeter performance prediction and the experimental study. The future direction for theoretical and experimental work on turbine flowmeters are recommended.

9.2 Conclusions

9.2.1 Flow Simulation

—— Vortex model

By using the newly introduced applying method of the Kutta condition, the flow around turbine flowmeter blades, which is unsteady during the wake development, can be easily obtained avoiding long iterative calculations. This method could be very useful for the simulation of unsteady flows between stator and rotor. This model is tested by applying it to a thin airfoil in steady flow at zero incidence without wake, the predicted pressure distribution agrees very well with the experimental data. It is also applied to the flows around oscillating airfoils. The simulated wake configurations show clear development of the wake flow. The predicted lift is compared with the experimental data as explained in chapter 4.

—— Leading edge flow simulation

The sharp leading edge has caused great difficulty in the accurate prediction of the flow around turbine flowmeter blades. Using the vortex model developed here, the leading edge flow separation and reattachment has been successfully simulated around both flat plates and the tested flowmeter blades as the results presented in chapter 5. The reattachment length of the separation bubble is found to depend on the leading edge shape and on the inlet flow incidence angle. In the simulation of the flows around the tested flowmeter blades, the simulated separation bubbles lengths show little variation with the blade geometrical variations from the hub to the tip, but large variation with the flow incidence angle. The simulated reattachment length is in agreement with the characteristics of the leading edge flows classified by Ota et al. To calculate the influence of the leading edge separation on the lift and drag acting on the flowmeter blades, a new simple method is developed from the model proposed by Lewis for blade design using the constant static pressure boundary condition around the separation bubble. Using this model, the displacement effect of the leading edge separation bubble is quite accurately simulated for the flowmeter blades.

—— Lift and drag prediction

Combining the wake simulation and the leading edge flow simulation models, the flow around turbine flowmeter blades can be calculated. In the calculations, the lift and drag characteristics of the flowmeter blades can be obtained. Generally speaking, the leading edge separation causes lift reduction and increased drag on the flowmeter blades. The change of the separation bubble with Reynolds number is included in the model by considering the shear flow outside the separation bubble. The results given in chapter 5 show that the separation bubbles are small and close to the blade surfaces due to the strong viscous effect for flows with small Reynolds numbers and they become larger when the Reynolds number is increased. The predicted shape of the separation bubbles is changing with flow Reynolds number, though the reattachment length stays constant when Re_b is over 200. The lift and drag for the flows with Re_b below 200 is obtained by linear interpolation from the obtained results.

9.2.2 Flowmeter Performance Prediction

—— Inlet velocity profile

The velocity profiles inside the annulus between the pipe wall and the hub surface change with Reynolds number and the hub geometry. For the tested flowmeter, when there is no swirl in the inlet flow, the inlet velocity profiles can be approximately predicted using the panel model presented in chapter 6. It can be seen from the inlet velocity comparison presented in chapter 8 that the panel model gives quite satisfactory results. The agreement becomes better as the flowrate increases. However, the boundary layer on the pipe wall is not very accurately calculated with the presence of the flowmeter. The boundary layer on the flowmeter hub surface is assumed thin, the prediction would not be very accurate at small Reynolds numbers. The developed panel method is only suitable for the cases without inlet swirl.

—— Performance prediction

The numerical model developed for flowmeter performance prediction is quite successfully applied to the tested cases with or without

inlet swirl so long as the inlet velocity profile is known.

In case A, a complete performance curve of the tested flowmeter is predicted and compared with the experimental results. Only one percent difference is present in the linear operating range. This agreement proves the accuracy of the prediction model.

Using the performance prediction model, the performance changes with tip clearance are also predicted in case A. A performance curve shift is found by changing the tip clearance size.

Using the measured inlet velocity profiles, the predicted flowmeter coefficients vary in the tested cases. In case B, C and D, relative accuracy is within 3.5 percent of the measured coefficients from flowrate Q2 to Q6, and within 4.23 percent in case E. Generally speaking, the predicting error increases as the flowrate becomes small. The following factors surely have contributed to this difference.

(a) The boundary layers on the annulus surfaces. These make the flowmeter inlet velocity profile non-uniform and cause large flow incidence angle in the boundary layer areas. Consequently, the leading edge separation bubble causes a reduction in lift force and an increase in drag.

(b) Tip leakage flow. The tip leakage flow in the tip clearance distorts the pressure distribution in the tip area and then reduces the driving torque.

(c) Bearing friction. At small flowrates, the pressurised fluid film inside the flowmeter bearing becomes very thin and the lubrication is in boundary state, the assumed linear change of the mechanical friction coefficient is only an approximation.

(d) Lift coefficient. When flow Re_b is below 200, the separation and reattachment flows become laminar separation and laminar reattachment, the reattachment length increases quickly as the Reynolds number decreases. The leading edge separation is then not accurately simulated and the interpolated blade characteristics must contain a certain level of errors.

9.2.3 Experimental Study

From the measurement of the flow fields throughout the flowmeter

rotor, a clear understanding of the flow development inside the flowmeter is obtained and the results are also used to validate the numerical model.

The position of the inlet section is chosen to be that on which the combined disturbance from both the flowmeter hub head and the flowmeter rotor is at its minimum. The measured velocity profiles on the inlet section are compared with the profiles predicted by the panel method in case A and are used for the flowmeter performance prediction in all the test cases at the tested flowrates.

Throughout the flowmeter rotor, the interaction between the fluid and the flowmeter rotor could have caused a slight radial flow, so that the axial velocity distributions are slightly different before and after the flowmeter rotor. Even so, the two dimensional assumption should be still quite accurate because the difference is quite small. The measured circumferential velocity profiles are much flatter compared with the predicted profiles.

9.3 Future work

9.3.1 Numerical Model

—Vortex model

The vortex model used in this research is an inviscid potential flow model, both the vortex panels and the point vortices employed in this research work remain constant in both shape and vorticity after their shedding. As a matter of fact, they would decay in vorticity and change in shape in real flows due to viscosity. The change in vorticity and shape can be quite important in the lift and drag simulations in some cases, so a vortex model with viscosity consideration is required for the higher accuracy of the predicted lift and drag. The introduction of viscosity effect in the vortex model makes not only the predicted results more accurate at large flowrates, it also allow the developed model to be applied at small flowrates.

—— Boundary layers

The boundary layer after the separation bubble on blade surface certainly increases the drag on the flowmeter blades, especially at small Reynolds numbers. To introduce the boundary layer on the blade surfaces, the difficulty is the accurate determination of the boundary layer parameters at the reattachment point. However, the inclusion of the boundary layers can improve the accuracy of the predicted blade lift and drag characteristics.

——Inlet velocity profile

To obtain a turbine flowmeter performance curve using the performance prediction model, the inlet velocity profile is needed. In this research, a simple source ring model is introduced to predict the inlet velocity profiles for flows without inlet swirl. Because turbine flowmeters may be applied in various situations with quite different inlet flow conditions, an inlet velocity predicting method for more general flow conditions is strongly suggested so that the flowmeter performance prediction model developed in this research can be extended to more general cases.

—Tip clearance model

It is clear that the tip clearance size directly influences the flowmeter performance. Because of the tip clearance, the pressure distribution on the rotor tip is distorted. The tip clearance model used in this research only considers the viscous resistance in the tip clearance. When the tip clearance is large, the change of lift caused by it would greatly effect the flowmeter performance. A more accurate tip clearance model is therefore necessary.

— Interaction between stator and rotor

In many turbine flowmeters, there is an upstream stator. No doubt, this stator generates its influence on the meter performance. The direct interaction between the stator and the rotor and the interaction between the wake flow of the stator with the rotor exist. The development of the wake flow inside the rotor could be simulated using the wake model developed in this research. Consequently, its influence on the lift and drag could be obtained. The direct interaction between the stator and the rotor can be predicted by the

potential model presented in chapter 3.

9.3.2 Experimental Investigation

— Leading edge flow

Since the blade leading edge flow is very much dependent on the Reynolds number and has a great influence on the lift and the drag on the flowmeter blade, so it might contributes a lot to the nonlinearity of the flowmeter performance at small flowrates. Further investigation of the leading edge flow could help to improve the leading edge flow simulation, and hence the accuracy of the predicted lift and drag characteristics of the flowmeter blades at small flowrates. This may also help to improve the design of turbine flowmeters.

—Trailing edge flow

In the experiment, a jump in the circumferential velocity is detected at the blade trailing edge. Near the trailing edge, flow mixing must occur due to the separated flows from both the upper surface and the lower surfaces. A good understanding of the trailing edge flow may help to design turbine flowmeters with good linearity and stability.

——Upstream stator influence

To examine the interaction between the rotor and stator, more accurate apparatuses are needed for measuring the instantaneous rotor speed corresponding to stator wake flow. Then an optimised design of the upstream stator and a best choice of the distance between stator and rotor might be found.

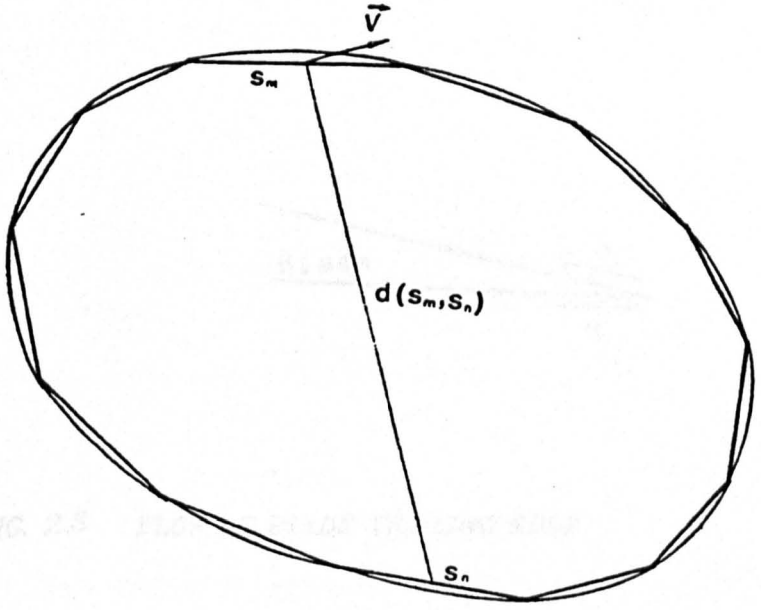

FIG. 2.1 DISCRETIZATION OF TWO DIMENSIONAL CONTOUR

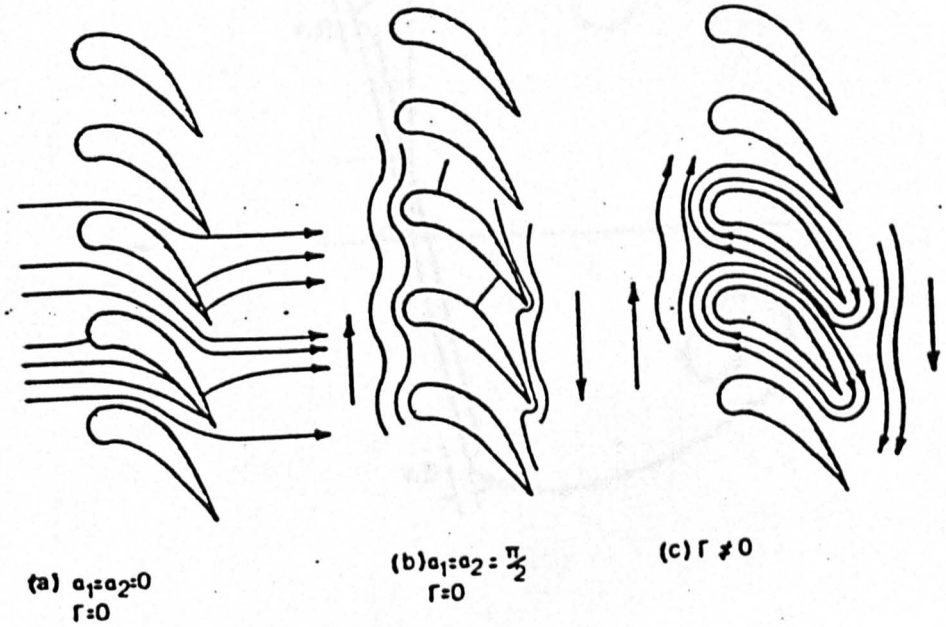

FIG. 2.2 MARTENSEN'S BASIC FLOWS

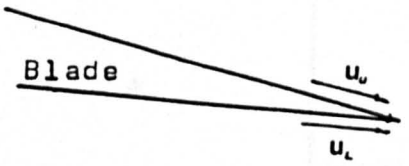

FIG. 2.3 FLOW AT BLADE TRAILING EDGE

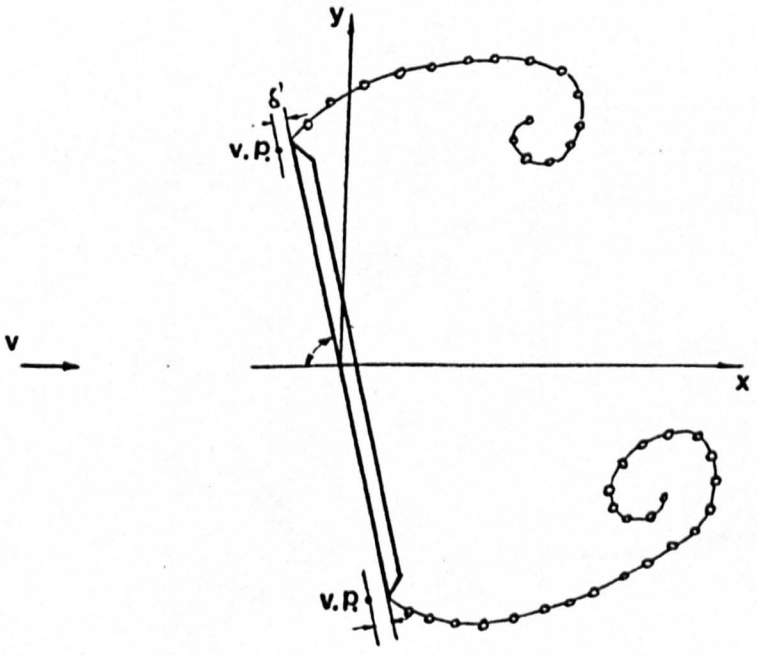

FIG. 2.4 KIYA ET AL SEPARATION MODEL

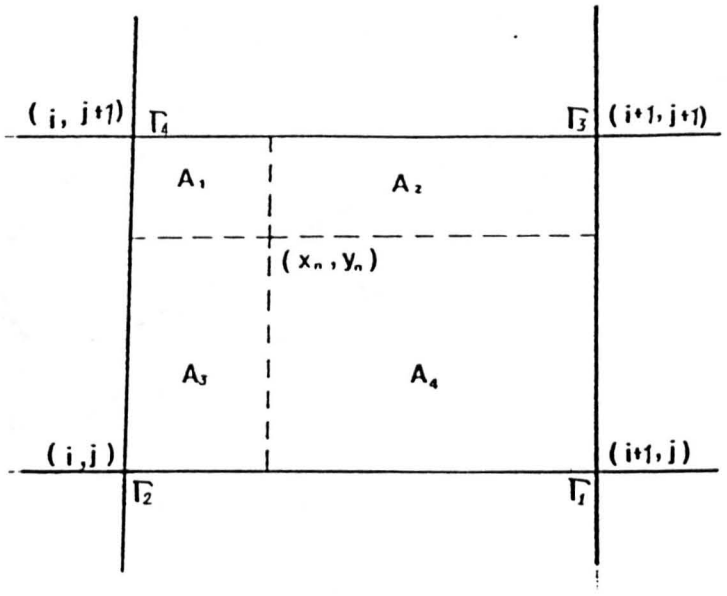

FIG. 2.5 AREA WEIGHT SCHEME FOR VORTEX–IN–CELL METHOD

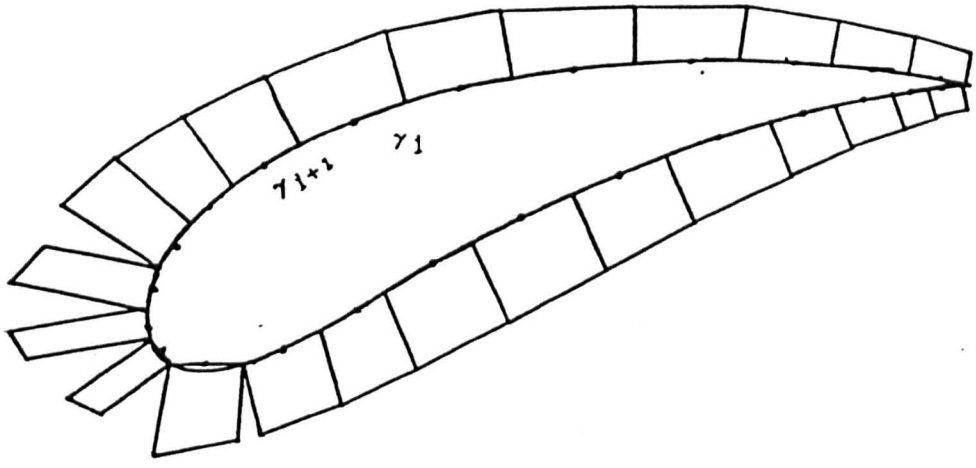

FIG. 3.1 POTENTIAL FLOW MODEL

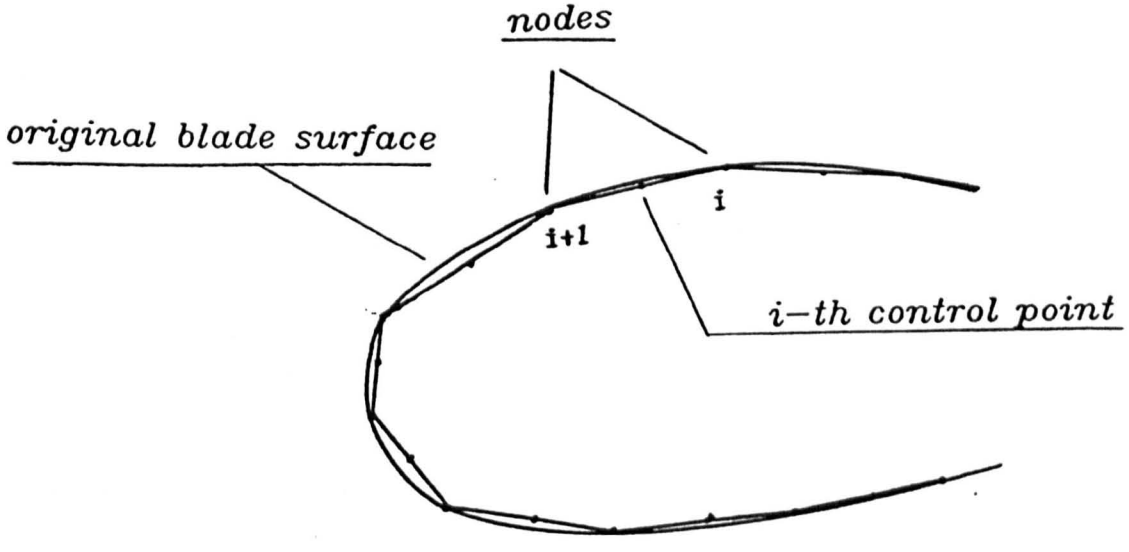

FIG. 3.2 BLADE SURFACE ELEMENT GEOMETRY

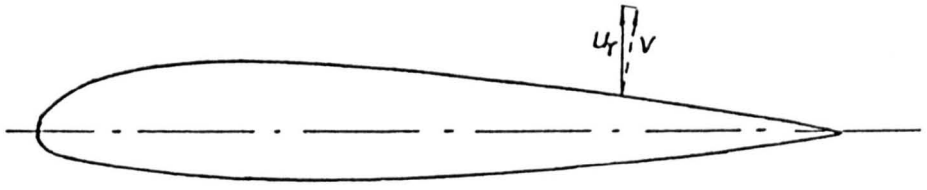

FIG. 3.3 VELOCITY ON MOVING BLADE SURFACE

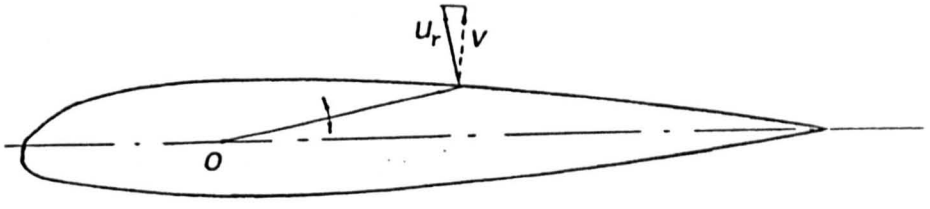

FIG. 3.4 VELOCITY ON OSCILLATING BLADE SURFACE

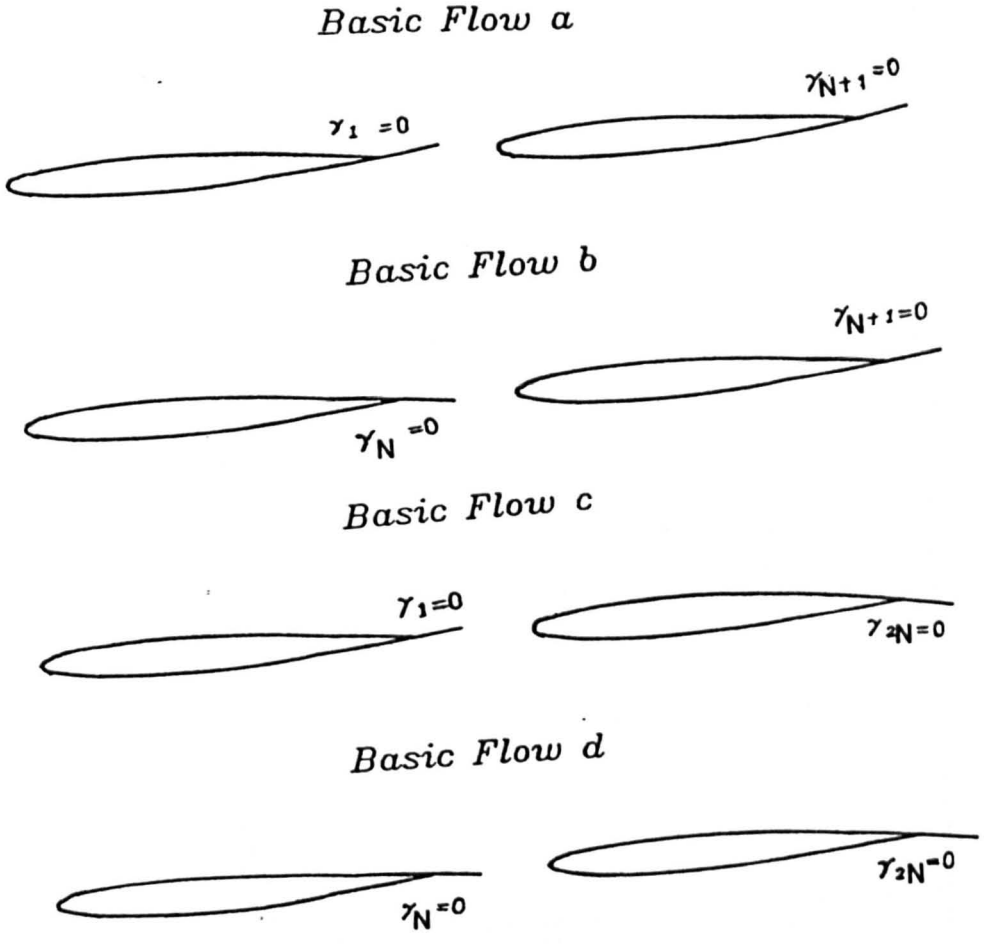

FIG. 3.5 BASIC FLOWS

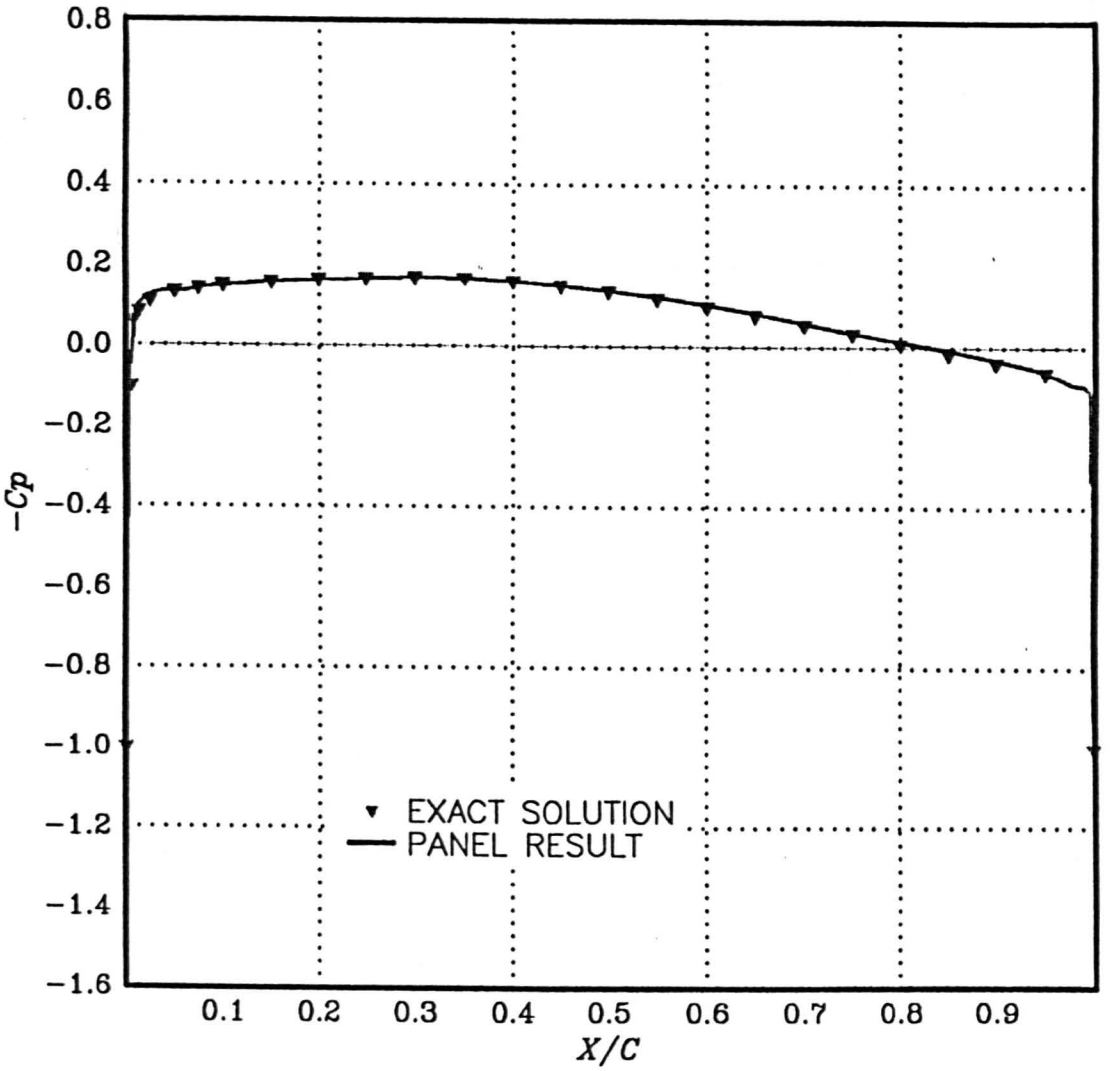

FIG. 3.6 COMPARISON OF PRESSURE DISTRIBUTION ON AIRFOIL NACA A006 WITH ZERO INCIDENCE

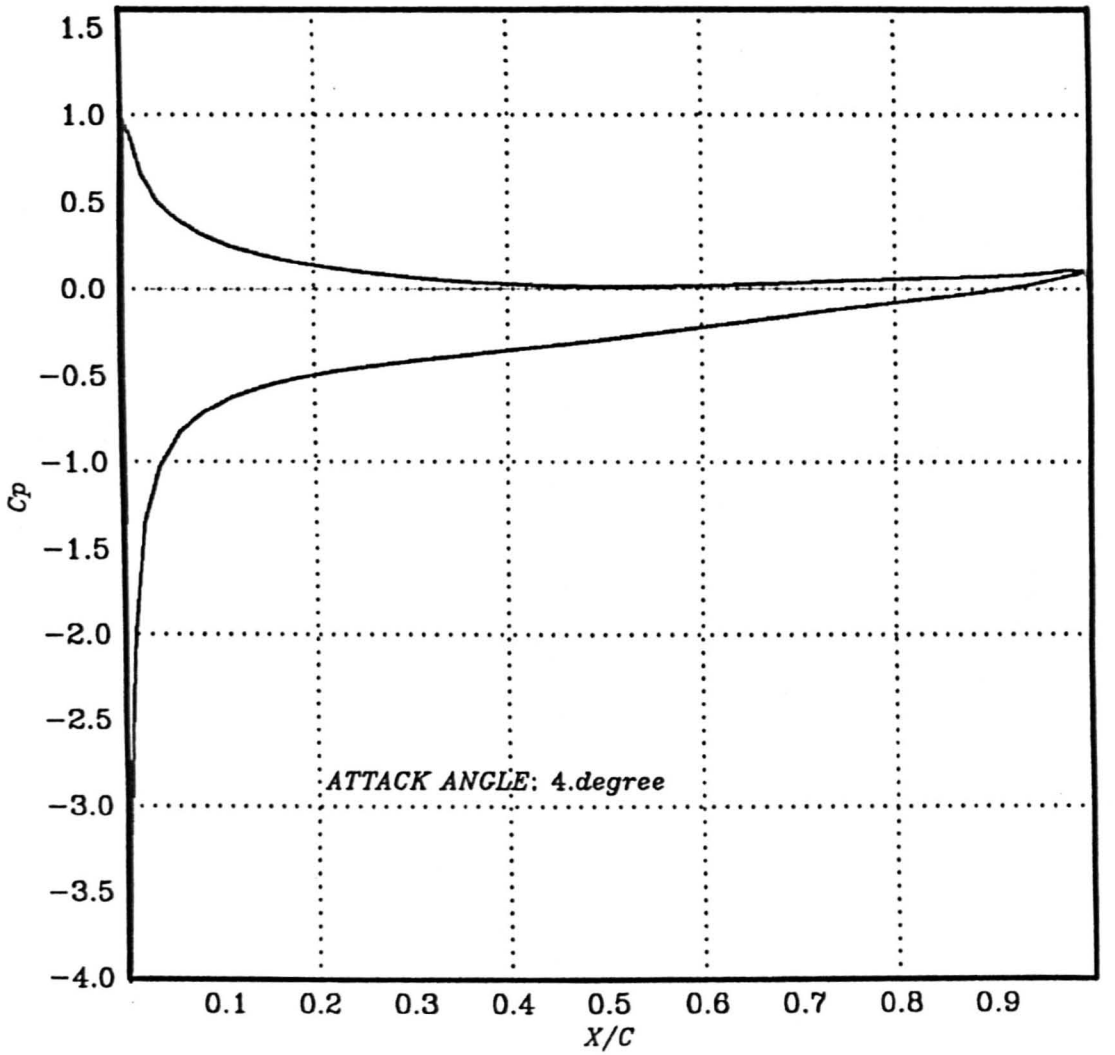

FIG. 3.7 PRESSURE DISTRIBUTION ON AIRFOIL NACA A006 WITH 4 deg. INCIDENCE

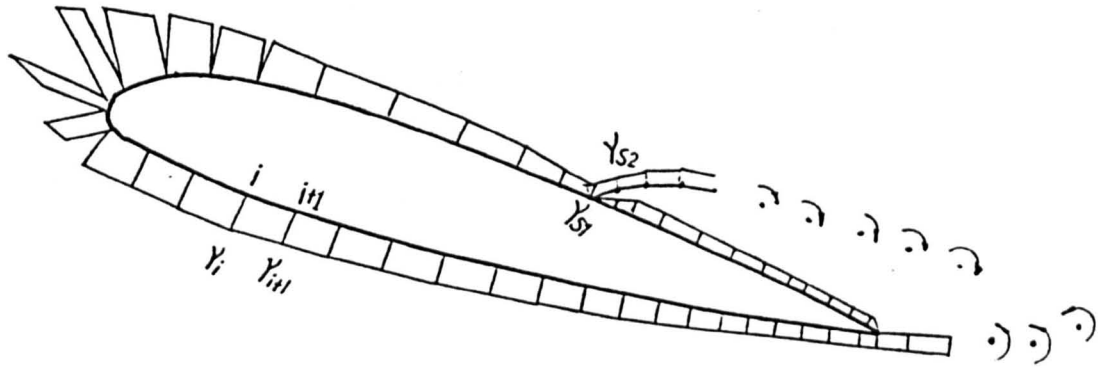

FIG 4.1 POTENTIAL FLOW SEPARATION MODEL

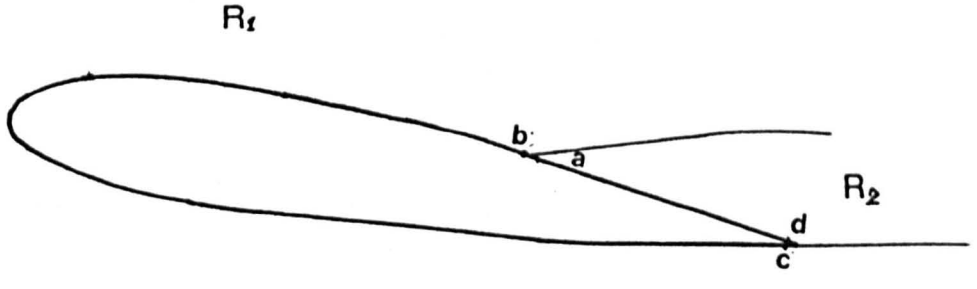

FIG 4.2 POTENTIAL SCHEME OF THE SEPARATED FLOW

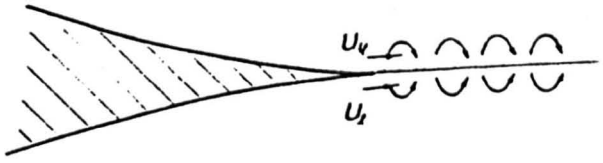

FIG. 4.3 CUSP TRAILING EDGE FLOW

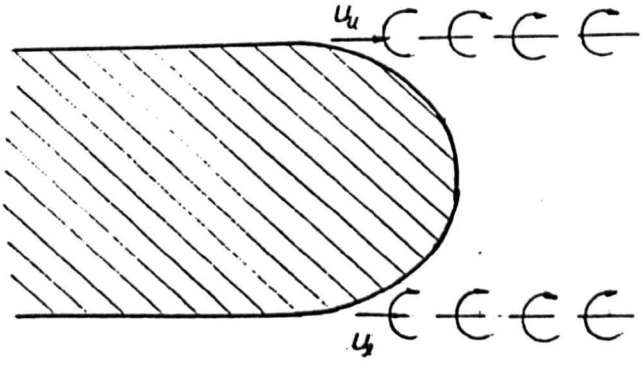

FIG. 4.4 BLUNT TRAILING EDGE FLOW

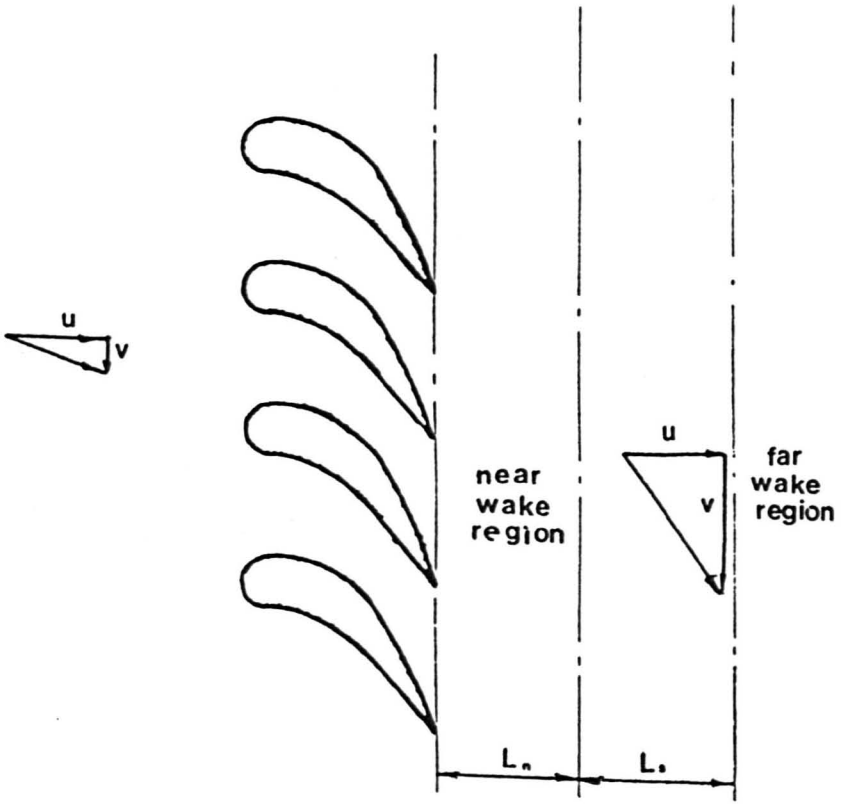

FIG. 4.5 CASCADE WAKE APPROXIMATION

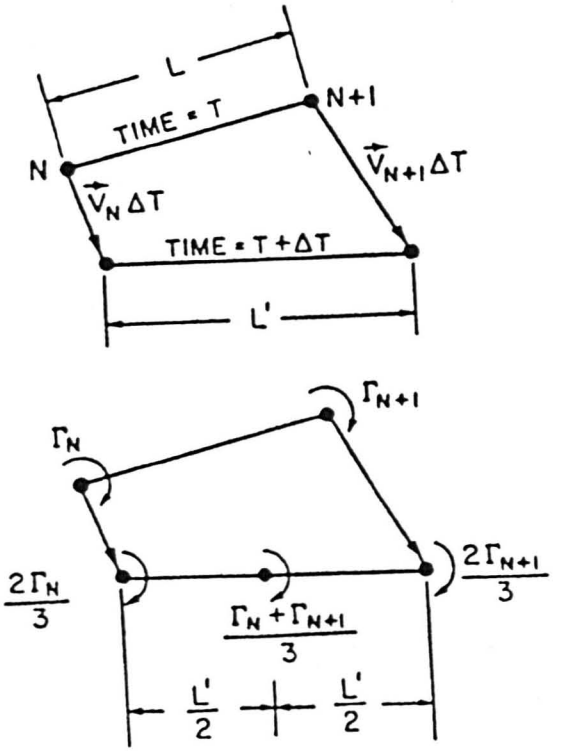

FIG. 4.6 VORTEX SPLITING MODEL

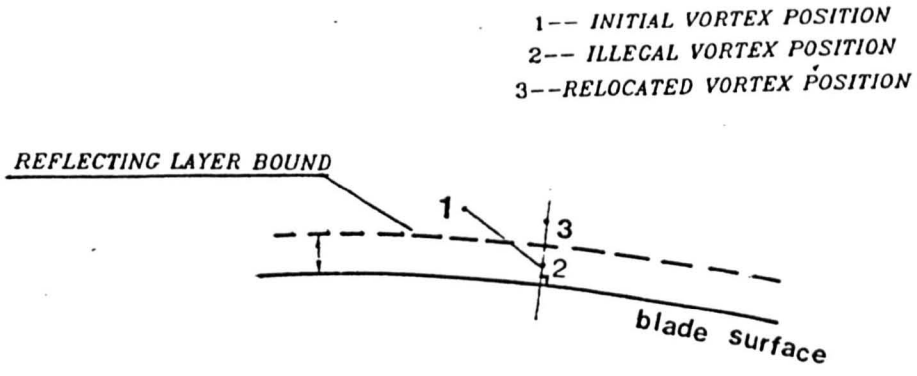

FIG. 4.7 VORTEX REFLACTION ON BLADE SURFACE

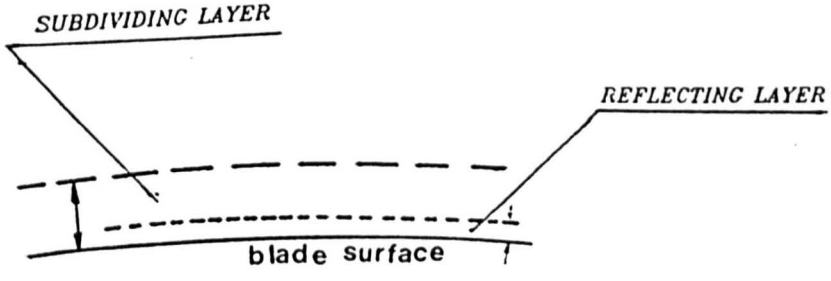

FIG. 4.8 VORTEX MOTION NEAR BLADE SURFACE

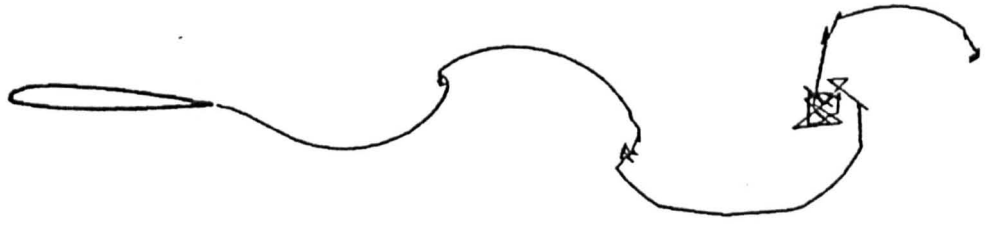

FIG. 4.9 WAKE VORTEX CONFIGURATION

$\alpha^{\circ} = 6SIN(3.14t)$

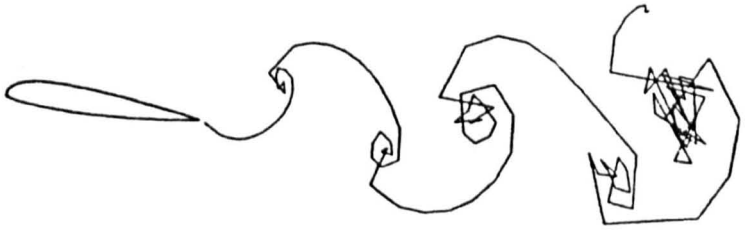

FIG. 4.10 WAKE VORTEX CONFIGURATION

$\alpha^{\circ} = 6sin(6.28t)$

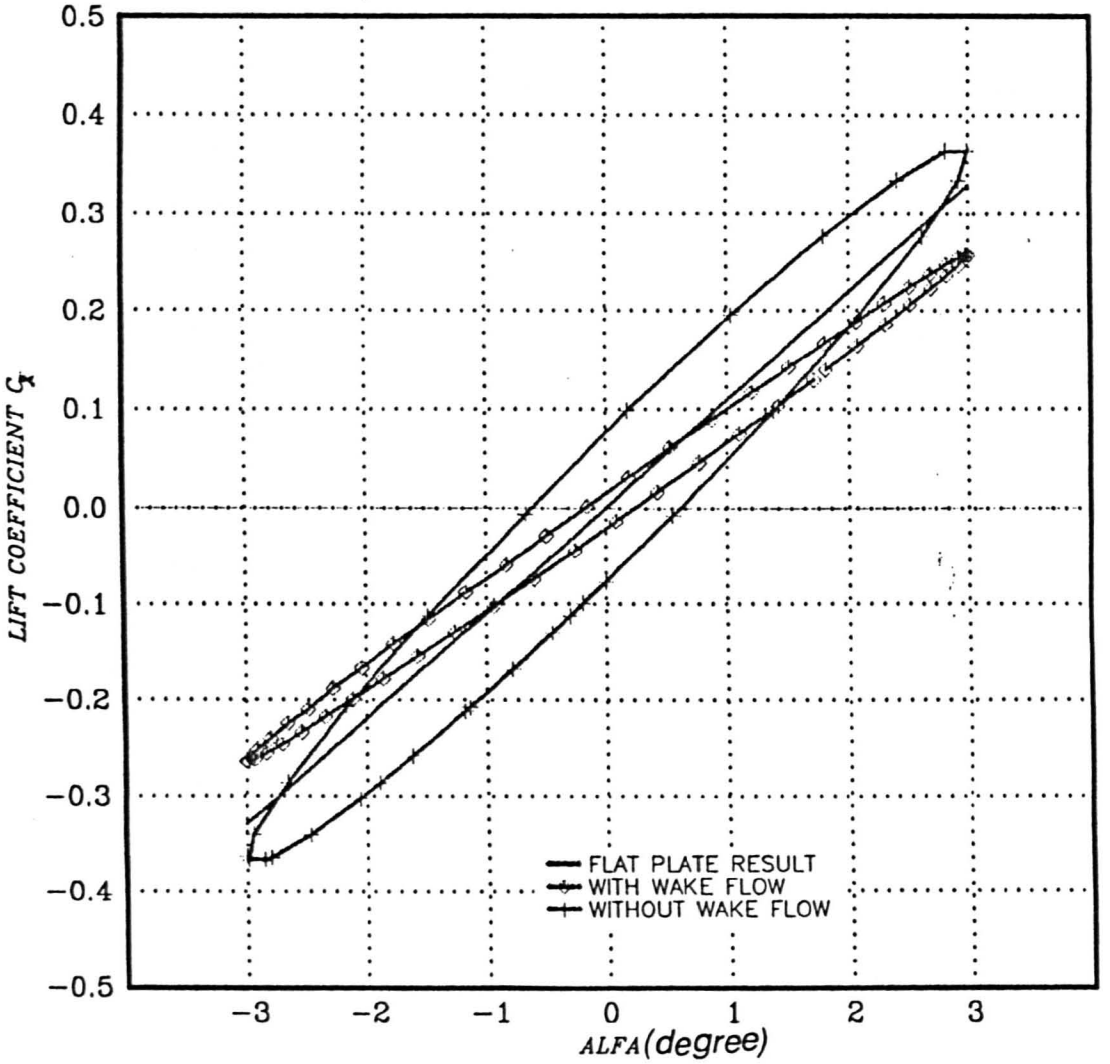

FIG 4.11 THEORETICAL LIFT ON AN OSCILATION AIRFOIL NACA0012

($ALFA = 3SIN(WT)$, $W=0.4$)

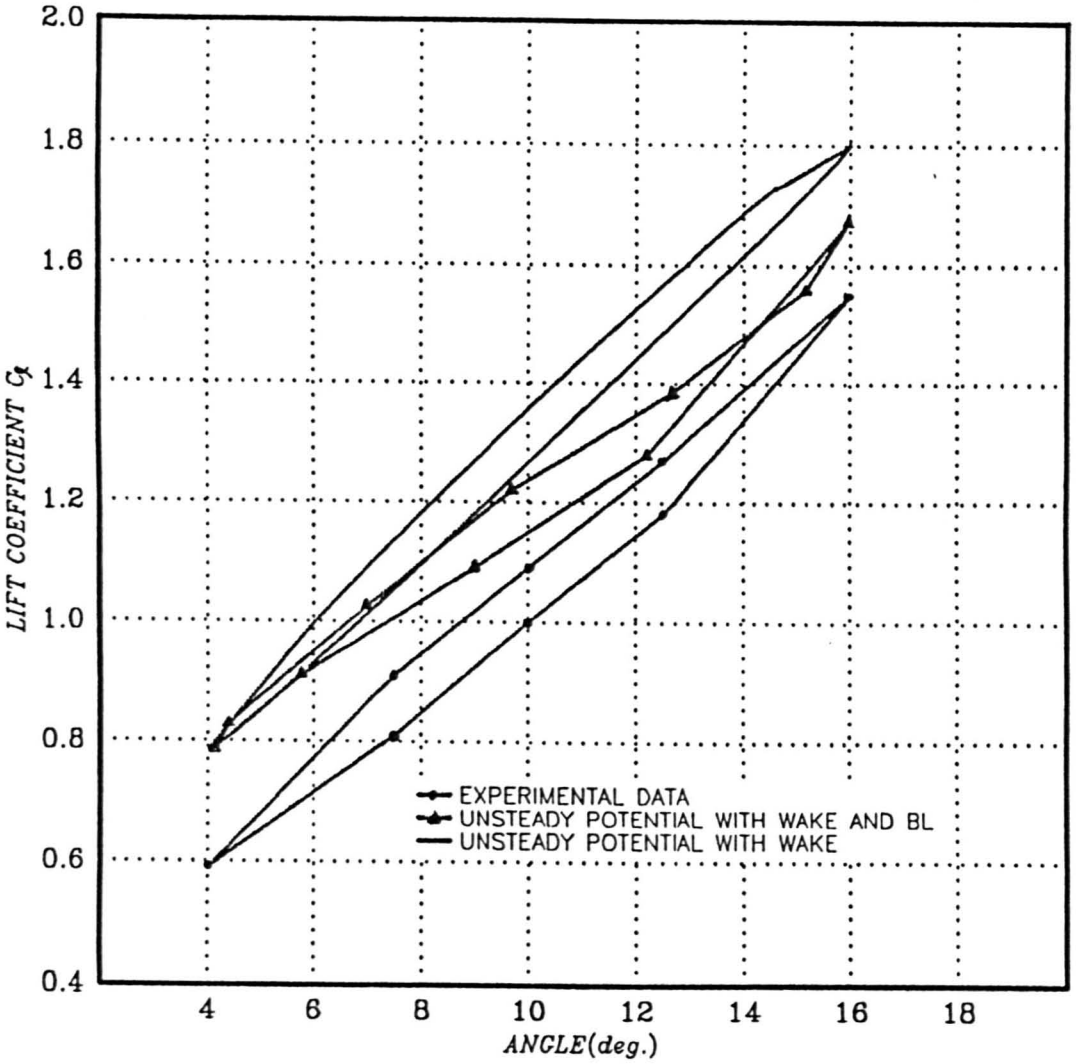

FIG. 4.12 LIFT FOR OSCILATION ABOUT 1/4 AIRFOIL NACA 23012

(α =10+6*SIN*(0.4*t*), *Reynolds Number*: 1e+6)

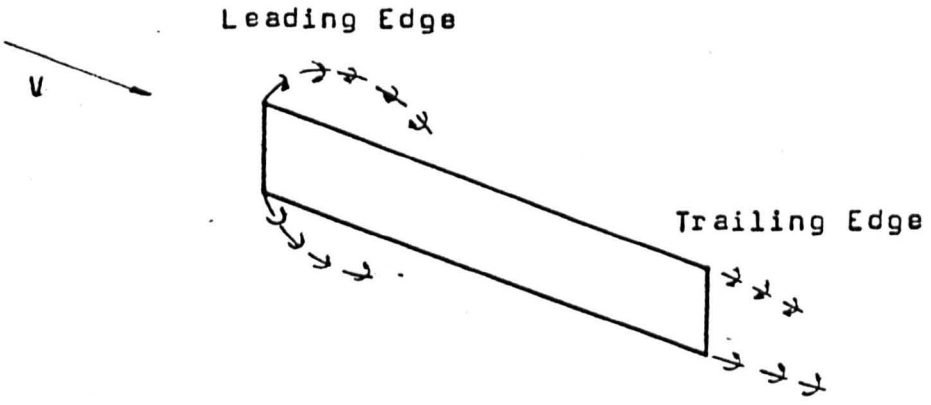

FIG.5.1 FLOW AROUND A TURBINE FLOWMETER BLADE

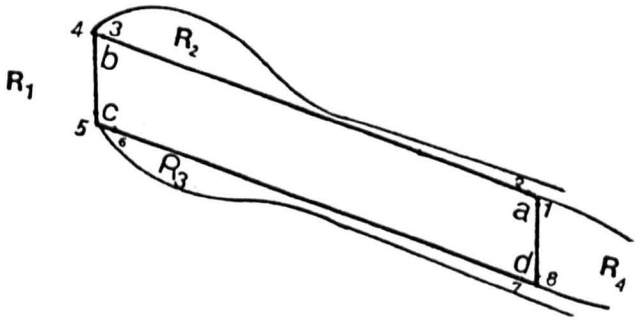

FIG.5.2 POTENTIAL SCHEME OF THE FLOW AROUND A FLOWMETER BLADE

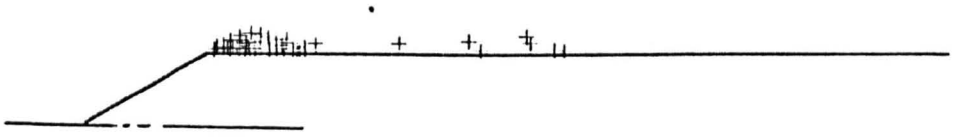

(a) *Half Leading Edge Apex Angle(deg): 30.0*

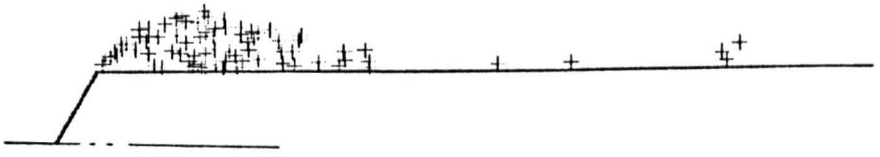

(b) *Half Leading Edge Apex Angle(deg.): 60.0*

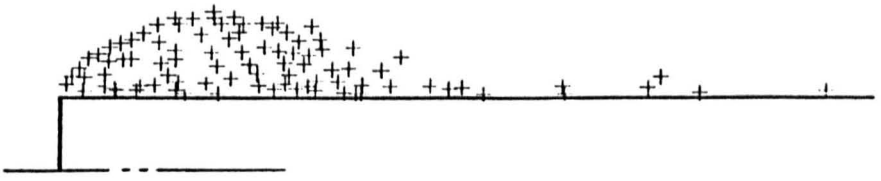

(c) *Half Leading Edge Apex Angle(deg.): 90.0*

FIG.5.3 SIMULATED FLAT PLATE LEADING EDGE SEPARATIONS

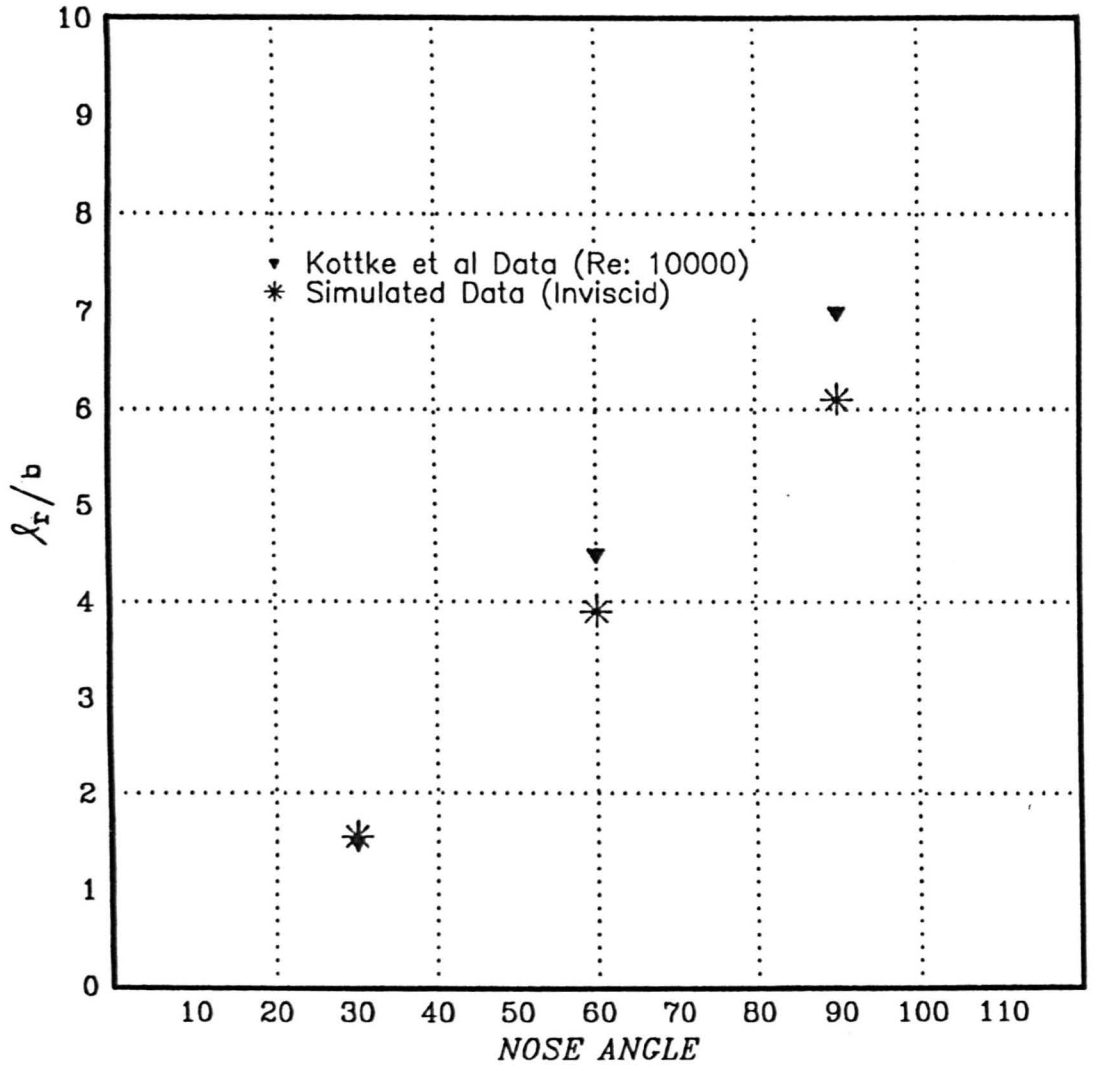

FIG.5.4 LEADING EDGE REATTACHMENT LENGTH COMPARISON BETWEEN THE PREDICTED AND Kottke's EXPERIMENTAL DATA

Hub Section

Zero Incidence Angle

Time Step: 0.0008

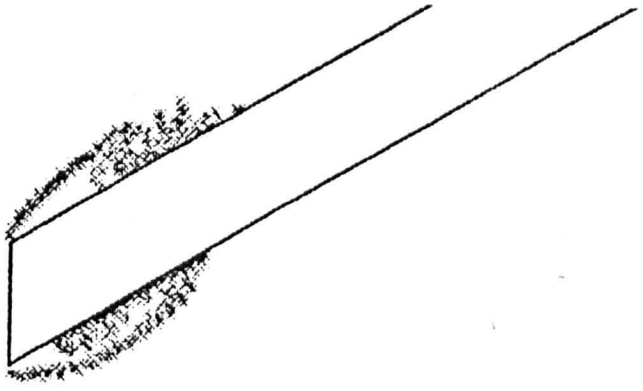

Midspan Section

Zero Incidence Angle

Time Step: 0.0008

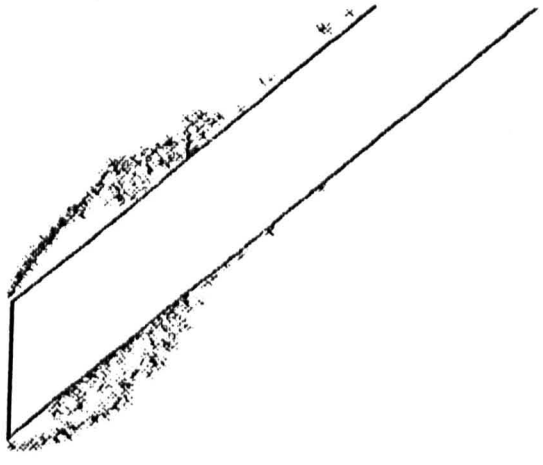

Tip Section

Zero Incidence Angle

Time Step: 0.0008

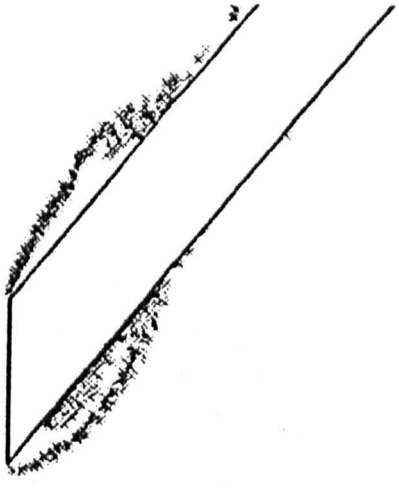

FIG.5.5 SIMULATED LEADING EDGE FLOWS AROUND FLOWMETER BLADES

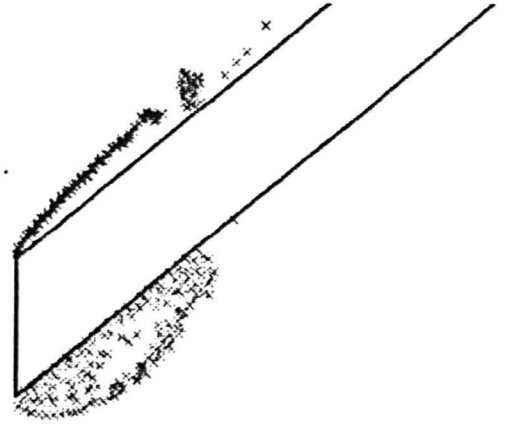

(a) *Incidence Angle(deg.): −8.0*

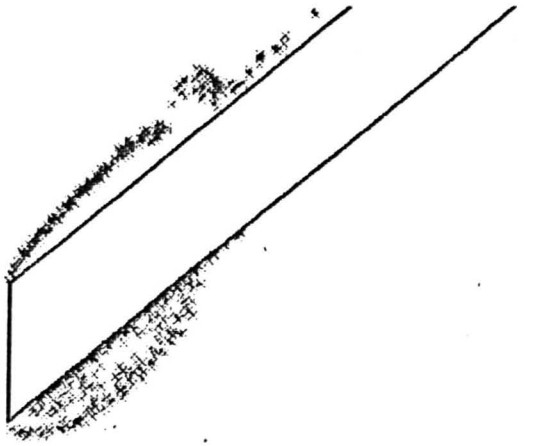

(b) *Incidence Angle(deg.): −4.0*

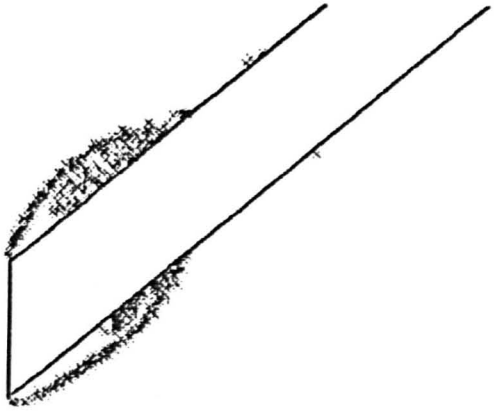

(c) *Incidence Angle(deg): 4.0*

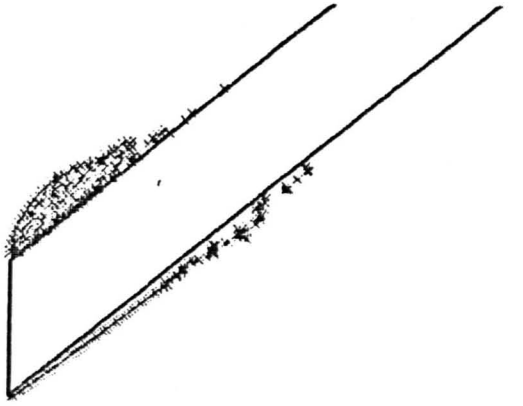

(d) *Incidence Angle(deg.): 8.0*

FIG.5.6 SIMULATED LEADING EDGE FLOWS AROUND THE MIDSPAN BLADE UNDER DIFFERENT INCIDENCE ANGLES

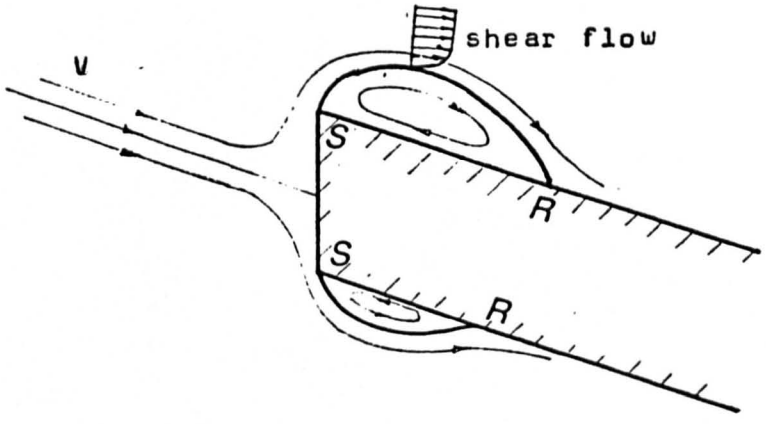

FIG.5.7 MODEL FOR THE SEPARATED LEADING EDGE FLOW

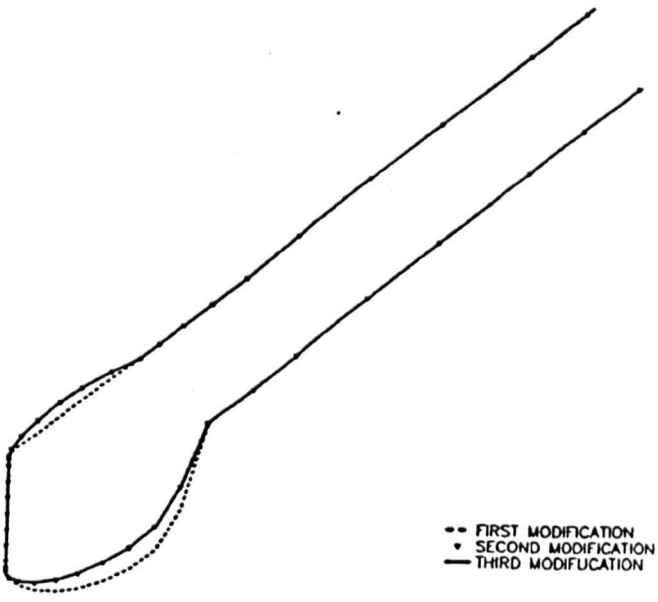

FIG. 5.8 BLADE LEADING EDGE MODIFICATION
Midspan section, Incidence angle(deg.): 0

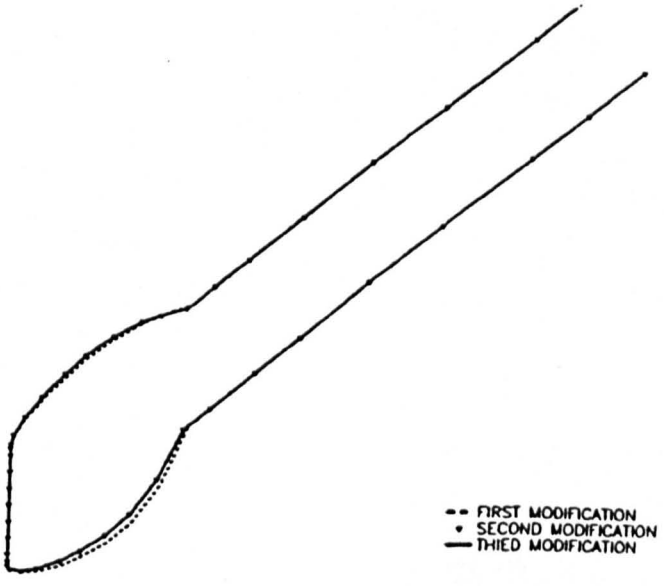

Fig. 5.9 BLADE LEADING EDGE MODIFICATION
Midspan section, Incidence angle(deg.): −8

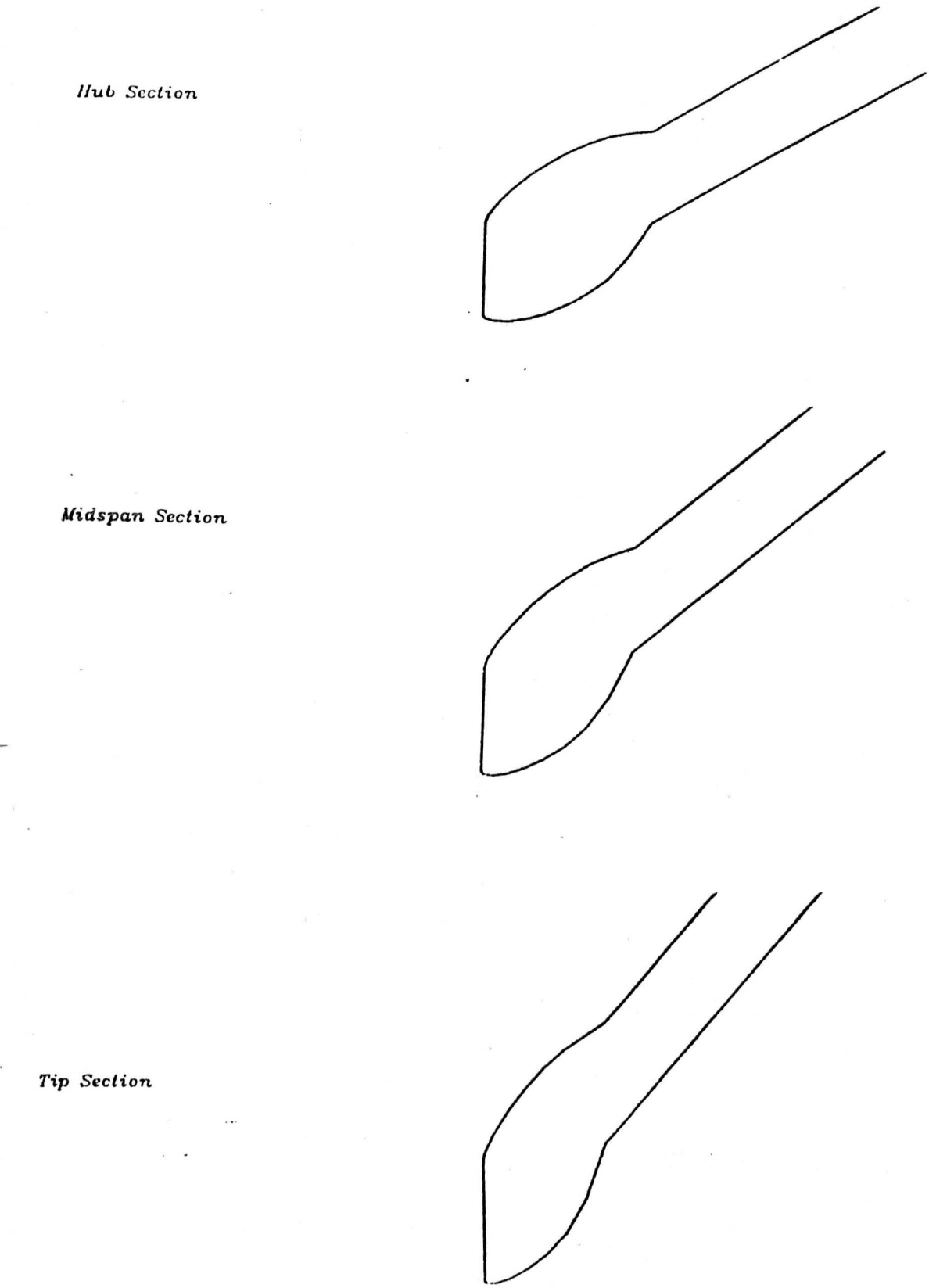

FIG.5.10 MODIFIED BLADE LEADING EDGE SHAPE

Hub Section

Zero Incidence Angle

Time Step: 0.0008

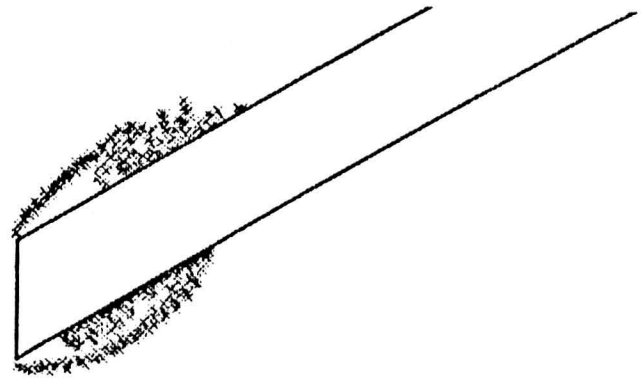

Midspan Section

Zero Incidence Angle

Time Step: 0.0008

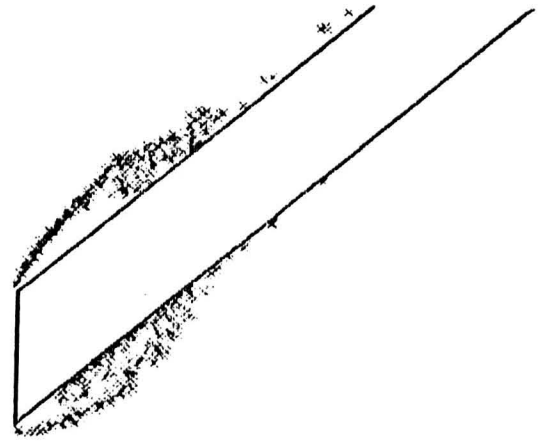

Tip Section

Zero Incidence Angle

Time Step: 0.0008

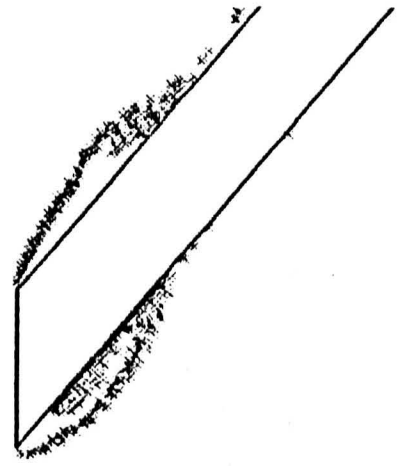

FIG.5.5 SIMULATED LEADING EDGE FLOWS AROUND FLOWMETER BLADES

Hub Section

Hub Section

Zero Incidence Angle

Time Step: 0.0008

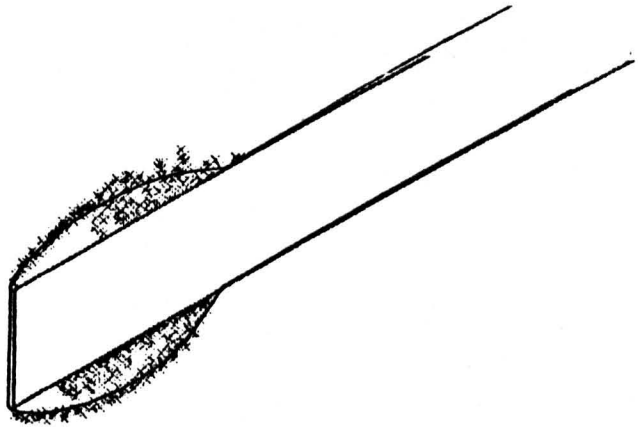

Midspan Section

Midspan Section

Zero Incidence Angle

Time Step: 0.0008

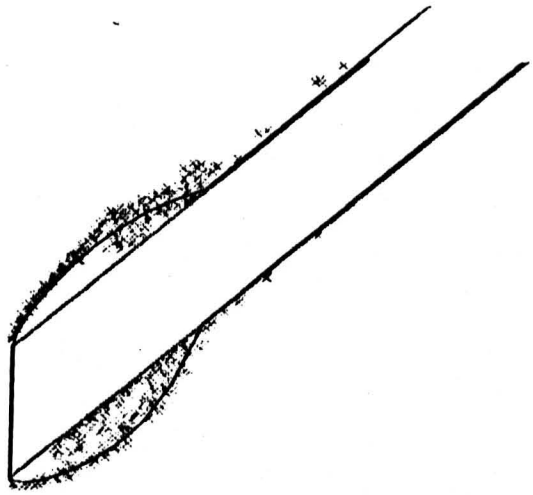

Tip Section

Tip Section

Zero Incidence Angle

Time Step: 0.0008

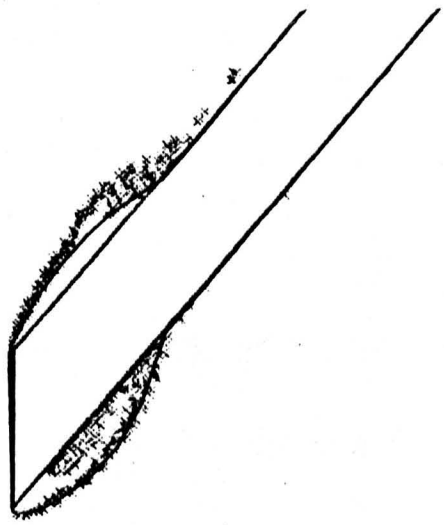

FIG.5.10 MODIFIED BLADE LEADING EDGE SHAPE

FIG.5.5 SIMULATED LEADING EDGE FLOWS AROUND FLOWMETER BLADES

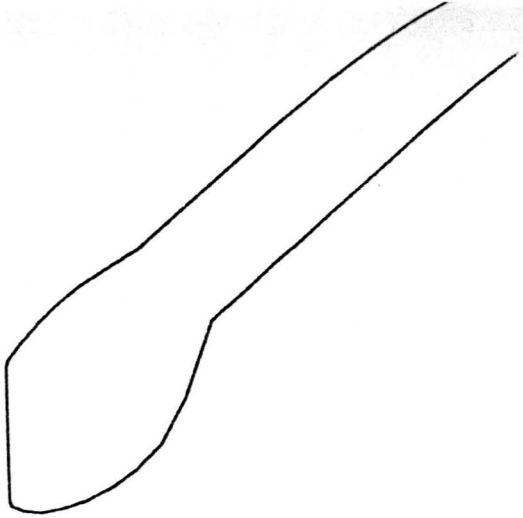

(a) *Incidence Angle(deg.): −8.0*

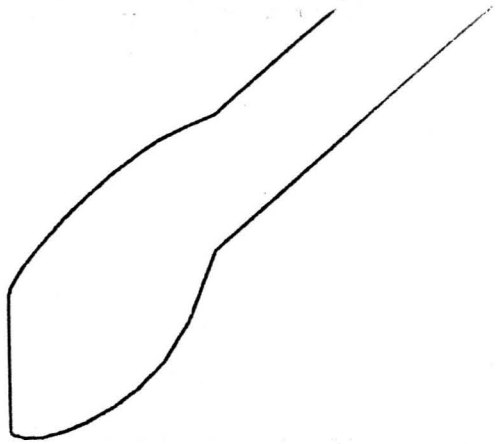

(b) *Incidence Angle(deg.): −4.0*

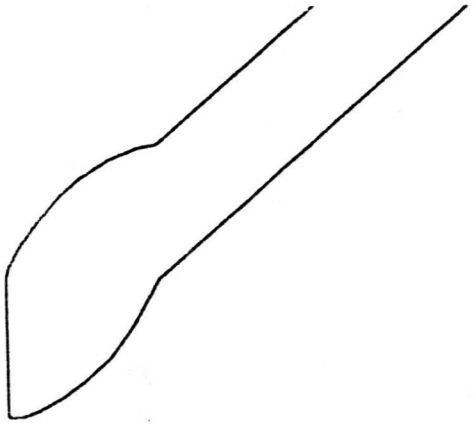

(c) *Incidence Angle(deg): 4.0*

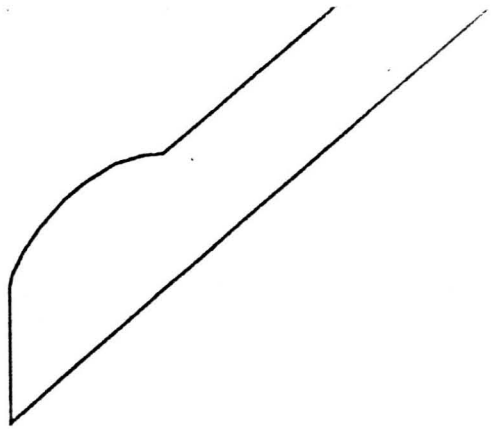

(d) *Incidence Angle(deg.): 8.0*

FIG.5.11 MODIFIED BLADE LEADING EDGE FOR THE MIDSPAN BLADE WITH DIFFERENT INCIDENCE ANGLES

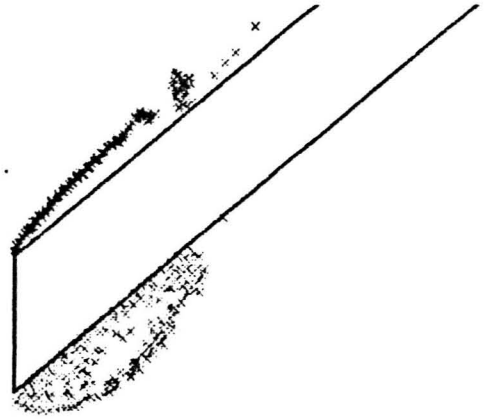

(a) *Incidence Angle(deg.): −8.0*

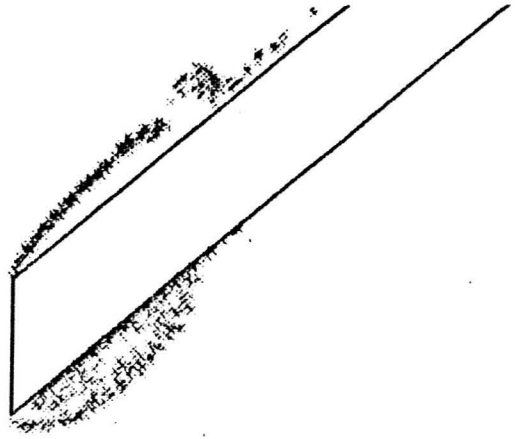

(b) *Incidence Angle(deg.): −4.0*

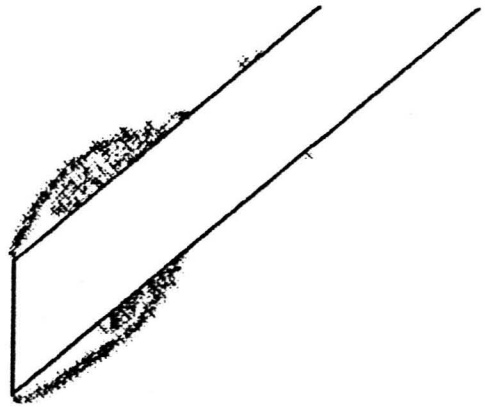

(c) *Incidence Angle(deg): 4.0*

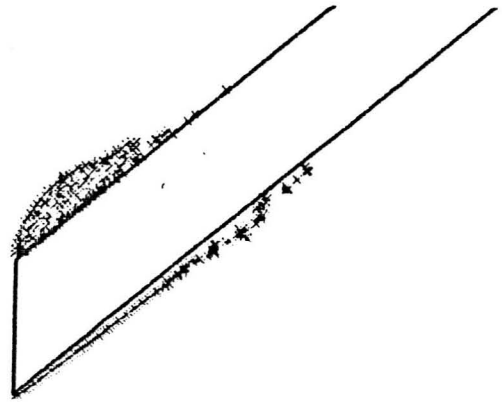

(d) *Incidence Angle(deg.): 8.0*

FIG.5.6 SIMULATED LEADING EDGE FLOWS AROUND THE MIDSPAN BLADE UNDER DIFFERENT INCIDENCE ANGLES

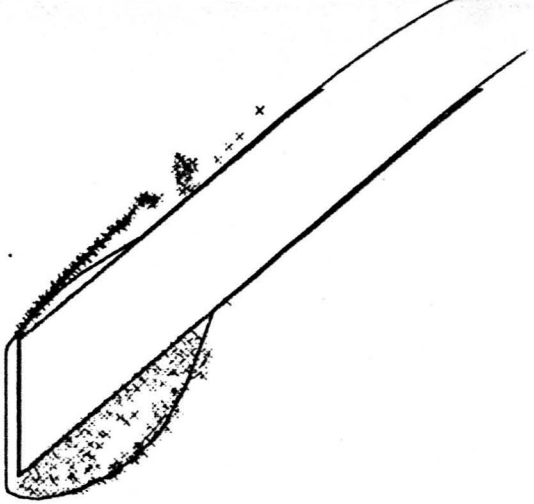

(a) Incidence Angle(deg.): −8.0

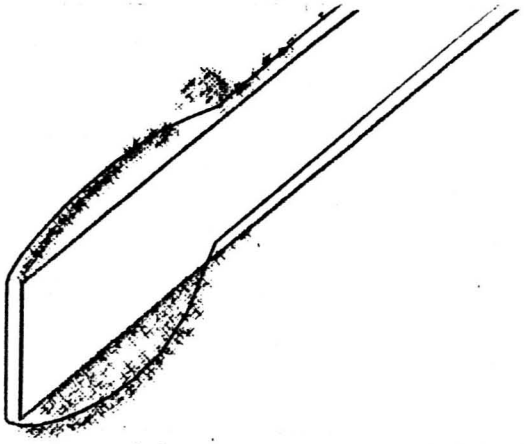

(b) Incidence Angle(deg.): −4.0

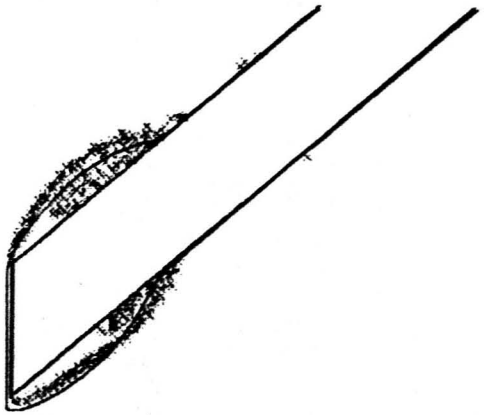

(c) Incidence Angle(deg): 4.0

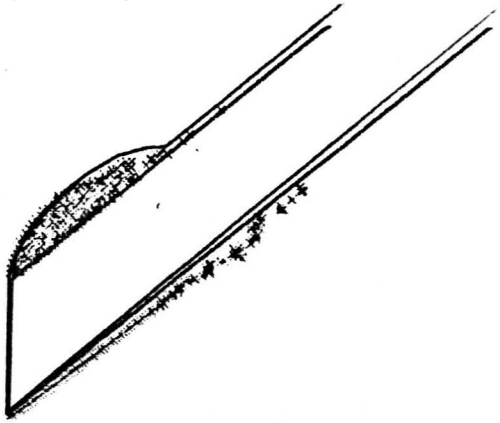

(d) Incidence Angle(deg.): 8.0

FIG.5.6 SIMULATED LEADING EDGE FLOWS AROUND THE MIDSPAN BLADE UNDER DIFFERENT INCIDENCE ANGLES

FIG.5.11 MODIFIED BLADE LEADING EDGE FOR THE MIDSPAN BLADE WITH DIFFERENT INCIDENCE ANGLES

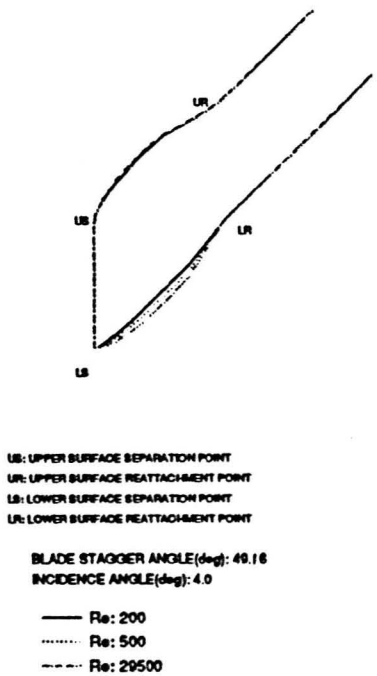

MODIFIED BLADE LEADING EDGE CONTOURS

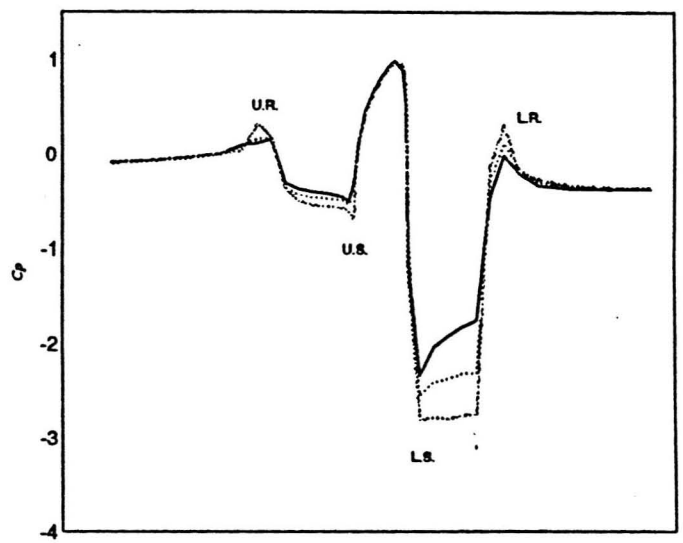

PRESSURE DISTRIBUTION ALONG BLADE LEADING EDGE

FIG.5.12 MODIFIED BLADE LEADING EDGE AND ITS PRESSURE DISTRIBUTION

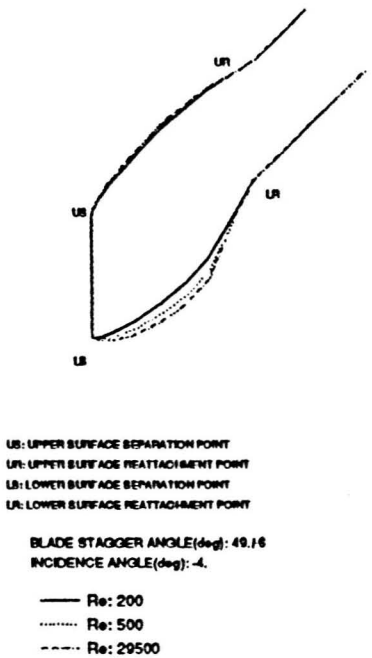

MODIFIED BLADE LEADING EDGE CONTOURS

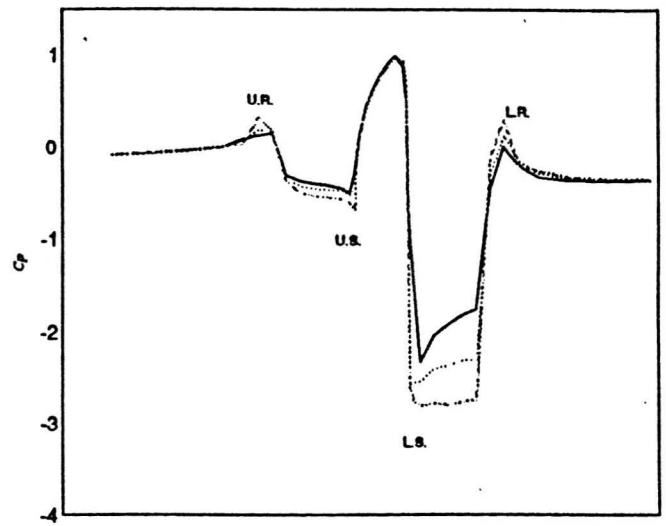

PRESSURE DISTRIBUTION ALONG BLADE LEADING EDGE

FIG.5.13 MODIFIED BLADE LEADING EDGE AND ITS PRESSURE DISTRIBUTION

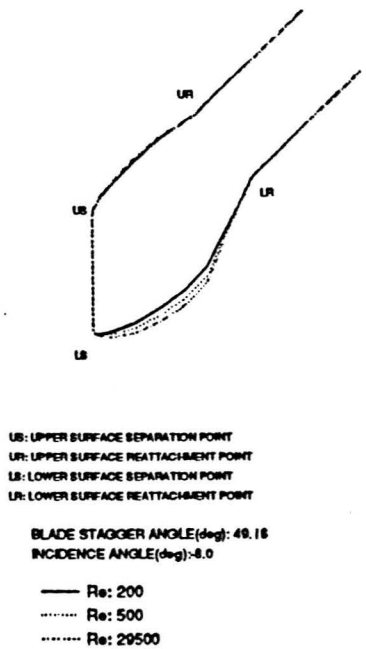

MODIFIED BLADE LEADING EDGE CONTOURS

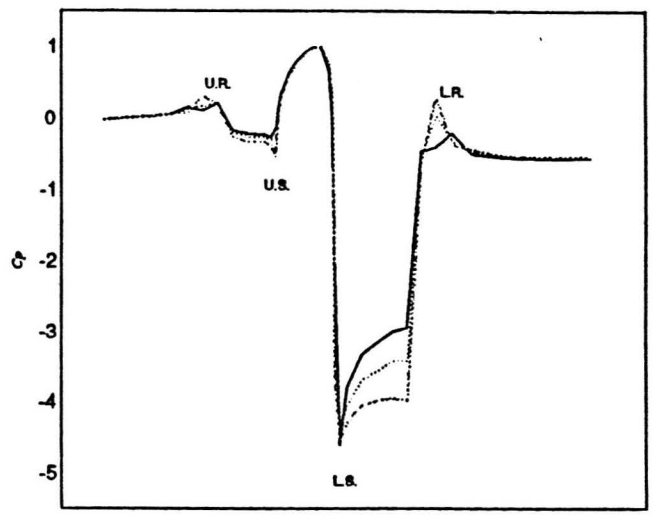

PRESSURE DISTRIBUTION ALONG BLADE LEADING EDGE

FIG.5.14 MODIFIED BLADE LEADING EDGE AND ITS PRESSURE DISTRIBUTION

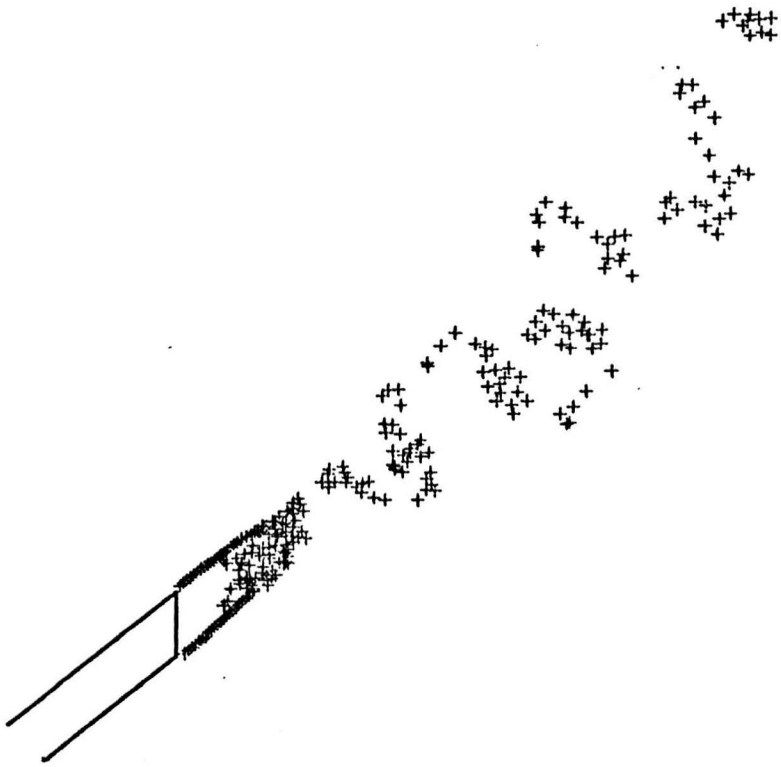

(A) *INCIDENCE ANGLE: −4 degree*

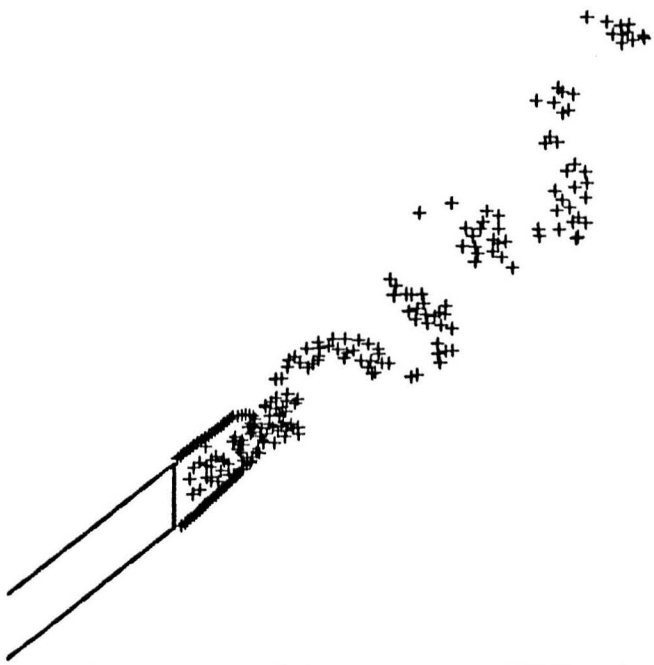

(B) *INCIDENCE ANGLE: 8 degree*

FIG. 5.15 SIMULATED WAKE CONFIGURATIONS FOR MIDSPAN BLADE

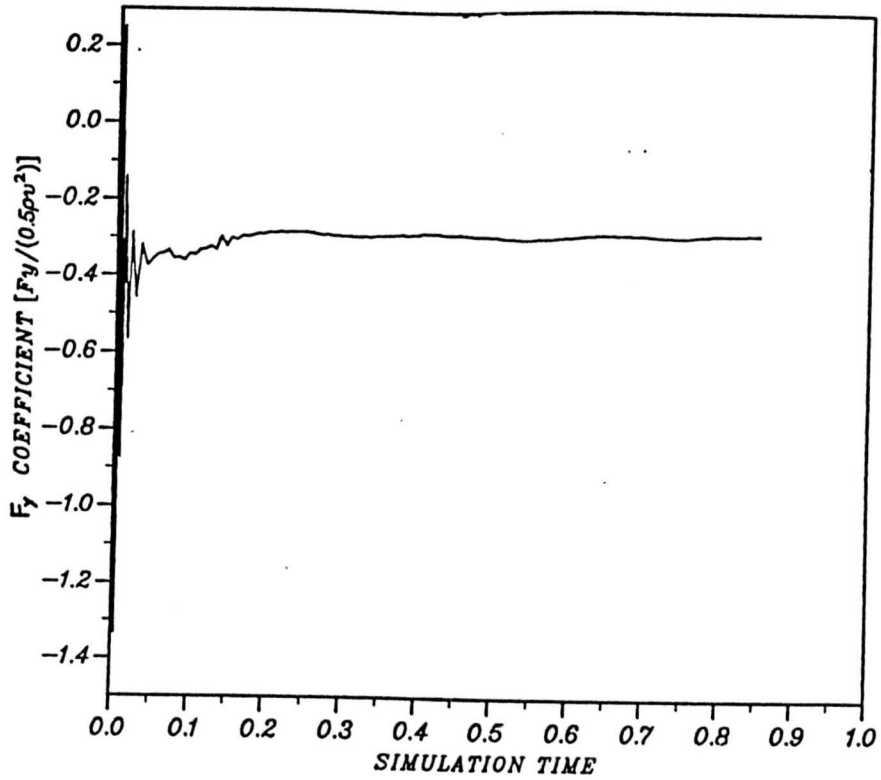

FIG. 5.16 Fy TRANSITION ON FLOWMETER BLADE DURING THE WAKE SIMULATION

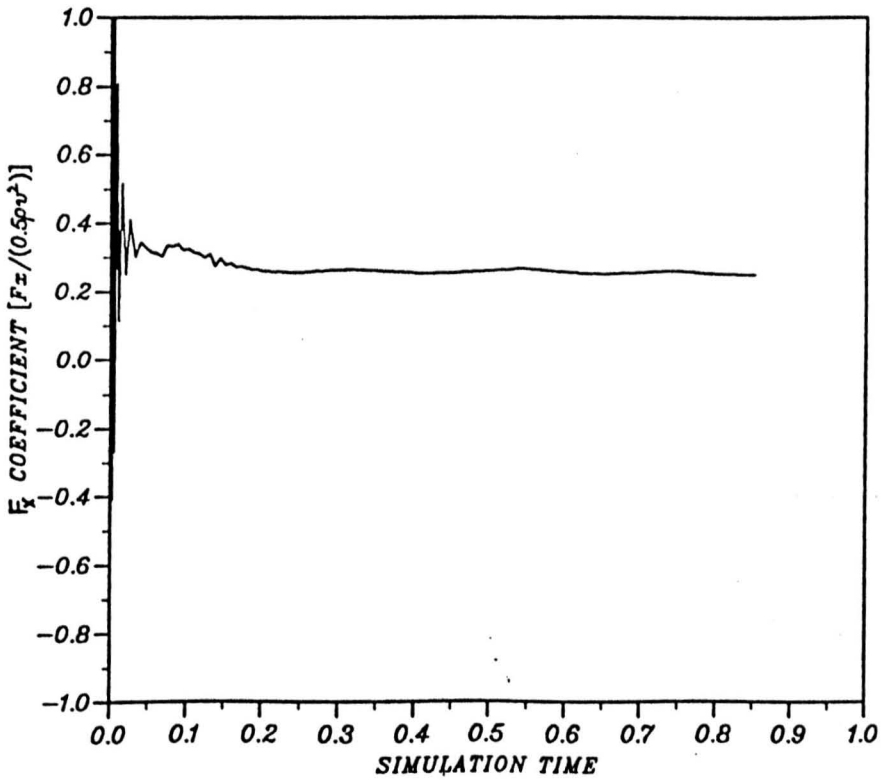

FIG. 5.17 Fx TRANSITION ON FLOWMETER BLADE DURING THE WAKE SIMULATION

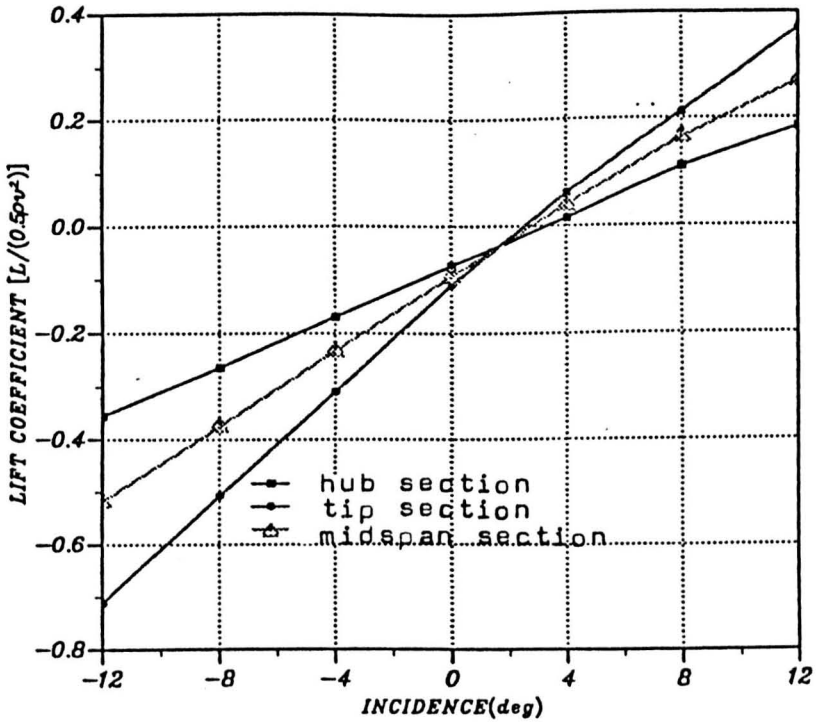

FIG. 5.18 BLADE LIFT VARIATIONS WITH FLOW INCIDENCE AND RADIAL POSITION

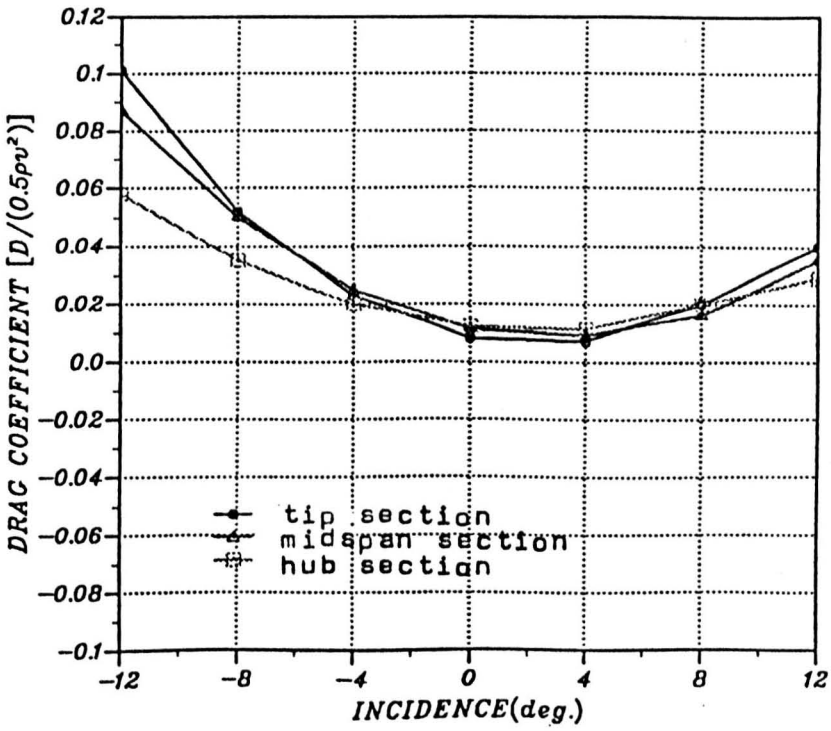

FIG. 5.19 BLADE DRAG VARIATIONS WITH FLOW INCIDENCE AND RADIAL POSITION

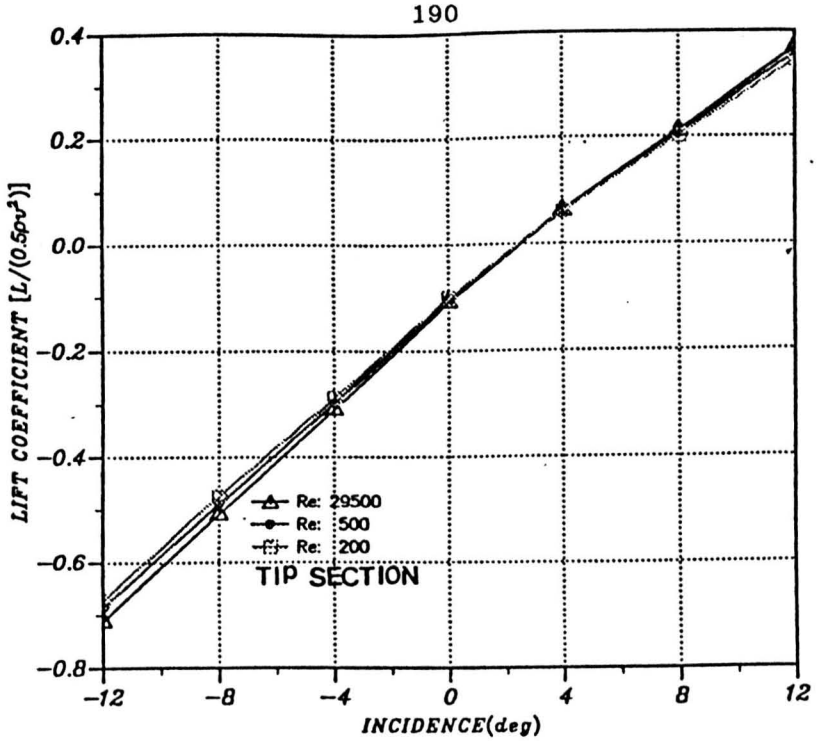

FIG. 5.20 *FLOWMETER BLADE LIFT VARIATIONS WITH FLOW REYNOLDS NUMBER*

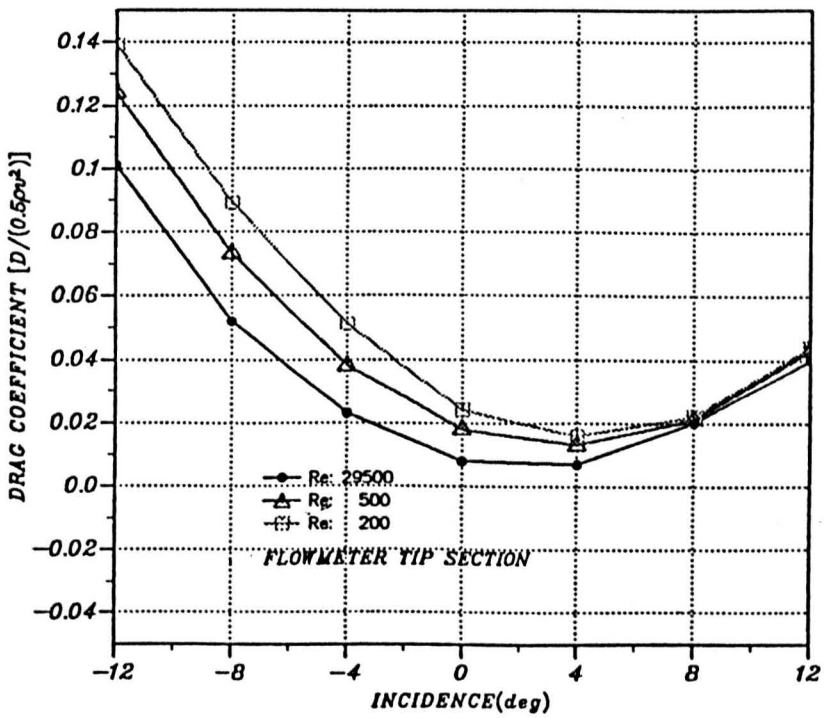

FIG. 5.21 *FLOWMETER BLADE DRAG VARIATIONS WITH FLOW REYNOLDS NUMBER*

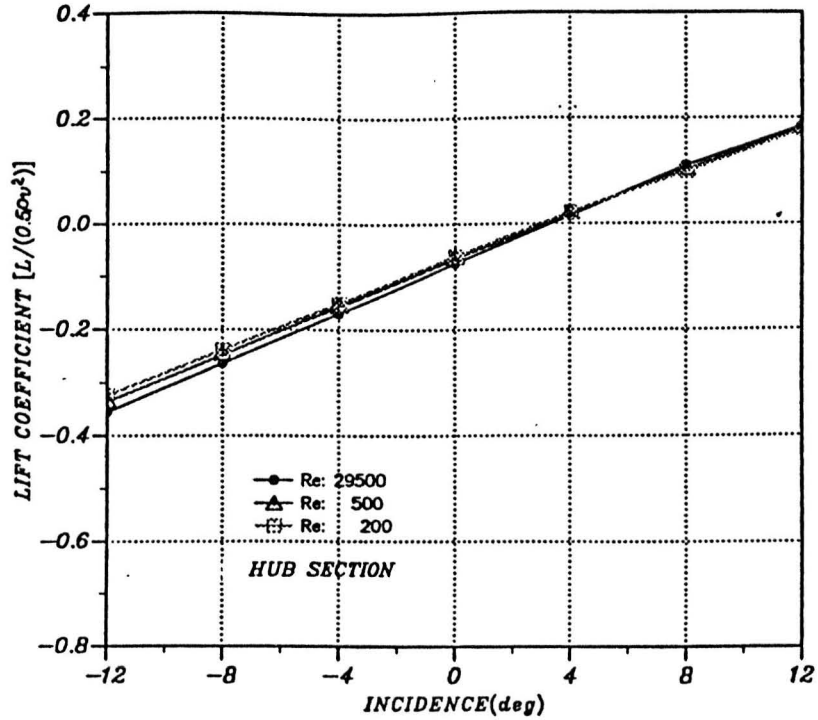

FIG. 5.22 *FLOWMETER BLADE LIFT VARIATIONS WITH FLOW REYNOLDS NUMBER*

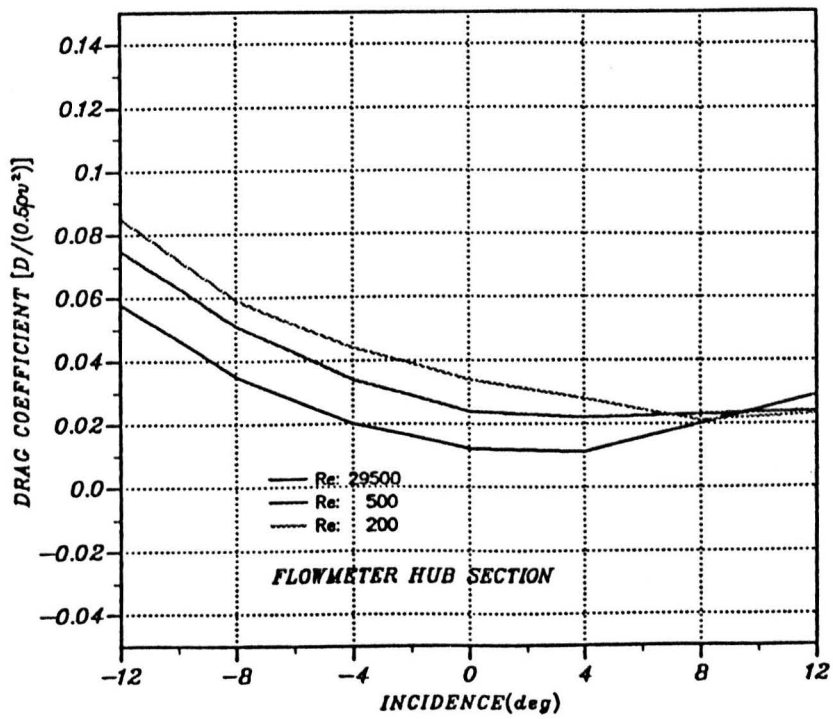

FIG. 5.23 *FLOWMETER BLADE DRAC VARIATIONS WITH FLOW REYNOLDS NUMBER*

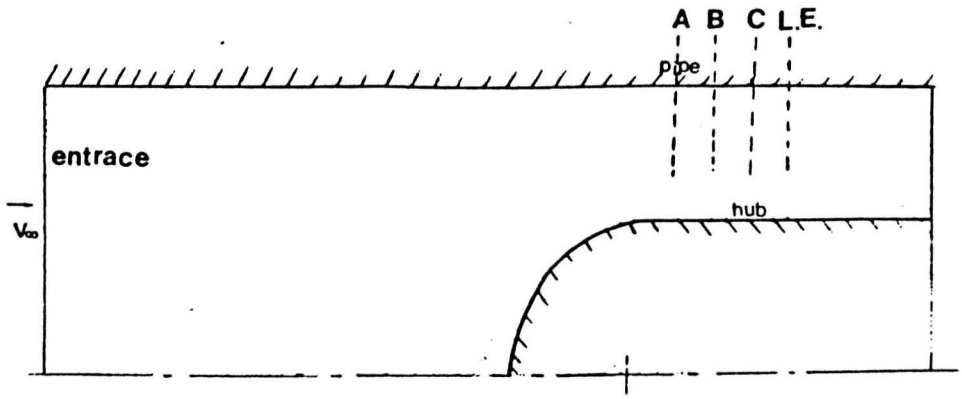

FIG.6.1 ANNULUS FLOW IN THE FLOWMETER SECTION

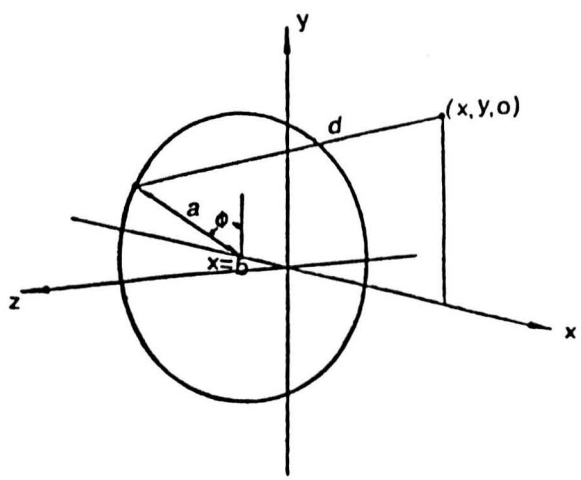

FIG.6.2 A RING SOURCE OF CONSTANT STRENGTH AT X=b

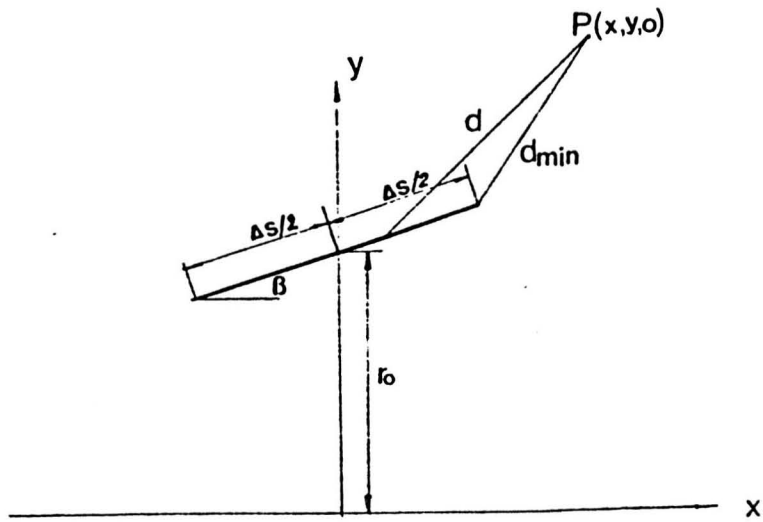

FIG.6.3 INTEGRATION OVER A RING SOURCE SEGMENT

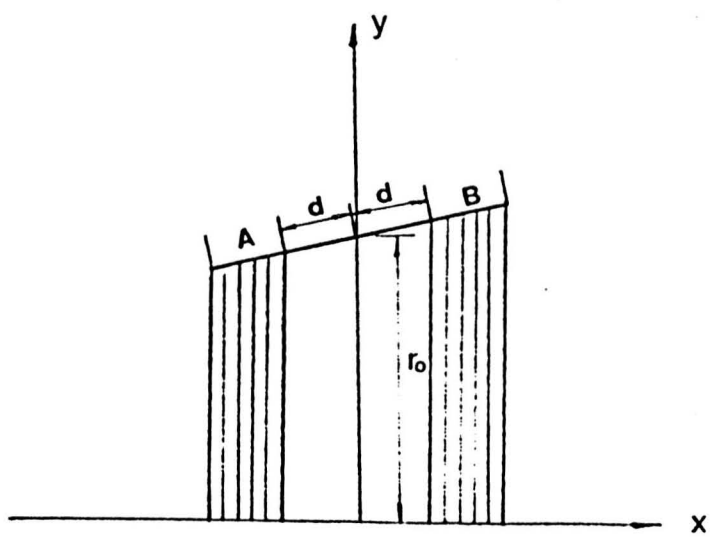

FIG. 6.4 THE SINGULAR SUB-ELEMENT

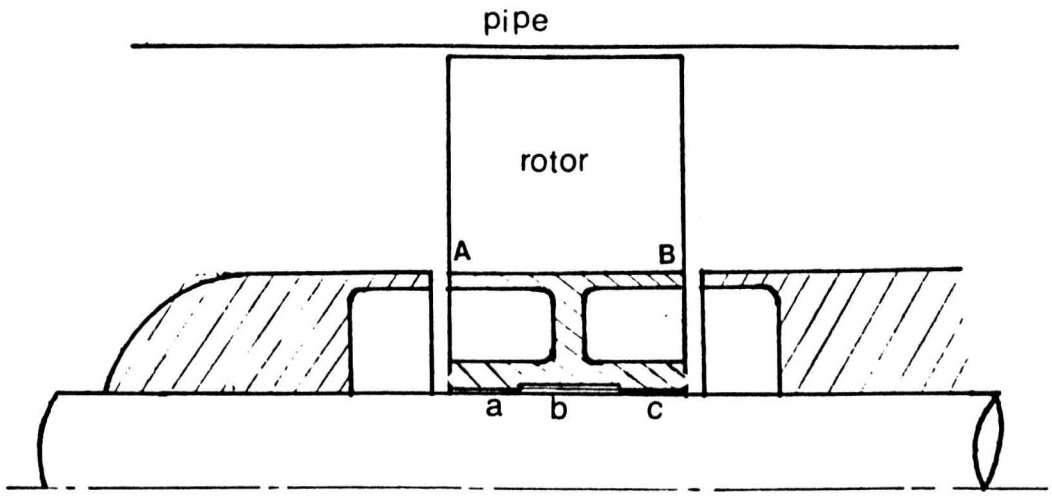

(a) *Flowmeter Configuration*

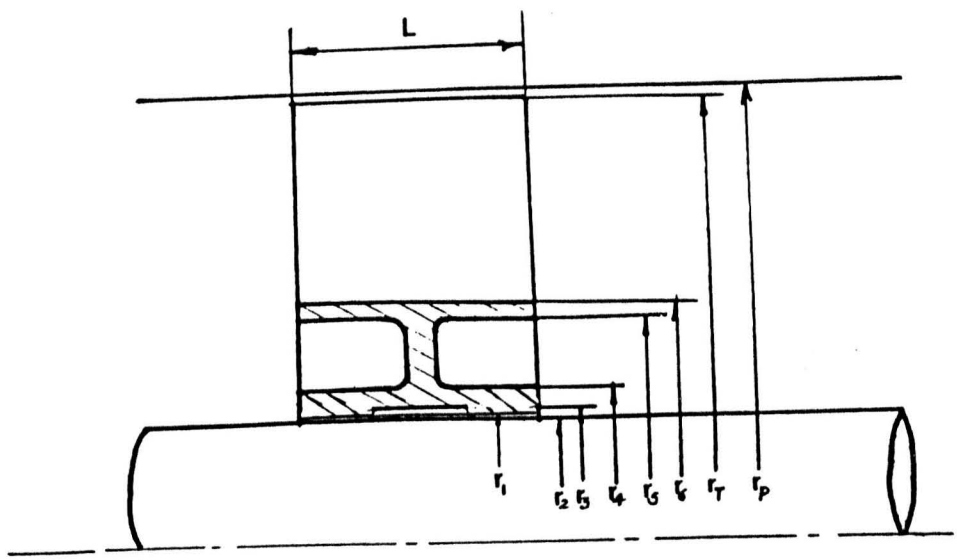

(b) *Flowmeter Dimensions*

FIG.6.5 GEOMETRY OF THE TESTED TURBINE FLOWMETER

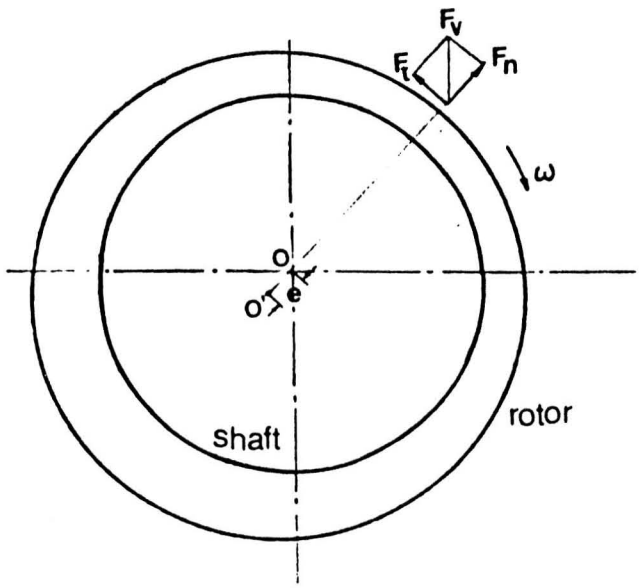

FIG.6.6 BEARING CONFIGURATION

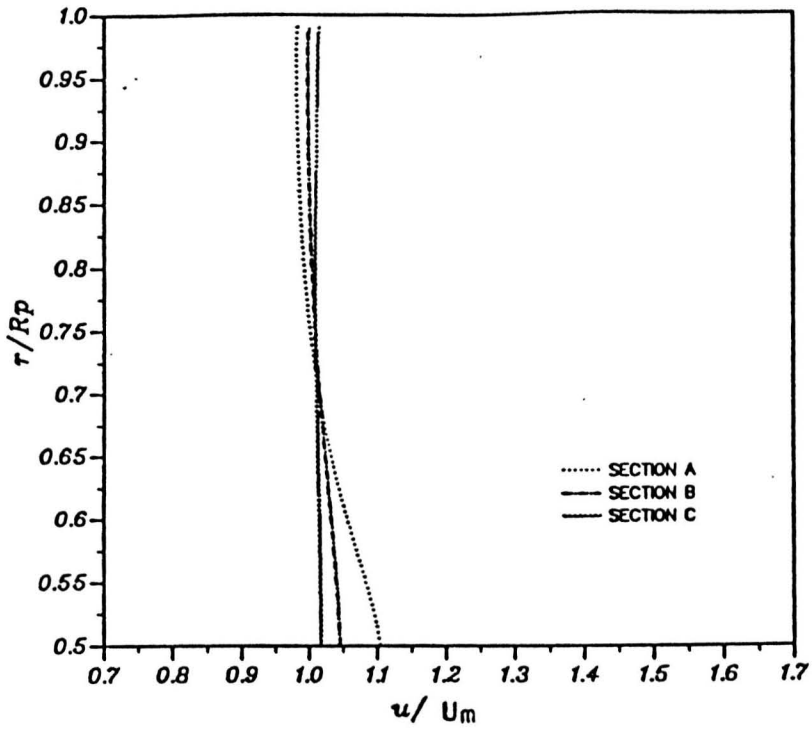

FIG.6.7 POTENTIAL FLOWMETER INLET VELOCITY PROFILES WITHOUT BOUNDARY LAYERS

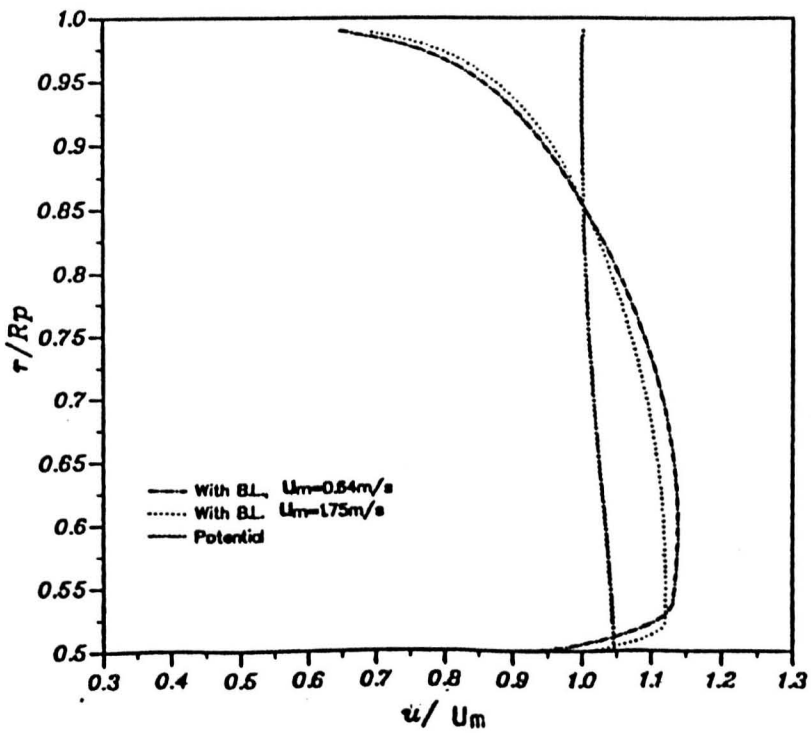

FIG. 6.8 PREDICTED FLOWMETER INLET VELOCITY PROFILES

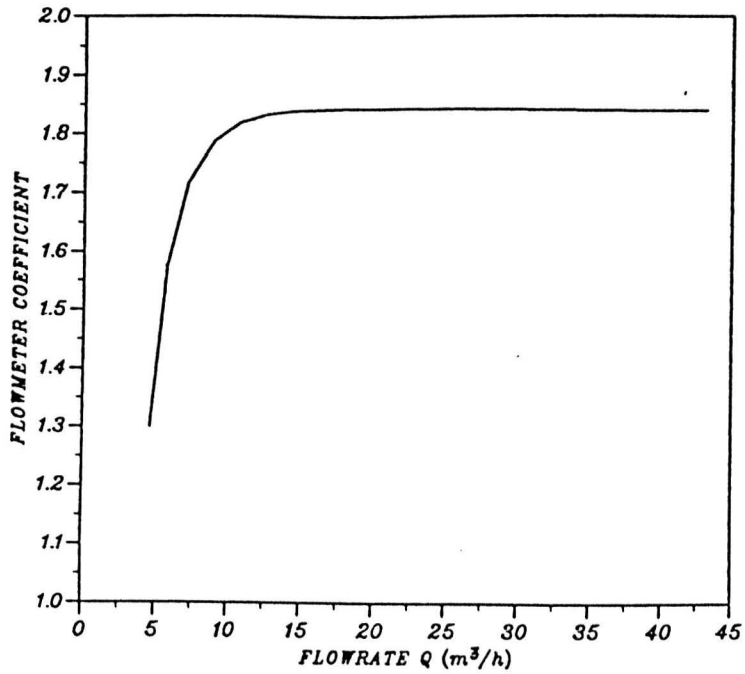

FIG. 6.9 PREDICTED FLOWMETER CALIBRATION CURVE(without swirl)

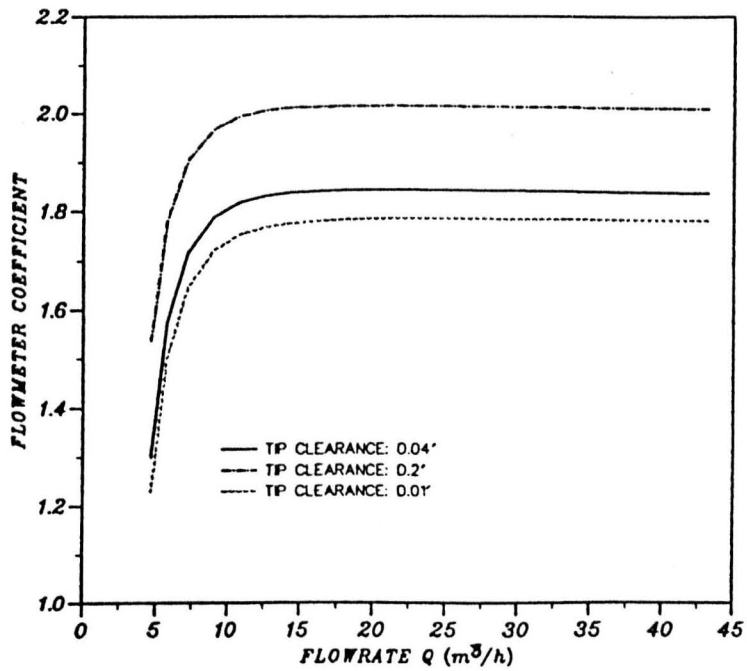

FIG. 6.10 PREDICTED FLOWMETER CALIBATION CURVES FOR DIFFERENT TIP CLEARANCES

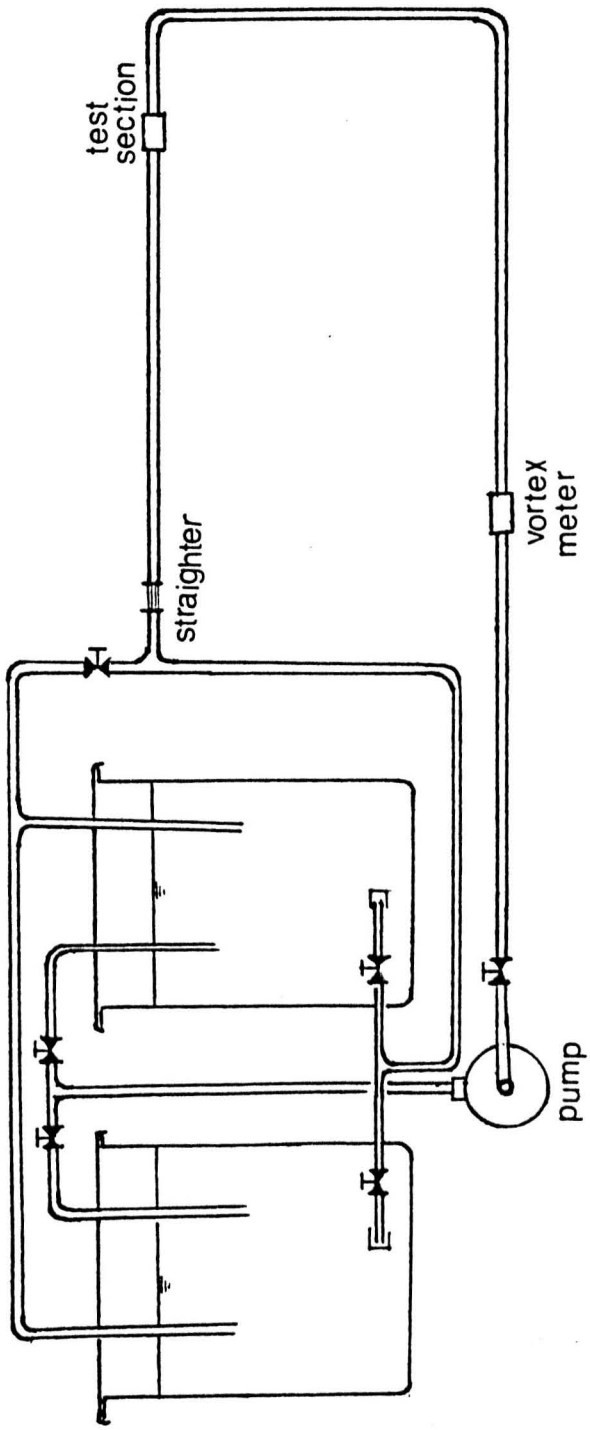

FIG. 7.1 EXPERIMENTAL RIG

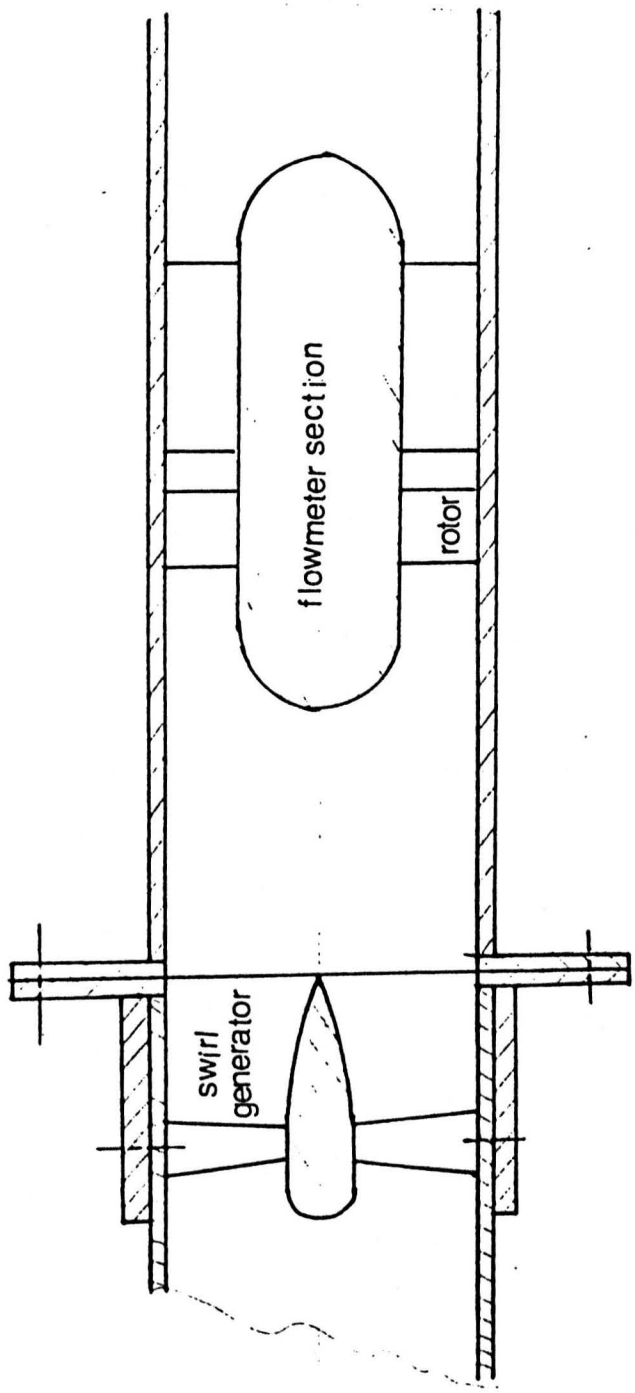

FIG.7.2 TEST SECTION

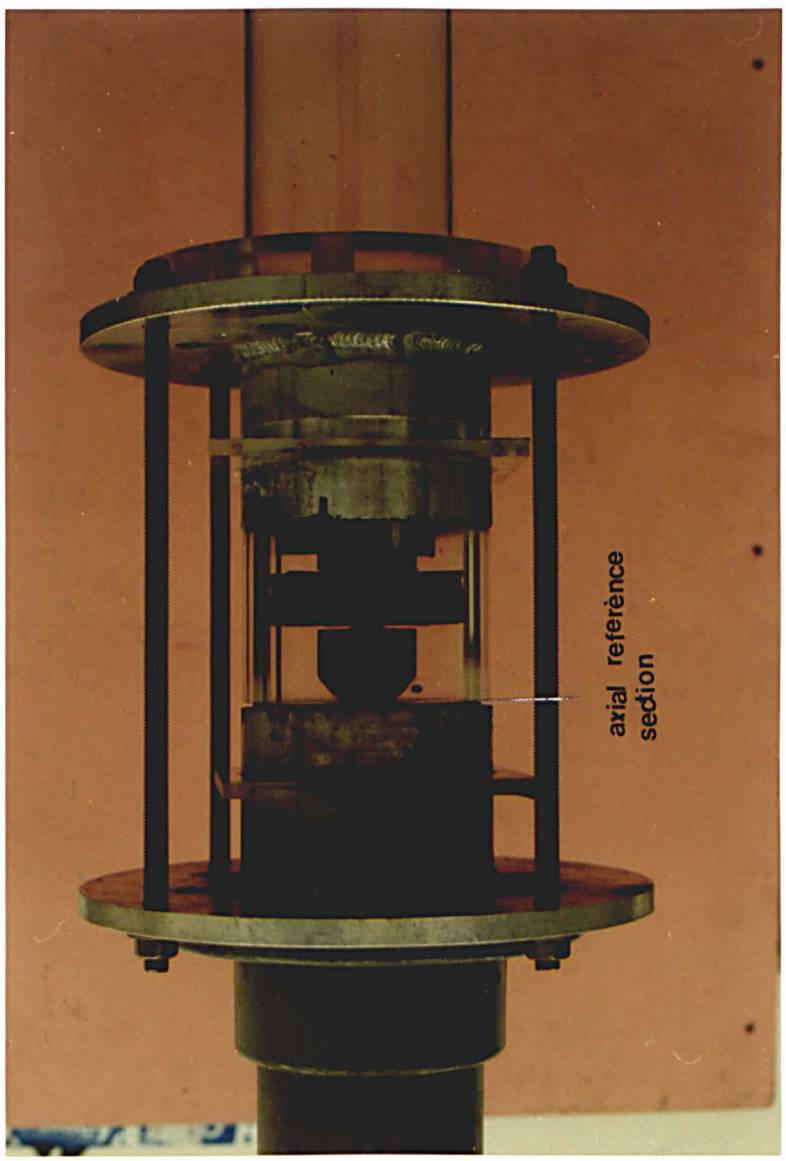

FIG.7.3 FLOWMETER SECTION ASSEMBLY

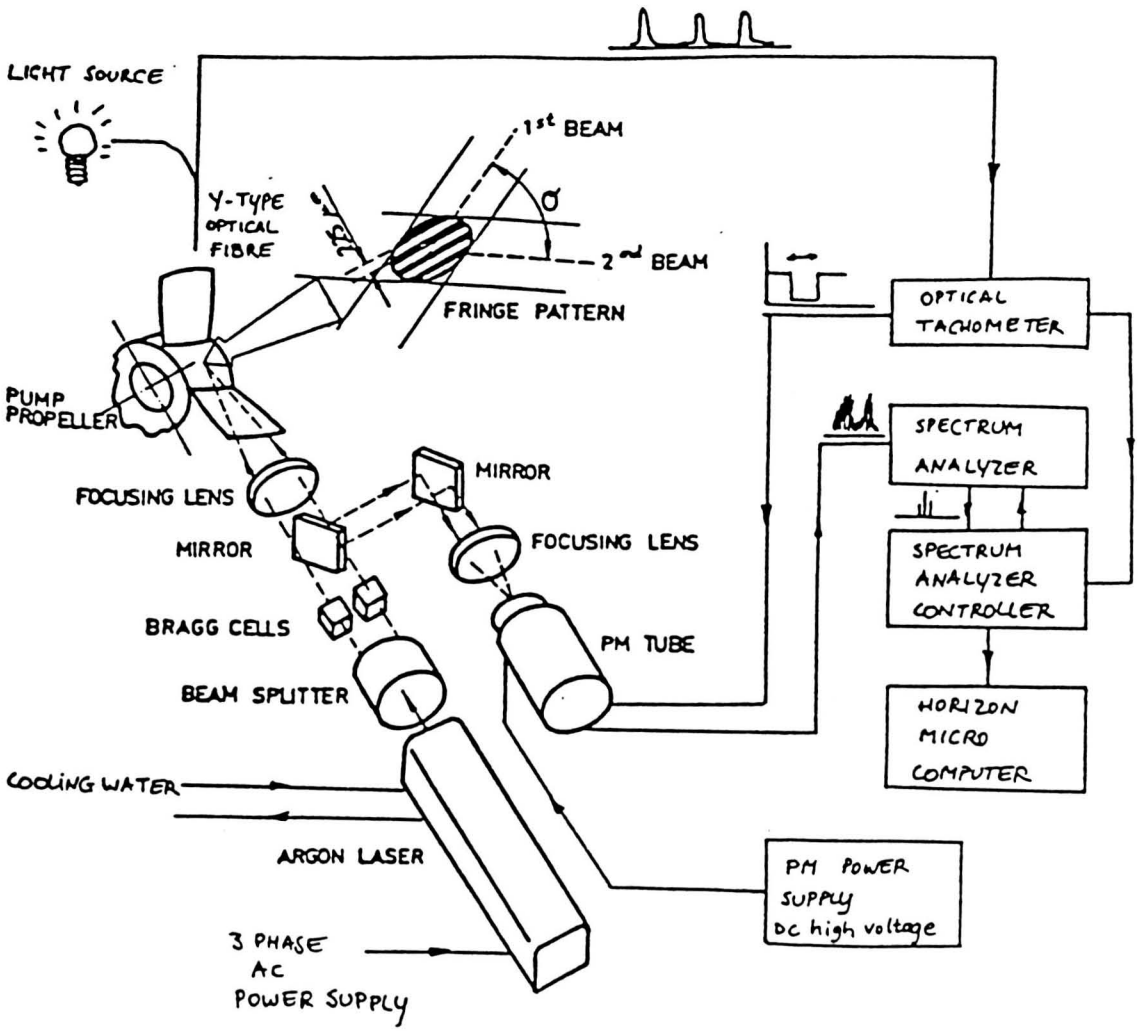

FIG.7.4 SCHEMATIC DIAGRAM OF LDA SYSTEM

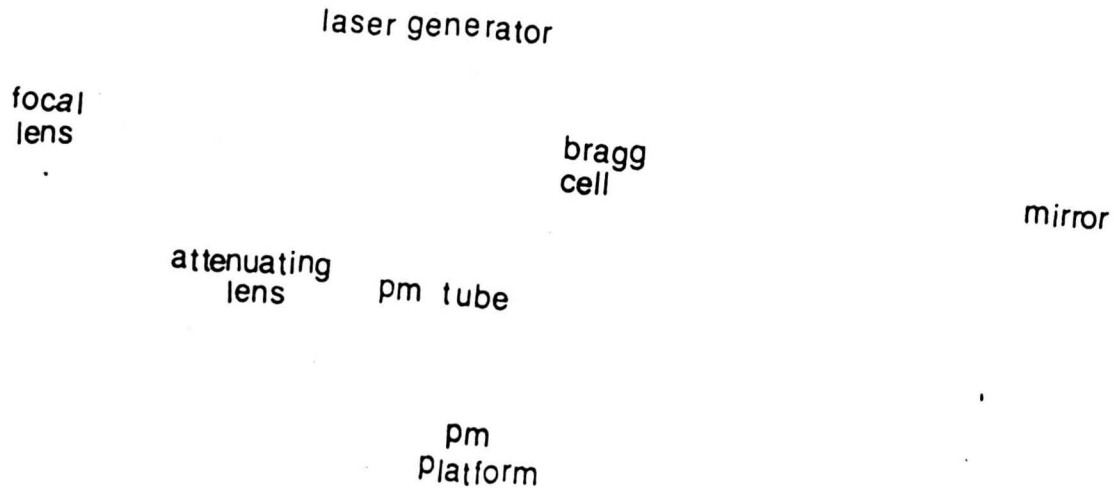
laser generator
focal lens
bragg cell
mirror
attenuating lens
pm tube
pm Platform

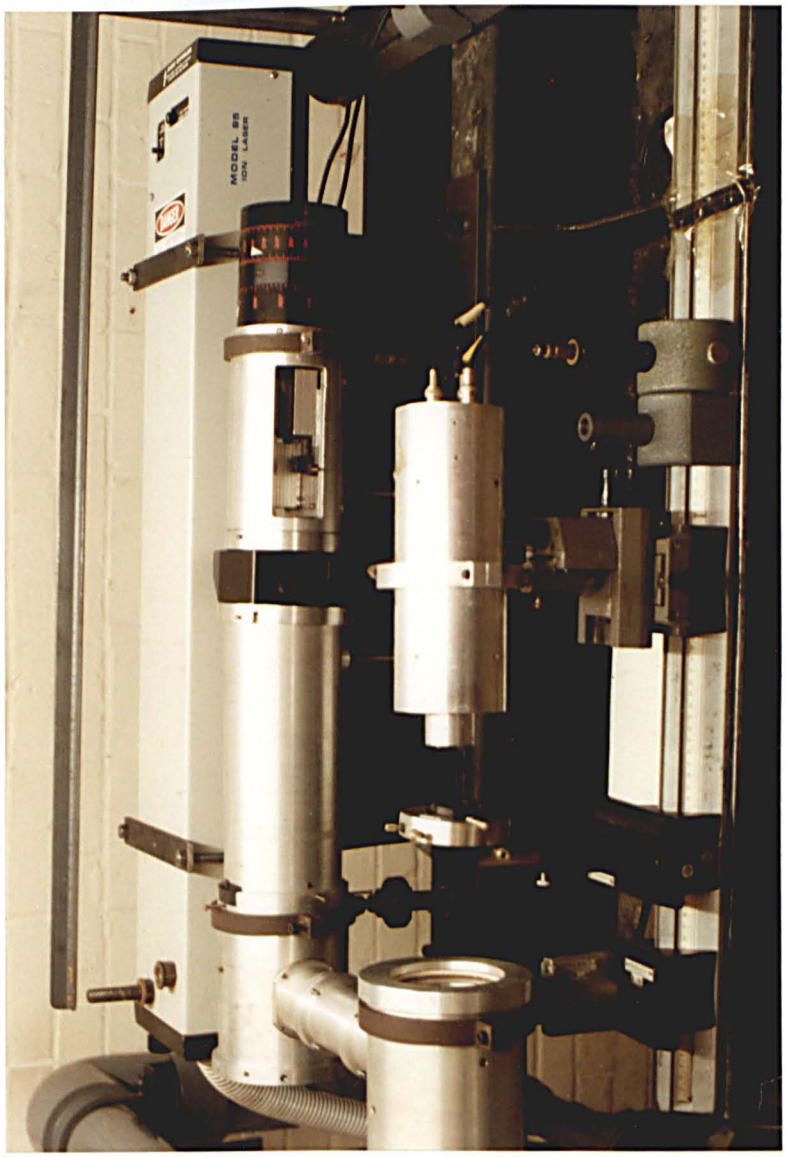

FIG.7.5 LDA OPTICAL SYSTEM

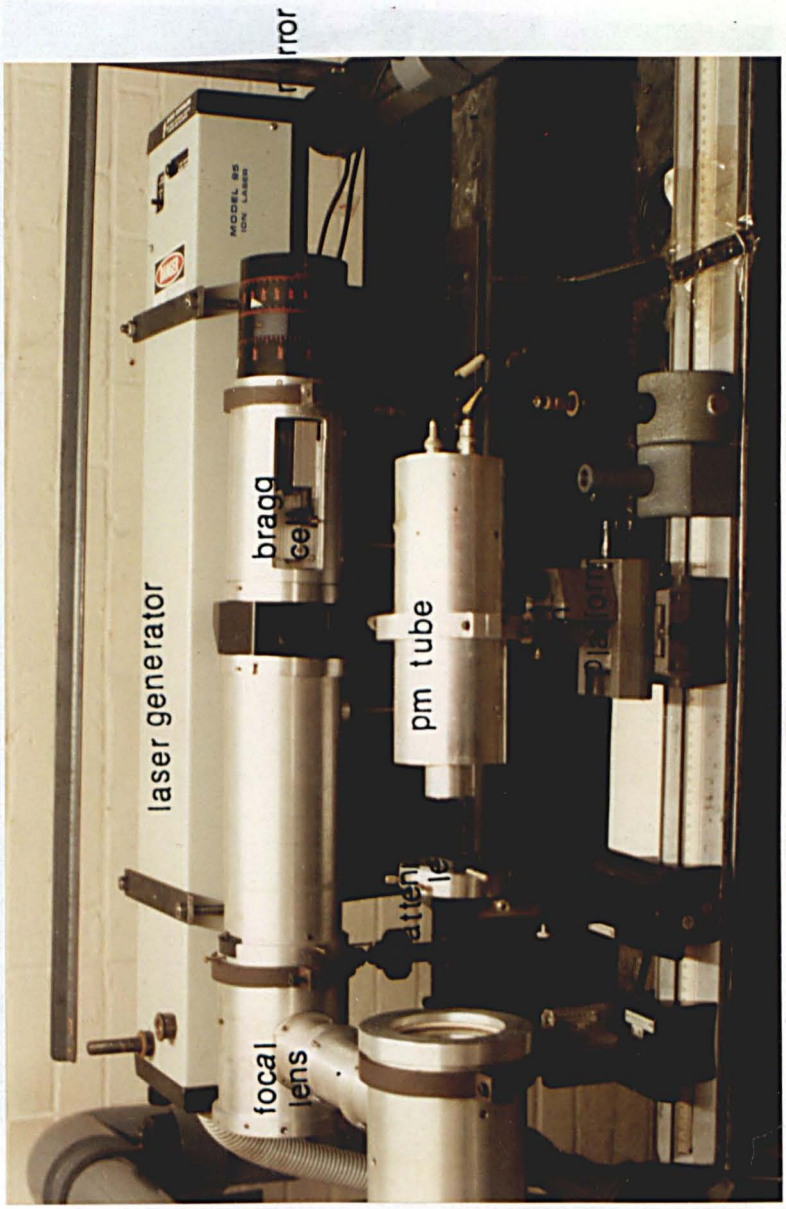

FIG.7.5 LDA OPTICAL SYSTEM

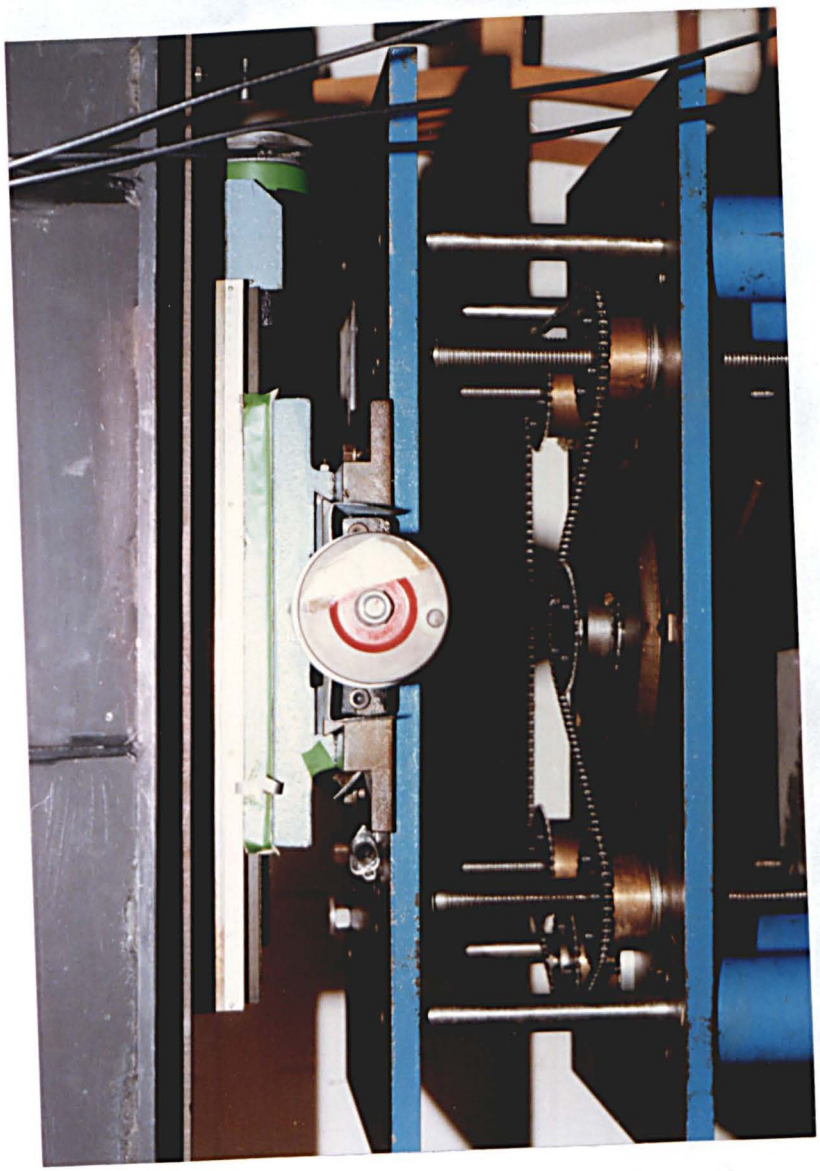

FIG.7.6 PLATFORM AJUSTMENT MECHANISM

FIG.7.7 SIGNAL PROCESSING SYSTEM

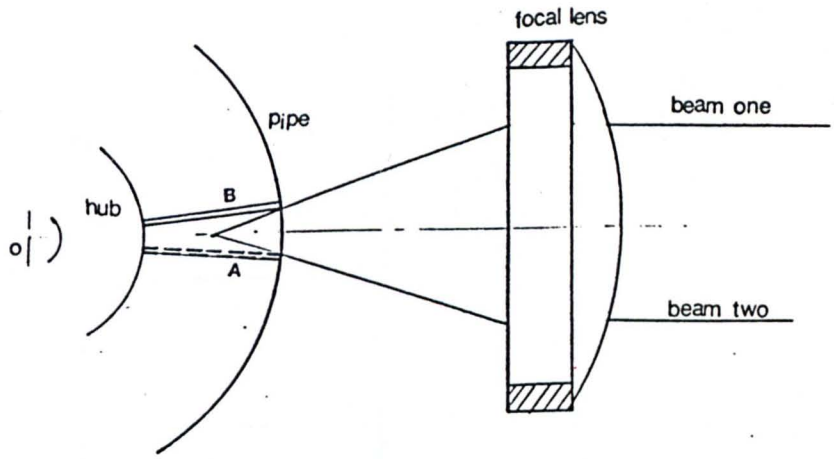

FIG. 7.8 LASER BEAMS CUT BY A ROTOR BLADE

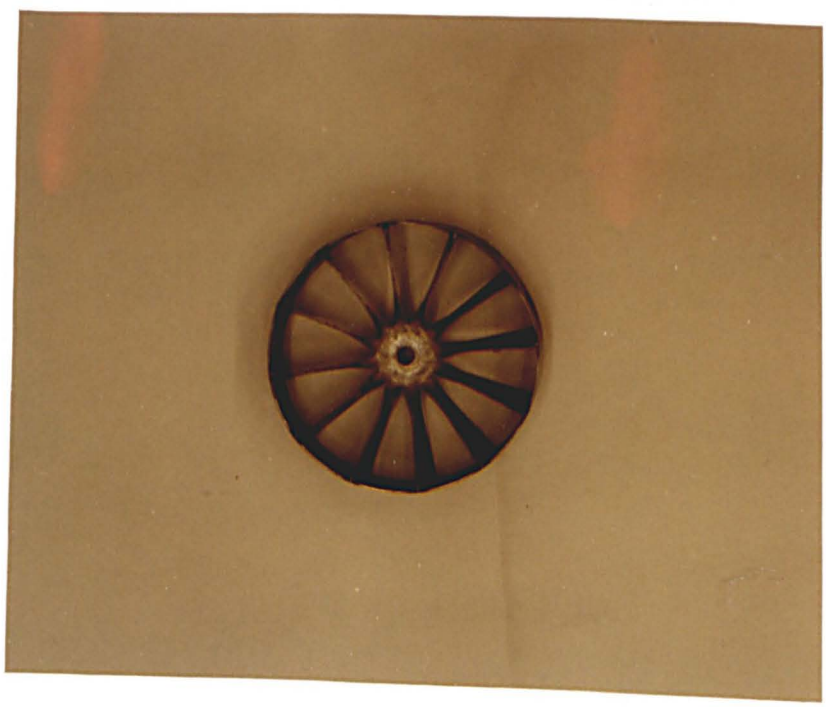

FIG.7.9 SWIRL GENERATOR

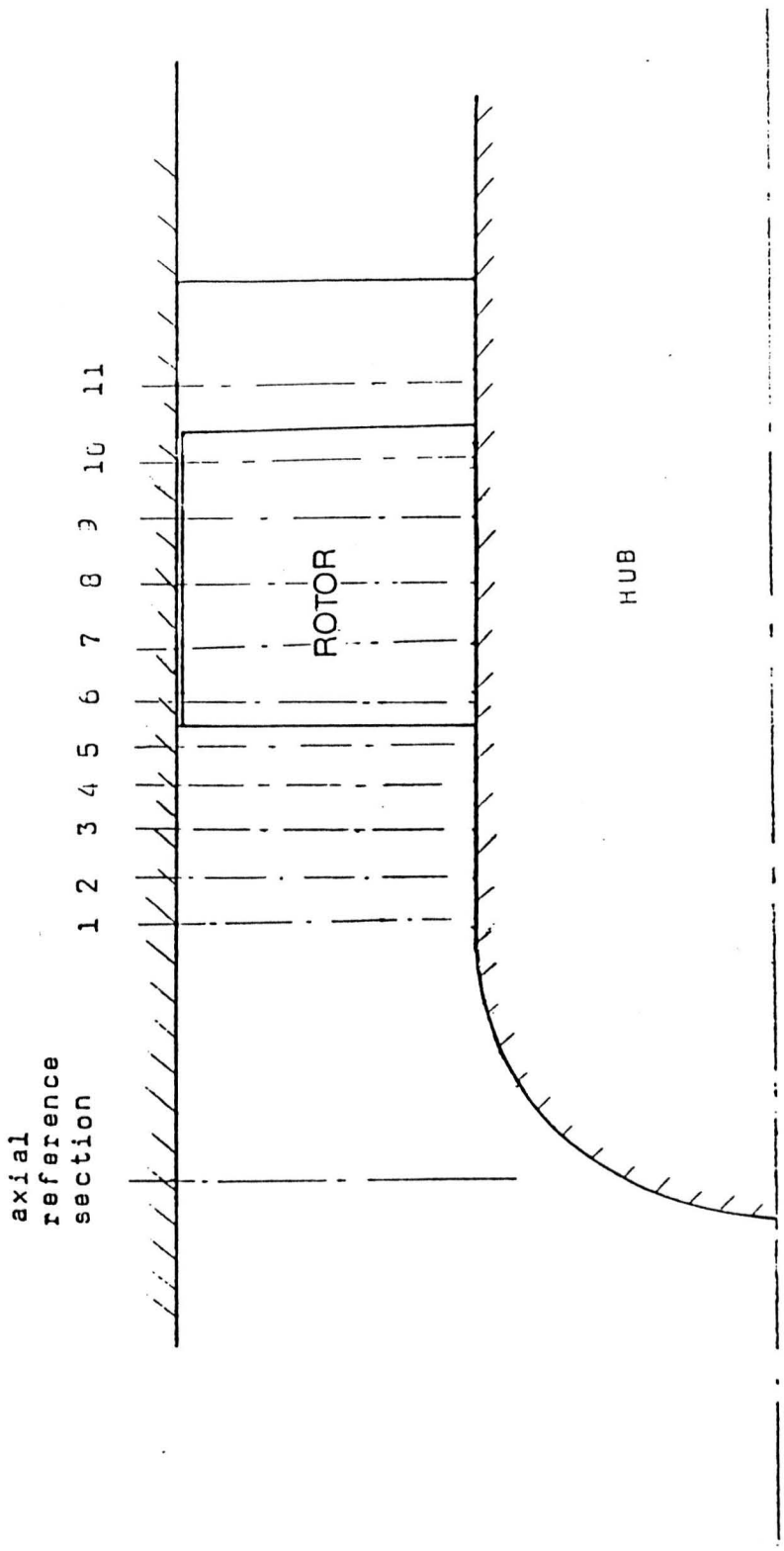

FIG. 7.10 AXIAL VELOCITY MEASUREMENT STATIONS

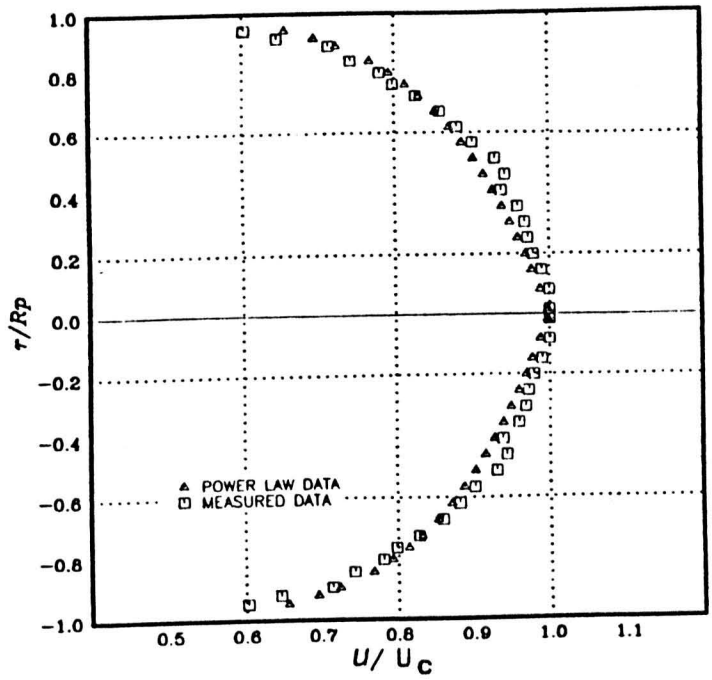

FIG.8.1 DEVELOPED PIPE VELOCITY PROFILE

(Reynolds Number: 1.12e+5)

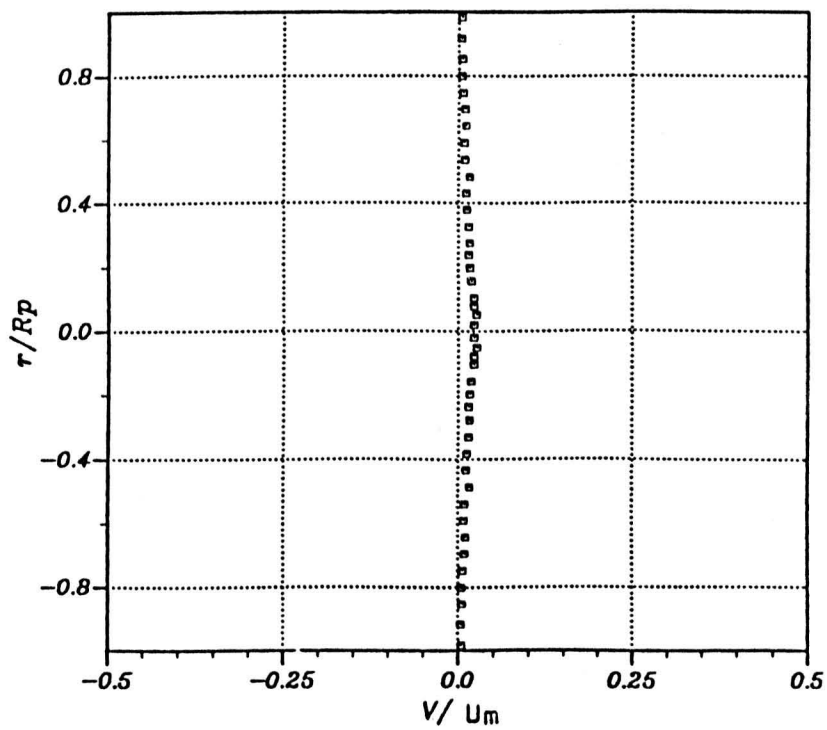

FIG.8.2 MEASURED CIRCUMFERENTIAL VELOCITY PROFILE ON PIPE CROSS SECTION

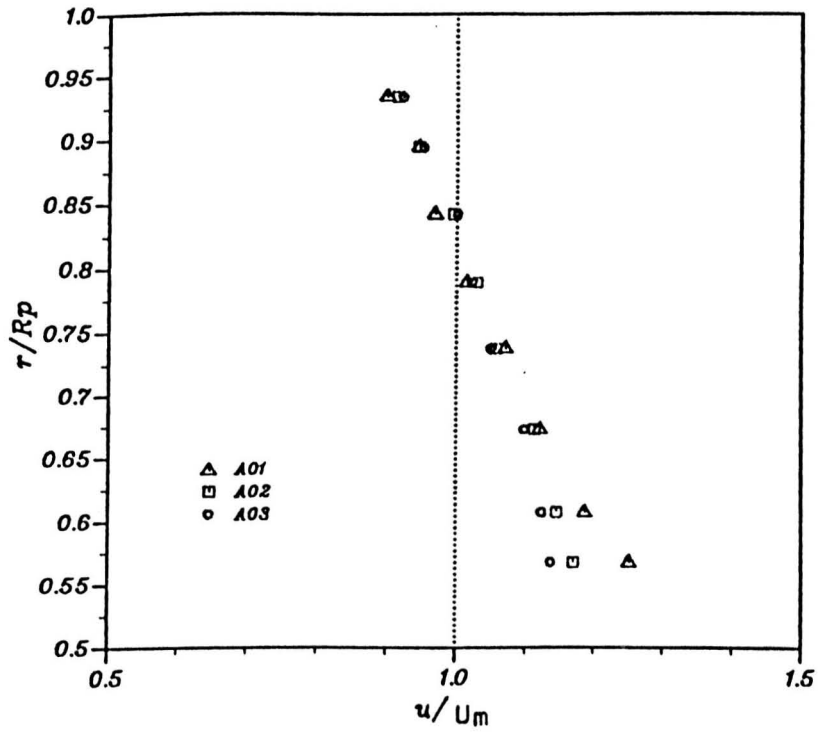

FIG. 8.3 MEASURED AXIAL VELOCITY PROFILES

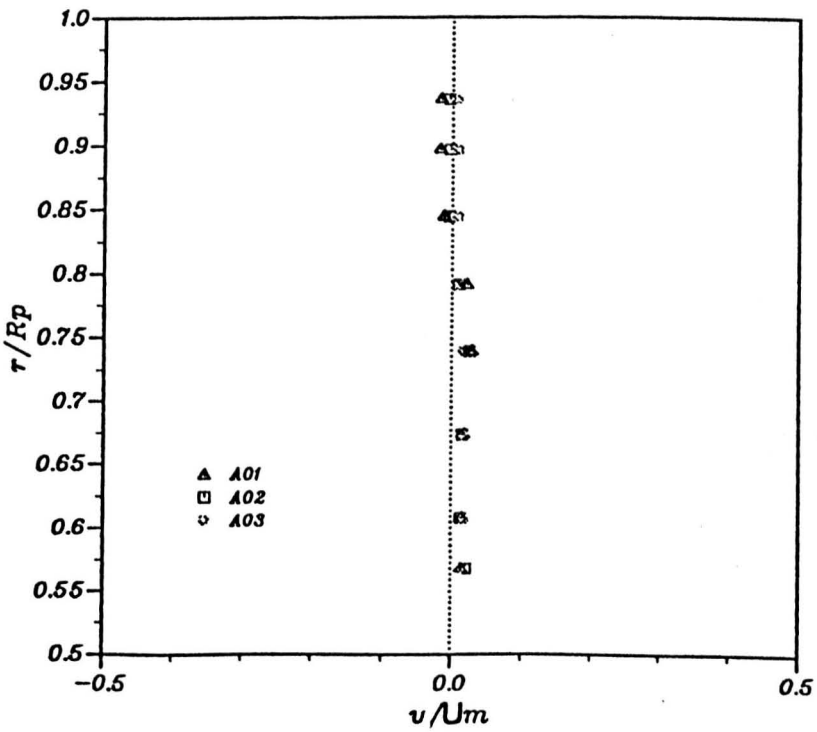

FIG. 8.4 MEASURED CIRCUMFERENTIAL VELOCITY PROFILES

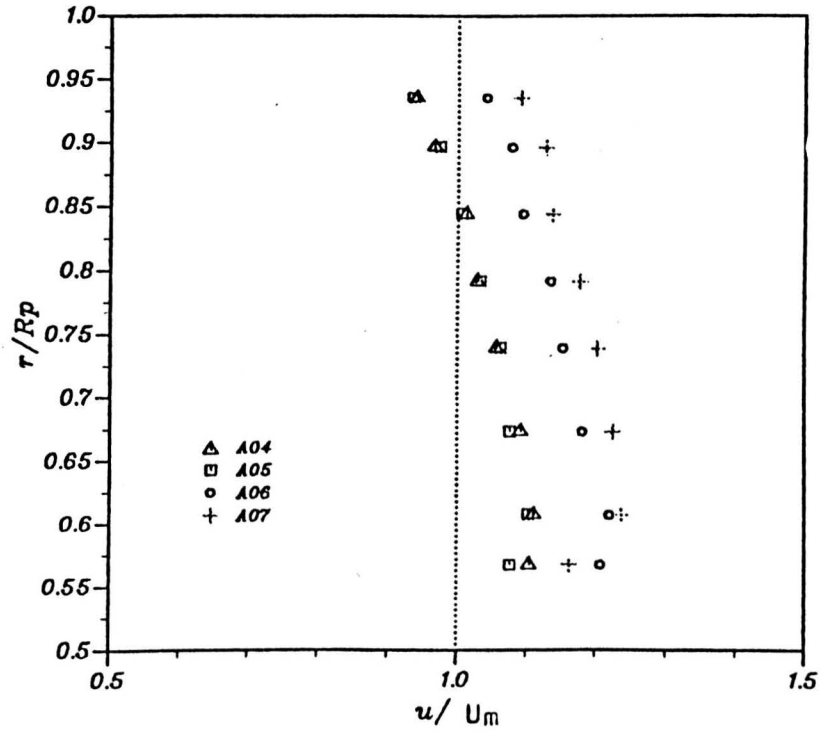

FIG. 8.5 MEASURED AXIAL VELOCITY PROFILES

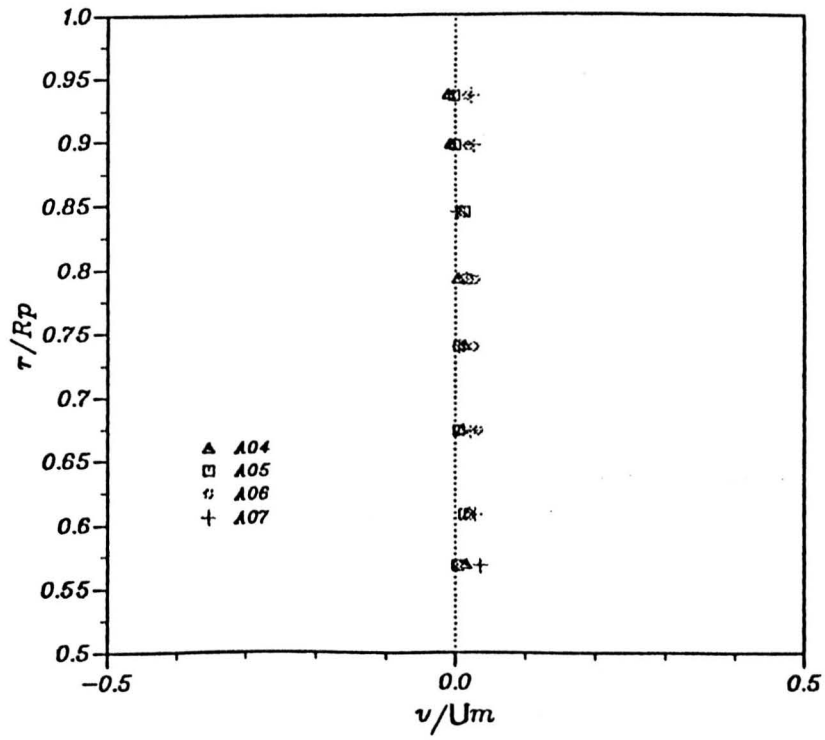

FIG. 8.6 MEASURED CIRCUMFERENTIAL VELOCITY PROFILES

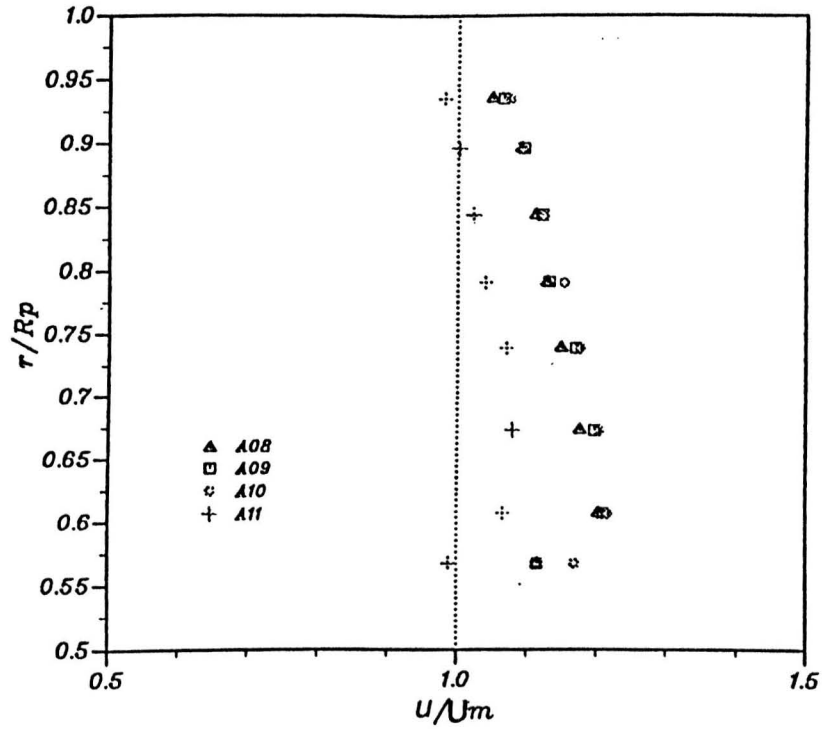

FIG. 8.7 MEASURED AXIAL VELOCITY PROFILES

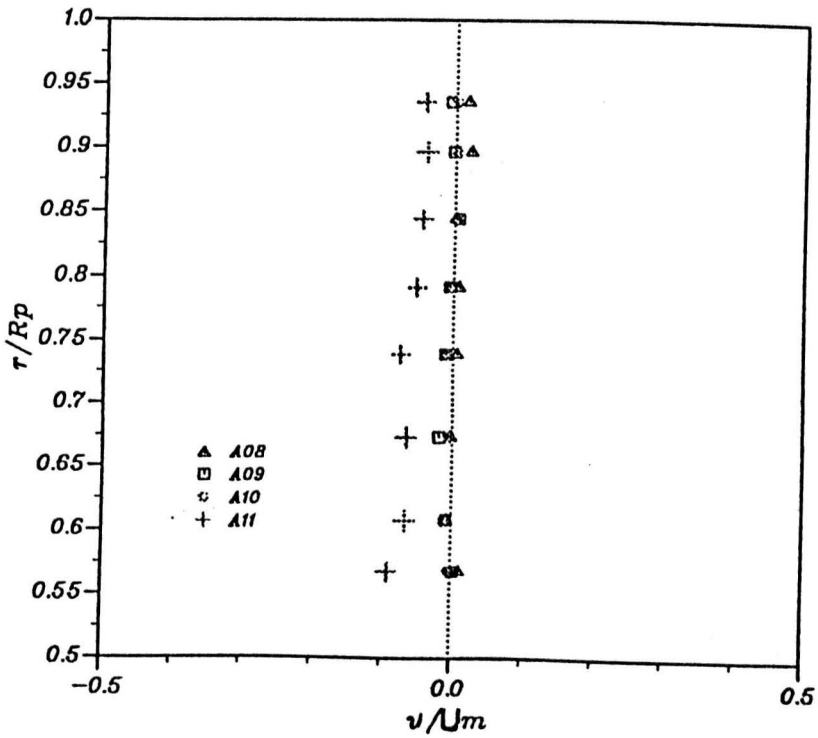

FIG. 8.8 MEASURED CIRCUMFERENTIAL VELOCITY PROFILES

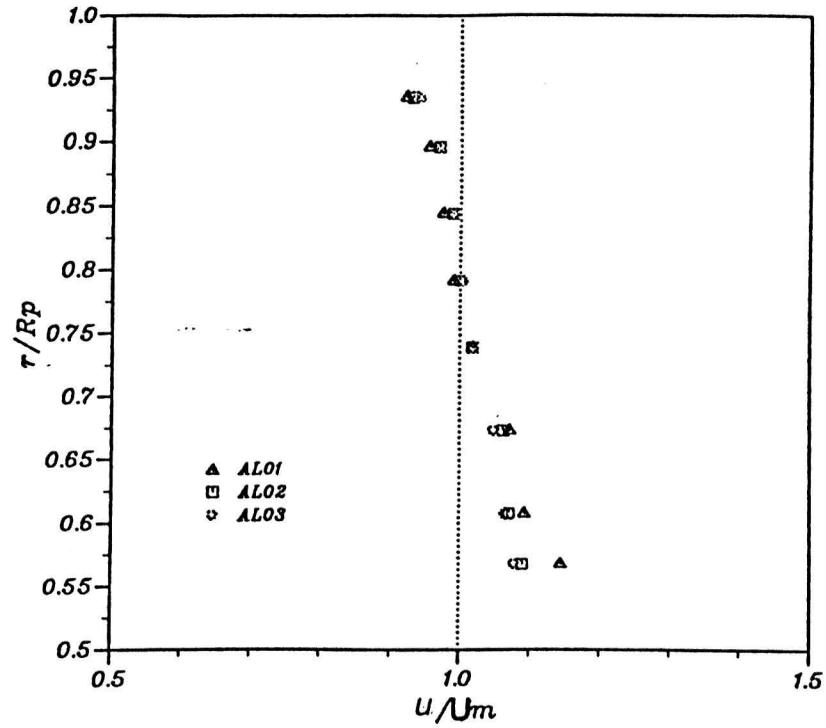

FIG. 8.9 MEASURED AXIAL VELOCITY PROFILES

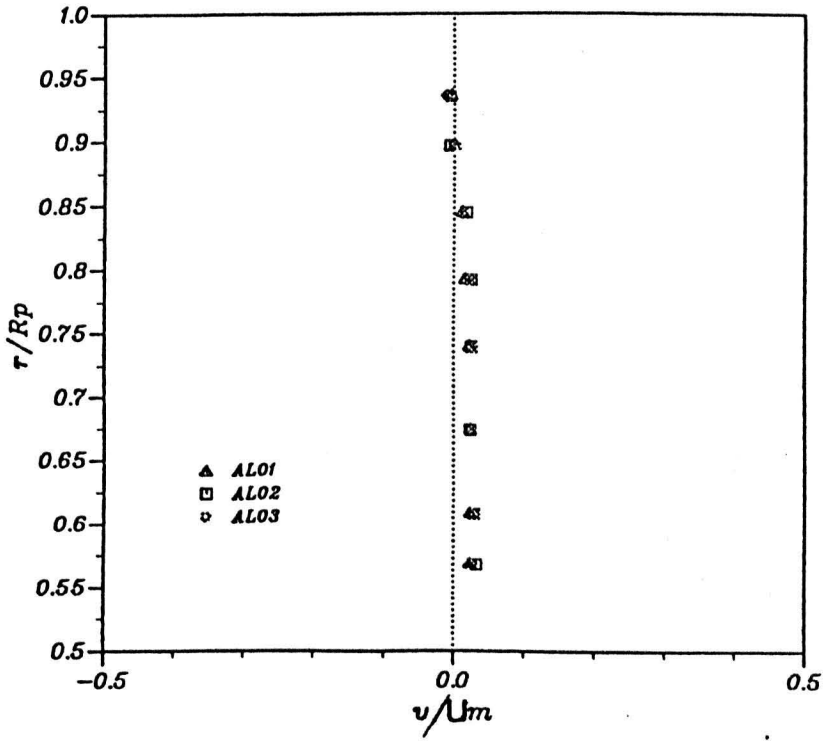

FIG. 8.10 MEASURED CIRCUMFERENTIAL VELOCITY PROFILES

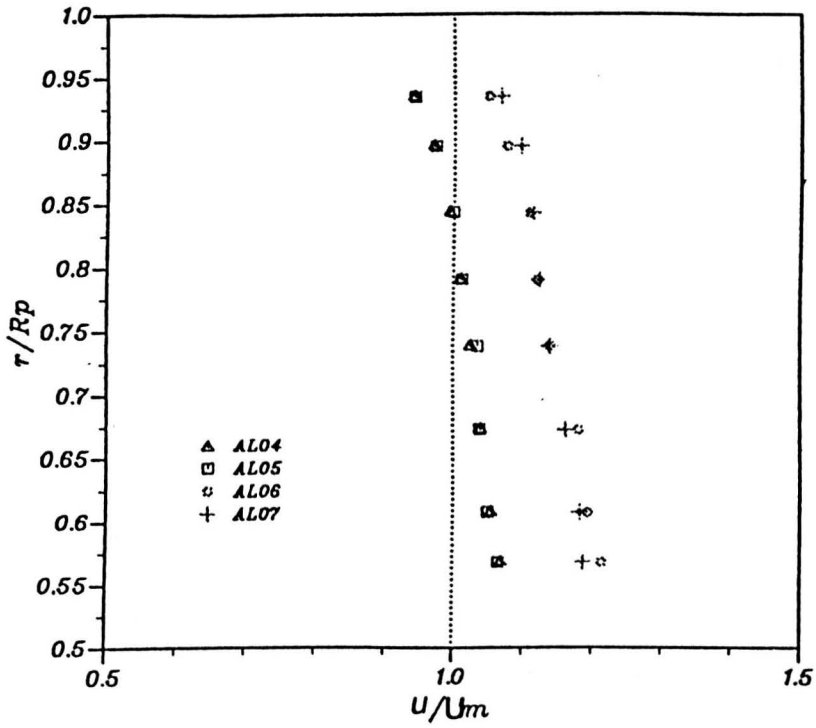

FIG. 8.11 MEASURED AXIAL VELOCITY PROFILES

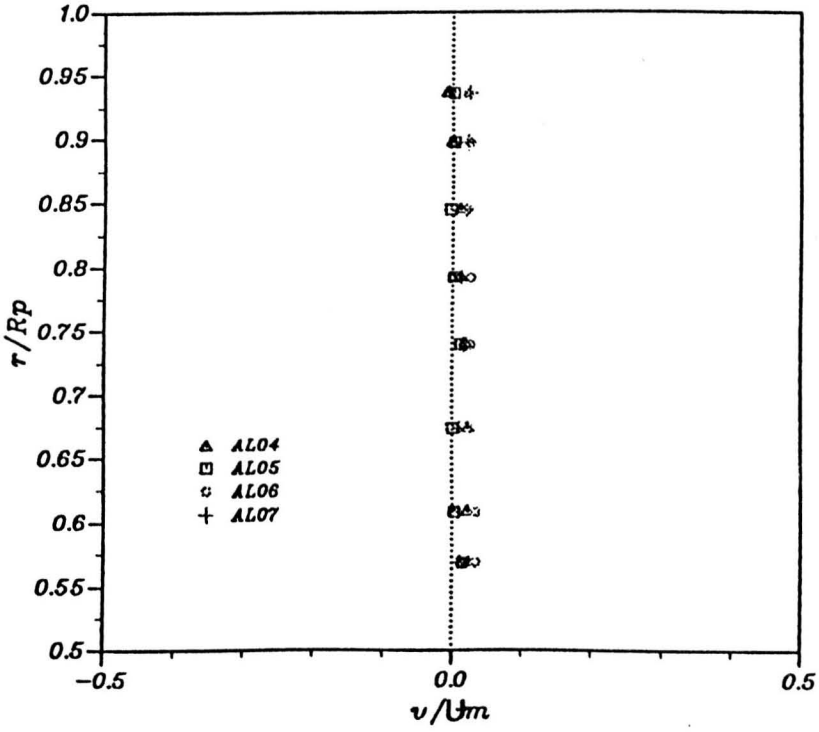

FIG. 8.12 MEASURED CIRCUMFERENTIAL VELOCITY PROFILES

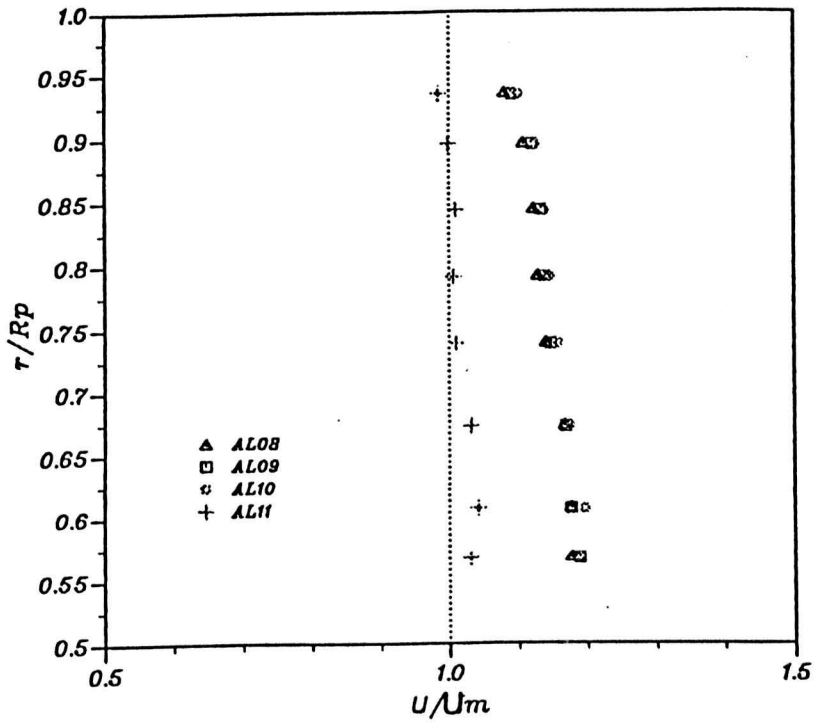

FIG. 8.13 MEASURED AXIAL VELOCITY PROFILES

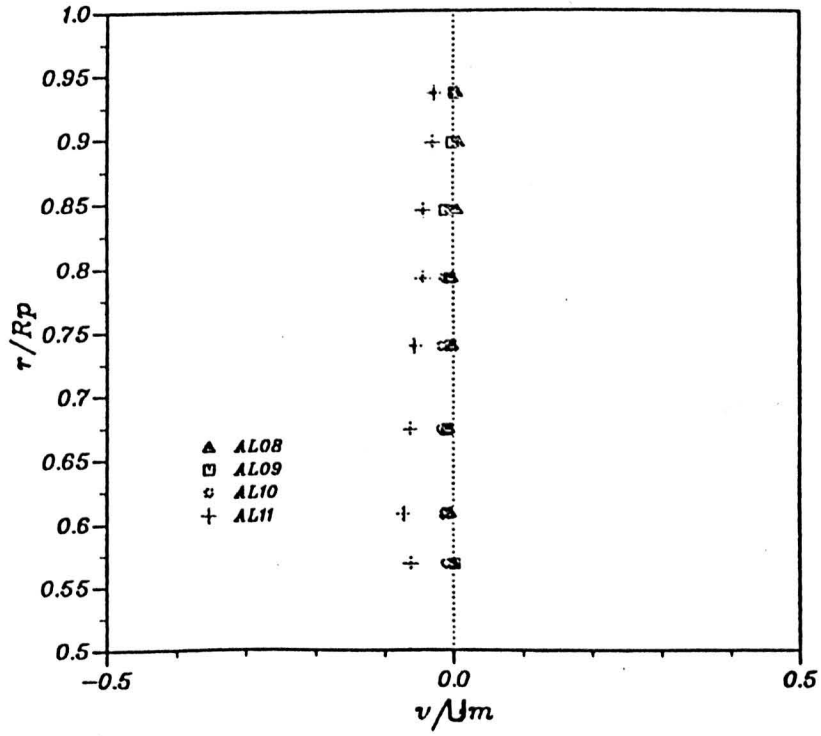

FIG. 8.14 MEASURED CIRCUMFERENTIAL VELOCITY PROFILES

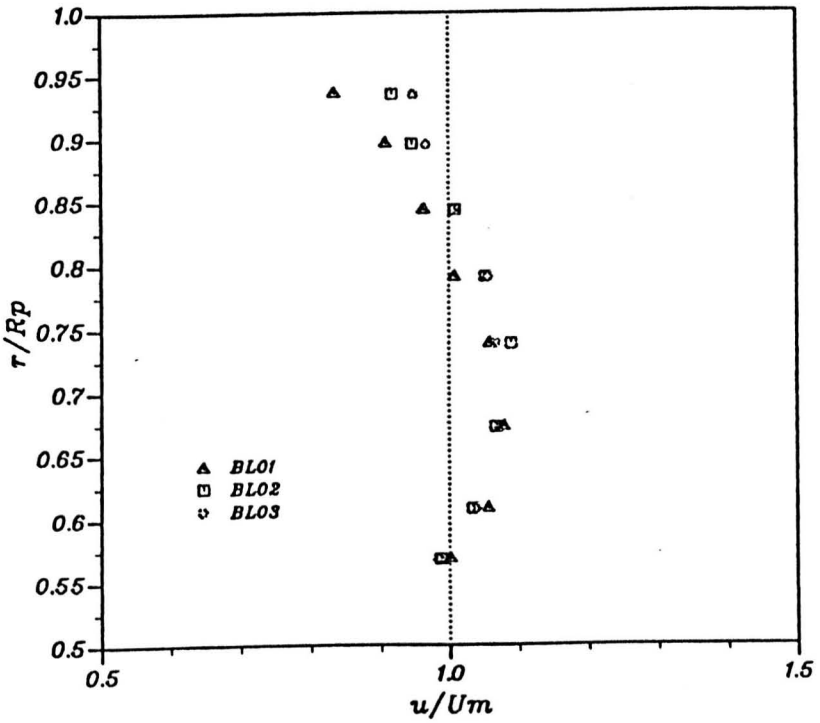

FIG. 8.15 MEASURED AXIAL VELOCITY PROFILES

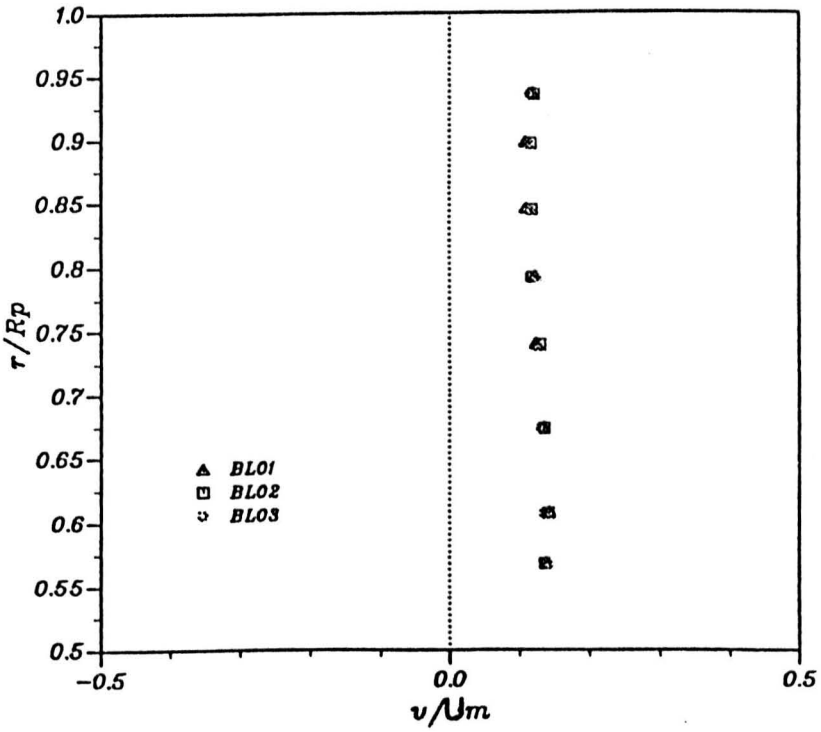

FIG. 8.16 MEASURED CIRCUMFERENTIAL VELOCITY PROFILES

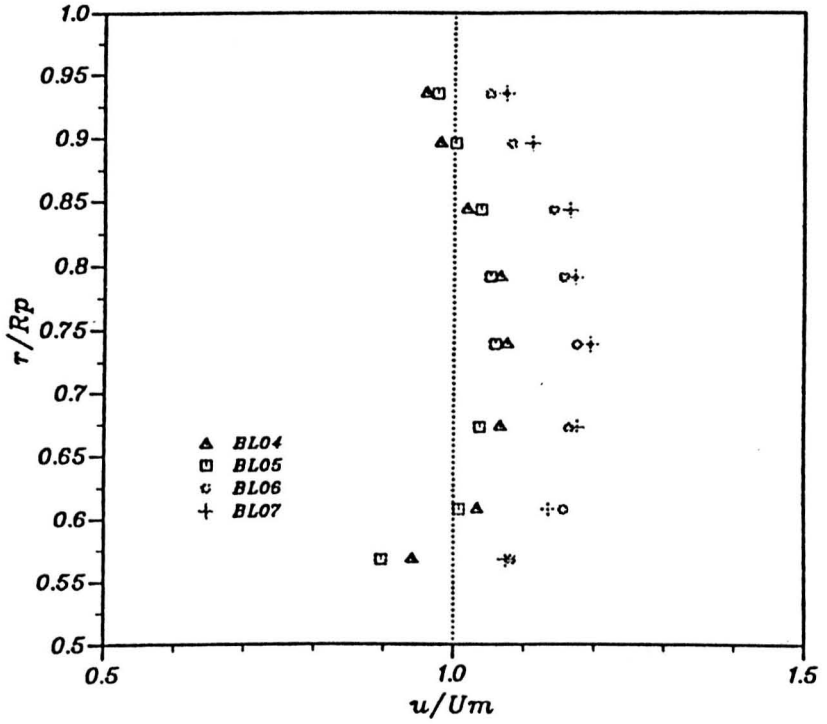

FIG. 8.17 MEASURED AXIAL VELOCITY PROFILES

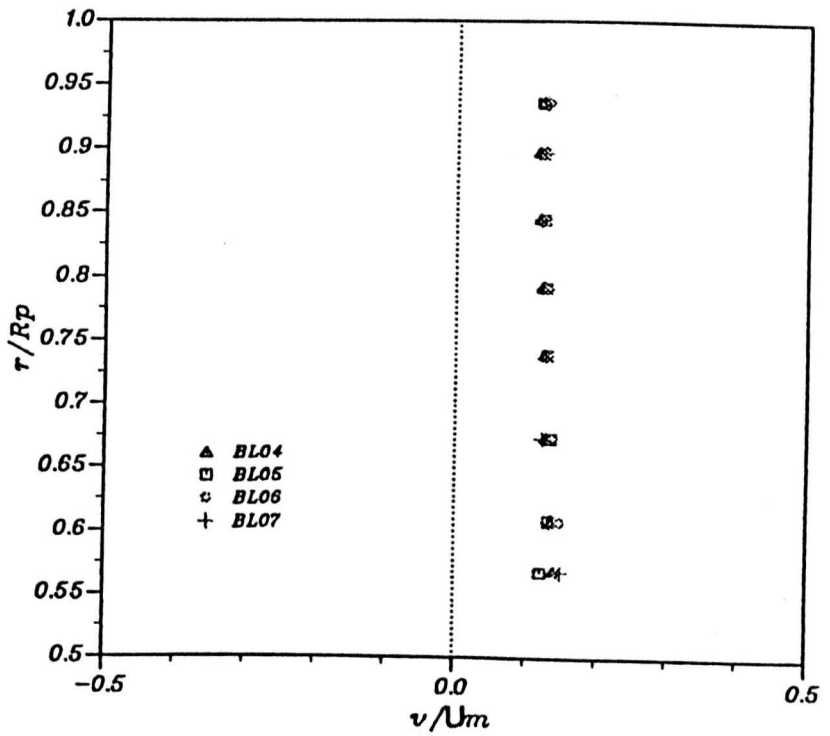

FIG. 8.18 MEASURED CIRCUMFERENTIAL VELOCITY PROFILES

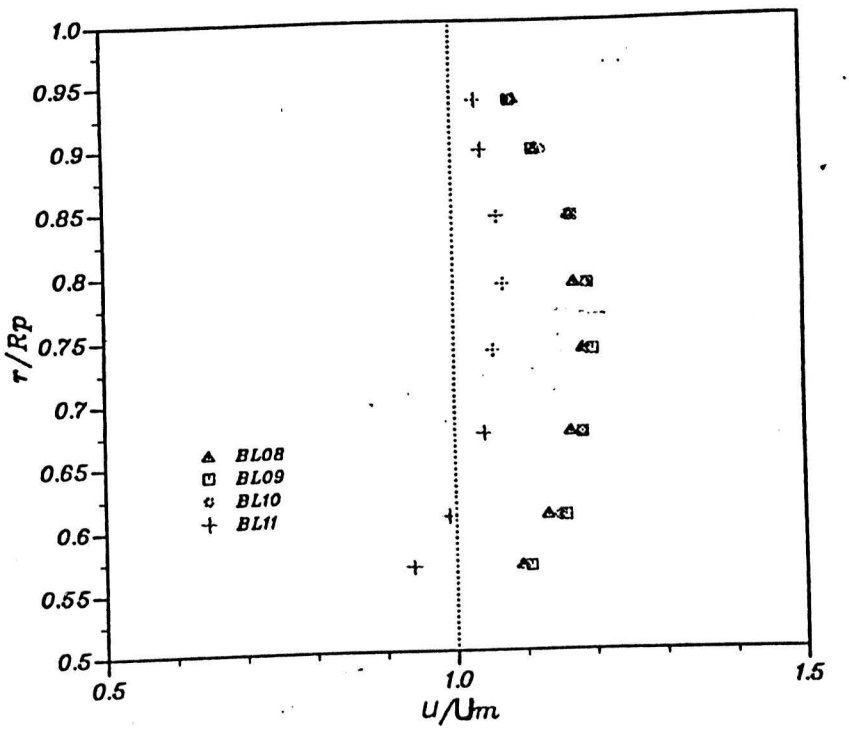

FIG. 8.19 MEASURED AXIAL VELOCITY PROFILES

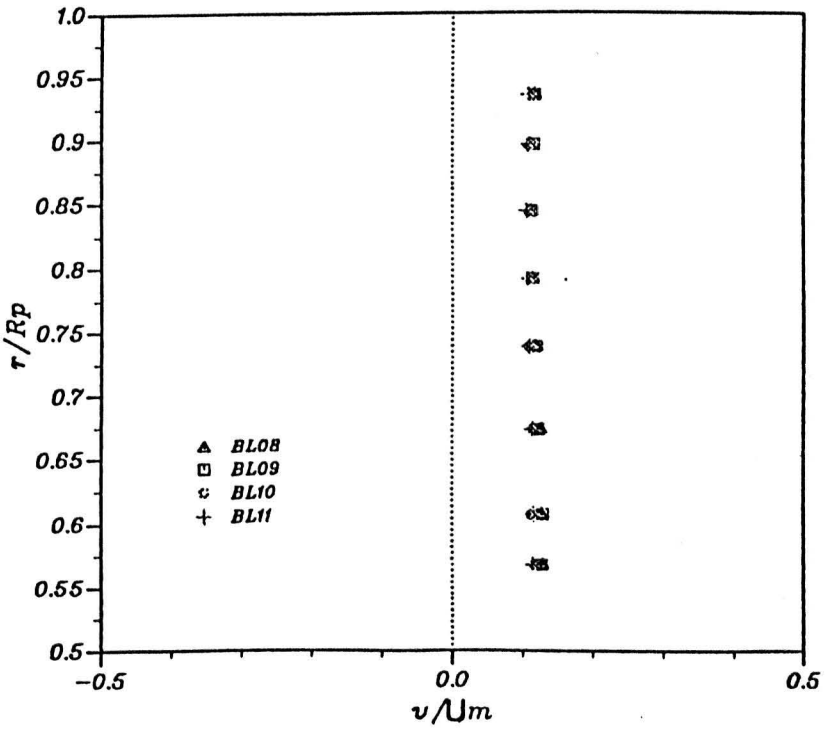

FIG. 8.20 MEASURED CIRCUMFERENTIAL VELOCITY PROFILES

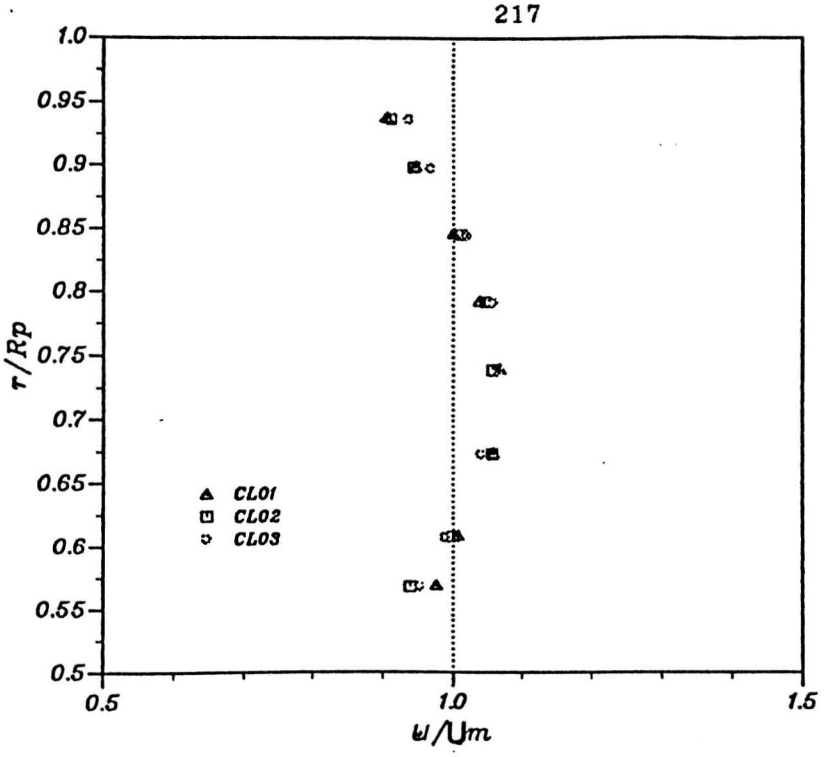

FIG. 8.21 MEASURED AXIAL VELOCITY PROFILES

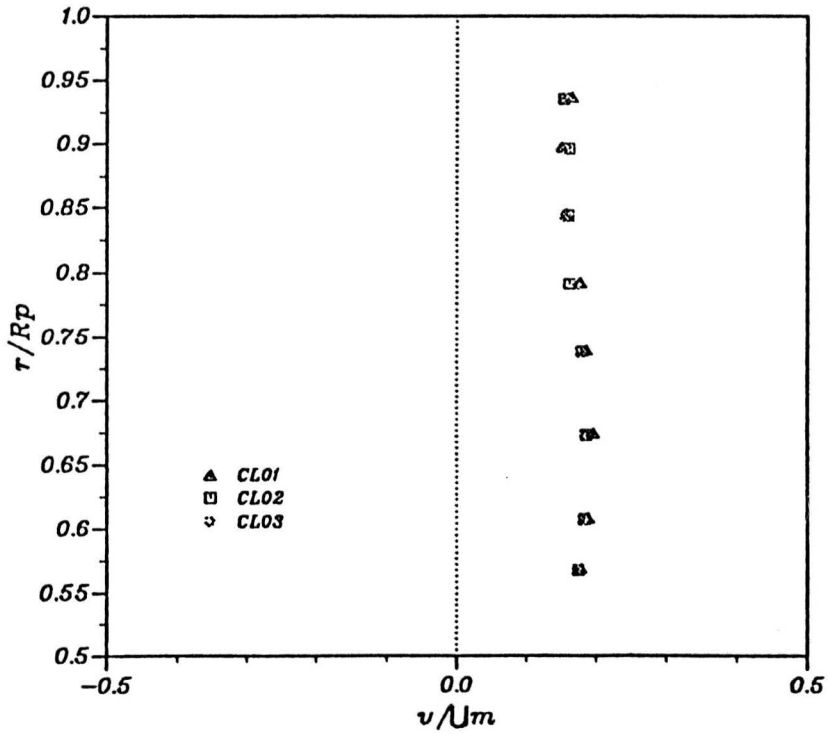

FIG. 8.22 MEASURED CIRCUMFERENTIAL VELOCITY PROFILES

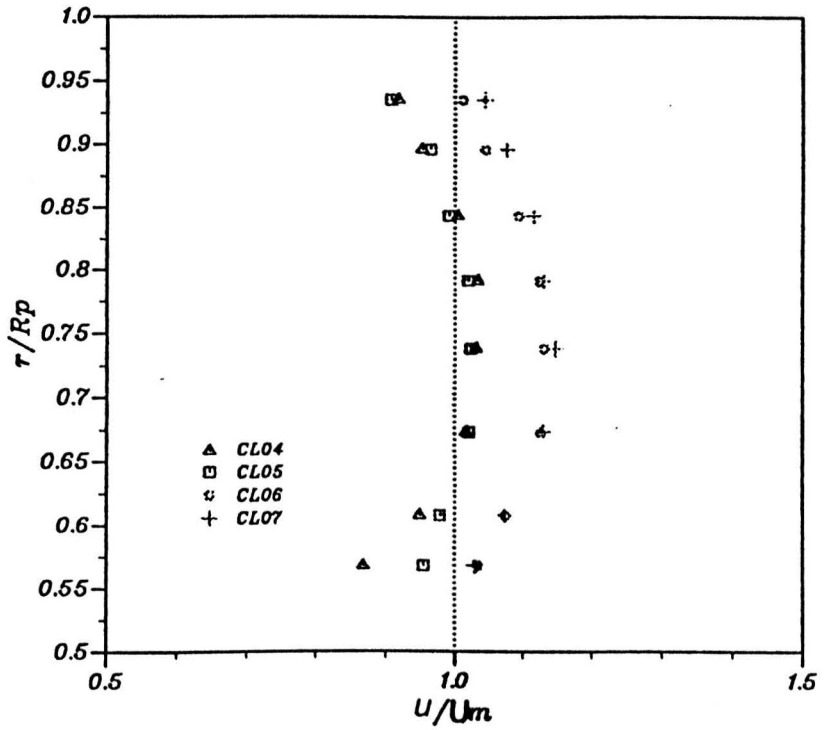

FIG. 8.23 MEASURED AXIAL VELOCITY PROFILES

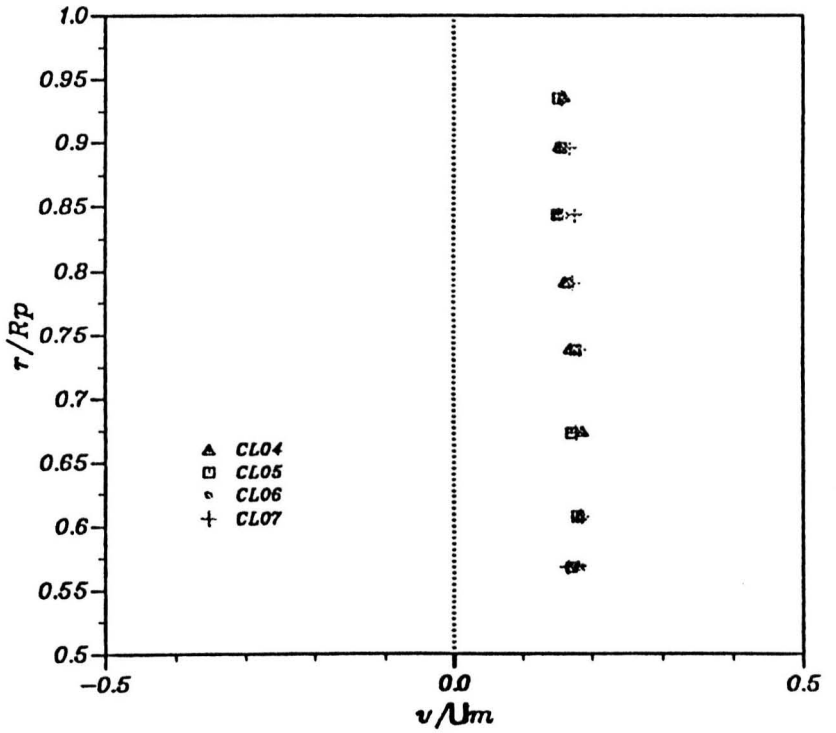

FIG. 8.24 MEASURED CIRCUMFERENTIAL VELOCITY PROFILES

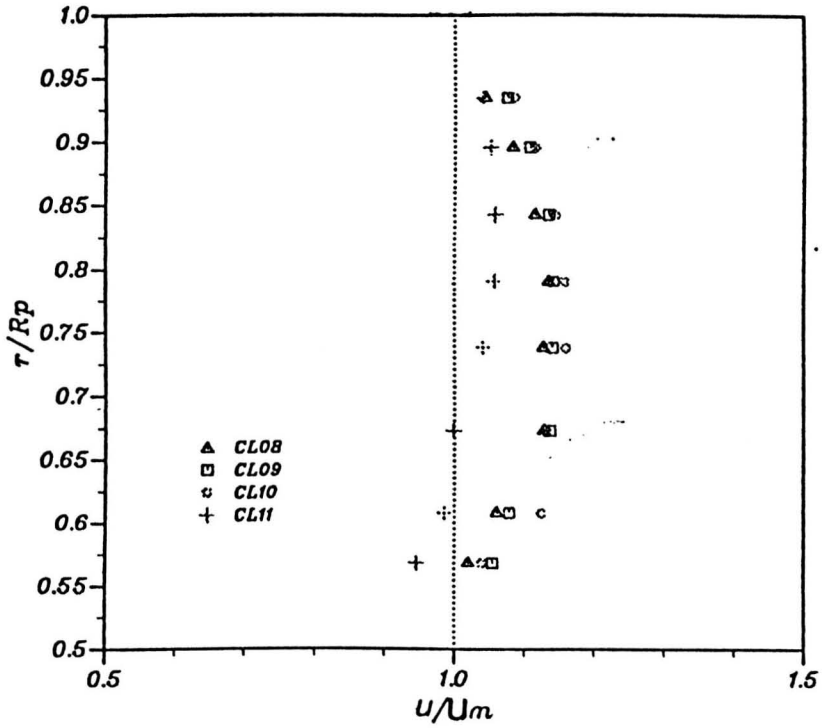

FIG. 8.25 MEASURED AXIAL VELOCITY PROFILES

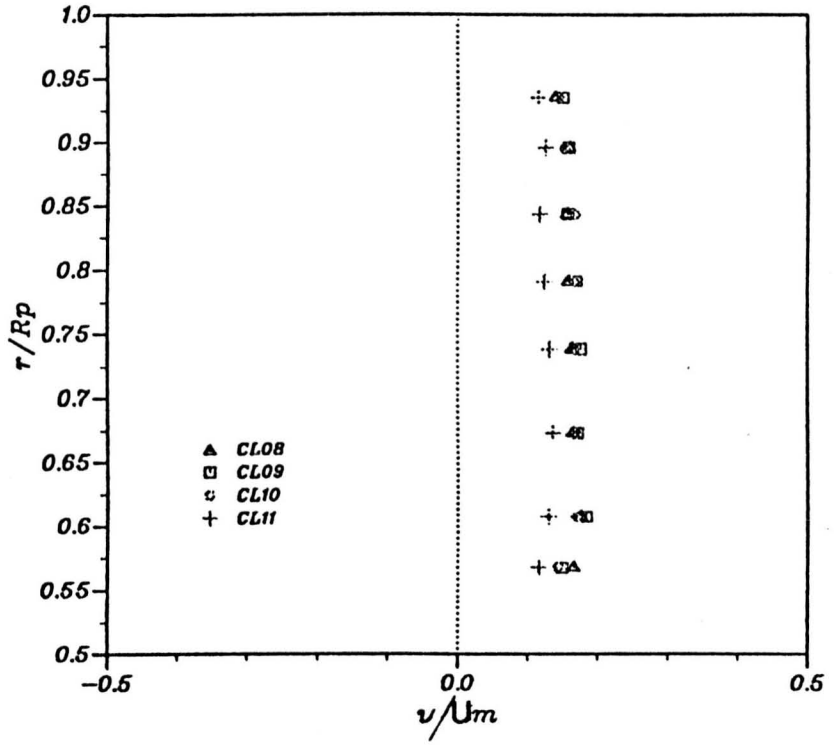

FIG. 8.26 MEASURED CIRCUMFERENTIAL VELOCITY PROFILES

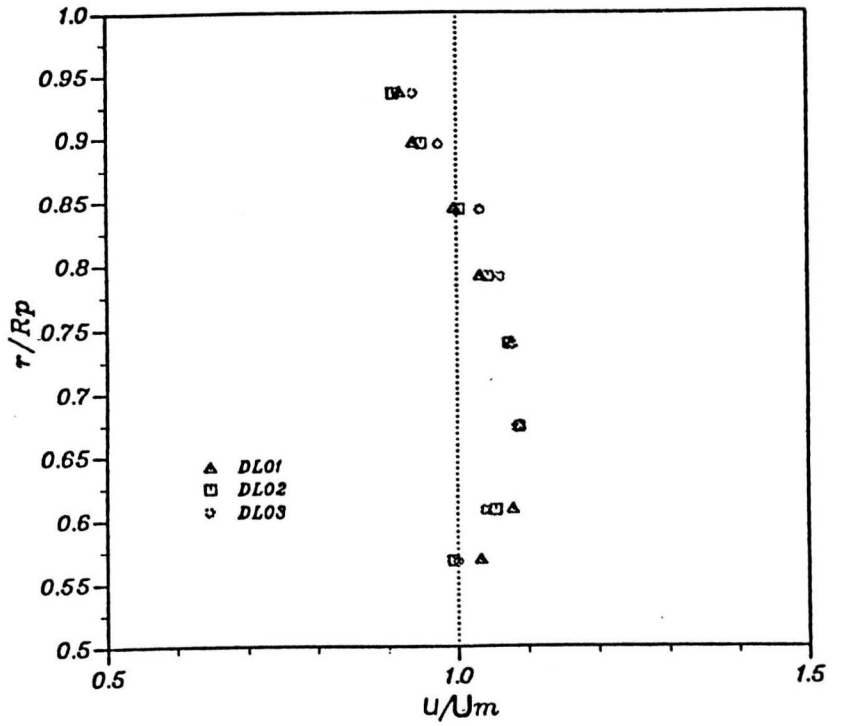

FIG. 8.27 MEASURED AXIAL VELOCITY PROFILES

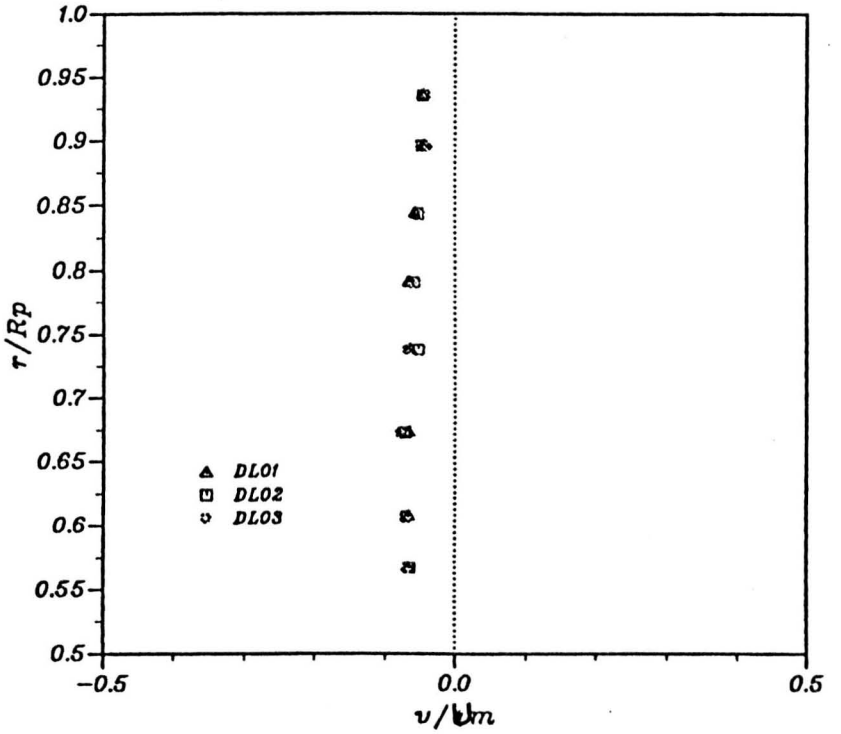

FIG. 8.28 MEASURED CIRCUMFERENTIAL VELOCITY PROFILES

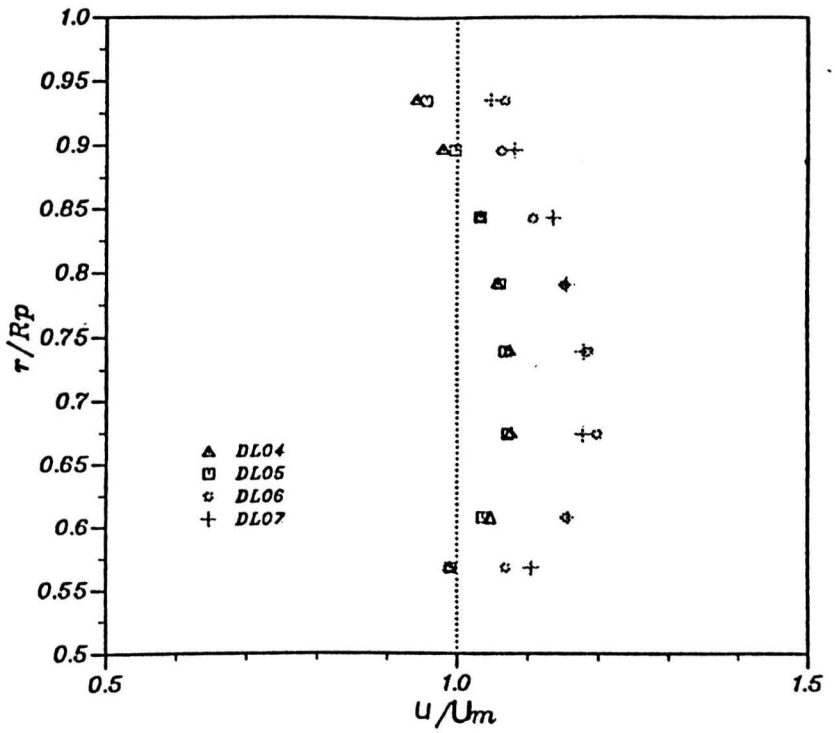

FIG. 8.29 MEASURED AXIAL VELOCITY PROFILES

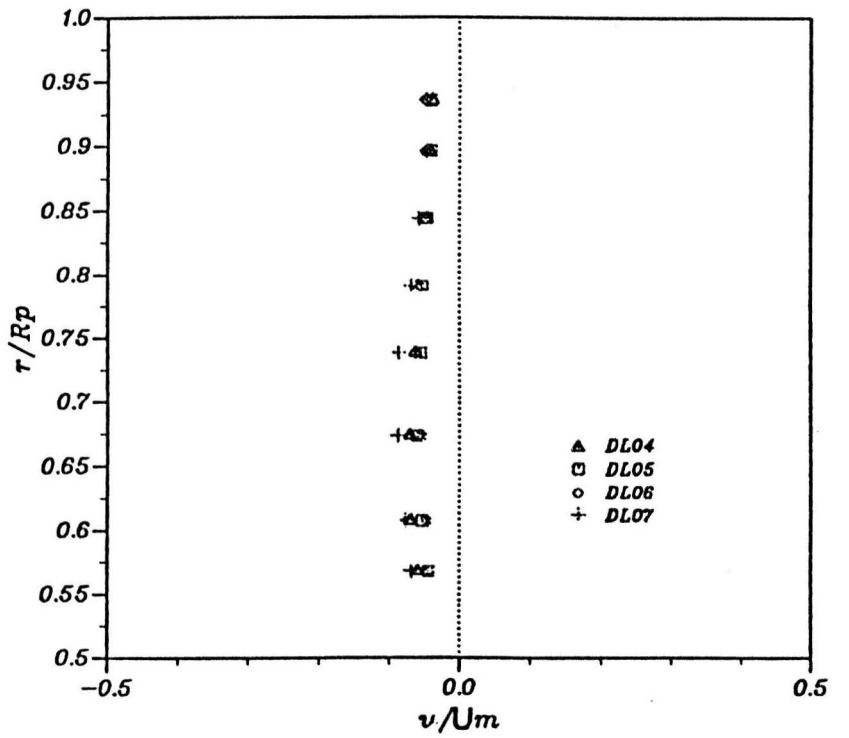

FIG. 8.30 MEASURED CIRCUMFERENTIAL VELOCITY PROFILES

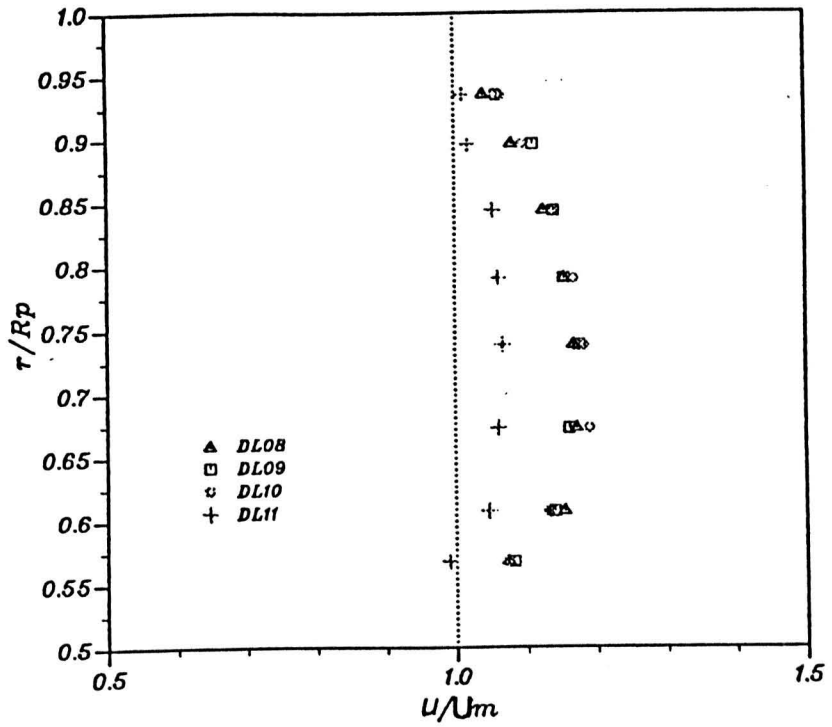

FIG. 8.31 MEASURED AXIAL VELOCITY PROFILES

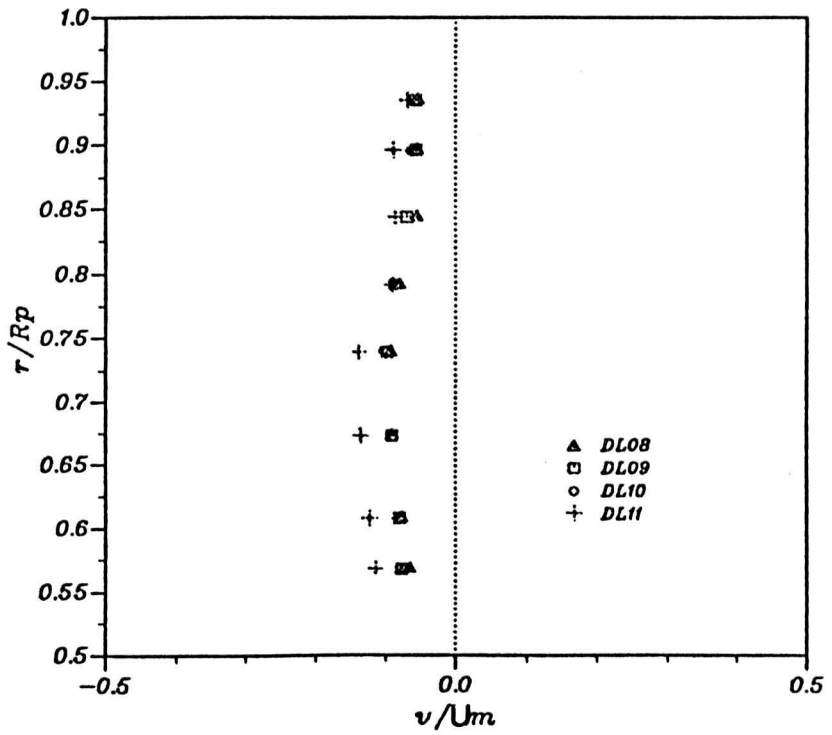

FIG. 8.32 MEASURED CIRCUMFERENTIAL VELOCITY PROFILES

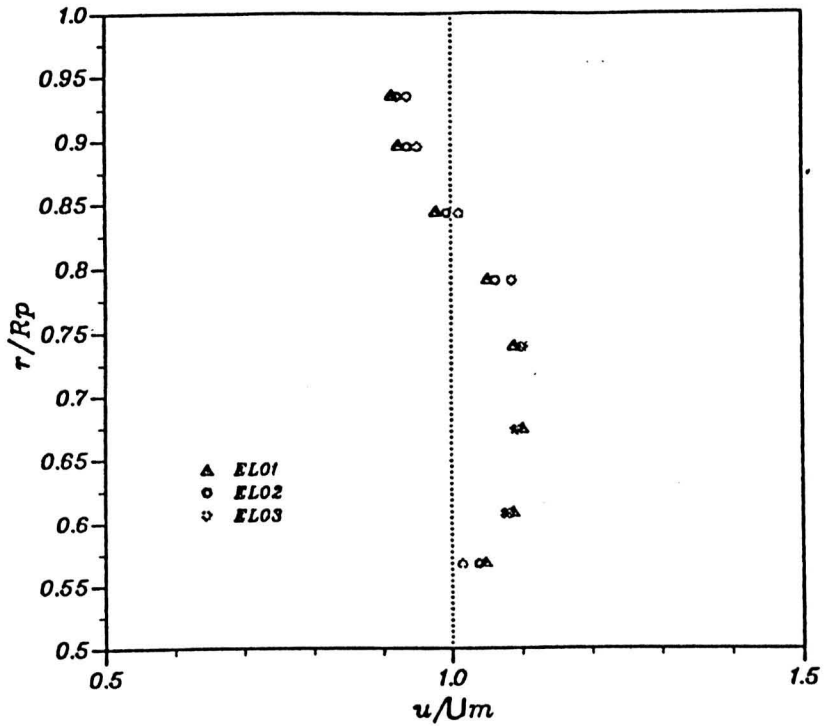

FIG. 8.33 MEASURED AXIAL VELOCITY PROFILES

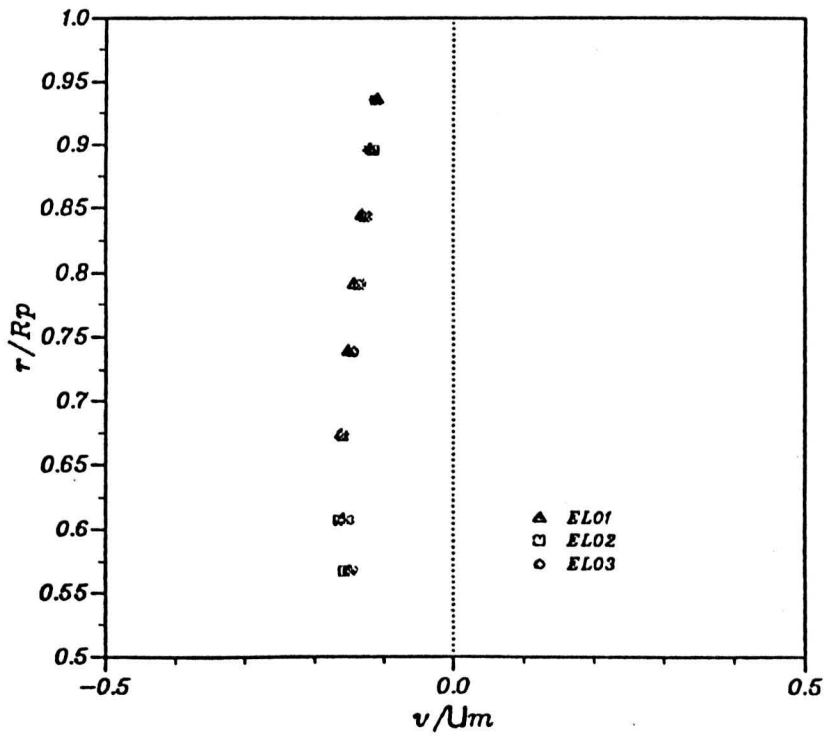

FIG. 8.34 MEASURED CIRCUMFERENTIAL VELOCITY PROFILE

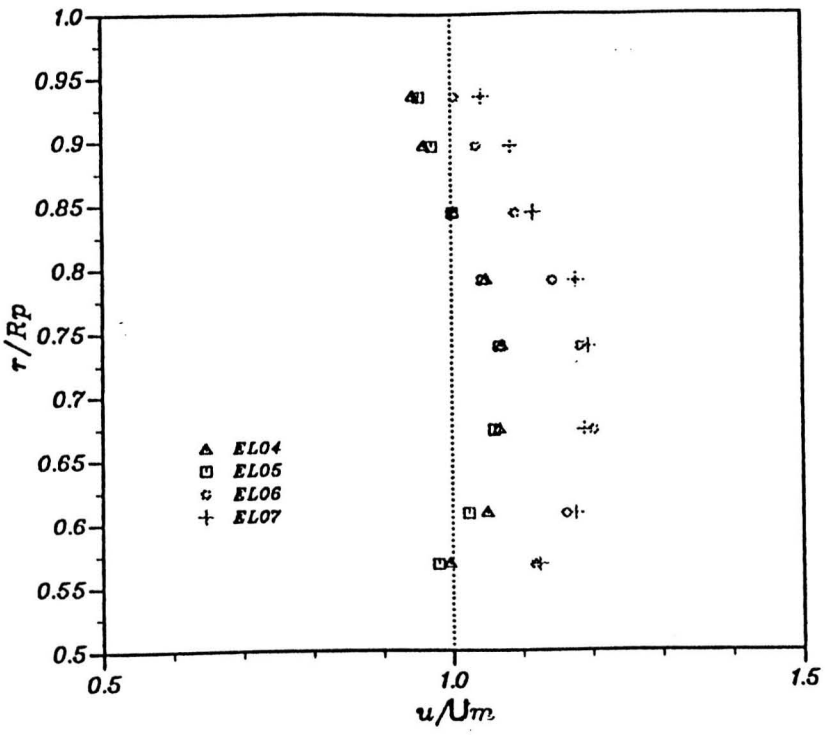

FIG. 8.35 MEASURED AXIAL VELOCITY PROFILES

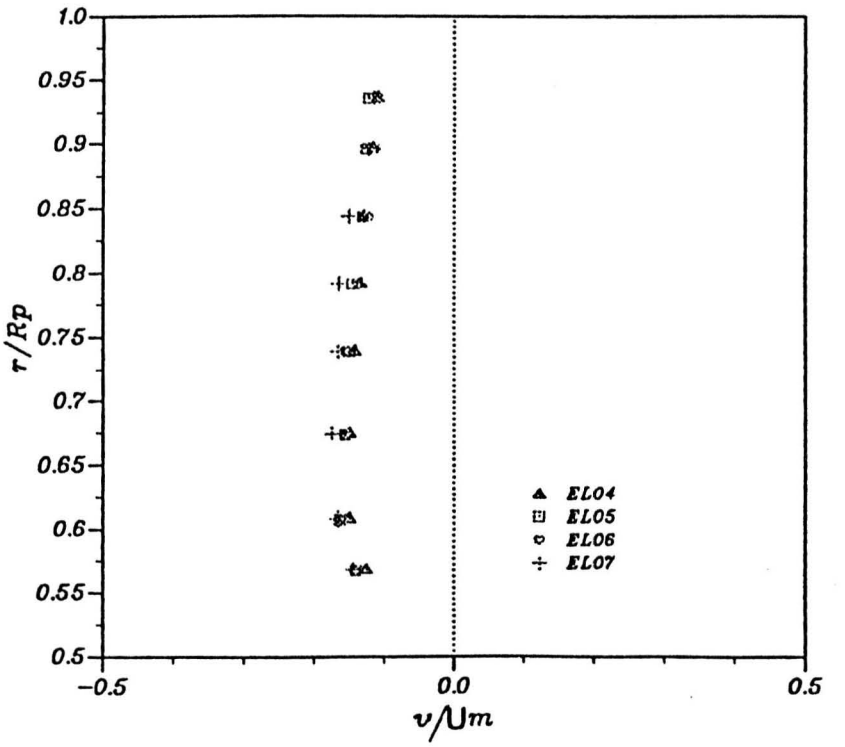

FIG. 8.36 MEASURED CIRCUMFERENTIAL VELOCITY PROFILE

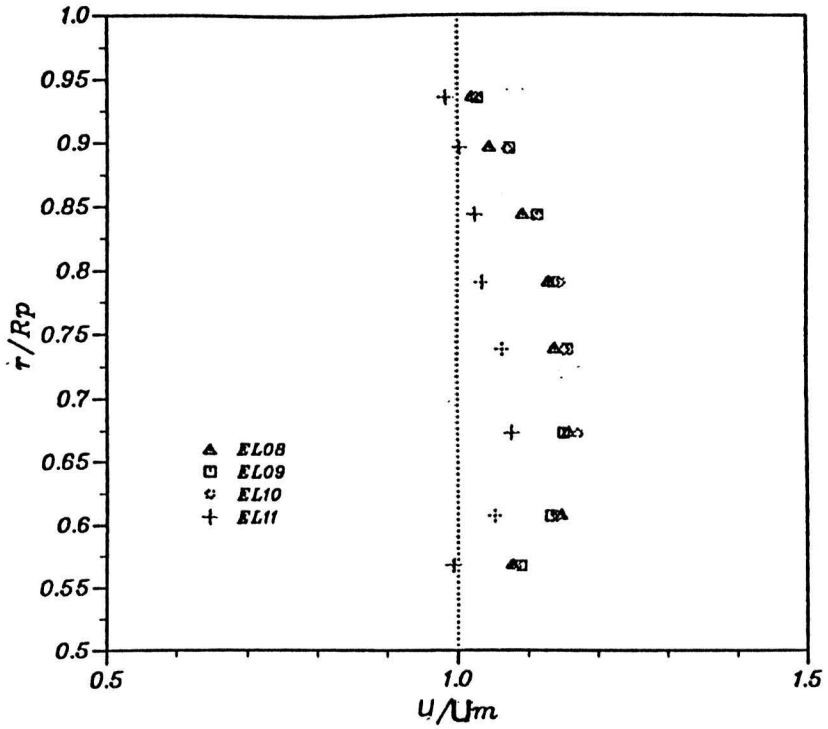

FIG. 8.37 MEASURED AXIAL VELOCITY PROFILES

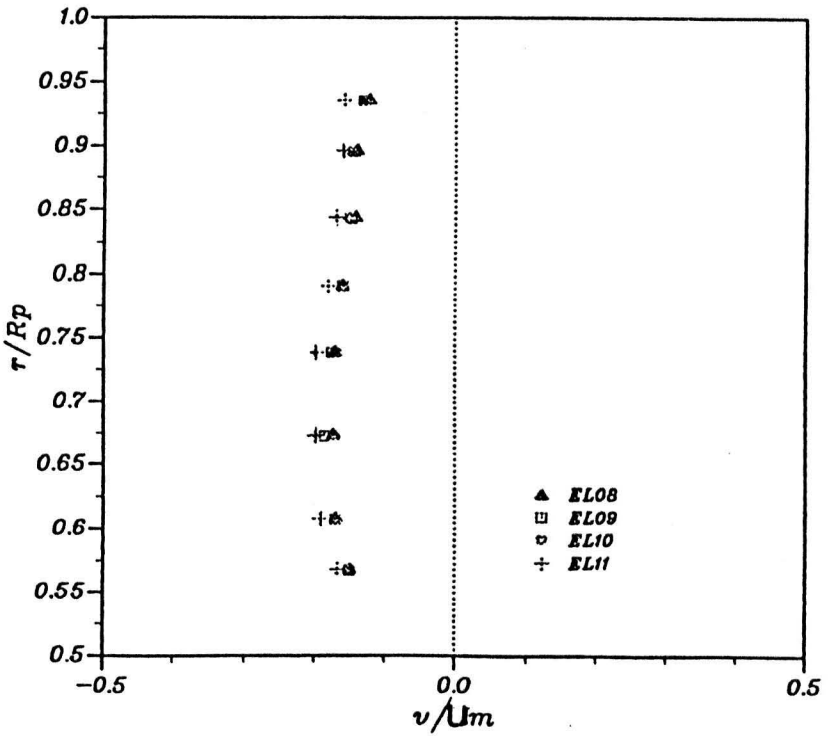

FIG. 8.38 MEASURED CIRCUMFERENTIAL VELOCITY PROFILE

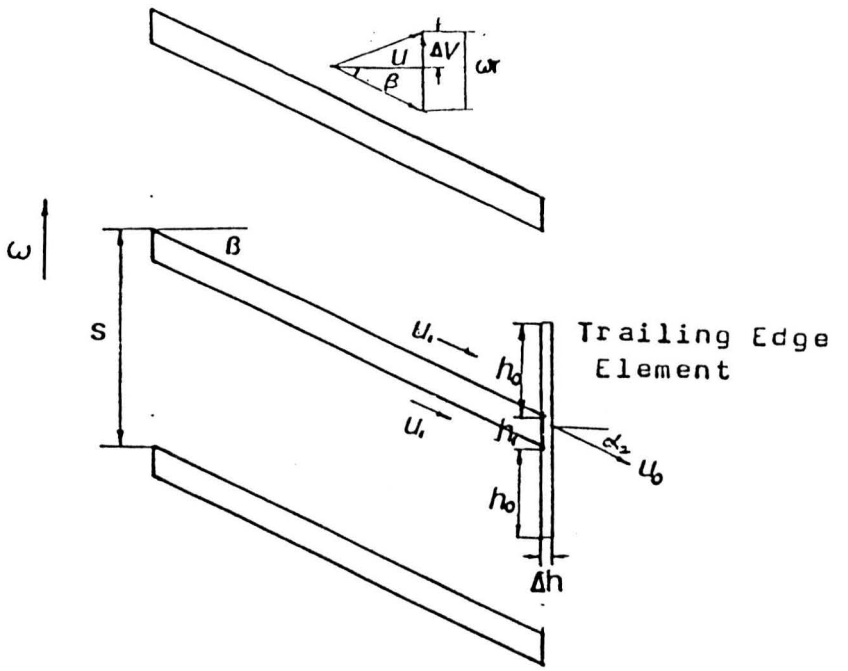

FIG 8.39 FLOWMETER TRAILING EDGE FLOW

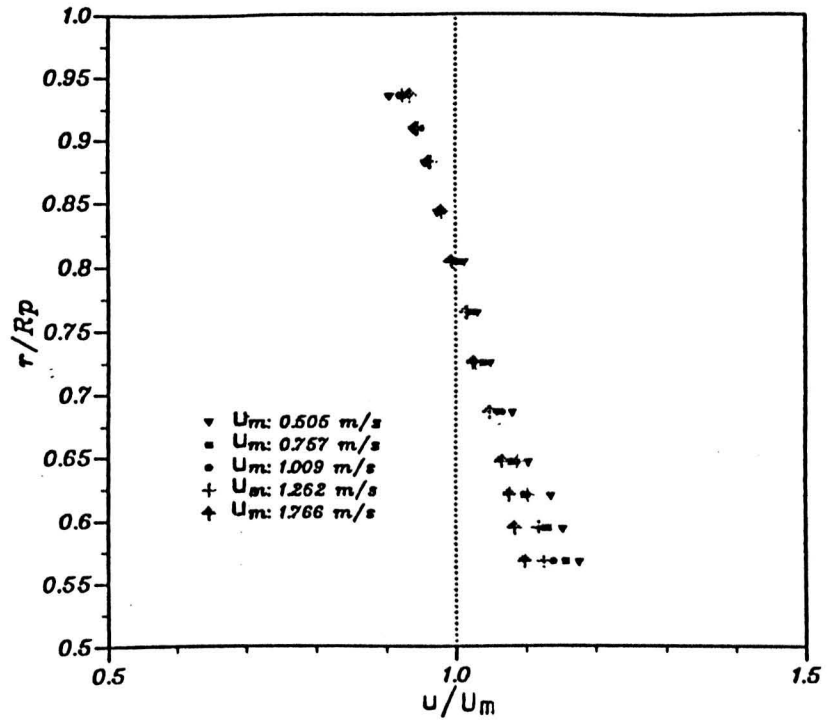

FIG. 8.40 MEASURED INLET AXIAL VELOCITY PROFILES(case A)

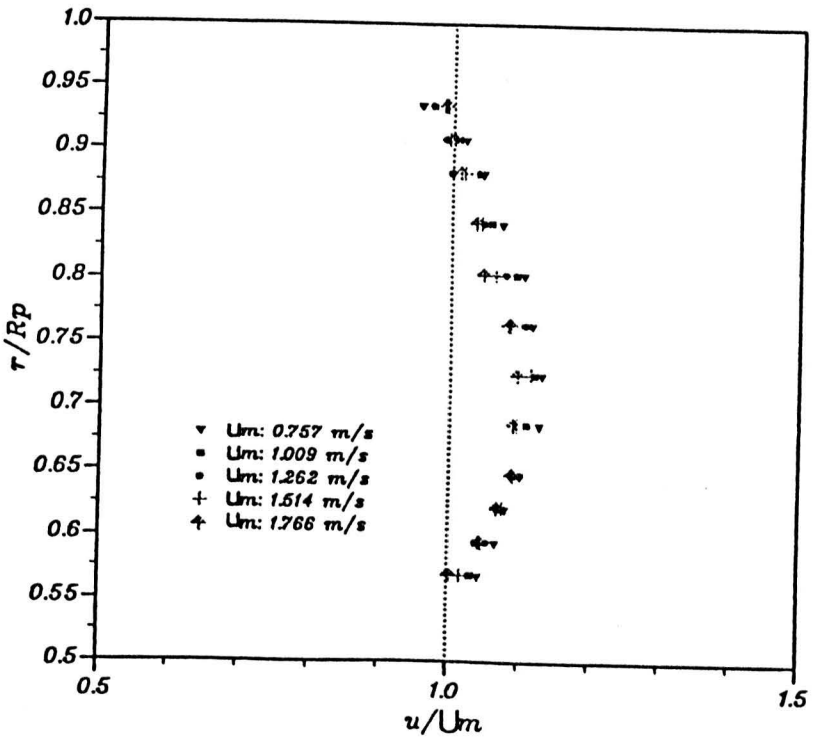

FIG. 8.41 MEASURED INLET AXIAL VELOCITY PROFILES(case B)

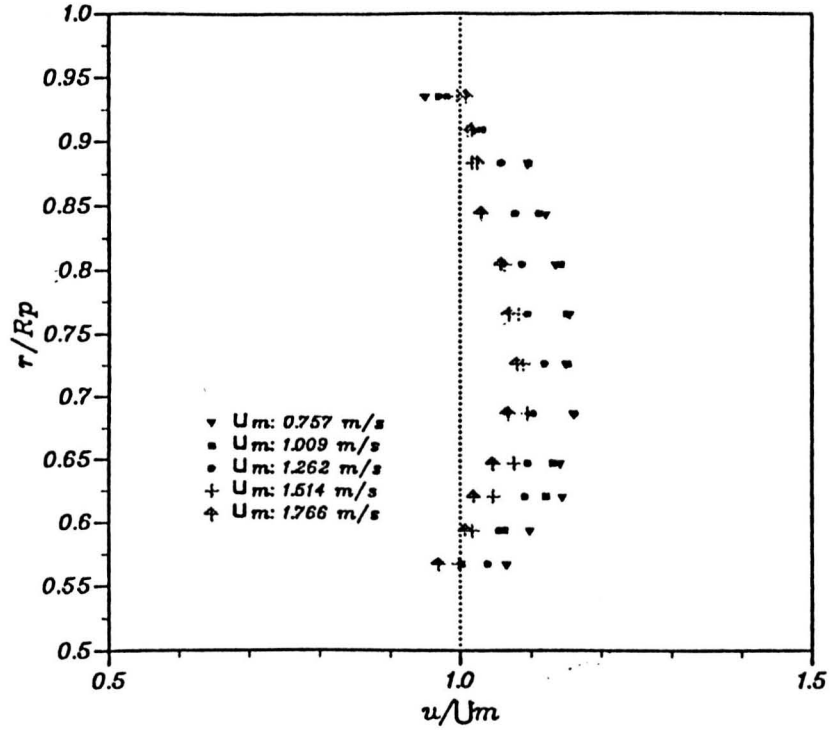

FIG. 8.42 MEASURED INLET AXIAL VELOCITY PROFILES(case C)

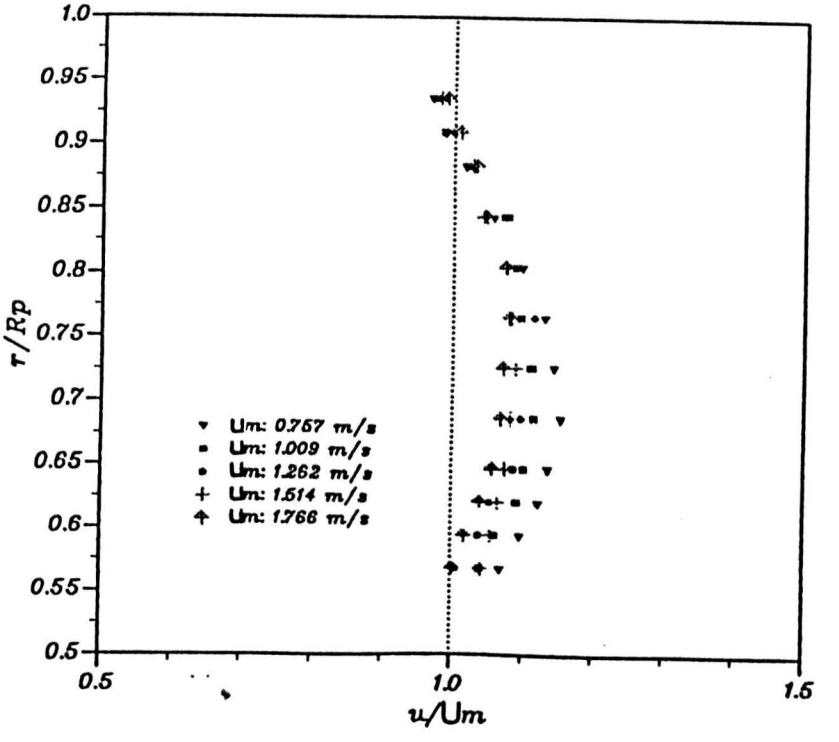

FIG. 8.43 MEASURED INLET XAILA VELOCITY PROFILES(case D)

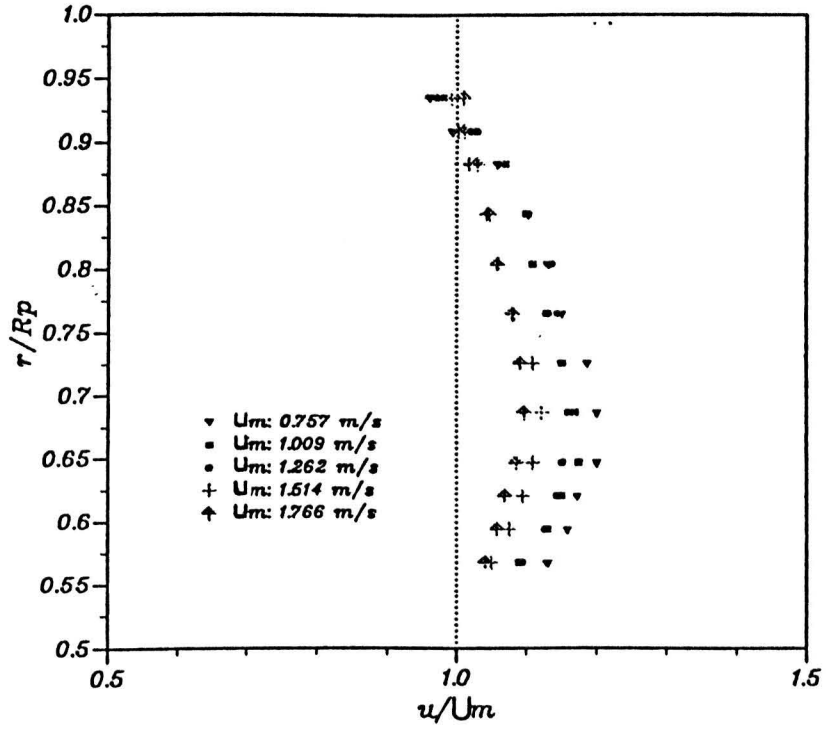

FIG. 8.44 MEASURED INLET AXIAL VELOCITY PROFILES(case E)

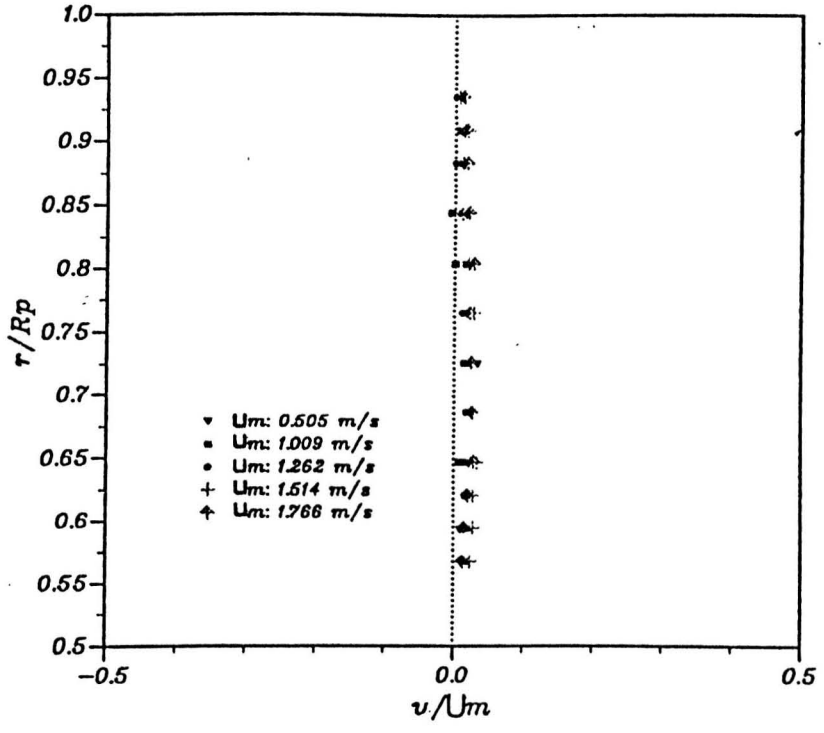

FIG. 8.45 MEASURED INLET CIRCUMFERENTIAL VELOCITY PROFILES(Case A)

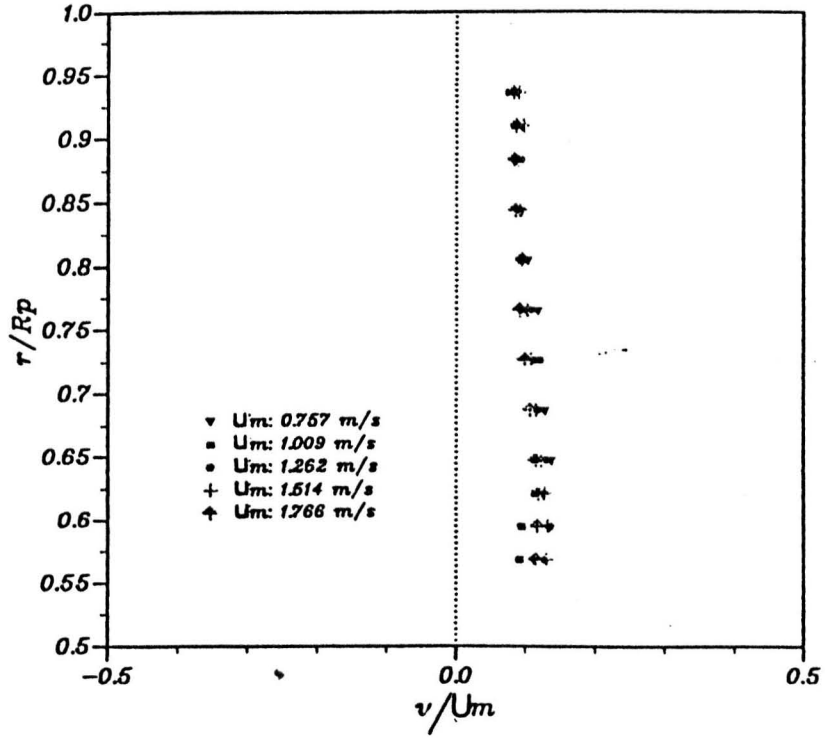

FIG. 8.46 MEASURED INLET CIRCUMFERENTIAL VELOCITY PROFILES(Case B)

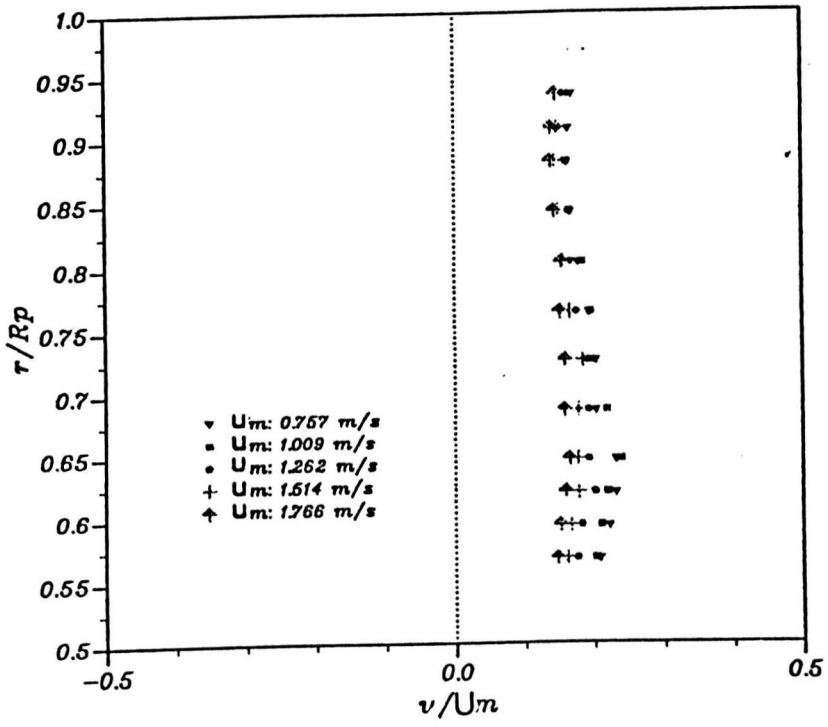

FIG. 8.47 MEASURED INLET CIRCUMFERENTIAL VELOCITY PROFILES(Case C)

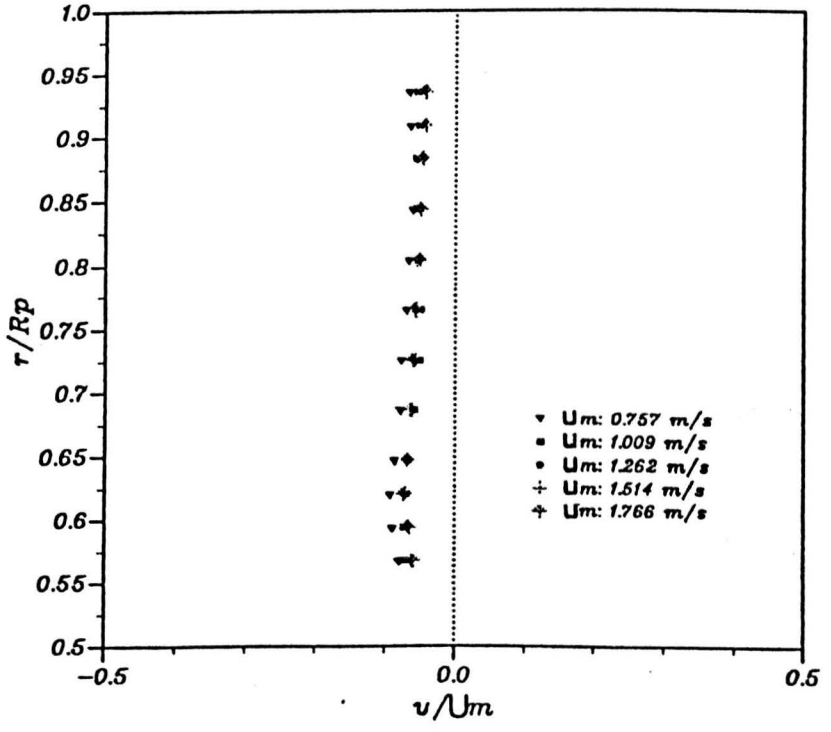

FIG. 8.48 MEASURED INLET CIRCUMFERENTIAL VELOCITY PROFILES(Case D)

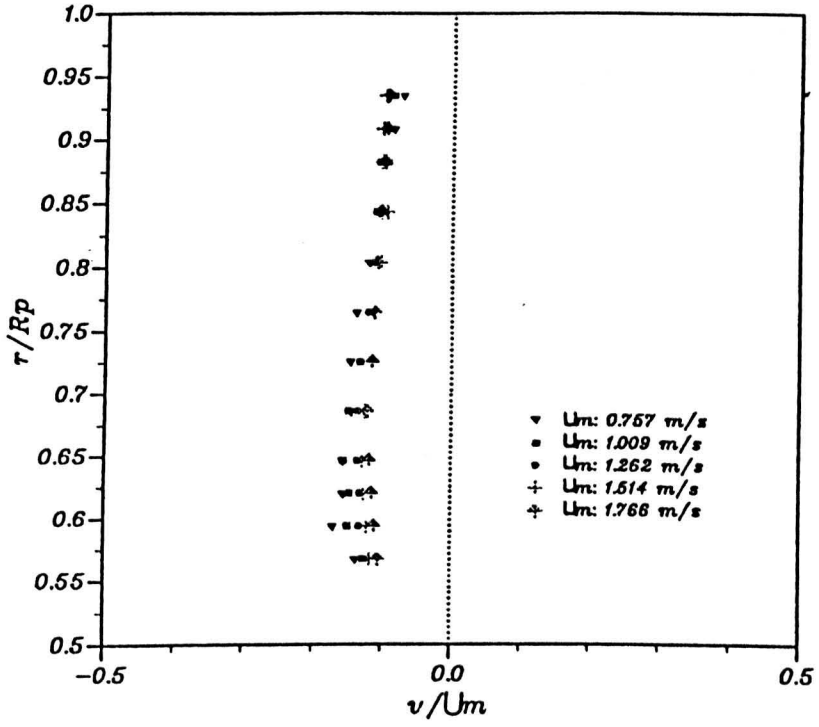

FIG. 8.49 *MEASURED INLET CIRCUMFERENTIAL VELOCITY PROFILES(Case E)*

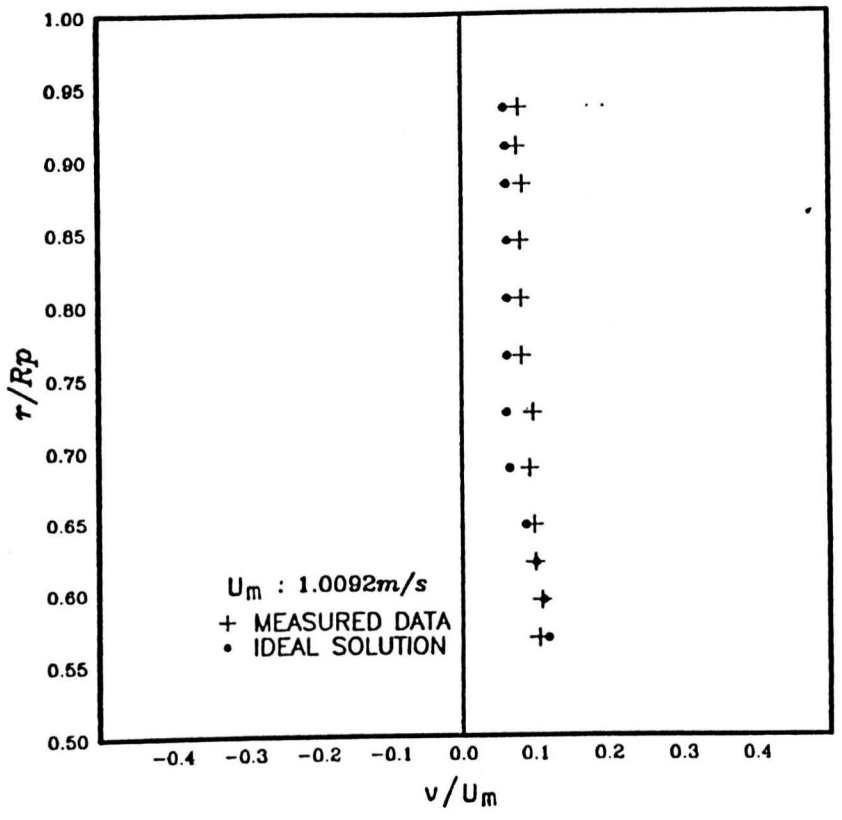

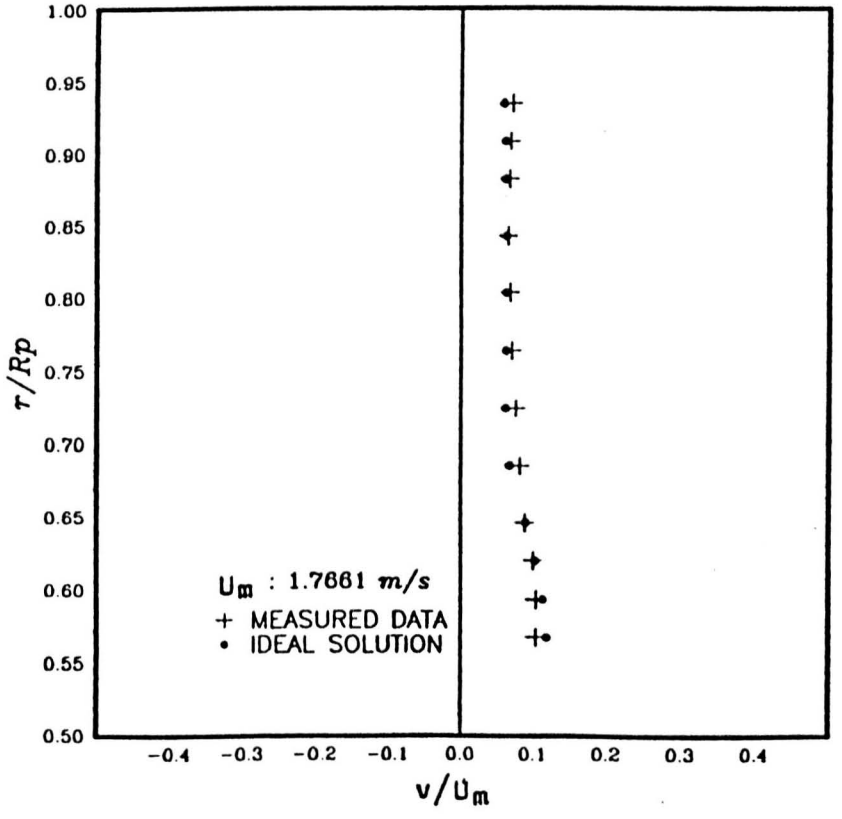

FIG. 8.50 INLET CIRCUMFERENTIAL VELOCITY COMPARISON(Case B)

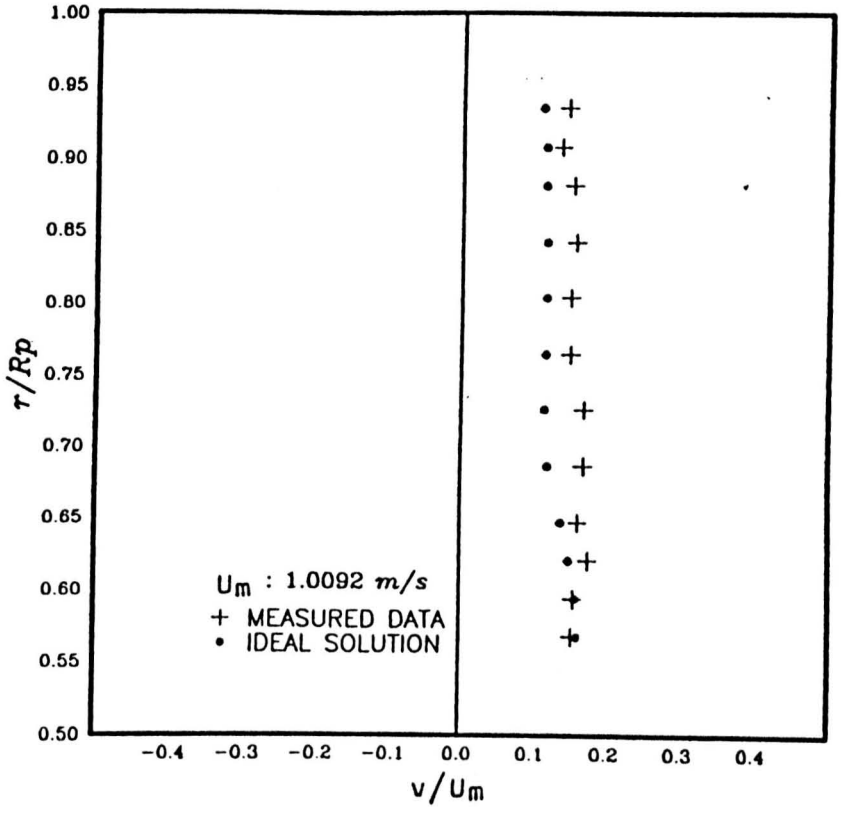

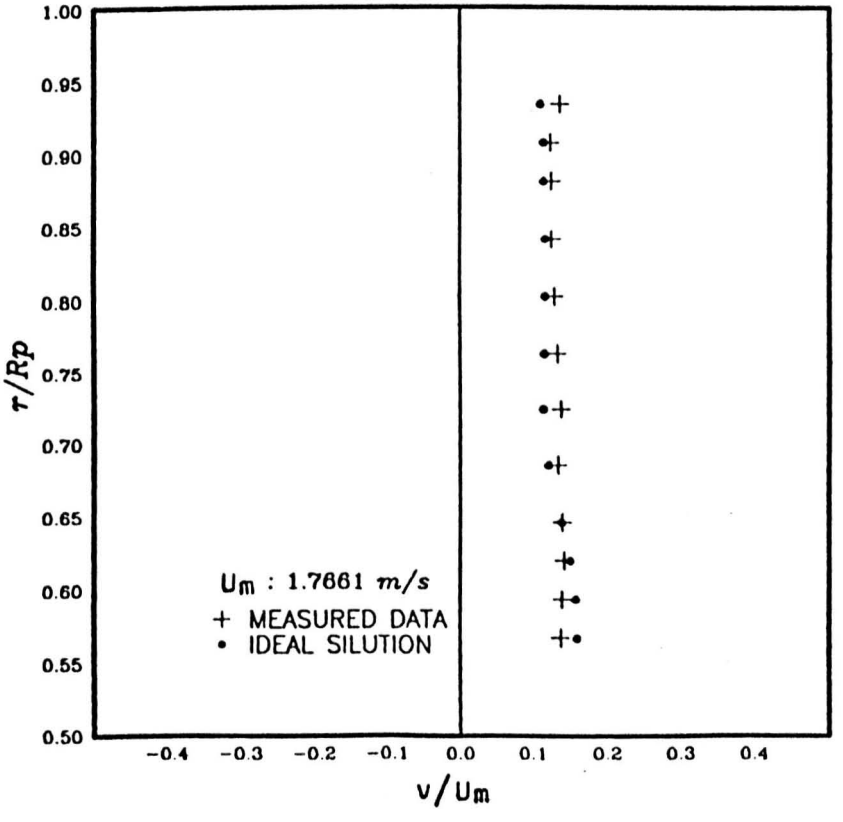

FIG. 8.51 INLET CIRCUMFERENTIAL VELOCITY COMPARISON(Case C)

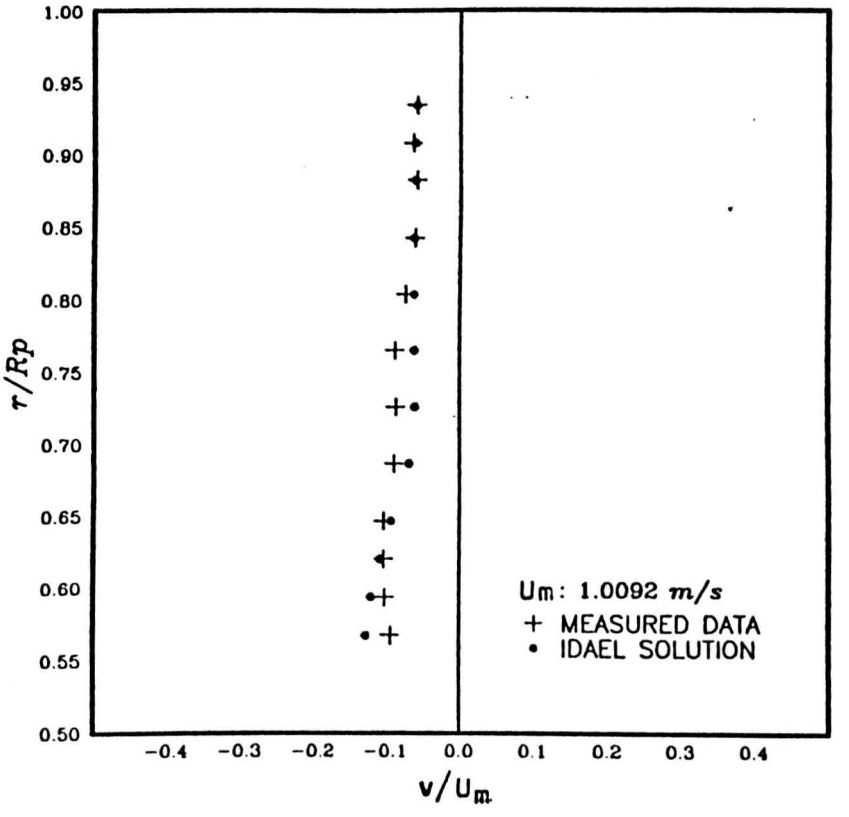

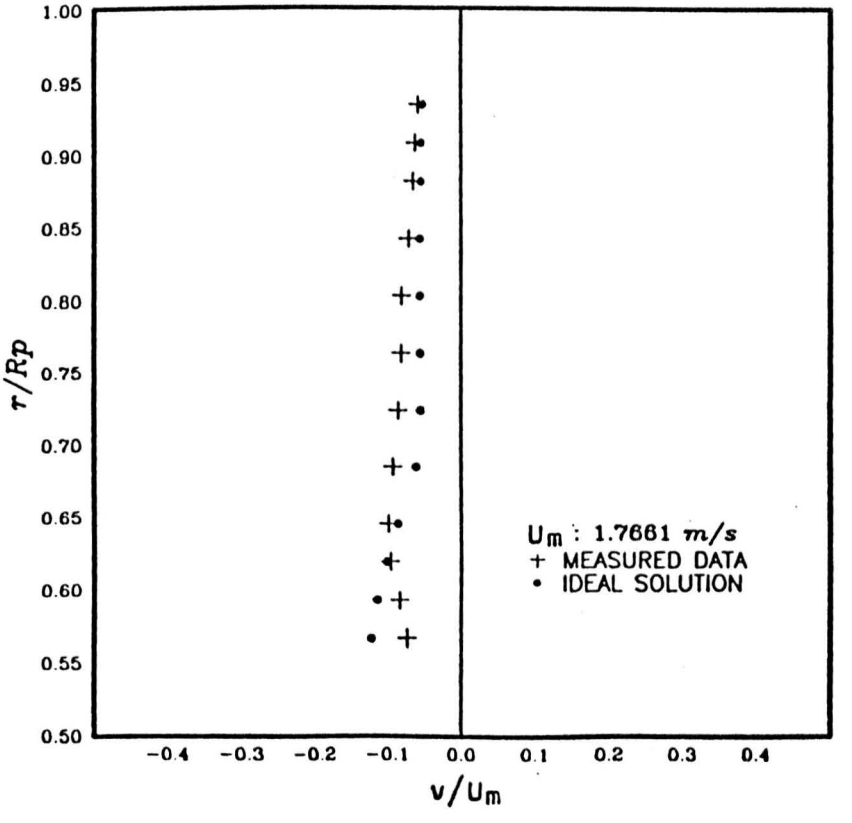

FIG. 8.52 INLET CIRCUMFERENTIAL VELOCITY COMPARISON(Case D)

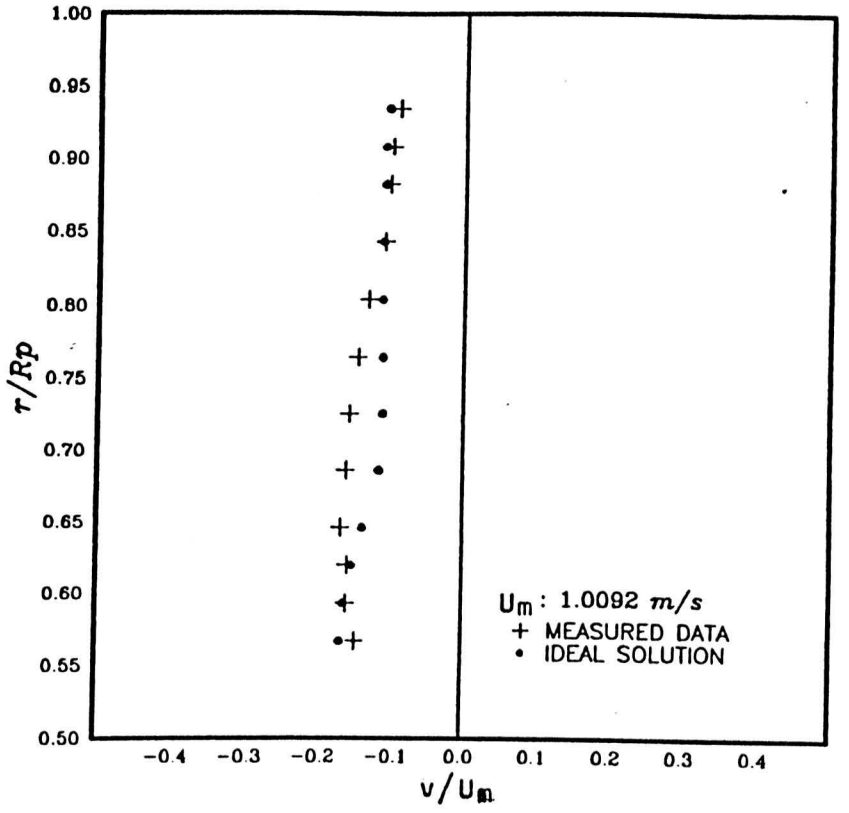

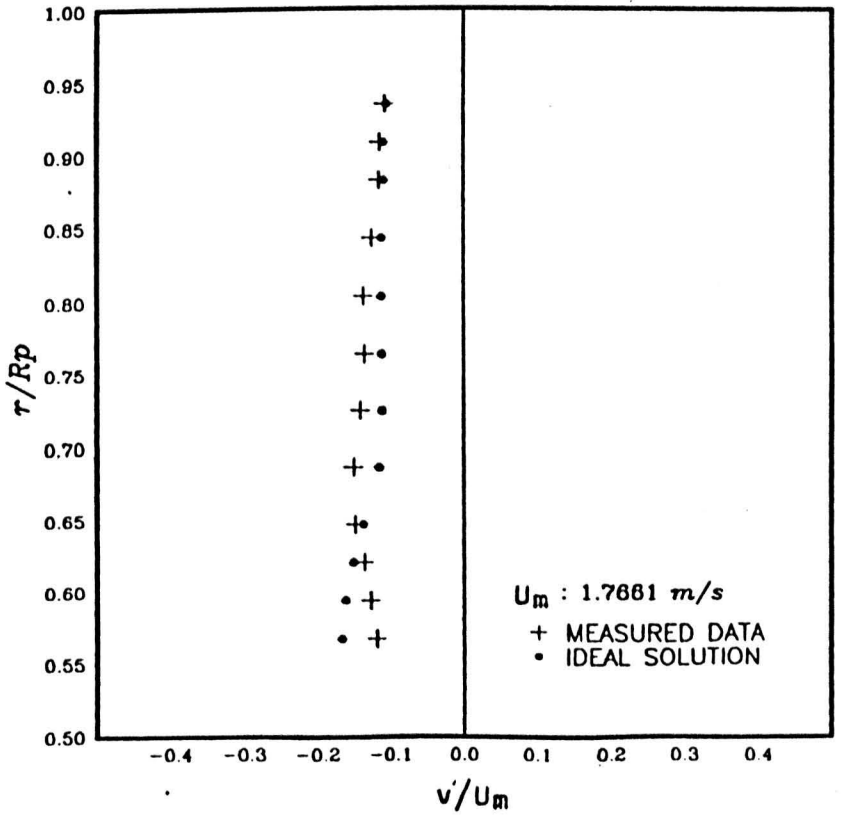

FIG. 8.53 INLET CIRCUMFERENTIAL VELOCITY COMPARISON(Case E)

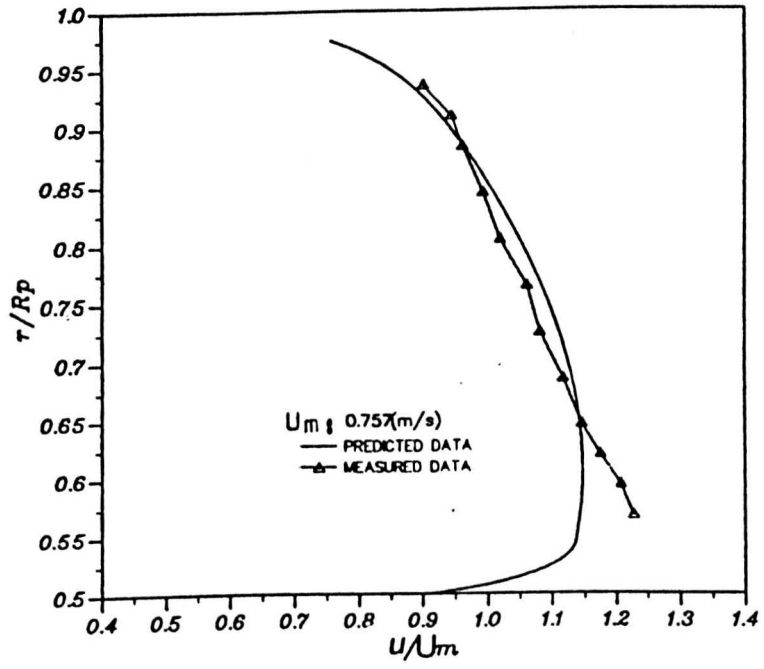

FIG. 8.54 INLET AXIAL VELOCITY PROFILE COMPARISON(U_m : 0.757m/s)

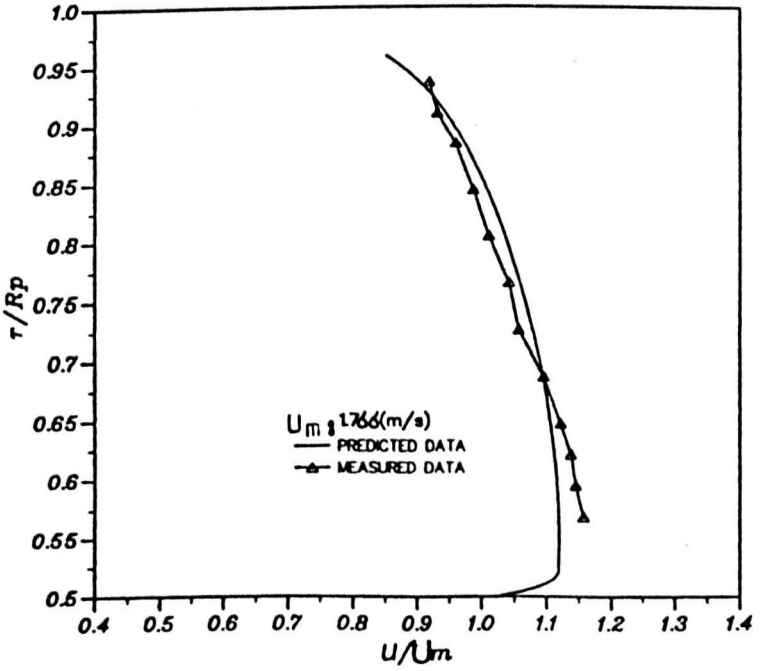

FIG. 8.55 INLET AXIAL VELOCITY PROFILE COMPARISON(U_m :1.766m/s)

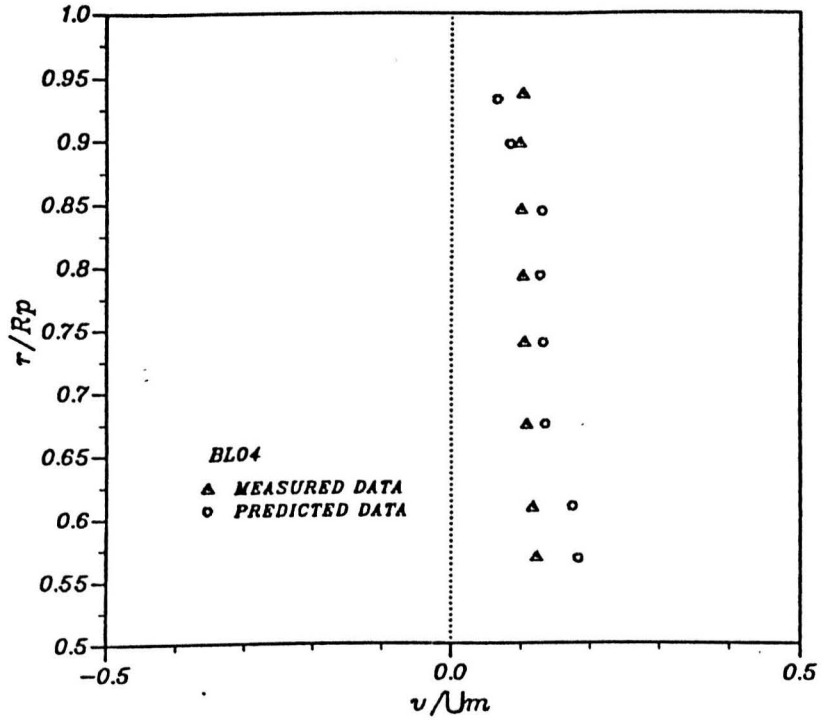

FIG. 8.56 CIRCUMFERENTIAL VELOCITY PROFILE COMPARISON

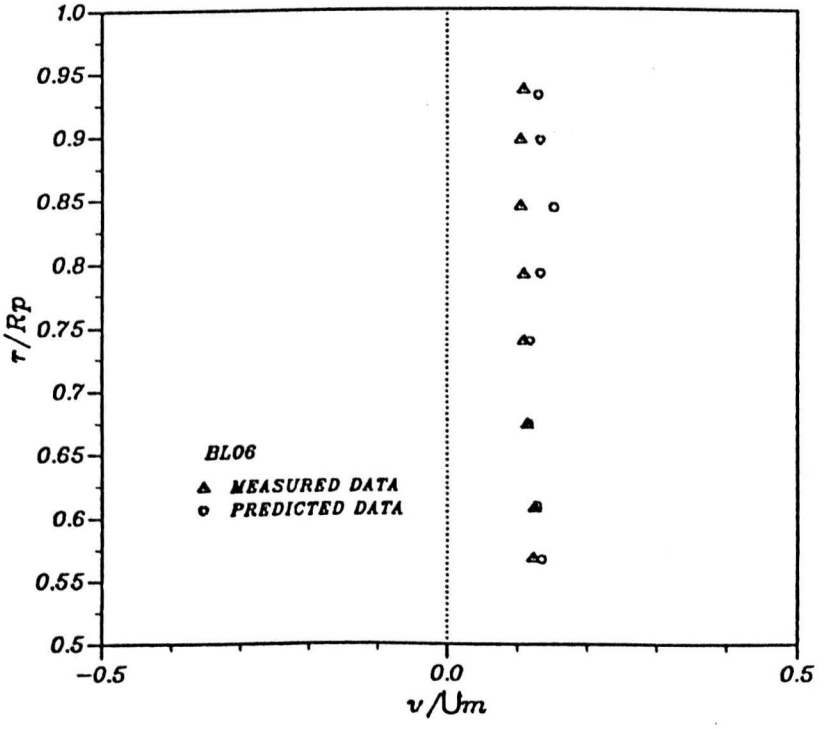

FIG. 8.57 CIRCUMFERENTIAL VELOCITY PROFILE COMPARISON

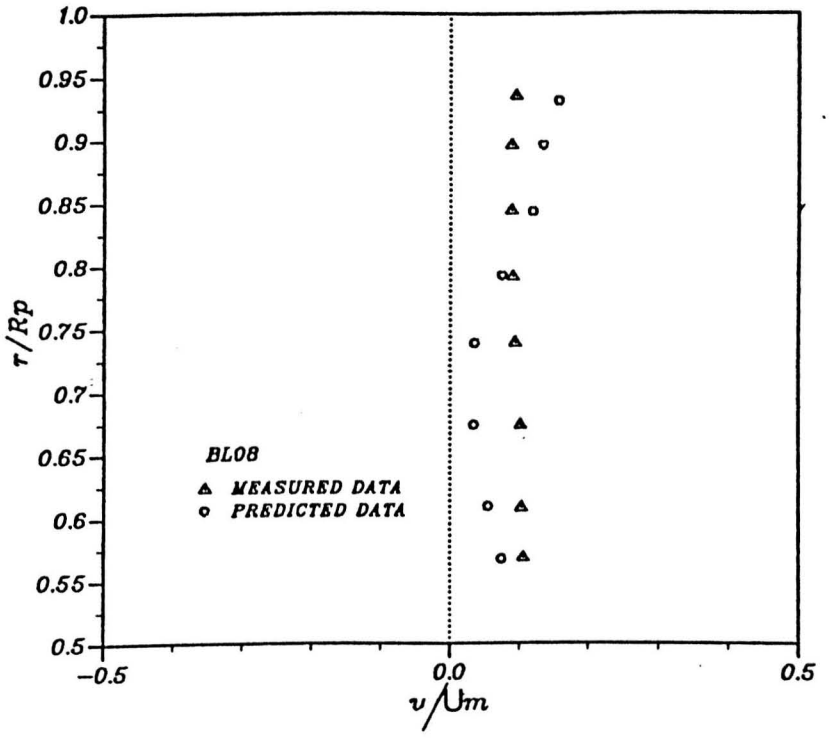

FIG. 8.58 CIRCUMFERENTIAL VELOCITY PROFILE COMPARISON

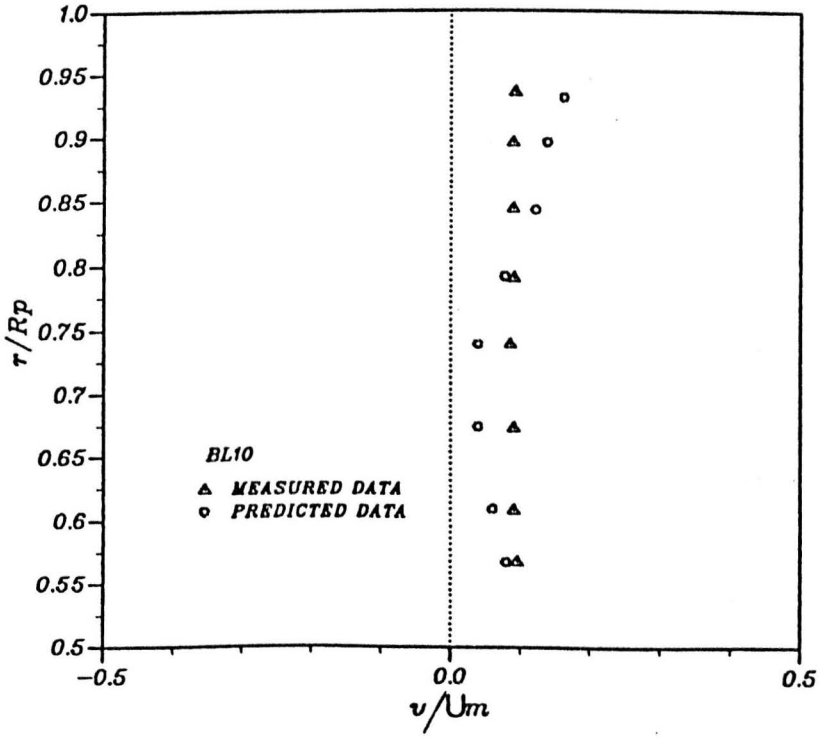

FIG. 8.59 CIRCUMFERENTIAL VELOCITY PROFILE COMPARISON

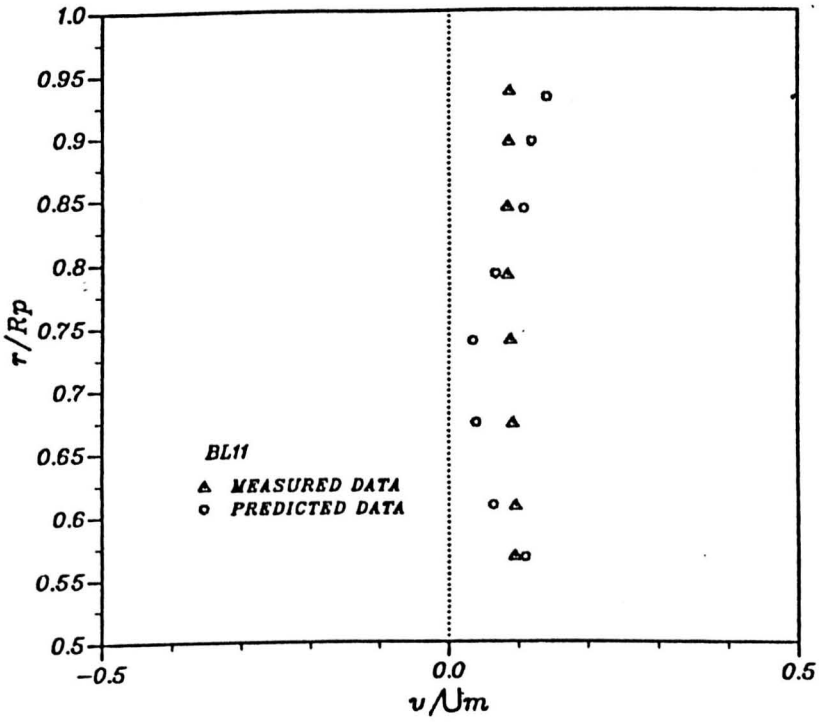

FIG. 8.60 CIRCUMFERENTIAL VELOCITY PROFILE COMPARISON

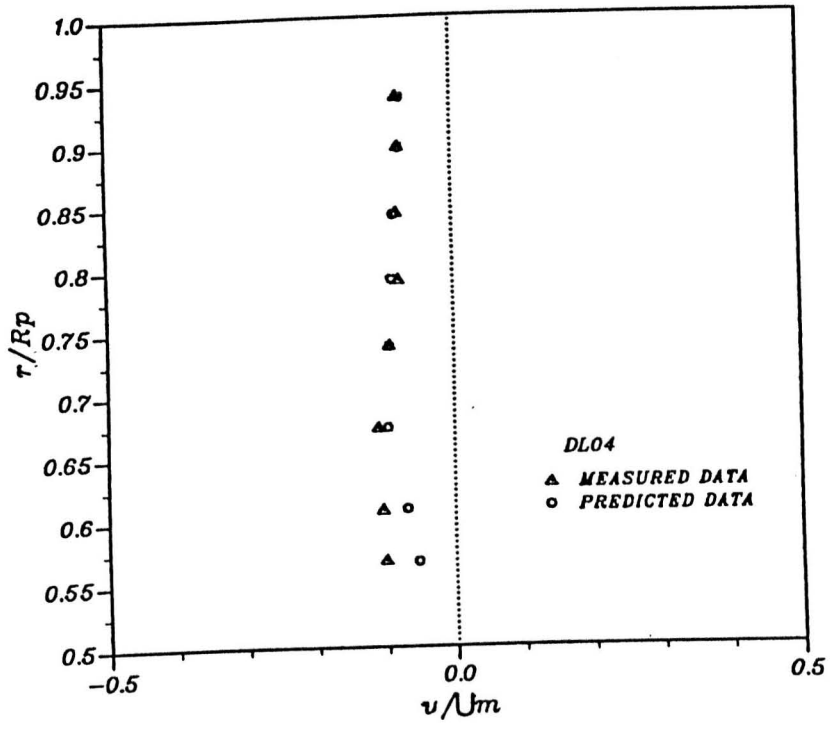

FIG. 8.61 CIRCUMFERENTIAL VELOCITY PROFILE COMPARISON

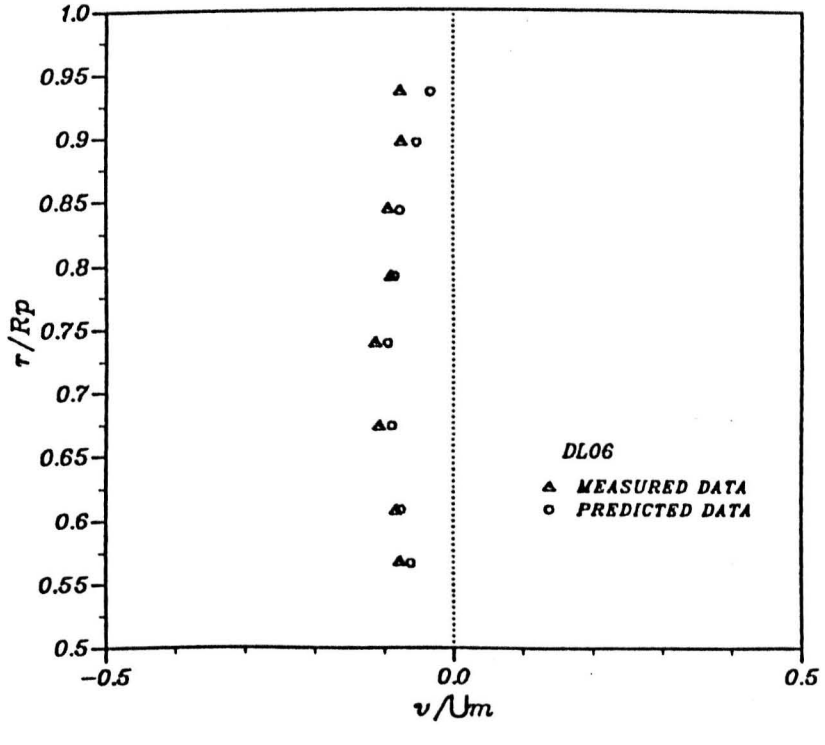

FIG. 8.62 CIRCUMFERENTIAL VELOCITY PROFILE COMPARISON

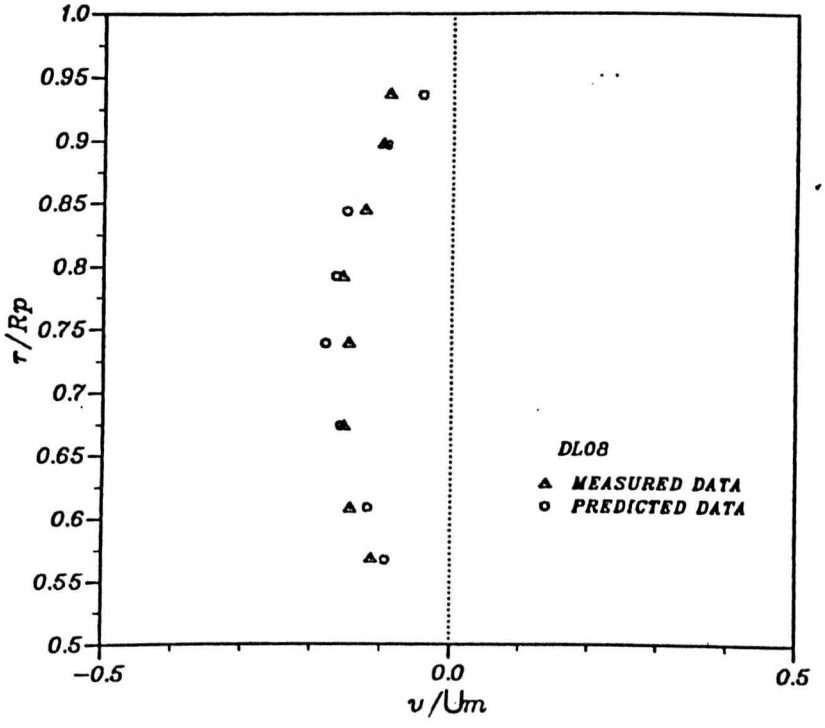

FIG. 8.63 CIRCUMFERENTIAL VELOCITY PROFILE COMPARISON

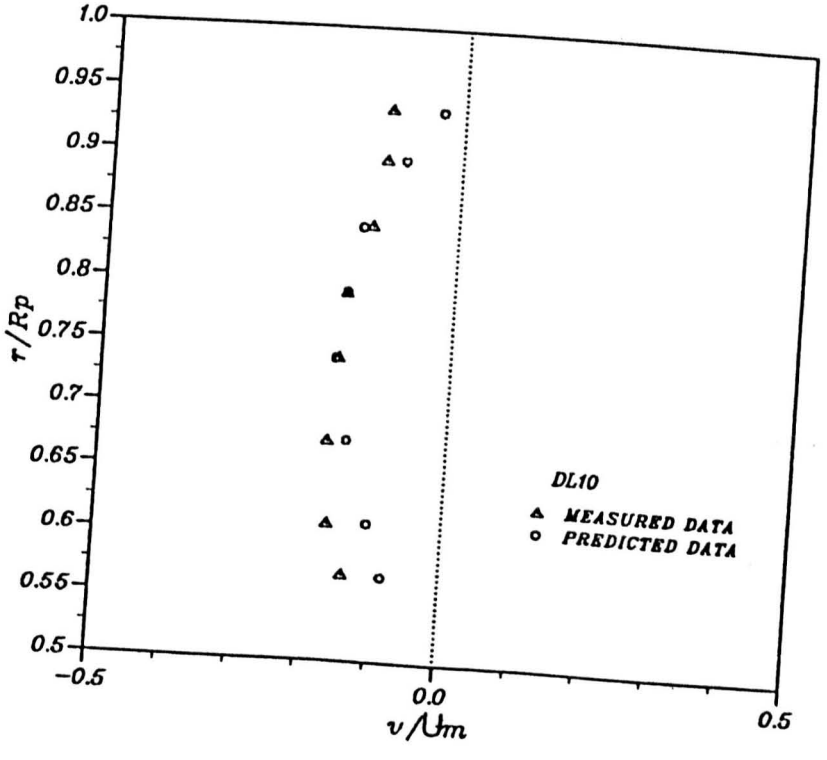

FIG. 8.64 CIRCUMFERENTIAL VELOCITY PROFILE COMPARISON

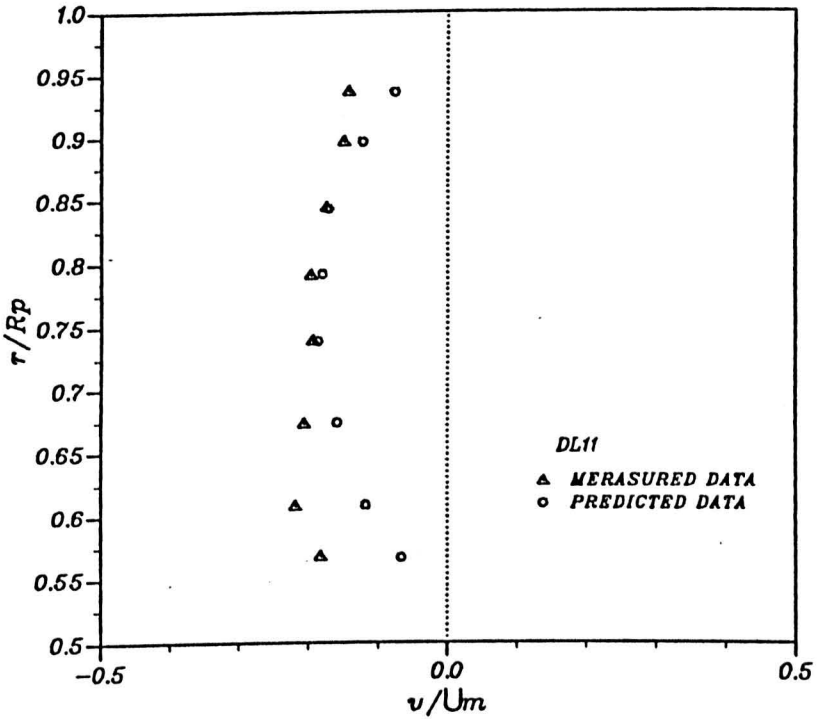

FIG. 8.65 CIRCUMFERENTIAL VELOCITY PROFILE COMPARISON

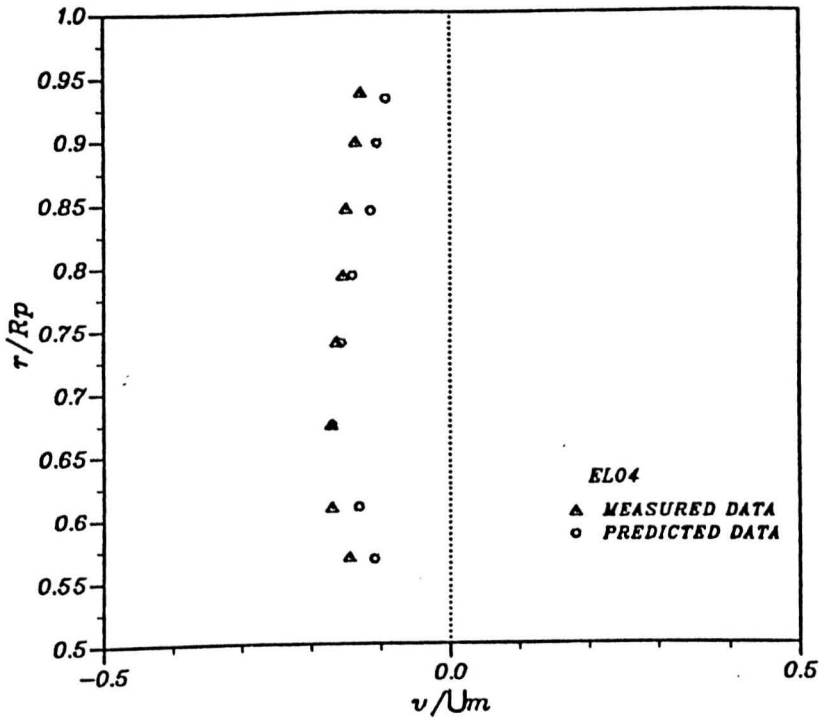

FIG. 8.66 CIRCUMFERENTIAL VELOCITY PROFILE COMPARISON

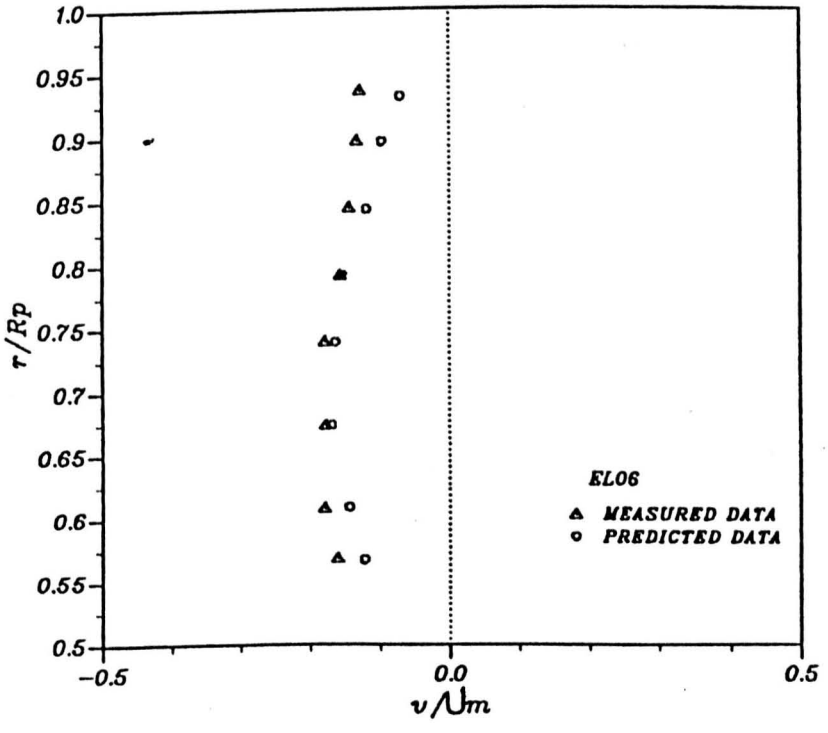

FIG. 8.67 CIRCUMFERENTIAL VELOCITY PROFILE COMPARISON

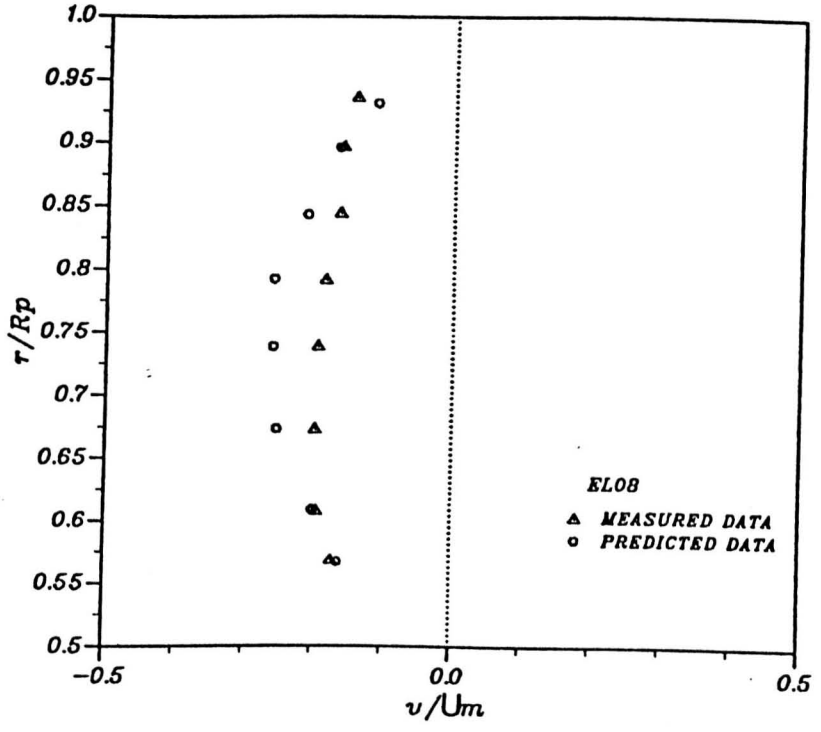

FIG. 8.68 CIRCUMFERENTIAL VELOCITY PROFILE COMPARISON

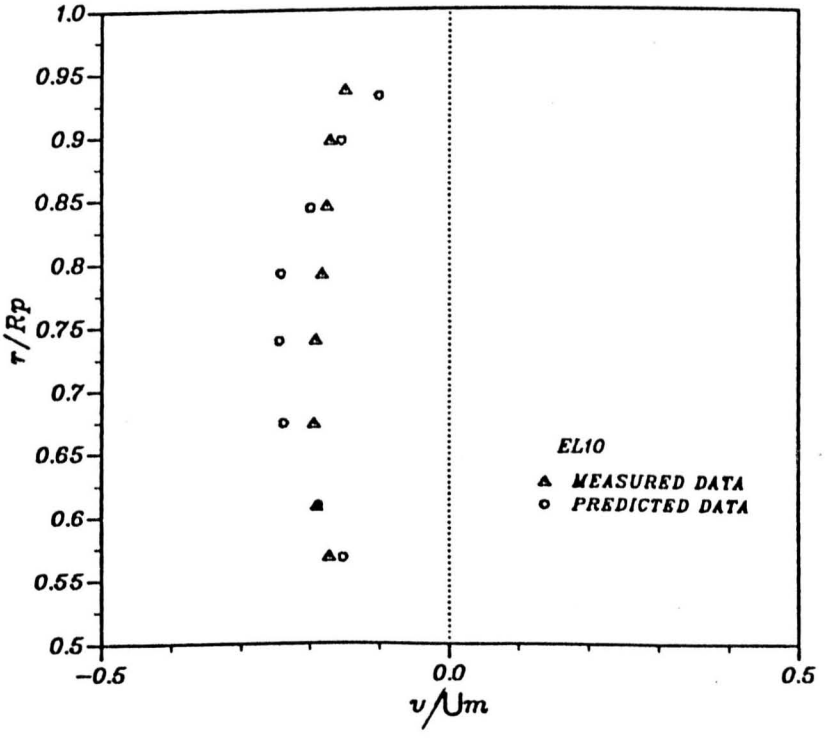

FIG. 8.69 CIRCUMFERENTIAL VELOCITY PROFILE COMPARISON

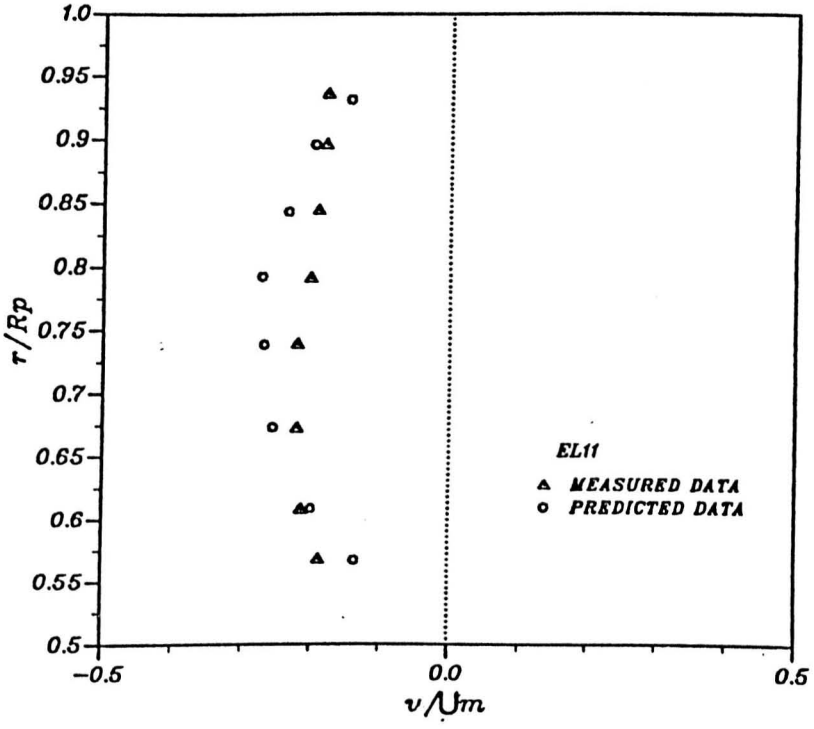

FIG. 8.70 CIRCUMFERENTIAL VELOCITY PROFILE COMPARISON

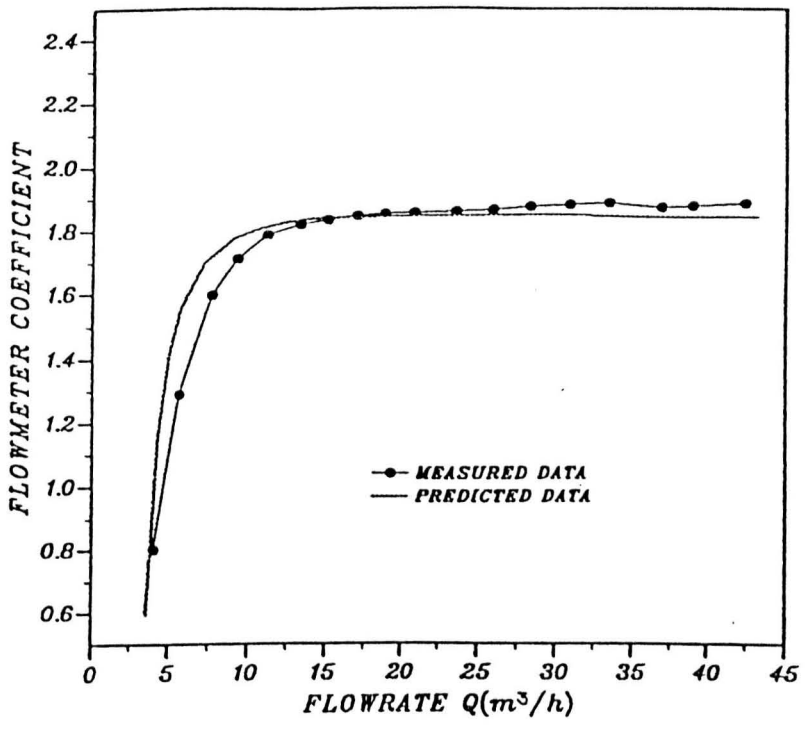

FIG. 8.71 FLOWMETER PERFORMANCE CURVE COMPARION(case A)
(the prediction with predicted inlet profiles)

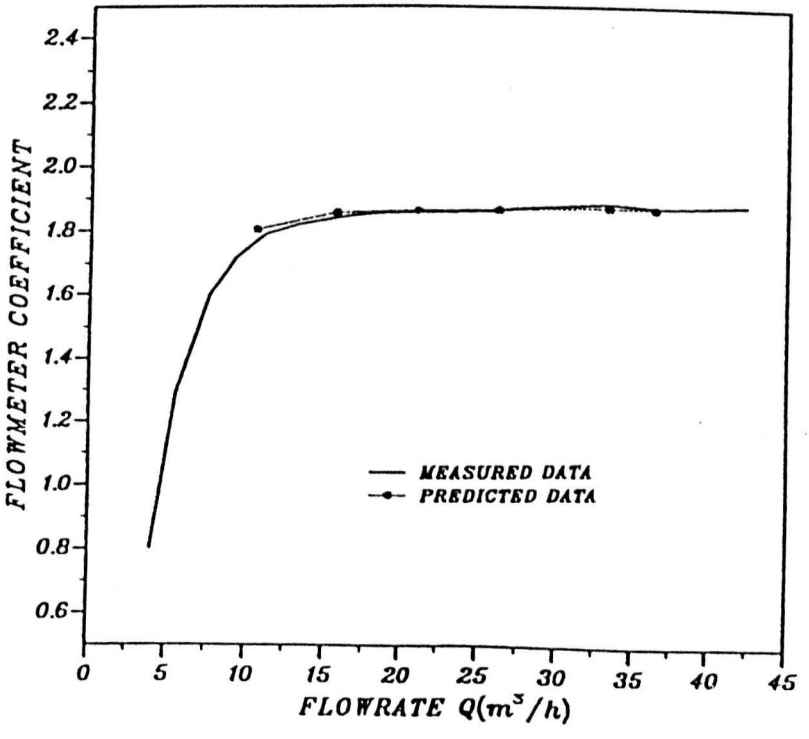

FIG. 8.72 FLOWMETER PERFORMANCE CURVE COMPARISON(case A)

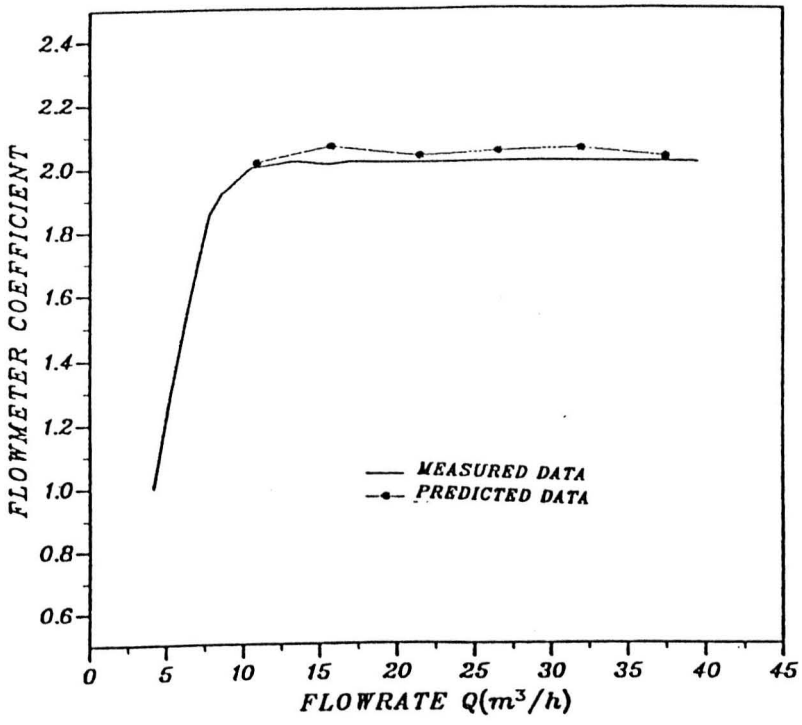

FIG. 8.73 FLOWMETER PERFORMANCE CURVE COMPARISON(case B)

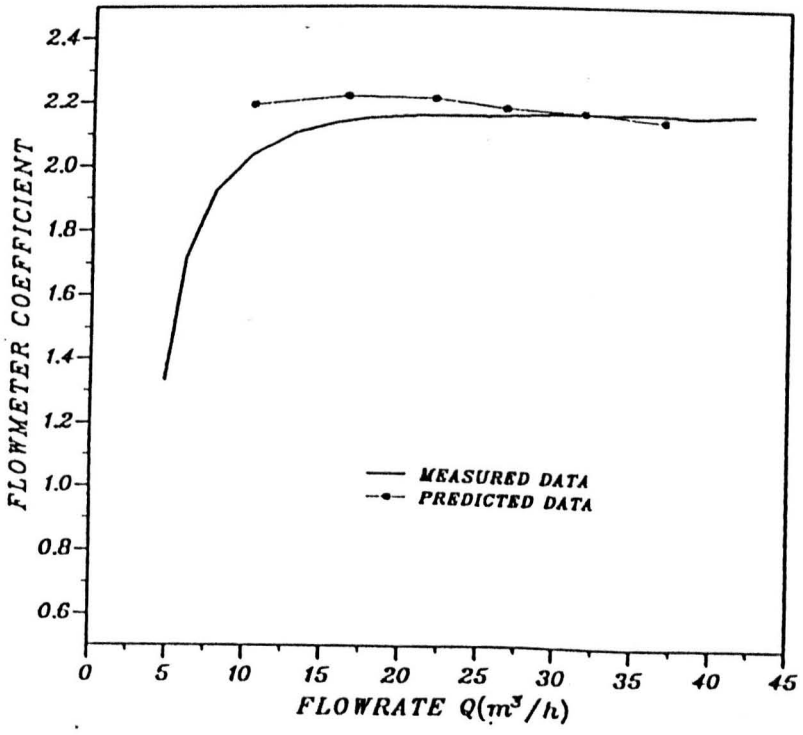

FIG. 8.74 FLOWMETER PERFORMANCE CURVE COMPARISON(case C)

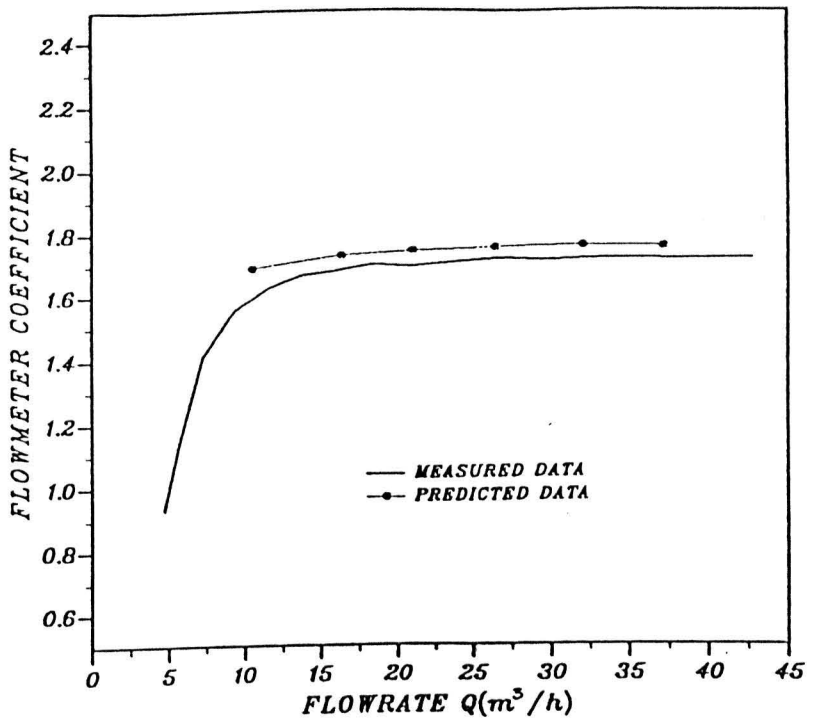

FIG. 8.75 FLOWMETER PERFORMANCE CURVE COMPARISON(case D)

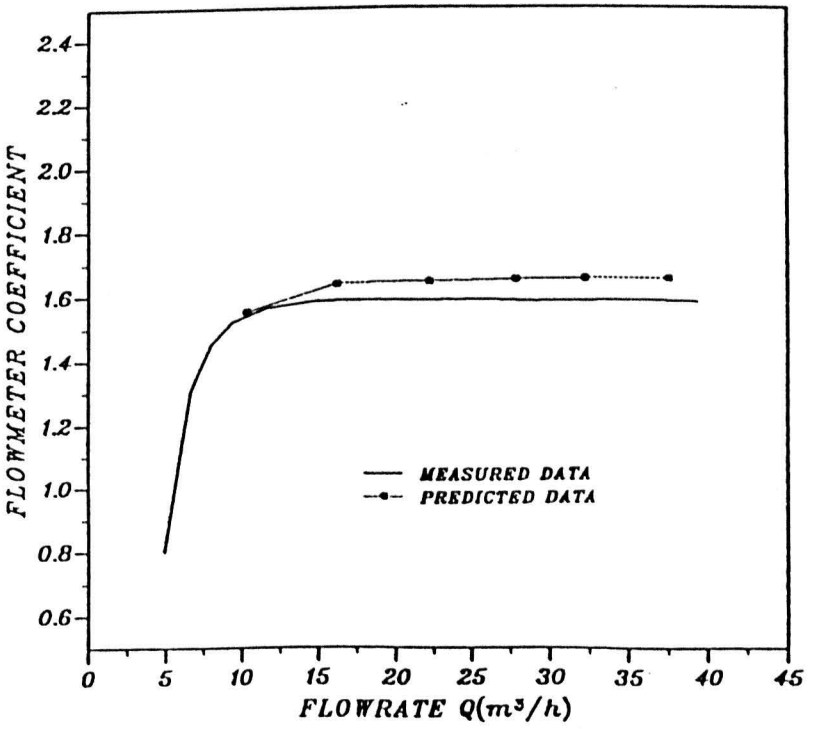

FIG. 8.76 FLOWMETER PERFORMANCE CURVE COMPARISON(case E)

REFERENCE

Abbott, I.H.
Doenhoff, A.E.V.
Theory of Wing Section
Dover Publications, Inc., New York, 1959

Bardina, J.
Lyrio, A.
Ferziger, J.H.
Johnston,J.P.
A Prediction Method for Planar Diffuser Flows
ASME J. of Fluid Engineering, Vol. 103, pp315,
1981

Barwell, F.T.
Bearing Systems
Oxford University Press, Oxford, 1979

Basu, B.C.
Hancock, G.J.
The Unsteady Motion of a Two-Dimensional Aerofoil
in Incompressible Inviscid Flow
J. Fluid Mech., Vol.87, art 1, pp 159-178,1978

Benedict, R.P.
Fundamentals of Pipe Flow
John Wiley & Sons, New York, 1980

Binder, A.
Forster. W.
Mach, K.
Rogge, H.
Unsteady Flow Interaction Caused by Stator
Secondary Vortices in a Turbine Rotor
J. of Turbomachinery, Vol.109, April,1987

Booth, E.R. Surface Pressure Measurement During Low Speed Two Dimensional Blade-vortex Interaction AIAA-86-1856, 1986

Blows, L.G. Towards a Better Turbine Flowmeter Int. Conf. on Advances in Flow Measurement Techniques, Paper L3,1981

Bradshaw, P. Turbulence Springer-Verlag, Berlin, 1976

Bromilow, I.G. Clements, R.R Some Techniques for Extending the Application of the Discrete Vortex Method of Flow Simulation Aeronautical Quarterly, pp 73-89, Feb 1982

Cebeci, T. Bradshaw, P. Momentum Transfer in Boundary Layer McGraw-Hill Book Company, 1977

Chorin, A.J. Numerical Study of Slightly Viscous Fluid J. Fluid Mech., Vol. 57, 1973

Chorin, A.J. Vortex Sheet Approximation of Boundary Layer J. of Computational Physics, Vol.27, pp 428-442,1978

Clements, R.R. An Inviscid Model of Two-dimensional Vortex Shedding J. Fluid Mech., Vol. 57, pp 321-336, 1973

Clement, R.R. Maull, D.J. The Representation of Sheets of Vorticity by Discrete Vortices Progress in Aeronautical Science, No. 16, 1975

Crighton, D. The Kutta Condition in Unsteady Flows Ann. Rev. Fluid Mech. Vol.17, 1985.

Cheer, A.Y. A Study of Incompressible 2D Vortex Flow Past

Smooth Surface
SIAM Journal, Scientific Statistics Computation, Vol. 4, pp 685-705

Dring, B.P.
Joslyn, H.D.
Hardin, L.W.
An Investigation of Axial Compressor Rotor Aerodynamics
ASME Journal of Engineering for Power, Vol. 104, Jan. 1982

Durst, F.
Principles and Practice of Laser-Doppler Anemometry
Academic Press Inc. (London) Ltd, London, 1981

East, L.F.
A Representation of Second-Order Boundary Layer Effects in the Momentum Integral Equation and Viscous-Inviscid Interaction
RAE Report, No.81002,1981

Favier, D.
Castex, A.
Maresca, C.
Unsteady Characteristics of an Airfoil Interacting with Vortical Wake
AIAA-85-1707,1985

Ferreira, V.C.S.
Flow Patterns Inside a Turbine Type Flowmeter
Ph.D Thesis, DFEI, Cranfield Institute of Technology, April, 1988

Ferziger, J.H.
Lyrio, A.A.
Bardina J.G.
New Skin Friction and Entrainment Correlations for Turbulent Boundary Layers
J. of Fluid Engineering, Vol.104, Dec, 1982

Fox, J.A.
An Introduction to Engineering Fluid Mechanics
The Maclillan Press Ltd, London and Basingstoke, 1977

Fukunishi, Y.
Influence of Ordered Motions on the Structure of Outer Region of the Turbulent Boundary Layer
Turbulence and Chaos in Fluids,IUTAM, 1984

Furness, R.A. Applications of Turbine Meters
Turbines and Vortex Meters, Short Course Notes,DFEI, Cranfield, 1982

Furness, R.A. Operating Problems with Turbine Meters
Turbines and Vortex Meters, Short Course Notes, DFEI, Cranfield, England, 1982

Giesing, J.P Nonlinear Two-Dimensional Unsteady Potential Flow with Lift
J. Aircraft, Vol.5, pp135-143, 1968

Giesing, J.P. Vorticity and Kutta Condition for Unsteady Multienergy Flows
J. Applied Mech., Vol.36, pp 608-613,1969

Gordaia, S.H. Analysis of High-Lift Wing Systems
Colwell, G. Aeronautical Quarterly, May, 1975

Goulas, A. A Computer Program for the Prediction of the
Heritage, J.E. Viscous Blade to Blade using an Integral Boundary Layer Method
DFEI Rept. 85/JEH/IR/13, Cranfield Institute of Technology, 1985

Goulas, A. A Guide and Operating Instructions to the Argon
Versteeg, H.K. LDA System
87/HKV/IR/12, DFEI,Cranfield, 1987

Gostelow, J.P. Cascade Aerodynamics
Pergamon Press,1984

Graham, J.M.R. Unsteady Flow Through a Cascade Using the 'Cloud-
Basuki, J. -in-cell' Vortex Method
Symposium of Unsteady Aerodynamics of Turbomachines and Propellers, Cambridge, England, 1984

Greitzer, E.M — An introduction to unsteady flow in Turbomachinery
Lecture series in Unsteady Flow in Turbomachinery,
Von Karman Institute,Belgium,1979

Hald, O.H.
Prete, V.M.D. — Covergence of Vortex Methods for Euler's Equations
Mathematics of Computation, Vol. 32, No. 143,
pp 791-809, 1978

Hastings, R.C.
Williams, B.R. — Studies of the Flow Field Near a NACA 4412 Airfoil
at Maximum Lift
Aeronautical Journal, pp 29-44,Jan 1987

Head, M.R. — Entrainment in the Turbulent Boundary Layers
ARC R&M 3152, 1958

Head, M.R.
Patel, V.C — Improved Entrainment Method for Calculating
Turbulent Boundary Layer Development
ARC R&M 3643, 1969

Herschr, R.W. — Streamflow Measurement
Elserier Applied Science Publishers, 1985

Hess, J.L.
Smith, A.M.O. — Calculation of Potential Flow About Arbitrary bodies
Progress In Aeronautical Science, Vol.6.

Hoeijmakers,H.W.M — Computational Vortex Flow Areodynamics
AGARD-CP-342, paper No. 18.

Hsu, T.M.
Wu, J.C. — Theoretical and Numerical Studies of a Vortex
-airfoil Interaction Problem
AIAA-86-1094, 1986

Hutton, S.P. — Introduction to Turbine Meters
Turbine and Vortex Meters, Short Course Notes,
DFEI, Cranfield, 1986

Jepson, P.
Bean, P.G.
Effect of Upstream Velocity Profiles on Turbine Flowmeter Registration
J. of Mech. Eng. Science, Vol. 11, No. 5. 1969

Kadhim,S.J.
Railly, J.W.
An Improvement in the Treatment of Separation in Cascade by Potential Flow Method
Proc. Inst. Mech. Eng., Vol.194, 1982

Karamcheti, K.
Principle of Ideal Fluid Aerodynamics
John Wiley& son, 1966

Katz, J.
A Discrete Vortex Method for the Non-Steady Separated Flow over an Airfoil
J. Fluid Mech., Vol. 102, pp. 315-328, 1981

Kemp, N.H.
Sears, W.R.
The Unsteady Forces due to Viscous Wakes in Turbomachines
J. of the Aeronautical Sciences, July,1955

Kim, M,J,
Mook, D.T.
Application of Continuous Vorticity Panels to General Unsteady Two-Dimensional Lifting Flows
AIAA-85-0282, 1985

Kiya, M.
Arie, M.
A Contribution to an Inviscid Vortex-Shedding Model for an Inclined Flat Plate in Uniform Flow
J. Fluid Mech., Vol 82, pp 223-240, 1977

Kiya, M.
Arie, M.
Discrete-Vortex Simulation of Unsteady Separated Flow Behind a Nearly Normal Plate
Bulletin of the JSME, Vol.23, No.183,
pp 1451-1458, 1980

Kiya, M.
Sasaki, K.
Arie, M.
Discrete-vortex Simulation of a Turbulent Separation Bubble
J. Fluid Mech. Vol. 120,pp219-244,1982

PAGE MISSING

Page 256

Lee, W.F.Z.
Karlby. H.
A Study of Viscosity Effects and its Compensation on Turbine-Type Flowmeter
ASME J. of Basic Engineering, Vol. 82, 1960

Leonard, A.
Vortex Methods for Flow Simulation
J. of Computational Physics, Vol.37,
pp 289-335,1980

Lewis, R.I.
Surface Vorticity Modelling of Separated Flow From Two-Dimensional Bluff Bodies of Arbitrary Shape
J. Mech. Eng. Science, Vol.23, No.1. 1981

Lewis, R.I.
A Method for Inverse Aerofoil and Cascade Design by Surface Vorticity
82-GT-154, ASME, 1982

Lewis, R.I.
PortHouse, D.T.C.
Numerical Simulation of Stalling flow by Integral Equation Method
AGARD-CP-351, Paper No. 13,1983

Lighthill, M.J.
On Displacement Thickness
J. of Fluid Mech., Part 4, 1958

Lock, R.C.
Firmin, M.C.P.
Survey of Techniques for Estimating Viscous Effects In External Aerodynamics
Numerical Methods in Aeronautical Fluid Dynamics, ed P.L.Roe, Academic Press, London, 1982

Ludwing, H.
Tillmann, W.
Investigation of the Wall Shearing Stress in Turbulent Boundary Layers
NACA Rept. TM 1285, 1949

MaCroskey, W.J.
Some Current Research in Unsteady Fluid Dynamics-The 1976 Freeman Scholar Lecture
J. of Fluid Engineering, March, 1977

Maskew, B.
Predicting Aerodynamic Characteristics of Vortical

Flows on Three-Dimensional Configurations using a Surface-Singularity Panel Method
AGARD-CP-342, Paper 13

MaFarland, E.R. Solution of Plane Cascade Flow Using Improved Surface Singularity Methods
81-GT-169,ASME, 1981

Massey, B.S Mechanics of Fluids
6th edition, Chapman and Hall, 1989.

McAlister, K.W.
Tung, C. Airfoil Interaction with an Impinging Vortex
NASA Technical Paper 2273, 1984

Millington, B.C.
Adams, C.W.
Kings, N.W. The Effect of Upstream Installation Conditions on the Performance of a Small Liquid Turbine Meters
Int. Symposium on Fluid Flow Measurement, Washington, 1986

Milne-Thomson,L.M. Theoretical Hydrodynamics
4th ed., The Macmillan Co., New York, 1960

Milinazzo, F.
Saffman, P.G. The Calculation of Large Reynolds Number Two-Dimensional Flow Using Discrete Vortices with Random Walk
Journal of Computational Physics, Vol. 23, pp 380-392, 1977

Moran, J. An Introduction to Theoretical Computational Aerodynamics
John Wiley & Son, 1976

Nagano, S.
Naito, M.
Takata, H. Numerical Analysis of Two-dimensional Flow Past a Rectangular Prism by a Discrete Vortex Model
Computers and Fluids, Vol.10,No.4, pp243-259,1982

Oliver, A.R. A Double Vortex Sheet Model for Viscous Flow near

the Trailing Edge for a Lifting Airfoil
J. for Heat and Fluid Flow, Vol.2, No.2,1982

Ota, T.
Asano, Y
Okawa, J.
Reattachment Length and Transition of the Separated Flow over Blunt Flat Plates
Bulletin of the JSME, Vol.24, No.24, 1981

Panaras, A.G.
Numerical Modelling of the Vortex/Airfoil Interaction
AIAA Journal, Vol.25, No.1, pp 5—11,1987

Peace, A.J.
A Multi-Vortex Model of Leading Edge Vortex Flows
International J. for Numerical Methods in Fluids, Vol. 3, pp 543-565, 1983

Platzer, M.F.
Unsteady Flows in Turbomachines — A Review of Current Developments
AGARD Proc. No. 227, 1977

Poling, D.R.
The Response of Airfoil to Periodic Disturbulence— The Kutta Condition
AIAA Journal, Vol.24, No.2, 1986

Poling, D.R.
Dadone, L.
Telionis, D.P.
Blade-Vortex Interaction
AIAA-87-0497,1987

Porthouse,D.T.C.
Lewis, R.I.
Simulation of Viscous Diffusion for Extension of the Surface Vorticity Method to Boundary Layer and Separated Flows
J. of Mech. Engineering Science, Vol. 23,No. 3, 1981

Psarudakis, P.
Aerodynamic Computation Method of Airfoil Cascade Subjected to Viscous Flow
AGARD-CP-315, Paper No. 12,

Ribaut, M. A Vortex Sheet Method for Calculating Separated Two-Dimensional Flows
AIAA J. Vol. 2, No. 8, pp 1079-1084, 1983

Roberts, W.B. Calculation of Laminar Separation Bubble and Their Effect on Airfoil Performance
AIAA Journal, Vol.18, No.1, pp 25-31,1980.

Rosenhead, L. Formation of Vortices from a Surface of Discontinuity
Proc. Royal Socity,134,pp170,192, 1932

Ryffels, R.
Geromino, J.H. Machinery's Handbook,
22nd Edition, Industries Press PLC, New York, 1984.

Saffman, P.G.
Baker, G.R. Vortex Interaction
Ann. Rev. Fluid Mech. 1979

Salami, L.A. Towards Standardization of Turbine-type Flowmeters
Proceedings of International Conference on Advances in Flow Measurement Techniques, BHRA Fluid Engineering, England, 1981

Salami, L.A. Effect of Upstream Velocity Profile and Integral Flow Straighteners on Turbine Flowmeter
Int. J. Heat & Fluid Flow, Vol. 5, No.3,
pp 155-165,1984

Sarpkaya, T. An Inviscid Model of Two Dimensional Vortex Shedding for Transient and Asymptotically Steady Separated Flow Over an Inclined Flat Plate
J. Fluid Mech., Vol. 68, pp. 109–128,1975

Sarpkaya, T.
Schoaff, R.L., Inviscid Model of Two-Dimensional Vortex Shedding By a Circular Cylinder
AIAA Journal, Vol.17, No.11, pp 1193–1200,1979

Sarpkaya, T.
Ihrig, C.J. Impulsively Started Steady Flow About Rectangular Prisms: Experiments and Discrete Vortex Analysis
J. of Fluid Eng., Vol 108, pp 47–54,1986

Sarpkaya, T. Computational Methods With Vortices — The 1989 Freeman Scholar Lecture
J. of Fluid Eng., Vol. 111, pp 5–52,1989

Schlichting, H Boundary Theory
McGraw-Hill, New York, 1960

Seath, D.D.
Wilson, D.R. Vortex–Airfoil Interaction Test
AIAA–86–0354, 1986

Seebohm, T
Newman, B.G. A numerical Method for Calculating Viscous Flow around Multiple-Section Aerofoils", Aeronautical Quarterly, pp 176–178. Aug 1975

SME Laser Doppler Anemometry
SME Short Course Notes, SME, Cranfield, 1989.

Smith, J.H.B. Achievements and Problems in Modelling Highly-swept Flow Separations
In Numerical Methods in Aeronautical Fluid Dynamics,ed. P.L.Roe. Academic Press, London, 1982

Smith, J.H.B. Vortex Flow in Aerodynamics
Ann. Rev. Fluid Mech., Vol.18, pp221-242,1986

Spalart, P.R.
Leonard,A. Computation of Separated flow by a Vortex Tracing Algorthm
AIAA-81-1246,1981

Spitzer, D.W. Industrial Flow Measurement
Instrument Society of America, 198

Strickland, J.H. On the Utilization of Vortex Methods for Parachute

Aerodynamic Predictions
AIAA Paper 86-2455, 1986

Sugeng, F
Fiedle, K
An Experiment Investigation into Unsteady Blade Force and Blade Loss in Axial Compressor Blade Cascade
ASME J. of Engineering for Gas Turbine and Power, Vol. 108, 1986

Theodorson,H.
Theory of Wing Section of Arbitrary Shape
NACA report 411,1931

Thompon, R.E.
Grey, J.
Turbine Flowmeter Performance Model
J. of Basic Engineering, Trans ASME, Dec,1973

THORN EMI
Photomultipliers
Technical Especification, PMC/86, 1986

Tsukamoto, H.
Hutton, S.P.
Theoretical Prediction of Meter Factor for a Helical Turbine Flowmeter
Fluid Control and Measurement, Meiji University, Tokyo 1985

Thwaites, B.
Approximate Calculation of the Laminar Boundary Layer
Aero. Quart, Vol. 1, 1949

Versteeg, H.
Singularity Distribution Methods
Advanced Computational in Turbomachinery, DFEI Short Course Notes of,1987

Vezza, M.
Galbraith, R.A.
An Algorithm for the Prediction of Unsteady Potential Flow About an Arbitrary Airfoil
G. U. Areo. Report No. 8306, 1983

Vezza, M.
Galbraith,R.A.M.
A Method for Prediction Unsteady Potential Flow About an Aerofoil

Int. J. for Numerical Method in Fluids, Vol.5, pp347-356,1985

Vezza, M.
Galbraith,R.A.M. An Inviscid Model of Unsteady Aerofoil Flow with Fixed Upper Surface Separation
Int. J. for Numerical Methods in Fluids, Vol.5, pp577-592,1985

Watson, G.A.
Furness, R.A. Development and Application of Turbine Meter
Proc. Transducer 77 Conf., Flow Measurement Session, London, 1977

Wilkinson, D.H. An Numerical Solution of the Analysis and Design Problem Past One or More Aerofoils or Cascades
ARC R&M-3454, 1964

APPENDIX

A

DETERMINATION OF INFLUENCE COEFFICIENTS

A.1 Influence Coefficients for a Point Vortex

Considering a point vortex at position(x,y), the stream function due to this point vortex at an arbitrary point P(a,b) is

$$\psi = \frac{\Gamma}{2\pi} \ln(d) \qquad (A,1,1)$$

where d is the distance between point P and the point vortex, i.e.

$$d = \sqrt{(a-x)^2 + (b-x)^2}$$

A.2 Influence Coefficients for a Vortex Panel

As shown in fig.A.1, the kth vortex panel considered here is straight. It lies along the x coordinate axis and the midpoint is located at the origin point of the coordinate. The vortex intensity along the panel is linearly distributed with intensity γ_k and γ_{k+1} at the kth and the (k+1)th node respectively. The distribution can be written as

$$\gamma = N_1 \gamma_k + N_2 \gamma_{k+1} \tag{A.2.1}$$

$$N_1 = (1 - x/L_k)/2 \tag{A.2.2}$$

$$N_2 = (1 + x/L_k)/2 \tag{A.2.3}$$

where L_k is the semilength of the kth panel.

The stream function induced by the panel at ith point P(a,b) is

$$\Psi = \frac{1}{2\pi} \int_{-L_k}^{L_k} (N_1 \gamma_k + N_2 \gamma_{k+1}) \ln|d| \, dx$$

$$= A_{i,k,k}{}^{*}\gamma_k + A_{i,k+1,k}{}^{*}\gamma_{k+1} \tag{A.2.4}$$

where

$$A_{i,k,k} = \frac{1}{2\pi} \int_{-L_k}^{L_k} N_1 \ln|d| dx \tag{A.2.5}$$

$$A_{i,k+1,k} = \frac{1}{2\pi} \int_{-L_k}^{L_k} N_2 \ln|d| dx \tag{A.2.6}$$

and

$$d = \sqrt{(a-x)^2 + b^2}$$

Substituting formula(A.2.2) into (A.2.5), the influence coefficient $A_{i,k,k}$ is

$$A_{i,k,k} = \frac{1}{2\pi} \int_{-L_k}^{L_k} \frac{1}{2} \left(1 - \frac{x}{L_k}\right) \ln \left[\sqrt{(a-x)^2 + b^2} \right] dx$$

$$= \frac{1}{8\pi} \int_{-L_k}^{L_k} \ln[(a-x)^2 + b^2] \, dx$$

$$- \frac{1}{8\pi L_k} \int_{-L_k}^{L_k} x \ln[(a-x)^2 + b^2] \, dx$$

$$= \frac{1}{8\pi} I_1 - \frac{1}{8\pi L_k} I_2 \tag{A.2.7}$$

where

$$I_1 = x\,\ell n\,[(a-x)^2+b^2]\,\Big|_{-L_k}^{L_k} + \int_{-L_k}^{L_k} \frac{2x(a-x)}{(a-x)^2+b^2}\,dx$$

$$= x\ell n[(a-x)^2+b^2]\Big|_{-L_k}^{L_k} - 2\int_{-L_k}^{L_k}\left(1+\frac{a}{2}\,\frac{2(x-a)}{(a-x)^2+b^2} - \frac{b^2}{(a-x)^2+b^2}\right)dx$$

$$= \{x\ell n[(a-x)^2+b^2]-2x- a\,\ell n[(a-x)^2+b^2] - 2b\,\tan^{-1}\left(\frac{a-x}{b}\right)\}\Big|_{-L_k}^{L_k} \qquad (A.2.8)$$

$$I_2 = \int_{-L_k}^{L_k} (a+x-a)\,\ell n[(a-x)^2+b^2]dx$$

$$= aI_1 + \frac{1}{2}\int_{-L_k}^{L_k} \ell n[(a-x)^2+b^2]d[(a-x)^2+b^2]$$

$$= aI_1 + \frac{1}{2}\,[(a-x)^2+b^2]\{\ell n[(a-x)^2+b^2]-1\}\Big|_{-L_k}^{L_k} \qquad (A.2.9)$$

Substituting I_1 and I_2 into (A.2.7) , $A_{i,k,k}$ is

$$A_{i,k,k} = \frac{1}{4\pi}\,[\,(a+L_k)\ell n(d_1) - (a-L_k)\ell n(d_2) - 2L_k + b^*J1]$$

$$- \frac{1}{4\pi}\,[\,\frac{a^2-b^2-L_k^2}{2L_k}\,(\ell n(d_1)-\ell n(d_2)) - a + \frac{ab}{L_k}\,J1) \qquad (A.2.10)$$

where

$$d_1 = \sqrt{(a+L_k)^2+b^2)}$$

$$d_2 = \sqrt{(a-L_k)^2+b^2)}$$

and

$$J1 = \tan^{-1}\left(\frac{a+L_k}{L_k}\right) - \tan^{-1}\left(\frac{a-L_k}{L_k}\right)$$

$A_{i,k+1,k}$ is obtained in the same manner as $A_{i,k,k}$. It is

$$A_{i,k+1,k} = \frac{1}{4\pi}\left[(a+L_k)\ln(d_1)-(a-L_k)\ln(d_2) -2L_k +b*J1\right]$$

$$+\frac{1}{4\pi}\left[\frac{a^2-b^2-L_k^2}{2L_k}(\ln(d_1) -\ln(d_2)) -a + \frac{ab}{L_k} J1\right) \qquad (A.2.11)$$

Expressions for the influence coefficients of a panel at its own nodes are determined using limit processing techniques.

At the node $a=-L_k$ and $b=0$, the influence coefficients are

$$A_{k,k,k} = \frac{L_k}{4\pi}[3-2\ln(2L_k)] \qquad (A.2.12)$$

$$A_{k,k+1,k} = \frac{L_k}{4\pi}[1- 2\ln(2L_k)] \qquad (A.2.13)$$

At the other node, $a=L_k$ and $b=0$, the influence coefficients are

$$A_{k+1,k,k} = \frac{L_k}{4\pi}[1-2\ln(2L_k)] \qquad (A.2.14)$$

$$A_{k+1,k+1,k} = \frac{L_k}{4\pi}[3- 2\ln(2L_k)] \qquad (A.2.15)$$

It can be seen from these formulae that the influence coefficients for a panel at an arbitary point depend only on their relative position and the vorticity distribution on the panel.

In calculations, vortex panels are in arbitary positions, so a coordinate transformation has to be done before the above influence coefficient formulae can be used. For example to find the influence of the panel AB in fig.A.2, the coordinates XOY is transfered to X'O'Y' through a rotation and non-rotational movement. After the transformation, the position of the point P in the new coordinate

system is

$$a=(x-x_{cen})\cos\theta+(y-y_{cen})\sin\theta \qquad (A.2.16)$$

$$b=-(x-x_{cen})\sin\theta+(y-y_{cen})\cos\theta \qquad (A.2.17)$$

Here $[x_{cen}, y_{cen}]$ is the midpoint coordinates of the panel in XOY coordinate system. They are

$$\begin{aligned} x_{cen} &= (x_a+x_b)/2 \\ y_{cen} &= (y_a+y_b)/2 \end{aligned} \qquad (A.2.18)$$

θ is the direction of the panel given by

$$\tan(\theta) = \frac{y_b - y_a}{x_b - x_a} \qquad (A.2.19)$$

The vortex panel lies on the x' coordinate and the midpoint is at the origin of coordinate X'O'Y'. In this new coordinate system, the coefficient formulae can be applied directly.

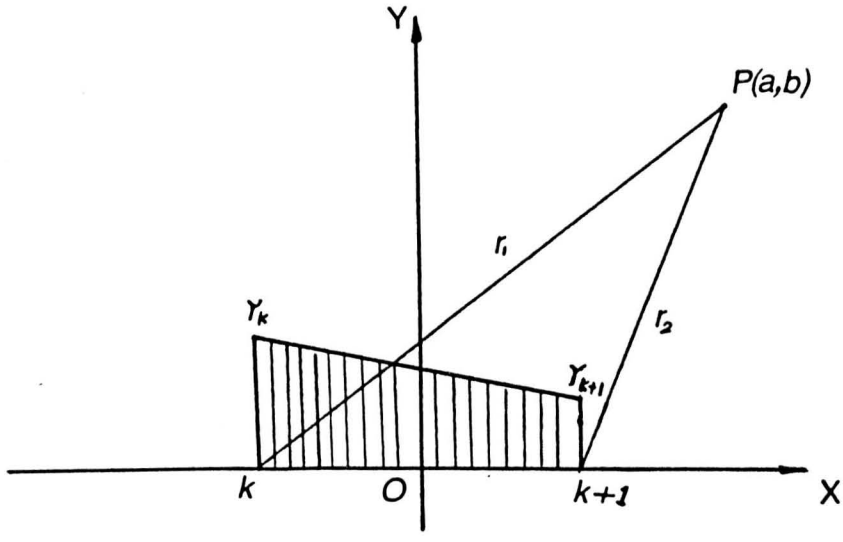

FIG A.1 LINEAR VORTEX PANEL

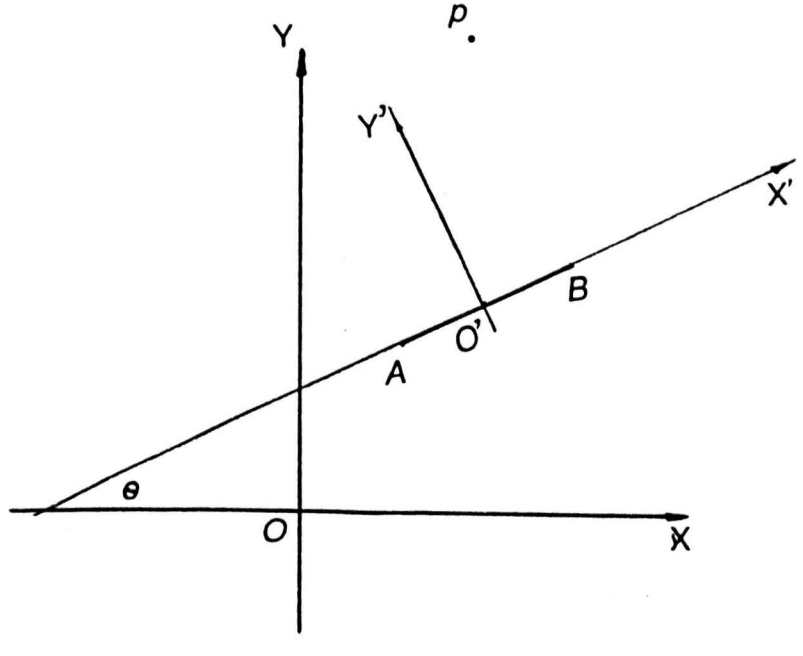

FIG A.2 COORDINATE TRANSFORMATION'

APPENDIX

B

DEPENDENCE BETWEEN THE BASIC FLOWS

For the flow around a blade, the governing equations from the boundary condition are

$$\sum_{j=1}^{N} K_{i,j}\,\gamma_j = RHS_i \qquad i=1,2,\ldots,N-1 \tag{B.1}$$

Because the rank of the influence coefficient matrix $K_{i,j}$ is N-1, only while one more equation is given, a unique solution to the flow can be obtained. In this calculation,the Kutta condition provides the extra equation. In the flow around two blades or cascades, the rank of the influence coefficient matrix becomes 2N-2 and the Kutta condition has to be applied to each blade or cascade.

In order to obtain the solution to the flow around two blades or cascades, the homogeneous equations (B.1) are discussed first. The equations are

$$\sum_{j=1}^{2N} K_{i,j} * \gamma_j = 0 \qquad i=1,2,\ldots,2N-2 \tag{B.2}$$

Because the rank of $|K_{i,j}|$ is 2N-2, equations (B.2) have an

infinite number of solutions. But all those solutions can be expressed as linear combinations of two independent solutions. Providing γ_i^a and γ_i^b are two independent solutions to the homogenious equations (B.2), the solutions of this homogenious equations can be expressed as

$$\gamma_i = k1*\gamma_i^a + k2*\gamma_i^b \tag{B.3}$$

where k1 and k2 are two constants.

The solution of the non-homogenious equations (B-1) can be written as

$$\gamma_i' = \gamma_i^o + k1'*\gamma_i^a + k2'*\gamma_i^b \tag{B.4}$$

Where γ_i^o is a particular solution to the non-homogenious equations (B.1).

If γ_i^1 and γ_i^2 are two independent solutions of the corresponding non-homogeneous equations of equations (B.2) and

$$\gamma_i^1 \neq \gamma_i^o$$

$$\gamma_i^2 \neq \gamma_i^o$$

Then

$$\begin{aligned} \gamma_i' &= (\gamma_i^o - \gamma_i^1) \\ \gamma_i'' &= (\gamma_i^o - \gamma_i^2) \end{aligned} \tag{B.5}$$

are the solutions of the homogeneous equations.

The solution of the non-homogeneous equations is written in the following form

$$\gamma_i = \{\gamma_1, \gamma_n, \gamma_{n+1}, \gamma_{2n}, \gamma_2, \cdots, \gamma_{n-1}, \gamma_{n+2}, \cdots, \gamma_{2n-1}\} \tag{B.6}$$

and γ_i^o, γ_i^1 and γ_i^2 are given solutions for basic flow a, b and c respectively. These solutions are

$$\gamma_i^o = \{0, \gamma_n^{(a)}, \gamma_{n+1}^{(a)}, 0, \gamma_2^{(a)}, \ldots, \gamma_{n-1}^{(a)}, \gamma_{n+2}^{(a)}, \ldots, \gamma_{2n-1}^{(a)}\} \tag{B.7}$$

$$\gamma_i^1 = \{0, \gamma_n^{(b)}, 0, \gamma_{2n}^{(b)}, \gamma_3(b), \ldots, \gamma_{n-1}^{(b)}, \gamma_{n+2}^{(b)}, \ldots, \gamma_{2n-1}^{(b)}\} \tag{B.8}$$

$$\gamma_i^2 = \{\ \gamma_1(c),\ 0,\ \gamma_{n+1}(c),\ 0,\ \gamma_3(c),\ldots,\gamma_{n-1}(c),\ \gamma_{n+2}(c),\ \ldots,\ \gamma_{2n-1}(c)\ \} \tag{B.9}$$

Substituting $\gamma_i(a)$, $\gamma_i(b)$ and $\gamma_i(c)$ into (B.5) gives

$$\begin{aligned}\gamma_i' &= \gamma_i^0 - \gamma_i^1 \\ &= \gamma_i(a) - \gamma_i(b) \\ &= \{\ 0,\ \gamma_n(a)-\gamma_n(b),\ \gamma_{n+1}(a),\ -\gamma_{2n}(b),\ \ldots\ \}\end{aligned} \tag{B.10}$$

and

$$\begin{aligned}\gamma_i'' &= \gamma_i^0 - \gamma_i^2 \\ &= \gamma_i(a) - \gamma_i(c) \\ &= \{\ -\gamma_1(c),\ \gamma_n(a),\ \gamma_{n+1}(a)-\gamma_{n+1}(c),\ 0,\ \gamma_2(a)-\gamma_2(c),\ \ldots\ \}\end{aligned} \tag{B.11}$$

It is obvious that γ_i' and γ_i'' are independent of each other, so they can be used as γ_i^a and γ_i^b in equation (B.4) to express other solutions of the non-homogenious equations.

Therefore, substituting equation(B.10) and(B.11) into equation (B.4), the solutions to the non-homogeneous equation (B.1) can be written in the following form:

$$\begin{aligned}\gamma_i &= \gamma_i(a) + k1' * \gamma_i' + k2' * \gamma_i'' \\ &= \gamma_i(a) + k1' * (\gamma_i(a) - \gamma_i(b)) + k2' * (\gamma_i(a) - \gamma_i(c)) \\ &= k1 * \gamma_i(a) + k2 * \gamma_i(b) + k3 * \gamma_i(c)\end{aligned}$$

It can be concluded that any solutions of the non-homogeneous equations of equation (B.2) can be expressed as linear combinations of any three solutions of the four defined basic flows.

APPENDIX C

DIRECTION OF VORTEX LEAVING BLADE TRAILING EDGE

The correct prediction of the position of the nascent vortex shed from the blade trailing edge is important because this position can effect the subsequent vortex shedding process. Hsu et al(1986) give a trailing edge flow model that determines the position.

Consider an infinitesimal control volume at the blade trailing edge as shown in fig.C.1 and applying the momentum to it, this gives

$$\sum \vec{F} = \frac{\partial}{\partial t} \int_{cv} \rho \vec{V} \, dv + \int_{cs} \rho(\vec{V} \, d\vec{s}) \vec{V} \qquad (C-1)$$

here cv is the control volume and cs is the control volume surface. F is the force acting on the control volume.

In the limit as dx tends to zero

$\vec{F} = 0$

$v = 0$

Therefore, equation(C-1) becomes

$$\int_{cs} \rho(\vec{V}\, d\vec{s})\, \vec{V} = 0 \qquad \text{(C-2)}$$

Applying equation (C-2) to the control volume in the x and y directions, the direction at which fluid leaves the trailing edge is found to be

$$\tan(\phi) = \frac{U_l^2\cos(\beta)\sin(\beta) - U_u^2\cos(\alpha)\sin(\alpha)}{U_u^2\cos^2(\alpha) + U_l^2\cos^2(\beta)} \qquad \text{(C-3)}$$

From this equation, when U_l equals zero, the flow direction after blade trailing edge is

$$\tan(\phi) = -\tan(\alpha)$$

This means the flow leaves the trailing edge parallel to the blade upper surface. The similar result can be found when U_u is equal to zero, the leaving flow is in the direction parallel to the lower surface at the trailing edge.

Applying continuity to the control volume, the velocity of the nascent vortex leaving the trailing edge is found to be

$$V = 0.5[U_u\cos(\alpha) + U_l\cos(\beta)]/\cos(\phi) \qquad \text{(C-4)}$$

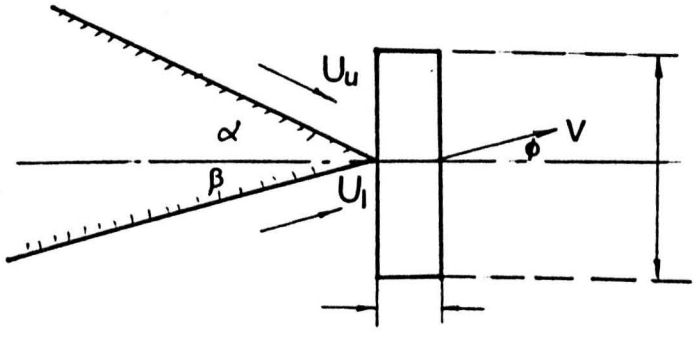

FIG C1 BLADE TRAILING FLOW MODEL

APPENDIX D

LDA MEASUREMENT UNCERTAINTY

D.1 Control Volume Position(CVP) and Half Intersection Angle(HIA)

As shown in fig.7.4, the two laser beams penetrate the perspex pipe and cross each other at a point inside the pipe after the front focusing lens. During the measurements, the crossing point of the two laser beams (also named the control volume) can be moved to any required position inside the test section by adjusting the platform on which the laser system is mounted. In circumferential velocity component measurements, a perspex matching box full of water is fitted around the perspex pipe to improve doppler signal quality. The laser beams then have to penetrate the box first then travel into the pipe.

Following the laser beams from the front lens to the crossing point and applying the law of geometrical optics, the CVP (control volume position) and the HIA (half intersection angle between these two beams) can be obtained. The experimental configurations for axial and circumferential velocity component measurements are shown in figures D.1 and D.2.

To calculate the CVP and the HIA, laser beams, perspex pipe walls and matching box surfaces have to be represented by mathematical equations. The relative positions of the test section and the LDA system are described in the coordinates shown in fig.D.1 and fig.D.2 for axial and circumferential velocity component measurements

respectively. These general equations are given below.

laser beam one

$$\frac{x-x_1}{p} = \frac{y-y_1}{q} = \frac{z-z_1}{r} \qquad (D.1.1)$$

laser beam two

$$\frac{x-x_a}{u} = \frac{y-y_a}{v} = \frac{z-z_a}{w} \qquad (D.1.2)$$

The parameters in the above equation are as the following

direction vectors (p,q,r) and (u,v,w)

starting positions (x_1,y_1,z_1) and (x_a,y_a,z_a)

In an ideal setting of the test section and the LDA system, the surface equations are

pipe surface equations:

$x^2+y^2= R_1^2$ outer surface (D.1.3)

$x^2+y^2= R_2^2$ inner surface (D.1.4)

matching box surface equations:

$y -D_O= 0$ (D.1.5)

$y -D_i= 0$ (D.1.6)

While all those parameters are known, the CVP and the HIA can be calculated.

D.2 Error Propagation Theory

In the experiments, because of the uncertainties in the LDA system, in the measurement system integration(such as the measured HIA in air and the alignment between the laser system and test section) and in the test section production, a certain level of uncertainty exist in both the CVP and the HIA. Consequently, uncertainty exists in the measured velocity components.

According to error propagation theory[Herschr(1985), Kighorn(1989)], given a quantity Q is a function of variables

$x_1, x_1, x_3 \ldots$, the error in Q due to the errors in these variables is

$$\delta Q = \sum_{i=1}^{N} \frac{\partial Q}{\partial x_i} \delta x_i \qquad \text{(D.2.1)}$$

Squaring the above equation gives

$$\delta Q^2 = \sum_{n=1}^{N} \left(\frac{\partial Q}{\partial x_i} \delta x_i\right)^2 \qquad \text{(D.2.2)}$$

Suppose the function Q is

$$Q = \prod_{i=1}^{N} X_i \qquad \text{(D.2.3)}$$

Then, the error in Q caused by the errors in its variables is

$$\delta Q^2 = \sum_{i=1}^{N} \left(\prod_{j \neq i} x_j\right)^2 \delta x_i^2 \qquad \text{(D.2.4)}$$

and the uncertainty of Q is

$$\frac{\delta Q}{Q} = \sqrt{\sum_{i=1}^{N} \left(\frac{\delta x_i}{x_i}\right)^2} \qquad \text{(D.2.5)}$$

Similarly, if

$$Q = \sum_{i=1}^{N} x_i \qquad \text{(D.2.6)}$$

The error of Q is

$$\delta Q^2 = \sum_{i=1}^{N} (\delta x_i)^2 \qquad \text{(D.2.7)}$$

and the uncertainty is

$$\frac{\delta Q}{Q} = \frac{\sqrt{\sum_{i=1}^{N} (\delta x_i)^2}}{Q} \qquad (D.2.8)$$

When the uncertainties of all the equation parameters are known, the uncertainty in the CVP and the HIA can be calculated by applying error propagation theory to the calculation of CVP and HIA.

The uncertainties in the CVP and HIA are in two groups, i.e. systematic and random components. The systematic component arises from the errors in the determined positions of the laser beams and the errors in the manufacture of the test section. These uncertainties can be either positive or negative. The random component comes from the misalignment between the laser system and the test section. The uncertainties in each laser beam caused by these alignment errors might have the same tendency. The errors due to the second group uncertainties are considered separately from the first group in this uncertainty analysis. Fig.D.3 shows a typical example of the axial velocity measurement with misalignment. This misalignment only produces a very small influence on the HIA, but the control volume can move from point o to o' and there is also some error in the measured velocity direction. To determine the uncertainties in the CVP and the HIA by the second group errors, several extreme misalignments are examined. The resulting maximum deviationsof the CVP and the HIA from their ideal setting value are taken as the possible uncertainties. The total uncertainties in the CVP and the HIA are the sum of the uncertainties in the two groups.

D.3 Parameter Uncertainties

D.3.1 Uncertainties in Test Section Production

The production uncertainties considered here are the reading errors of the machine tool used in its production. The possible reading error of the used scale is 0.02mm and the uncertainty is taken as 0.04mm for 95% confidence level. The uncertainties of the

pipe outer and inner diameters are 0.04mm, i.e.

$$\delta R_1 = 0.04\text{mm} \quad \text{and} \quad \delta R_2 = 0.04\text{mm}$$

Another error which can cause large uncertainty is the fitting error of the matching box in the circumferential velocity measurement. The ideal box should have its surfaces parallel to the pipe axis as shown in fig.D.4. Because of the manufacture errors of the box and the pipe, the uncertainty in AB is

$$\delta = \sqrt{\delta L_{b1}^2 + \Delta^2 + \delta R_1^2} \qquad \text{(D.3.1)}$$

where Δ is the manufacturing tolerance between the fitting surfaces.

The same uncertainties exist at both ends of the box. Due to these uncertainties, the box wall surface probably formed an angle with the pipe axis as shown by the dotted lines in fig.D.4. This angle is

$$\tan(\delta\theta_b) = \frac{2\,\delta}{L} \qquad \text{(D.3.2)}$$

where

δ is the possible error at each box end, δ= 0.156 mm

L is the length of the box, L=150 mm

Hence

$$\delta\theta_b = 0.12^o$$

D.3.2 Uncertainty in the Measured HIA in Air

As shown in fig.D.5, the HIA in air is measured using a very sensitive light power detector. There is a small pinhole of 0.1mm diameter at the head of the detector. This head is mounted on a track and can be adjusted in all directions. The centre of each laser beam is decided according to the maximum light intensity detected by a sensor behind the pinhole. The distance between the two laser beams is measured twice at two different stations as shown in fig.D.6. Among these two measurements, the crossing point of the two laser beams is chosen as one of them. The HIA of the two laser beams in air is

$$\tan(\theta) = \frac{AB}{2L} \qquad \text{(D.3.3)}$$

The readings from the twice measurements are:

AB= 59.05 ± 0.1 mm

L= 260 ± 0.5 mm

The calculated HIA and its uncertainty are

θ=6.478624 ± 0.0167°

D.3.3 Uncertainties in Alignments

D.3.3.1 Axial misalignment

—— Axial measurement

Fig.D.7 shows the possible axial misalignment between the LDA system and the test section in axial velocity measurements. In an ideal setting, the bisection line of the two laser beams should be perpendicular to the pipe axis. The alignment is achieved by adjusting the laser system until the reflected laser beams from the pipe surface form symmetric images on a reflection device fixed in the front of the front lens. Because of the blurred diameters of the reflected laser beam images, errors could occur in the determination of their central positions. The uncertainties in the determined central positions are half the image diameter and one diameter error is taken for 95% confidence level. The diameter of the used laser beam is 1.3mm at an intensity of $1/e^2$.

In fig.D.7, C is the ideal image position of the reflected laser beam from point A, so

$$\overline{AB} = \overline{BC} \qquad (D.3.4)$$

Due to the possible misalignment, the determined image position might be at C'. The distance between point C and point C' is one laser image diameter. As shown in fug.D.7, δ is given by

$$\delta = L[\tan(\theta+2\delta\theta_{axiz})-\tan(\theta)] \qquad (D.3.5)$$

In the alignment, L is 220mm and δ is 1.3mm.

Hence the uncertainty in the angle is

$\delta\theta_{axiz}$ = 0.167°

———Circumferential measurement

Fig.D.8 shows the possible axial misalignment between the laser system and the test section in circumferential velocity measurements. Ideally, the plane formed by the two laser beams should be perpendicular to the test section. The alignment is adjusted to allow the reflected beams in the same plane as the incident beams on the reflection device. The uncertainties are also caused in the determination of the central positions of the reflected laser beam images on the reflection device. Because of the uncertainty, the laser beams probably have a small angle with the y axis as shown in fig.D.8. This angle is

$$\tan(\delta\theta_{cirz}) = \frac{\delta}{2L} \qquad (D.3.6)$$

In the alignment, L= 220 mm and δ = 1.3mm, then

$\delta\theta cirz = 0.169^{\circ}$

D.3.3.2 Angular misalignments

—— Axial measurement

The angular uncertainty is the possible errors between the laser system and the test section in the pipe tangential direction. In the axial velocity measurements, this error can cause the two laser beams and the pipe axis in different horizontal planes as shown in fig.D.9.

Due to the error Δx_{axix}, an incident angle exists at the reflection point on the pipe surface and the laser beams are not reflected back in the same horizontal plane as their incident beams. The incident angle is

$$\sin(\delta\theta) = \frac{\Delta x_{axix}}{R_1} \qquad (D.3.7)$$

and

$$\tan(2\delta\,\theta_{axix}) = \frac{\delta}{L} \qquad (D.3.8)$$

In the alignment, L= 220 mm, δ = 1.3 mm and R_1= 62.23 mm. So

$\delta\theta_{axix} = 0.169^{\circ}$

Δx_{axix} = 0.184 mm

——Circumferential measurement

In circumferential velocity measurements, the angular alignment between the pipe and the laser system is adjusted without the matching box. The alignment is achieved by moving the laser system to make the reflected laser beams producing symmetric reflected images on the reflection plane. As shown in fig.D.10, the ideal image of the laser beam one is at point C, the possible image of the beam is point C' due to the misalignment Δx_{cirx}. Therefore

$$\sin(\delta\theta_{cirx}) = \frac{\Delta x_{cirx}}{R_i} \qquad (D.3.9)$$

and

$$\delta = CC' = L\,[\tan(\theta) - \tan(\theta - 2\delta\,\theta_{cirx})] + \Delta x_{cirx} \qquad (D.3.10)$$

In the alignment, L is 220 mm and δ is 1.3 mm, so

$\delta\theta_{cirx}$=0.147°

Δx_{cirx} = 0.160 mm

After this alignment is finished, the matching box is fitted on. Its position is adjusted as shown in fig.D.11. The angular uncertainty of the front surface of the box is

$$\tan(\theta + 2\,\delta\theta_{cirb}) - \tan(\theta) = \delta/L \qquad (D.3.11)$$

δ is equal to the diameter of the blurred laser beam image of 1.3mm and L is 220mm, so

$\delta\theta_{cirb}$ =0.167°

D.4 Uncertainties in CVP and HIA

All those uncertainties analysed above contribute to the uncertainties in the CVP and the HIA. The input parameters and their uncertainties are summarised here.

D.4.1 Laser beams

D.4.1.1 Axial measurement:

The direction parameters and their uncertainties are

$p=0$	$\delta p=\delta\theta_{axiz}$
$q=-\cos\theta$	$\delta q=\delta\theta*\sin\theta$
$r=-\sin\theta$	$\delta r=\delta\theta*\cos\theta$
$u=0$	$\delta u=\delta\theta_{axiz}$
$v=-\cos\theta$	$\delta v=\delta\theta*\sin\theta$
$w=\sin\theta$	$\delta w=\delta\theta*\cos\theta$

In the measurements, the laser platform is moved to the required position relating to a reference position crossed by three reference planes. In the x direction, the reference plane is the horizontal plane with the pipe axis. The position is determined as the angular alignment between the laser system and the pipe in axial velocity measurements. The reference plane in the y direction is the vertical plane tangential to the inner surface of the pipe wall. By moving the control volume across the inner surface of the pipe in y direction on the x reference plane, the inner seuface of the pipe wall is found when the PM output reachs its maximum value. The reference plane in z direction is chosen at a cross section of the step edge on the perspex pipe. When the control volume is moving cross the step edge in z direction, a large PM output can be detected. Those three planes together determine the reference point.

The position of the reference plane in x direction is determined according to the reflected images as the angular alignment for axial velocity measurements. So the uncertainty in the x coordinate of the reference position is δx_{axix}, i.e. $\delta x_r = \delta x_{axix}$.

The determination of the reference point in y and z directions is based on the PM output and the output is dependent on the central position of the control volume. The maximum output can be only found when the central section of the control volume is on the reference planes. The dimension of the control volume(Herschy, 1985) is

$$l_c = \frac{\lambda f_f}{\pi D_{e-2}} \frac{1}{\sin\theta} \qquad (D.4.1)$$

$$d_c = \frac{\lambda f_f}{\pi De-2} \frac{1}{\cos\theta} \qquad (D.4.2)$$

$D_{e^{-2}}$ is the beam diameter at an intensity of $1/e^2$ and f_f is the focal length of the front lens. In the used laser system, l_c is 0.97mm and d_c is 0.12mm.

Because only when the central cross section of the control volume is focused on the reference plane, the maximum scattered signal can be obtained from the PM output, so the uncertainties of the control volume position are half dimensions of the control volume. The uncertainties of the reference position are

δy_r = 0.48mm

δz_r = 0.06mm

After the reference point is determined, the control volume is moved to the required position by adjusting the platform in three directions. The uncertainties of each platform setting are

$\delta x'$= 0.1mm

$\delta y'$= 0.1mm

$\delta z'$= 0.1mm

And the total uncertainties of every setting are

δx_i=0.21mm

δy_i=0.49mm

δz_i=0.1mm

δx_a=0.21mm

δy_a=0.49mm

δz_a=0.1mm

D.4.1.2 Circumferential measurement:

The direction parameters and their errors are

p_i =-sinθ	δp_i=δθ*cosθ
q_i=-cosθ	δq_i=δθ*sinθ
r_i=0.	δr_i=$\delta\theta_{cirz}$
u_a= sinθ	δu_a=δθ*cosθ
v_a=-cosθ	δv_a=δθ*sinθ
w_a=0	δw_a=$\delta\theta_{cirz}$

The uncertainties of laser platform setting are

δx_i=0.21mm

δy_i=0.49mm

δz_i=0.1mm

δx_a=0.21mm

δy_a=0.49mm

δz_a=0.1mm

D.4.2 Uncertainties of the Matching Box Surfaces

The uncertainty of the matching box comes from the manufacture uncertainties $\delta\theta_b$ in axial direction and the angular uncertainties of its setting. The actual equation would be

$$Ax + By + Cz + D = 0$$

The parameters in the above equation and their uncertainties are

$$A = B\tan\alpha_{cirb}$$

$$B = 1/\sqrt{1. + \tan^2\alpha_{cirb} + \tan^2\delta\theta_b}$$

$$C = B\tan\alpha_b$$

The input parameters and their uncertainties are

A_o=0	δA_o=6.6x10^{-3}
B_o=1	δB_o=4.46x10^{-4}
C_o=0	δC_o=2.7x10^{-3}
D_o=77.38.mm	δD_o=0.2mm
Ai=0	δA_i=6.6x10^{-3}
Bi=1.	δB_i=4.46x10^{-4}
C_i=0	δC_i=2.7x10^{-3}
D_i= 75 mm	δD_i=0.2mm

D.4.3 Uncertainties of the pipe radii

The uncertainties of the pipe radii are

R_1 =62.23mm	δR_1 = 0.04mm
R_2 =50.8 mm	ΔR_2 = 0.04mm

Using the uncertainties of those parameters, the uncertainties in the CVP and the HIA can be calculated, the result is presented in chapter 7.

D.5 Uncertainties of Doppler Signals

The uncertainties of the obtained doppler signals depend on the nature of the used fluid, the used laser light and the signal processing system. Actually, the signal processing system contributes almost all the doppler signal uncertainty. The standard deviation of the transit time of the PM is only 0.6ns according to manufacturer's specification(THORN EMI 1986), so the uncertainty due to the PM is ignored here. The main uncertainties of the signal processing system are:

(1) δf_1: frequency shift modulators.

(2) δf_2: spectrum analyser.

(3) δf_3: ADC.

(1) δf_1 — After the laser beams pass through the bragg cell, a different shifted frequency is presented to each of them.

The 40MHz nominal modulator has an output of:

$$f_1 = 39.99457 \pm 1.999 \times 10^{-4} \text{ MHz} \qquad \text{(D.5.1)}$$

The 37.6MHz nominal modulator hasan output of:

$$f_2 = 27.59848 \pm 1.879 \times 10^{-4} \text{ MHz} \qquad \text{(D.5.2)}$$

The difference between them is

$$f_S = f_1 - f_2 \qquad \text{(D.5.3)}$$

The uncertainty of the frequency difference is

$$\delta f_S = \sqrt{\delta f_1^2 + \delta f_2^2} = 2.734 \times 10^{-4} \text{ MHz} \qquad \text{(D.5.4)}$$

(2) δf_2 ——The uncertainty of the spectrum analyser comes from the errors of the central frequency position setting, the scan width accuracy(SWA), the long term drift (LTD) and the temperature drift(TD). Their uncertainties are

CFP at 0 to 11 MHz	0.005MHz
SWA at 0.05MHz/Div	0.010 MHz
LTD	0.1×10^{-3} MHz/10min
TD	0.2×10^{-3}MHz/C

To reduce the long term shaft, the central frequency is checked in every two hours, the LTD uncertainty is 1.2×10^{-3} MHz.

The maximum temperature difference surrounding the spectrum analysis during one day testing is 8^{o}. The uncertainty of the temperature shaft TD is 1.6×10^{-3} MHz.

Then the SA total uncertainty is

$$\delta f_2=10^{-3}\sqrt{5^2+10^2+1.6^2+1.2^2}=0.0112\text{MHz} \qquad (D.5.5)$$

(3) δf_3 —— A ramp function from 0 to 8 VDC resolves the whole screen of the SA. Any signal inside the SA frequency definition is converted into a voltage digital signal through an ADC. The uncertainty of the output voltage is

$$\delta V = 2.\times 8/256 = 0.0625 \text{ (volts)} \qquad (D.5.6)$$

On SA front panel, the central frequency is set at 2.4MHz and the Scan width is always set at 0.05MHz/div for circumferential velocity measurements. The relation between the doppler frequency and the output voltage for circumferential velocity measurements is

$$f_d \text{ (MHz)} = 0.05V + 2.2 \qquad (D.5.7)$$

So the doppler frequency uncertainty due to the ADC is

$$\delta f_3 = 3.125\times10^{-3} \text{ MHz}.$$

The total uncertainty of the doppler signal is

$$\delta f_{d1} = \sqrt{\delta f_1^2+\delta f_2^2+\delta f_3^2} = 0.0116 \text{ MHz}$$

Scan width is set at 0.1MHz/div for axial velocity measurements. The relation between the doppler frequency and the output voltage is

$$f_d \text{ (MHz)} = 0.1V + 2 \qquad (D.5.8)$$

and the total uncertainty of the doppler signal is

$$\delta f_{d2} = \sqrt{\delta f_1^2+\delta f_2^2+\delta f_3^2} = 0.0128 \text{ MHz}$$

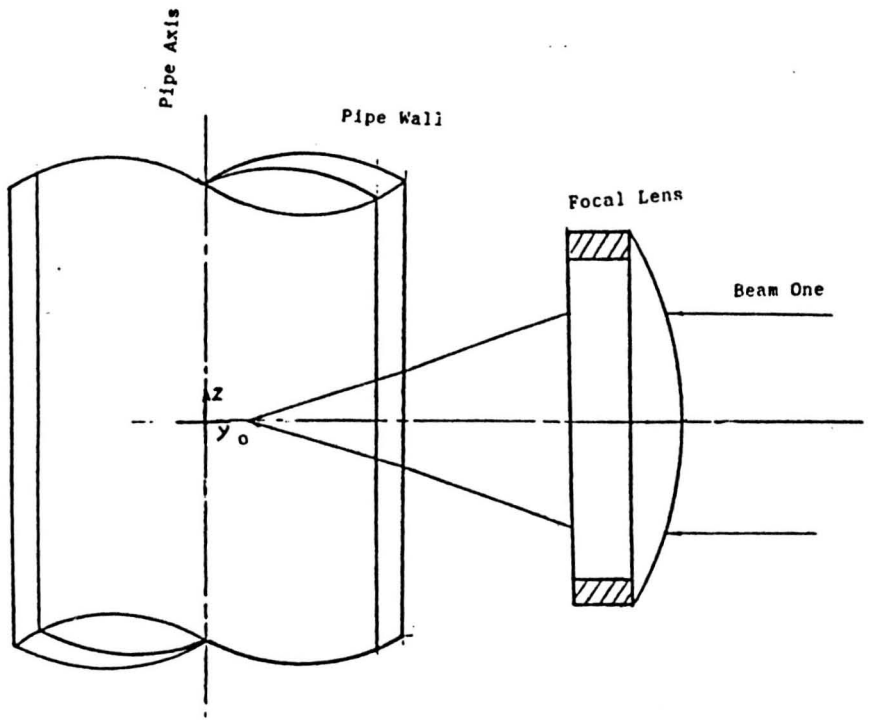

FIG. D.1 LAYOUT FOR AXIAL MEASUREMENT

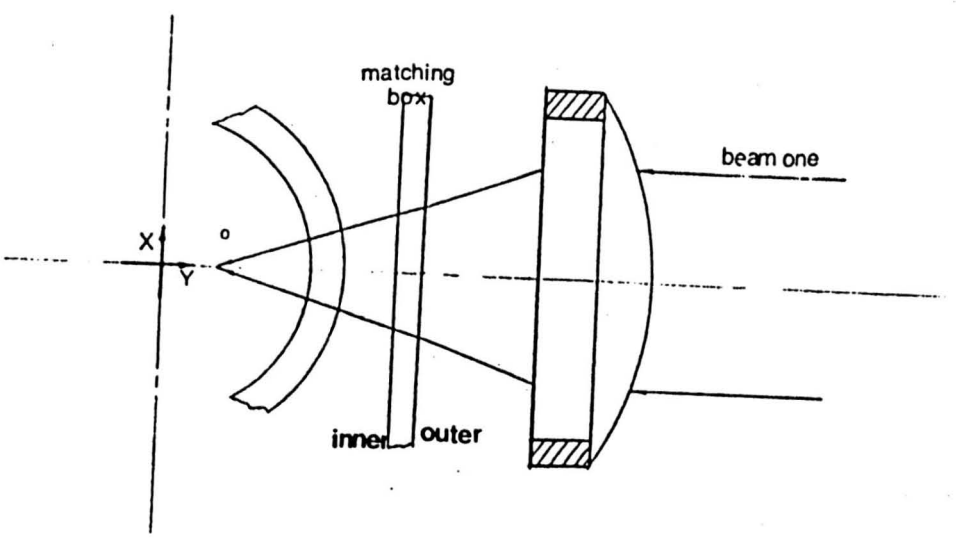

FIG. D.2 LAYOUT FOR CIRCUMFERENTIAL MEASUREMENT

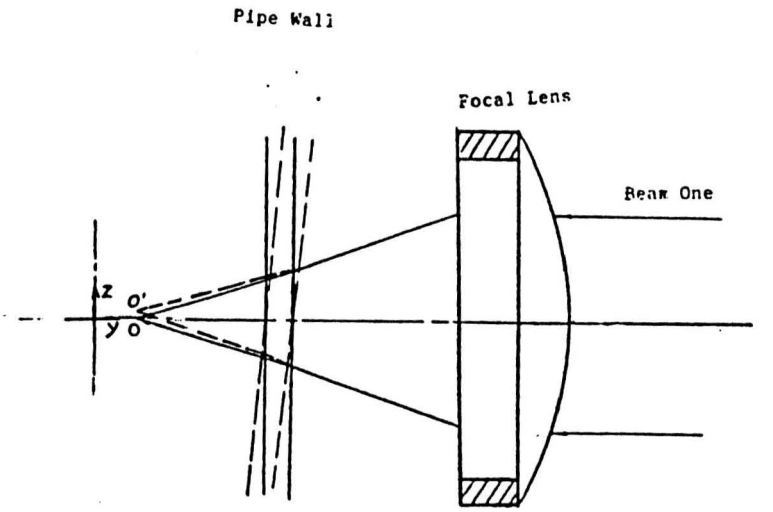

FIG. D.3 EXAMPLE OF MEASUREMENT WITH MISALIGNMENT

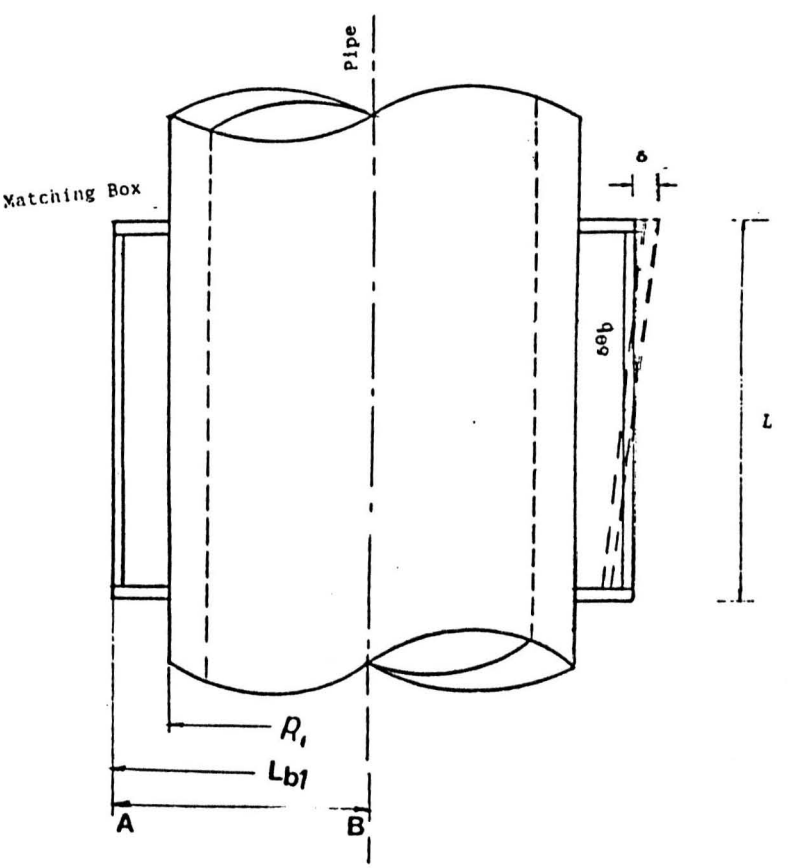

FIG. D.4 MATCHING BOX UNCERTAINTIES

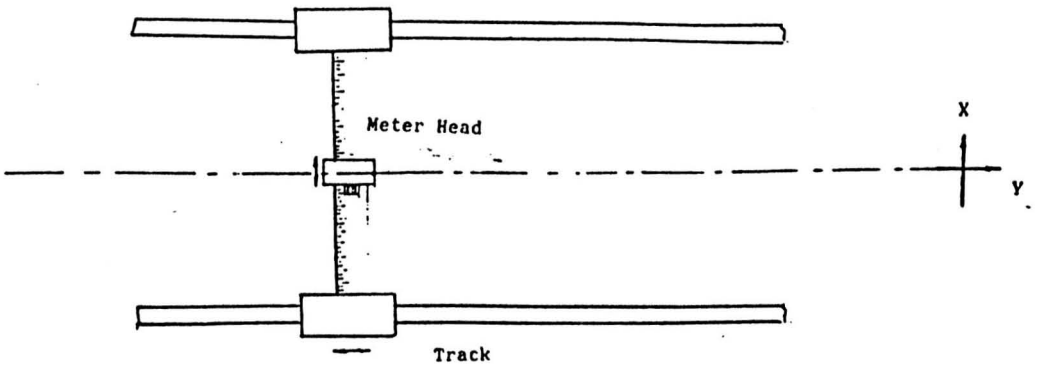

FIG. D.5 TRACK FOR LASER CONSTANT MEASUREMENT

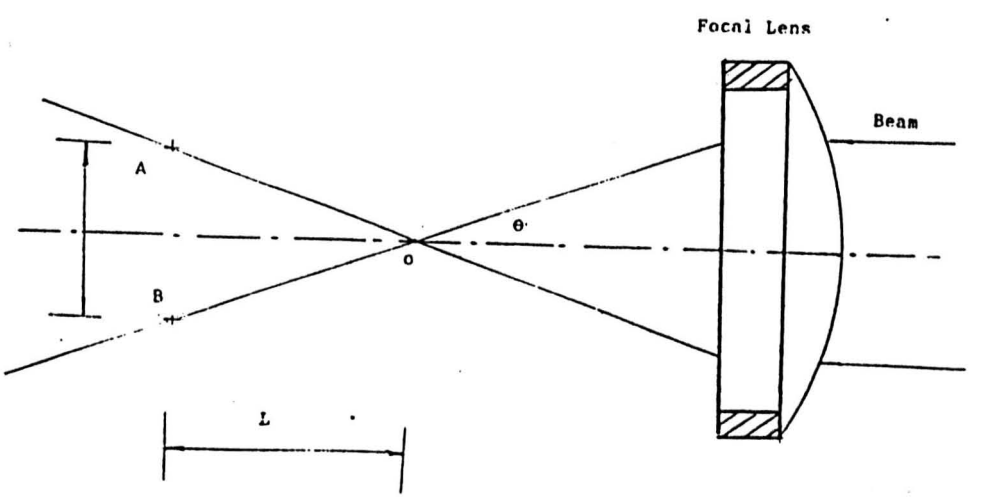

FIG. D.6 LASER CONSTANT MEASUREMENT

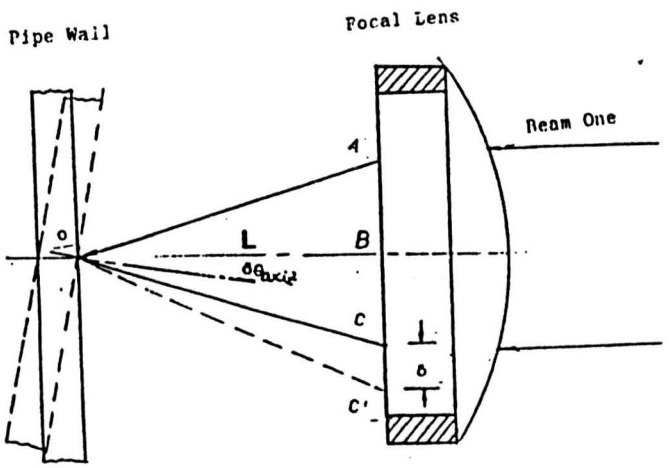

FIG. D.7 AXIAL MISALIGNMENT (axial measurement)

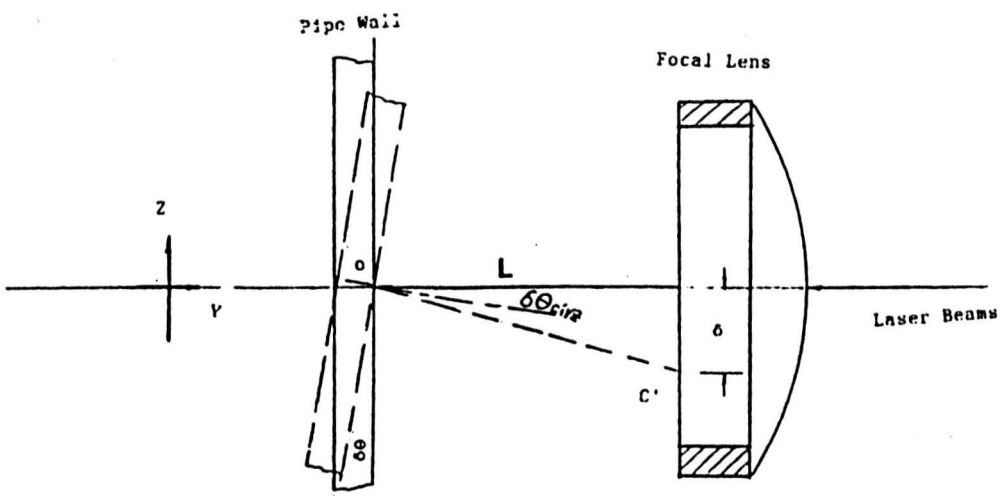

FIG. D.8 AXIAL MISALIGNMENT (circumferential measurement)

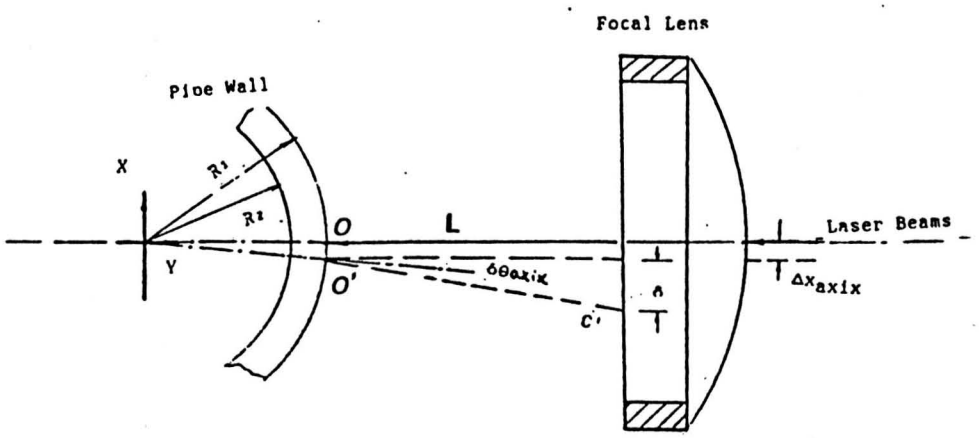

FIG. D.9 ANGULAR MISALIGNMENT(axial measurement)

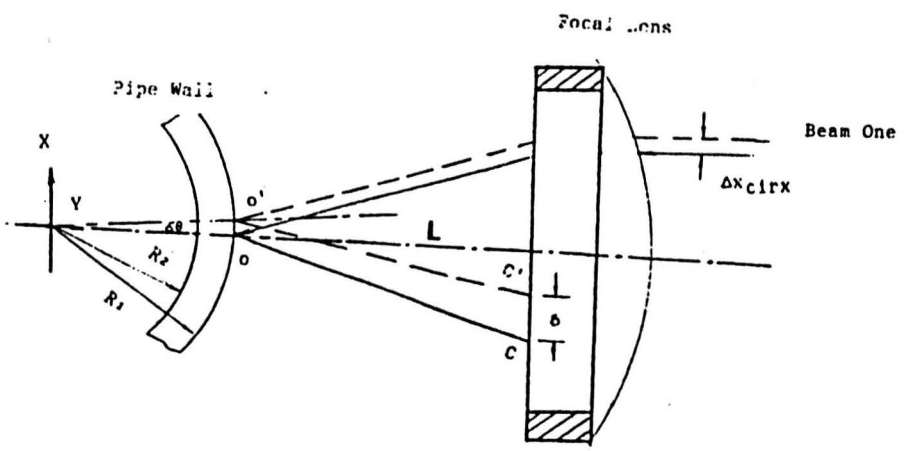

FIG. D.10 ANGULAR MEASUREMENT (circumferential measurement)

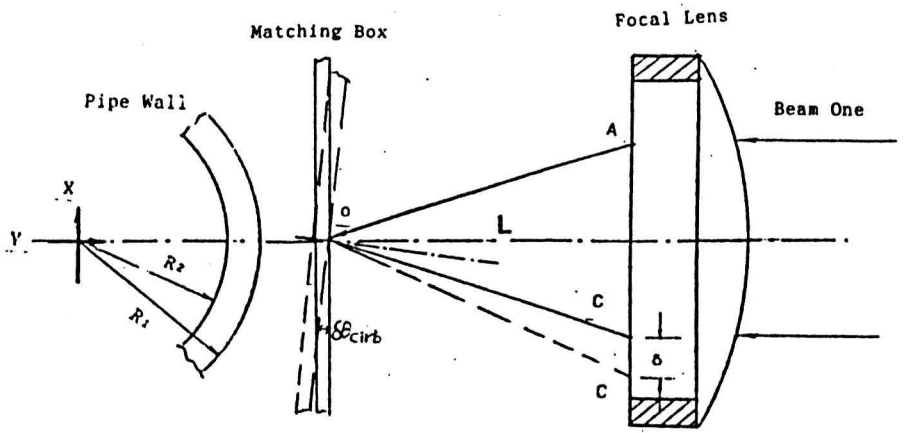

FIG. D.11 MATCHING BOX MISALIGNMENT